TECHNETIUM AND RHENIUM SCHIFF BASE COMPLEXES

FOR NUCLEAR MEDICINE

_____

A Dissertation

presented to

the Faculty of the Graduate School

at the University of Missouri-Columbia

_____

In Partial Fulfillment

of the Requirements for the Degree

Doctor of Philosophy

_____

by

JAKOB EDWIN BAUMEISTER

Dr. Silvia S. Jurisson, Dissertation Supervisor

DECEMBER 2019

The undersigned, appointed by the Dean of the Graduate School, have examined the

dissertation entitled

TECHNETIUM AND RHENIUM SCHIFF BASE COMPLEXES FOR

NUCLEAR MEDICINE

presented by Jakob Edwin Baumeister

a candidate for the degree of Doctor of Philosophy

and hereby certify that in their opinion it is worthy of acceptance

Professor Silvia S. Jurisson   _____

Professor Wesley H. Bernskoetter   _____

Professor Susan Z. Lever   _____

Professor Michael R. Lewis   _____

ACKNOWLEDGMENTS

ii

TABLE OF CONTENTS

LIST OF FIGURES

xi

LIST OF TABLES

LIST OF SCHEMES

TECHNETIUM AND RHENIUM SCHIFF BASE COMPLEXES FOR NUCLEAR MEDICINE

Jakob Edwin Baumeister

Dr. Silvia S. Jurisson, Dissertation Supervisor

ABSTRACT

This dissertation investigates the synthesis of rhenium and technetium Schiff base complexes for potential applications in nuclear medicine. In Chapter 2, a series of mixed ligand Re(III) complexes of the form *trans*-[Re(PR$_3$)$_2$(tmf$_2$en)]$^+$ were prepared by microwave assisted synthesis. A two-step (one-pot) procedure was utilized. In the first step, the Re(V) precursor (*n*Bu$_4$N)[ReOCl$_4$] is reacted with the Schiff base ligand forming *trans*-[ReOCl(tmf$_2$en) *in situ*. In the second step, a tertiary phosphine ligand is added yielding the reduced *trans*-[Re(PR$_3$)$_2$(tmf$_2$en)]$^+$ species. The preparation of these *trans*-[Re(PR$_3$)$_2$(tmf$_2$en)]$^+$ complexes by microwave assisted synthesis resulted in higher reaction yields and shorter reaction times compared to syntheses of similar Re(III) Schiff base complexes. The general methodology proved to be useful for the synthesis of mixed ligand Re(III) complexes with a diverse range of Schiff base ligands and phosphines.

Chapter 3 investigated the steric influence of salicylaldehyde-based N$_2$O$_2$ Schiff base ligands on the formation and stability of mixed ligand Re(III) and Tc(III) compounds. A series of Re(III) complexes of the form trans-[Re(PR$_3$)$_2$(L)]$^+$ were prepared with the Schiff base ligands sal$_2$en and sal$_2$ibn. Rhenium(III) complexes with the sterically unencumbering sal$_2$en ligand were observed to be stable in solution, while complexes with the sterically encumbering sal$_2$ibn ligand were observed to oxidize to isoelectronic oxorhenium(V) species. The ^{99m}Tc compounds [^{99m}Tc][Tc(PEt$_3$)$_2$(sa$_2$len)]$^+$

and $[^{99m}Tc][Tc(PEt_3)_2(sa_2libn)]^+$ were prepared for an assessment of their stability in aqueous solution. The $[^{99m}Tc][Tc(PEt_3)_2(sa_2len)]^+$ species stable in solution. The $[^{99m}Tc][Tc(PEt_3)_2(sa_2libn)]^+$ species underwent rapid degradation in solution. The degradation product was identified as $[^{99m}Tc][TcO(PEt_3)(sal_2ibn)]^+$ indicating that conversion of the ^{99m}Tc(III)-sal$_2$ibn species mirrored that of the Re(III)-sal$_2$ibn species.

Chapter 4 examined the formation and stability mixed ligand Re(III) and Tc(III) complexes with model bifunctional Schiff base ligands. A series of backbone-functionalized Schiff base ligands was used to prepare Re(III) complexes of the form *trans*-[Re(PEt$_3$)$_2$(L)]$^+$ in order to assess strategies for incorporating biomolecules into Q-complexes. The two primary strategies under investigation for biomolecule incorporation were the use of propanamide linkers or benzamide linkers in the Schiff base backbone. The ^{99m}Tc(III) compounds $[^{99m}Tc][Tc(PEt_3)_2(L)]^+$ were prepared for comparison with their Re(III) analogues. A preliminary stability study of the various ^{99m}Tc(III) complexes was performed in aqueous solution. Technetium-99m complexes with the flexible propanamide linker were observed to oxidize in solution, whereas ^{99m}Tc complexes with the rigid benzamide linker displayed superior stability in solution. Mixed ligand Re(III) and Tc(III) Schiff base complexes incorporating benzamide-linked targeting biomolecules are proposed as a novel class of bifunctional radiopharmaceuticals.

CHAPTER 1

Introduction

1.1 Nuclear Medicine

Nuclear medicine is a specialized field of radiology that utilizes radioactive compounds—called radiopharmaceuticals—for diagnostic or therapeutic purposes. Foundational to nuclear medicine is the radiotracer principle—the idea a radioactive compound can be used as a marker for a chemically identical stable compound. The radiotracer principle is credited to George de Hevesy, who in 1913 used radioisotopes of lead to study the solubility of lead salts.[1] After realizing this principle could be applied to biological systems, de Hevesy used radioisotopes to study lead uptake in plants, and phosphorus metabolism in rats.[2, 3] The 1943 Nobel Prize in Chemistry was awarded to de Hevesy for his pioneering work on radiotracers. The radiotracer principle allows for the non-invasive investigation of chemical processes, such that the system under investigation is unperturbed. The radiotracer principle was first applied to humans in 1926 when Hermann Blumgart and Otto Yens injected 37-222 MBq of ^{214}Bi in human patients to measure arm-to-arm blood circulation times.[4] Their work birthed the field of diagnostic nuclear medicine. The first therapeutic application of nuclear medicine occurred in 1936 when John Lawrence used ^{32}P for the treatment of leukemia and polycythemia vera in human patients.[5] Early research in nuclear medicine focused on targeting whole organs using radioactive ions or colloids. Iodine-131 was developed as a treatment for thyroid disorders, such as hyperthyroidism and thyroid cancer.[6] The use of $[^{131}I]I^-$ relies on the high natural affinity of the thyroid gland for ionic iodine. Phosphorus-32 was applied to the treatment of painful bone metastases taking advantage

of the natural affinity of bone tissue for inorganic phosphates.[7] Strontium-89 was similarly used to treat painful bone metastases utilizing $[^{89}Sr]Sr^{2+}$, which functions as a Ca^{2+} mimic.[7] These radionuclides were successful largely due to their simple targeting mechanisms, however, few biological processes can be targeted using such rudimentary methods however. Simple coordination complexes incorporating radionuclides began to be developed in the 1970s in response to this limitation. One of the first complexes of this type was $[^{99m}Tc]Tc$-DTPA (**Figure 1.1**).[8, 9] Technetium-99m-DTPA is formed by the addition of $[^{99m}Tc]TcO_4^-$ to a radiopharmaceutical kit containing DTPA (diethylene triamine pentaacetic acid) and a reducing agent. The $[^{99m}Tc]Tc$-DTPA complex is injected intravenously and subsequently removed from the bloodstream by glomerular filtration. Physicians use $[^{99m}Tc]Tc$-DTPA clinically to assess kidney function and measure glomerular filtration rates. Other examples of coordination complexes developed for nuclear medicine are $[^{153}Sm]Sm$-EDTMP (Quadramet®) for treatment of bone metastases and $[^{99m}Tc]Tc$-sestamibi (Cardiolite®) for myocardial perfusion imaging (**Figure 1.1**). While the development of radiometal coordination complexes expanded the diagnostic and therapeutic scope of nuclear medicine, these complexes were largely limited to targeting whole organs. Modern nuclear medicine has focused on receptor-specific targeting. Radiopharmaceuticals of this nature incorporate a radionuclide into a biological targeting vector—such as a peptide or antibody—allowing for uptake at a specific biological receptor. This is especially useful for cancer diagnosis and treatment as cancerous tissues can often be discriminated from healthy tissues by their unique receptor expression. One example of a receptor-specific radiopharmaceutical is $[^{177}Lu]Lu$-DOTATATE (Lutathera®), which was recently approved in the United States

2

for treatment of adult patients with somatostatin receptor-positive gastroenteropancreatic neuendocrine tumors (GEP-NETS) (**Figure 1.2**).[10] Although nuclear medicine has become more sophisticated, the radiotracer principle remains foundational to the field. The aim of nuclear medicine is to give physicians more and better tools for the diagnosis and treatment of disease.

[99mTc]Tc-DTPA   [153Sm]Sm-EDTMP   [99mTc]Tc-sestamibi
                        Quadramet®   Cardiolite®
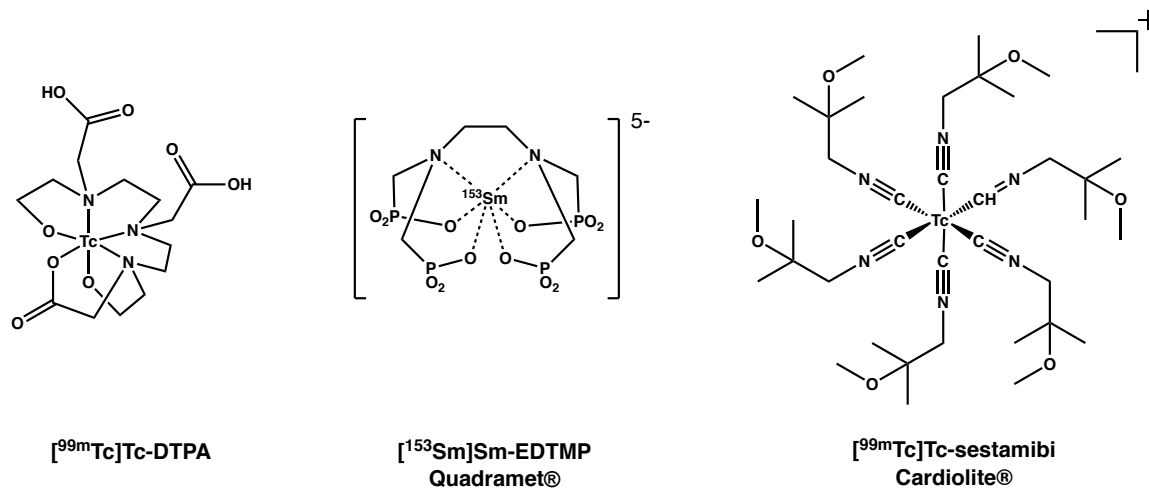
Figure 1.1. Structures of [99mTc]Tc-DTPA, [153Sm]Sm-EDTMP (Quadramet®), and [99mTc]Tc-sestamibi (Cardiolite®).
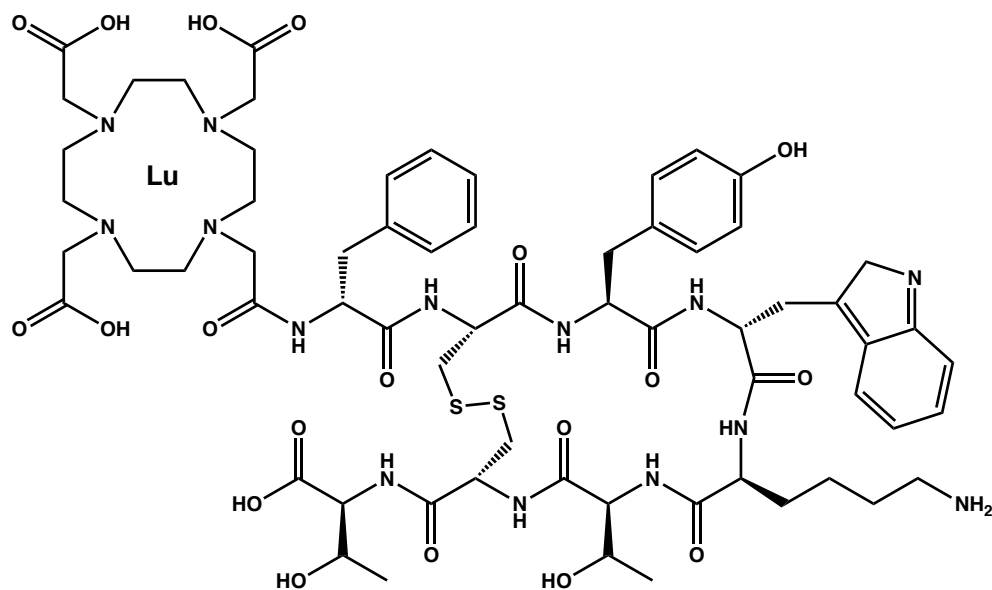
Figure 1.2. Structure of [177Lu]Lu-DOTATATE (Lutathera®).

3

1.2 Introduction to Radiopharmaceuticals

Radiopharmaceuticals are compounds containing a radionuclide used for diagnostic or therapeutic purposes. Diagnostic radiopharmaceuticals generate images of the inner functionality of the human body. Therapeutic radiopharmaceuticals provide treatment for a specific disease. While the goals for these two types of radiopharmaceuticals differ, their overarching design is quite comparable.

Diagnostic Imaging

Nuclear medicine has been instrumental to observing human physiology that is inaccessible to other diagnostic methods such as magnetic resonance imaging (MRI) or X-ray imaging. Diagnostic radiopharmaceuticals are distinctive as internal imaging tools. A diagnostic radiopharmaceutical administered to a patient will localize at a particular organ or tissue where radioactive decay by the radionuclide produces gamma ray or photon emissions. The poor interaction of gamma rays with cellular tissues allows for internalized radionuclides to be observed by external detectors with high spatial resolution. Diagnostic radiopharmaceuticals can be used for disease diagnosis by indicating the presence and extent of malignant tissues. They can also for functional imaging of organs, as with agents for myocardial perfusion or gastric emptying.

The two principle radiopharmaceutical imaging techniques are single photon emission computed tomography (SPECT) and positron emission tomography (PET). SPECT imaging utilizes radionuclides that emit gamma rays either through isomeric transition or nuclear de-excitation. An ideal SPECT radionuclide will emit a single, monoenergetic gamma ray. SPECT imaging uses a gamma camera to obtain multiple 2-D images, each at a different angle. The 2-D data set can be reconstructed through

computed tomography to yield a 3-D data set. The most important SPECT radionuclides are ^{99m}Tc, ^{111}In, and ^{123}I.

PET imaging utilizes proton rich radionuclides that decay by emission of a positron—a positively charged electron—from the nucleus. A positron emitted from the nucleus will collide with an electron, resulting in electron-positron annihilation. The masses of the electron and positron are converted into two 511 keV photons emitted at nearly 180 degrees to each other. The two photons can be counted by coincidence detection using a ring of detectors encircling the patient. High-resolution 3-D images can be obtained by imaging a patient over multiple orientations and then using computed tomography to reconstruct the data. The most important PET radionuclides are ^{11}C, ^{18}F, and ^{68}Ga.

The image clarity obtained from SPECT imaging is lower than that obtained from PET imaging. SPECT scans are significantly cheaper than PET scans, in part because they use longer-lived and more readily available radionuclides than PET. Although PET provides superior image quality, the practical application of this technology is limited by the paucity of positron emitters, their relative short half-lives, and their expensive accelerator-based production methods. There is ongoing research to develop radiopharmaceuticals with longer half-life positron emitters such as ^{44}Sc, 7^2As, and ^{89}Zr.

Radiotherapy

Therapeutic radionuclides emit charged particles—alpha particles, beta particles, Auger electrons, or conversion electrons—that deposit their decay energy within biological tissues. Radioactive decay in biological tissues causes DNA damage—through direct or indirect action—resulting in cell death. Direct damage occurs through the action

of emitted particles on the DNA structure causing single- and double-strand breaks. Indirect damage occurs by the action of free radicals and reactive oxygen species generated by emitted particles on the DNA structure.

Beta decay results in the emission of beta particles (β^-) exhibiting a continuous kinetic energy spectrum. Beta particles are highly penetrating in biological tissues due to their small mass and low charge. Linear energy transfer (LET) is the measure of the energy deposited by ionizing radiation over a given distance. Beta particles exhibit low LET meaning they deposit their decay energy over a relatively long distance in the body. This can be useful in the treatment of large tumors as the beta particles can penetrate throughout the entire tumor volume. It can also be a disadvantage as beta particles can potentially penetrate into healthy tissues adjacent to targeted tissues. Examples of beta-emitting therapeutic radionuclides include ^{67}Cu, ^{90}Y, ^{153}Sm, and ^{188}Re.

Alpha decay results in the emission of monoenergetic alpha particles (He^{2+}). Alpha particles exhibit high LET as their large mass and significant charge results in a short path length in biological tissues. Alpha particles affect substantial cell death within a short distance. Alpha-emitting radiopharmaceuticals maximize radiation dose to targeted tissues while minimizing radiation dose to non-targeted tissues. Many alpha emitters decay through radioactive decay chains yielding multiple alpha particles. This further increases the therapeutic dose given to targeted tissues. One disadvantage of alpha therapy is the instability of many metal chelate complexes containing alpha emitters. The recoil energy associated with alpha decay can be strong enough to eject the daughter radionuclide from the chelate leading to unbound daughter radionuclides accumulating in non-targeted sites. It is important that chelates for alpha-emitters exhibit high

thermodynamic stability. Alpha therapy is most effective for treatment of small tumors or for neoadjuvant therapy. Examples of alpha-emitting therapeutic radionuclides include ^{211}At, ^{213}Bi, ^{223}Ra, ^{225}Ac, ^{226}Th, and ^{230}U.

Electron capture is a process that can result in the emission of low-energy Auger electrons. Electron capture occurs when a proton rich nucleus absorbs an inner-shell atomic electron. The vacancy left by the absorbed electron is filled by the downward transition of an outer shell electron. This transition will sometimes be accompanied by emission of a gamma photon whose energy matches the energy gap between the upper and lower level. In other cases, the energy released from the downward transition is transferred to an outer shell electron that is subsequently ejected from the atom with energy equal to the transition energy minus the electron binding energy. Each electron capture event produces a multiplicity of these low-energy Auger electrons. Auger electrons are a high LET form of radiation. They bear the same mass and charge of a beta particle. Due to their lower energy, Auger electrons deposit their decay energy over a much shorter range than beta particles. They are useful for treatment of small tumor and neoadjuvant therapy due to their short range in tissue. Examples of Auger-emitting radionuclides include ^{119}Sb, ^{111}In, and ^{161}Ho.

Internal conversion results in the emission of inner-shell orbital electrons from deexcitation of an excited nucleus. Electrons emitted through internal conversion—termed conversion electrons—are low in energy and have a discrete energy spectrum. Internal conversion is possible for any radionuclide that emits gamma rays. It is common for low-energy Auger electrons and X-rays to be emitted alongside conversion electrons during the process of internal conversion. Many beta-emitting radionuclides also emit

conversion electrons. Conversion electrons, similar to Auger electrons, are a high LET form of radiation. Examples of conversion-electron emitting radionuclides include ^{58m}Co, ^{103m}Rh, and ^{117m}Sn.

1.3 Radiopharmaceutical Design

Nuclear medicine requires the effective delivery of specific radionuclides to specific sites in the body. In some cases, this can be accomplished using the radionuclide in a simple ionic form (i.e., $[^{131}I]I^-$ for thyroid treatments or $[^{89}Sr]Sr^{2+}$ for palliative bone therapy). In most cases, however, the radionuclide must be incorporated into a larger chemical complex. Radiopharmaceutical development requires designing complexes with attention to the chemistry of the radionuclide, the radionuclide decay properties, and the desired biological application. There are three main radiopharmaceutical design strategies—the small molecule approach, the integrated approach, and the bifunctional chelate approach (BFCA).

Small Molecule Approach

The small molecule approach (**Figure 1.3**) utilizes coordination complexes composed of a radionuclide and one or more ligands. Multidentate ligands called chelators are often employed. Small molecule radiopharmaceuticals are typically used as diagnostic agents to probe organ function. These complexes do not employ a receptor-specific targeting mode, rather, they exhibit an intrinsic interaction with a particular biological system on account of their chemical properties. It is possible to tune the biological properties of these complexes by modifying the ligand(s) with different functional groups. The overall charge of the complex can also be controlled through the selection of donor atoms or by changing the metal oxidation state. Neutral lipophilic

complexes can cross the blood-brain-barrier and are useful for brain imaging. Cationic lipophilic complexes will show heart uptake and are useful for myocardial perfusion imaging.

Bifucntional Chelate Approach

The bifunctional chelate approach (BFCA) is a target-specific method for radiopharmaceutical design (**Figure 1.3**). Bifunctional chelate complexes are composed of three distinct subunits—a chelator, a targeting vector, and a linker. The chelator serves to bind a specific radiometal. The targeting vector serves to guide the entire radiopharmaceutical to a specific site in the body. The targeting vector can be any peptide, antibody, DNA fragment, small molecule, or other moiety that allows for selective uptake at a tumor site. Tumor sites can be selectively targeted by biomolecules that bind to specific receptors overexpressed on tumors, target hypoxia, or exploit any other difference between tumor tissues and healthy tissues. The linker serves to connect the chelator to the targeting vector without compromising the biological activity of the latter. This type of modular approach allows for facile modification of bifunctional agents. Different linkers can be used to change the overall charge of the agent, vary the overall lipophilicity, or alter the spacing between the chelate and targeting vector. Different chelators can be used to alter the thermodynamic stability of the metal chelate complex or even to incorporate a different radiometal. Different targeting vectors can be incorporated to alter receptor binding properties. An example of the bifunctional radiopharmaceutical is [177Lu]Lu-DOTATATE (Lutathera®) used for the treatment GEP-NETs. The radiopharmaceutical is composed of 1,4,7,10-tetraazacyclododecane-1,4,7,10-

tetraacetic acid (DOTA) chelate that binds [^{177}Lu]Lu^{3+}, and the somatostatin-receptor targeting peptide Tyr^3-octreotate (D-Phe-Cys-Tyr-D-Trp-Lys-Thr-Cys-Thr-OH).

Integrated Approach

The integrated approach (**Figure 1.3**) is a target specific method of radiopharmaceutical design in which the radionuclide is directly integrated into the targeting vector. The radionuclide becomes an essential component of the targeting vector. This design allows for a better union between the radionuclide and the targeting vector, which can enhance receptor targeting. Although the integrated approach lacks ease of modification compared to the BFCA, it eliminates potential interference cause by a linker or chelate. Examples of the integrated approach include [^{18}F]FDG and [^{99m}Tc]Tc-TRODAT.
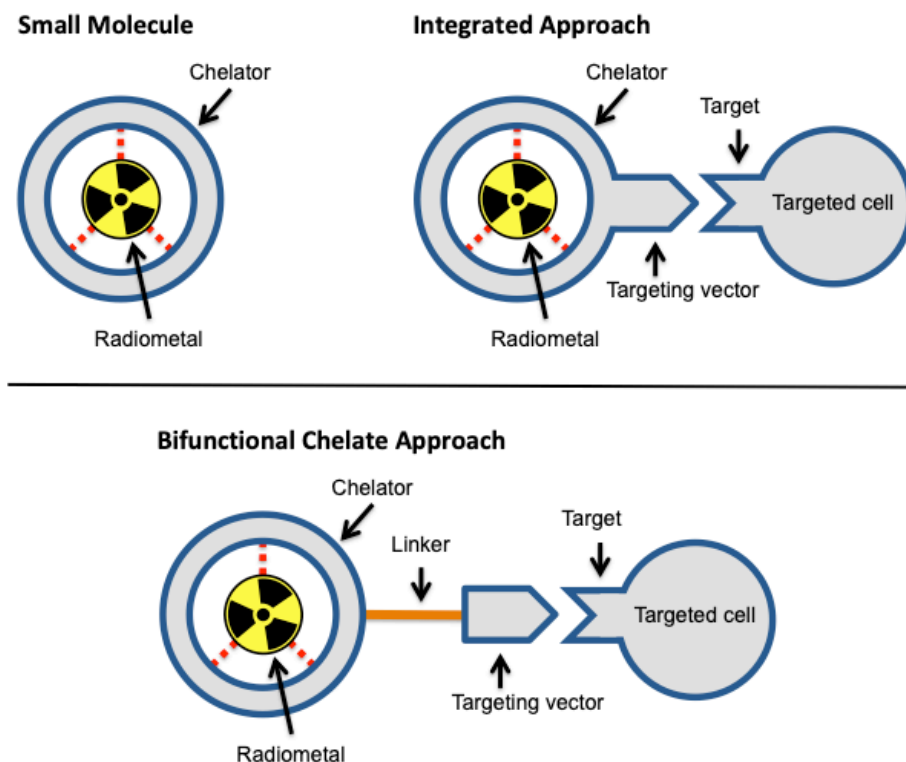
Figure 1.3. Comparison of radiopharmaceutical design approaches.

Practical Radiopharmaceutical Considerations

A number of practical considerations must be accounted for in radiopharmaceutical design. Radiopharmaceuticals should be prepared in high radiochemical purity and radiochemical yield. The goal for radiopharmaceutical synthesis is the formulation of a radiopharmaceutical kit, which contains all the reagents necessary for complex formation except the radionuclide. Addition of a radionuclide solution to the kit results in complex formation such that the radiopharmaceutical is ready for immediate injection. Kit formulations allow radiopharmaceuticals to be easily prepared and administered in hospital settings. Radiopharmaceuticals should exhibit high affinity for their intended biological target. The goal is to maximize the radiation dose delivered to targeted tissues, while minimizing the radiation dose delivered to non-targeted tissues. For diagnostic imaging, this produces higher quality images. For radiotherapy, this ensures healthy tissues are spared from radiation damage.

1.4 Radiochemistry of Technetium

Technetium-99m (^{99m}Tc; $t_{1/2} = 6.01$ h; $E\gamma = 140$ keV) is the most commonly used radionuclide in nuclear medicine owing to its favorable nuclear properties and availability from the $^{99}Mo/^{99m}Tc$ radionuclide generator. An estimated 40 million diagnostic imaging procedures are performed with ^{99m}Tc annually, with 16 million of these procedures occurring in the United States.[11] Technetium-99m decays by isomeric transition (89%) to the ground state ^{99g}Tc ($t_{1/2} = 2.11E+5$ y). The low incidence of conversion electrons (11%) minimizes the radiation dose absorbed by patients. The emission of a single 140 keV gamma ray is ideal for accurate detection by SPECT imaging. The half-life is long enough to obtain high-quality images of biological process,

while short enough to minimize patient radiation dose. Technetium-99m is obtained indirectly from beta decay of ^{99}Mo ($t_{1/2}$ = 66 h) in the form of the ^{99}Mo/^{99m}Tc generator. Technetium-99m generators exploit the transient equilibrium established by ^{99}Mo ($t_{1/2}$ = 66.0 h) as it decays to ^{99m}Tc. The ^{99}Mo/^{99m}Tc generator is prepared by loading [^{99}Mo]MoO$_4^{2-}$ onto an acidic alumina column. The beta decay of [^{99}Mo]MoO$_4^{2-}$ produces [^{99m}Tc]TcO$_4^-$. Elution of the column with 0.9% saline affords radiochemically pure [^{99m}Tc]TcO$_4^-$, while [^{99}Mo]MoO$_4^{2-}$ is retained on the column. The isolated [^{99m}Tc]TcO$_4^-$ can then be used to synthesize any of the various ^{99m}Tc SPECT radiopharmaceuticals. Technetium-99m generators can be transported over long distances for use in hospitals that do not have access to a nuclear reactor or other radionuclide production facilities.

Table 1.1: Selected nuclear decay properties for ^{99}Mo, ^{99m}Tc, and ^{99}Tc.

Radionuclide	$t_{1/2}$	Decay mode	E_x (I_x)	$J\pi$
Mo-99	65.4 h	β⁻ (100)	γ: 141 (89)	1/2+
			β⁻: 436 (16), 1214 (82)	
Tc-99m	6.01 h	IT (100)	γ: 140 (100)	1/2-
Tc-99	2.111E+5 y	β⁻ (100)	β⁻: 293 (100)	9/2+

E_x = endpoint energy in keV; I_x = percent incidence; J_π = nuclear spin and parity

Reactor Production of ^{99}Mo

Conventional production of ^{99}Mo utilizes the ^{235}U(n,f)^{99}Mo nuclear reaction requiring neutron irradiation of highly enriched uranium (HEU, $\geq$ 20% ^{235}U) solid targets in a nuclear reactor. Despite being the principal global user of ^{99m}Tc, the United States currently imports 100% of its supply. The long-term viability of nuclear reactor-based ^{99}Mo production routes has become a recent concern as reactor production of ^{99}Mo relies on six aging nuclear reactors (**Table 1.2**).[12] An extended shutdown of any of these six

nuclear reactors could lead to a global ^{99}Mo shortage requiring clinicians to ration ^{99m}Tc imaging procedures, or use older, less reliable diagnostic techniques.

Table 1.2. Reactors that irradiate targets for global ^{99}Mo suppliers as of August 2019.[12]

Reactor	Country	Power (MWt)	Fuel Type	Target Type	Opened
BR-2	Belgium	100	HEU	HEU	1961
HFR	Netherlands	45	LEU	HEU	1961
LVR-15	Czech Republic	10	LEU	HEU	1957
Maria	Poland	30	LEU	HEU	1974
OPAL	Australia	20	LEU	LEU	2006
SARAFI-1	South Africa	20	LEU	HEU/LEU	1965

Notes: BR-2 = Belgian Reactor 2; HFR = High Flux Reactor; OPAL = Open Pool Australian Lighwater; SAFARI-1 = South African Fundamental Atomic Research Installation 1; HEU = highly enriched uranium; LEU = low enriched uranium.

The use of HEU for ^{99}Mo production also poses a nuclear proliferation security concern. It is the long-standing policy of the United States—implemented by the U.S. National Nuclear Security Administration (NNSA)—to reduce and eliminate the use of HEU in civilian applications by transitioning research reactors and medical isotope production facilities to the use of low-enriched uranium (LEU, $\leq$ 20% ^{235}U). As a result, there has been a considerable effort to establish a domestic supply of the ^{99}Mo for ^{99}Mo/^{99m}Tc generator production using non-HEU production routes. A concurrent effort has been made to directly produce ^{99m}Tc for radiopharmaceutical applications.

Alternative ^{99}Mo Production Routes

Photonuclear production of ^{99}Mo is possible through the reactions ^{nat}U(γ,f)^{99}Mo and ^{100}Mo(γ,n)^{99}Mo. Cross sections suitable for estimation of ^{99}Mo yield are known for these reactions.[13, 14] Production of clinically relevant amounts ^{99}Mo is seen as beyond the capability of modern accelerators.[15]

Molybdenum-99 is accessible using the neutron induced reactions ^{98}Mo(n,γ)^{99}Mo and ^{100}Mo(n,2n)^{99}Mo. The cross section for ^{100}Mo(n,2n)^{99}Mo is known to be 1.5 b in the

neutron energy range of 12-17 MeV.[16] Although this route can produce ^{99}Mo with reasonable specific activity, an intense 14 MeV neutron source is required.[16] The thermal neutron-capture cross section for ^{98}Mo is fairly low at 0.13 b.[17, 18] The advantage of the ^{98}Mo(n,γ)^{99}Mo route is that it can be performed in nuclear reactors operating with LEU. Molybdenum-98 is also the most naturally abundant stable isotope of Mo at 24.3%. Irradiation of enriched ^{98}Mo targets in a nuclear reactor produces low-specific activity ^{99}Mo. Technetium-99m generators prepared with low-specific activity ^{99}Mo must use larger alumina columns in order to accommodate the added mass of non-radioactive ^{98}Mo. NorthStar Medical Radioisotopes is currently developing ^{99}Mo/^{99m}Tc generators based on the ^{98}Mo(n,γ)^{99}Mo nuclear reaction. Technetium-99m generators are medical devices. The use of a larger alumina column constitutes a change to the medical technology, which will require FDA approval for clinical use.

Proton induced fission of ^{232}Th by the reaction ^{232}Th(p,f)^{99}Mo has been investigated as a source of ^{99}Mo.[19, 20] A recent study reported the production of 50 GBq of ^{99}Mo from the irradiation of ^{232}Th with 40 MeV protons.[19] This production route is potentially useful if a high-current and high-energy accelerator is utilized for production. A suitable separation scheme still needs to be developed for further implementation.

The most promising route for production of ^{99}Mo is by spallation neutron induced reactions of ^{nat}U by the reaction ^{nat}U(n,f)^{99}Mo. Spallation neutrons have been investigated as a means of inducing fission without a nuclear reactor.[21] Researchers at Argonne National Laboratory have reported the production of ^{99}Mo from accelerator-driven subcritical fission of a uranyl sulfate solution containing LEU. An electron linear accelerator (LINAC) bombards a tantalum target with electrons creating a beam of fast

neutrons. An aqueous uranyl sulfate solution functions as both a moderator—reducing the neutrons to thermal energies—and a medium for ^{235}U fission.[21] Production of ^{99}Mo within a concentrated aqueous LEU solution removes the lengthy dissolution procedures required for solid-target processing. An added benefit of this process is the ability to reuse the target solution for multiple irradiations. Automated systems have been developed for processing the LEU target solution post-irradiation. A pilot-scale process has been reported to produce 51.8 GBq of purified ^{99}Mo from irradiation of 5 L of a 149-g U/L uranyl sulfate solution.[22] This technology requires further development for scale up to production of medically relevant quantities of ^{99}Mo.

Direct Production of ^{99m}Tc

Direct production of ^{99m}Tc in a medical cyclotron via the ^{100}Mo(p,2n)^{99m}Tc nuclear reaction has been investigated as an alternative source of the radionuclide. This production route eliminates the ability to formulate a ^{99}Mo/^{99m}Tc radionuclide generator. Given the short half-life of ^{99m}Tc, the radionuclide would need to be produced daily at a cyclotron facility and either used onsite or shipped to a regional radiopharmacy. The ^{100}Mo(p,2n)^{99m}Tc excitation function exhibits a peak at 15-16 MeV proton energy that aligns well with the capabilities of the low-energy cyclotrons present in many existing PET centers.[23-25] As such, existing infrastructure for the production and distribution of PET radionuclides (i.e., ^{18}F, ^{11}C, and ^{15}N) could be appropriated for cyclotron-produced ^{99m}Tc.

Cyclotron-produced ^{99m}Tc requires the use of highly enriched ^{100}Mo (9.74% natural abundance) in order to minimize the co-production of technetium contaminants. Enrichment of ^{100}Mo up to 99.86% is available commercially in both metal and oxide

forms. The primary contaminants using enriched ^{100}Mo are the long-lived isotopes ^{98}Tc and ^{99g}Tc produced via the ^{100}Mo(p,3n)^{98}Tc and ^{100}Mo(p,2n)^{99g}Tc nuclear reactions respectively. Technetium-98 production can be minimized by keeping the incident proton energy below 17 MeV.[26] The ^{100}Mo(p,2n)^{99g}Tc excitation function is approximately four times higher than that of ^{100}Mo(p,2n)^{99m}Tc over the same proton energy range.[23] Despite a high cross section for ^{99g}Tc production, only a small amount of ^{99g}Tc will be produced during irradiation due to its long half-life. It was demonstrated that the ratio of ^{99m}Tc/^{99g}Tc from cyclotron irradiation is in compliance with standard values for 24-hour frequency generator eluted ^{99m}Tc.[23]

Separation technologies have been investigated for the purification of ^{99m}Tc and recovery of expensive ^{100}Mo target material.[27] The goal has been to develop an automated module for *in situ* extraction and purification of ^{99m}Tc from the irradiated ^{100}Mo target. Automated separation devices serve to minimize radiation dose to workers, maximize extraction yield, provide the activity in a useable form, and decrease processing time.

1.4.4 Technetium-99m radiopharmaceuticals

Technetium exhibits rich coordination chemistry, which has allowed for the development of a diverse set of complexes for diagnostic imaging. Technetium (Z = 43) is a second row transition metal situated in Group VII of the periodic table. Complexes of technetium are known with oxidation states ranging from -1 to +7, with the oxidation states +4 and +7 being the most thermodynamically stable. Technetium radiopharmaceutical complexes are primarily found in the +5, +3 and +1 oxidation states.[28] Any radiosynthesis with ^{99m}Tc begins with [^{99m}Tc]TcO$_4^-$ in the +7 oxidation

state. Lower oxidation states are accessible with the use of appropriate reducing agents and coordinating ligands.

Technetium forms five- and six-coordinate complexes in the +5 oxidation state. Most Tc(V) radiopharmaceuticals exhibit the mono oxo (Tc≡O^{3+}) core. The oxotechnetium agents [^{99m}Tc]Tc-$_{D,L}$-HMPAO (Ceretec®) and [^{99m}Tc]Tc-$_{L,L}$-ECD (Neurolite®) were developed for cerebral perfusion imaging. These neutral, lipophilic species cross the blood-brain-barrier through passive diffusion. They can help visualize areas of altered cerebral blood flow after stroke. Another oxotechnetium agent is [^{99m}Tc]Tc-MAG$_3$ (MAG3®), which consists of the tripeptide mercaptoacetyltriglycine (MAG$_3$) bound to the oxotechnetium core. The anionic [^{99m}Tc]Tc-MAG$_3$ complex undergoes tubular renal excretion and is used extensively for functional kidney imaging. Technetium-99m-tetrofosmin is a cationic, lipophilic complex designed for myocardial perfusion imaging. Tetrofosmin is comprised of two bidentate diphosphine ligands bound to the dioxo (O=Tc=O) core.

Technetium forms kinetically inert, low-spin d^6 complexes in the +1 oxidation state. It is common to use π-accepting ligands (i.e., CO, RNC) to stabilize the electron-rich Tc(I) metal center. The myocardial perfusion imaging agent ^{99m}Tc-sestamibi (Cardiolite®) is composed of six methoxyisobutylisonitrile ligands bound to a Tc(I) metal center. Recent development of Tc(I) radiopharmaceuticals has centered on the Tc(CO)$_3$$^+$ synthon. A radiosynthesis for the [^{99m}Tc][Tc(CO)$_3$(O$_2$H)$_3$]$^+$ intermediate from aqueous [^{99m}Tc][TcO$_4$]$^-$ was first reported in 1998.[29] A kit preparation was later developed using potassium boranocarbonate (K$_2$[CO$_2$BH$_3$]) as both a reducing agent and an *in situ* source of CO.[30] The [^{99m}Tc][Tc(CO)$_3$(O$_2$H)$_3$]$^+$ intermediate can be easily

coordinated to mono, di, or tridentate chelates by displacement of the labile aquo ligands. A myriad of bifunctional ^{99m}Tc agents have been developed using the Tc(CO)$_3^+$ synthon.[31]

Technetium forms five- and six-coordinate complexes in the +3 oxidation. These complexes are low-spin d^4. Organometallic Tc(III) '4+1' complexes, [Tc(NS$_3$)(CNR)], with the tripodal ligand tris(2-mercaptoethyl)amine (NS$_3$) and functionalized isocyanaides have been reported as a novel template for bifunctional radiopharmaceuticals.[32-37] Technetium-99m '4+1' complexes are easily prepared from the ^{99m}Tc(III)-EDTA precursor and a mixture of H$_3$NS$_3$ and Cu(I)-isocyanide. Mixed-ligand Tc(III) "Q-compounds", [^{99m}Tc[Tc(PR$_3$)$_2$(L)]$^+$, where Tc(III) is coordinated by two tertiary phosphine ligand and a tetradentate N$_2$O$_2$ Schiff base ligand, have been extensively investigated as SPECT imaging agents for myocardial perfusion.[38-41] Technetium-99m Q-compounds can be prepared by a one-step kit formulation in which the phosphine ligand acts as the sole reducing agent and a coordinating ligand.[38]

1.5 Radiochemistry of Rhenium

Rhenium (Z = 75) is a third-row transition metal situated in Group 7 of the periodic table. The electronic configuration of Re is [Xe] 4f^{14}5d^{5}6s^2 giving seven valence electrons available for bonding.[42] Nine rhenium oxidation states are known—ranging from -1 to +7—leading to rich coordination chemistry for the element. Rhenium is often employed as a non-radioactive surrogate for technetium, which lacks a stable isotope.[43] Three rhenium radioisotopes—^{186}Re, ^{188}Re, and ^{189}Re—possess nuclear properties suitable for therapeutic nuclear medicine (**Table 1.3**). Each radionuclide emits a therapeutic beta particle in addition to a gamma photon suitable for SPECT imaging. Due

to the chemical similarity between rhenium and technetium, the therapeutic rhenium radionuclides form a "matched pair" with ^{99m}Tc. In principle, one molecular template can be developed encompassing a ^{99m}Tc analogue for diagnostic imaging and an $^{186/188/189}$Re analogue for targeted radiotherapy. The utility of each rhenium radionuclide is a function of their respective nuclear properties and the desired therapeutic application.

1.5.1 Rhenium Radionuclides

Rhenium-186 ($t_{1/2}$ = 3.72 d) decays 92.5% by β^- emission and 7.5% by electron capture (EC). The β^- endpoint energy is 1070 keV (I_β = 71.0%). A concomitant 137 keV γ-ray (I_γ = 9.5%) is also emitted allowing for diagnostic imaging by SPECT. Several methods have been investigated for the production of ^{186}Re. Reactor production of ^{186}Re by neutron irradiation of an enriched ^{185}Re target results in low specific activity.[44, 45] Low specific activity ^{186}Re is useful for developing radiolabelling protocols, performing preclinical studies of radiolabelled compounds, and evaluating radiochemical separations, however, clinical application generally requires high specific activity. Production of high specific activity ^{186}Re has focused on the nuclear reactions ^{186}W(p,n)^{186}Re and ^{186}W(d,2n)^{186}Re.[46-54] Deuteron irradiation is higher yielding and produces fewer radionuclidic impurities, although deuteron beams of sufficient energy are less common than proton beams. Although research into production and separations of high specific activity ^{186}Re is ongoing, clinical scale production has yet to be reported.

Rhenium-188 ($t_{1/2}$ = 17.00 h) decays solely by β^- emission. The β^- endpoint energy of 2120 keV (I_β = 71.1%). A 155 keV γ-ray (I_γ = 15%) suitable for diagnostic imaging is also emitted. High specific activity ^{188}Re is available from the commercially

available ^{188}W/^{188}Re generator system made through double neutron capture on ^{186}W targets.[55, 56]

Rhenium-189 (t$_{1/2}$ = 24.3) decays solely by β$^-$ emission. The β$^-$ endpoint energy is 1009 keV (I_β = 64%). A 217 keV γ-ray (I_γ = 5.5%) suitable for diagnostic imaging is also emitted. Although ^{189}Re has suitable nuclear properties for radiotherapy, there have been no reports on the production of this radionuclide for medical applications. Several potential production routes exist. The cross section for the nuclear reaction ^{189}Os(n,p)^{189}Re has been reported.[57, 58] An alternative method for the production of ^{189}Re is the ^{192}Os(p,α)^{189}Re nuclear reaction. Rhenium-189 produced via the ^{192}Os(p,α)^{189}Re nuclear reaction has been observed from proton irradiation of ^{nat}OsS$_2$.[52] Photonuclear production of ^{189}Re is also possible through the ^{190}Os(γ,p)^{189}Re reaction. Although no data is available for the ^{190}Os(γ,p)^{189}Re reaction, researchers at Argonne National Laboratory are actively investigating this production route.

Table 1.3: Selected nuclear decay properties for ^{186m}Re, ^{186}Re, ^{188}Re, and ^{189}Re.

Radionuclide	t$_{1/2}$	Decay mode	E_x (I$_x$)	Jπ
Re-186m	2.0E+5 y	IT (100)	γ: 59 (18)	1-
Re-186	89.2 h	β$^-$ (93); EC (7)	γ: 137 (9)	(8+)
			β$^-$: 1070 (71); 932 (22)	
Re-188	17.0 h	β$^-$ (100)	γ: 155 (15)	1-
			β$^-$: 2120 (71); 1965 (26)	
Re-189	24.3 h	β$^-$ (100)	γ: 217 (6)	5/2+
			β$^-$: 1009 (64); 790 (8)	

E_x = endpoint energy in keV; I$_x$ = percent incidence; J$_\pi$ = nuclear spin and parity

1.6 Multidrug Resistance

Chemotherapy remains an important and broadly used tool for the treatment of malignant tumors. One obstacle to effective chemotherapy is the resistance of many

tumors to common chemotherapeutic agents. Some tumors are inherently resistant to chemotherapy, while other tumors show an initial response to chemotherapy before developing resistance to cytotoxic agents throughout treatment. Multidrug resistance (MDR) is the cross-resistance or insensitivity of tumor cells towards various chemotherapy agents that are structurally or functionally dissimilar and have divergent molecular targets.[59] These agents include vinca alkaloids, anthracyclines, platinum agents, nucleoside analogs, or other cytotoxic natural products. Numerous cellular and non-cellular mechanisms have been proposed to mediate MDR in tumor cells. The most well characterized cellular mechanisms of MDR are those that involve drug efflux by the adenosine triphosphate (ATP) binding cassette transporter family, known as the ABC transporter family.[60] One ABC-transporter implicated in tumor MDR is the cell membrane protein P-glycoprotein (Pgp) encoded by the MDR1 gene.[61] Human Pgp is localized on the luminal surface of the plasma membrane in polarized epithelial cells. It acts as a molecular vacuum by intercepting toxic compounds in the lipid bilayer of the cell and pumping them out of the cell. Tumors exhibiting MDR overexpress the P-glycoprotein leading to poor accumulation of chemotherapeutic drugs within the cells and diminished therapeutic efficacy. Repeated use of chemotherapy agents in MDR tumors can even trigger the P-glycoprotein to acquire cross-resistance to other cytotoxic agents.

Diagnosis of MDR is potentially useful in cancer treatment, as identification of chemotherapy resistant patients would allow for effective treatment planning, and the avoidance of costly, ineffective therapeutic methods. Multidrug resistance can be visualized using radiopharmaceuticals that are P-glycoprotein substrates. Technetium-99m agents have been extensively investigated for MDR imaging due to the favorable

cost, half-life, and coordination chemistry of the radionuclide.[60] Cationic [99mTc] SPECT agents, originally developed for myocardial perfusion imaging, were found to function as MDR substrates. These cationic compounds accumulate in tumors due to the increased negative mitochondrial potentials exhibited by tumor cells.[62-65] The first [99mTc] radiopharmaceutical investigated for MDR imaging was [[99mTc]Tc-sestamibi], which displayed cellular uptake in MDR cells lines with varying amounts of P-glycoprotein expression.[63] By utilizing SPECT imaging, the rates of [[99mTc]Tc-sestamibi] cellular uptake and washout were quantified. Individual factors affecting cellular uptake of [[99mTc]Tc-sestamibi] were also investigated. In particular, the use of P-glycoprotein biomodulators in concert with [[99mTc]Tc-sestamibi] was shown to increase cellular uptake in MDR tumors, compared to the use of [[99mTc]Tc-sestabmibi] alone.

Biomodulators are compounds that decrease the rate of efflux by the P-glycoprotein. When used alongside diagnostic [99mTc] radiopharmaceuticals, they allow for improved discrimination between normal and MDR tumors. Biomodulators operate by actively blocking the exocellular P-glycoprotein. This property can be utilized to diagnose MDR in a two-step diagnostic procedure. In the first step, the [99mTc] agent is administered and the patient is imaged to establish a baseline. In the second step, the patient is pretreated with a biomodulator prior to administration of the [99mTc] agent and then imaged a second time. By comparison of the two scans, MDR tumors with high P-glycoprotein expression can be identified. Development of novel biomodulators for P-glycoprotein is of interest for improved MDR tumor imaging and for understanding the fundamental processes governing P-glycoprotein function.

The initial success of [^{99m}Tc]Tc-sestabmibi towards MDR tumor imaging led to the investigation of other myocardial perfusion imaging agents as potential diagnostic agents for MDR tumors. Technetium Q-complexes, which take the general structure [^{99m}Tc][Tc(PR$_3$)$_2$(Schiff base)]$^+$, have been established as avid transport substrates recognized by the human MDR1 P-glyprotein.[62, 66-68] The prototypical Tc Q-complex is [^{99m}Tc]Tc-furifosmin (Q12), which is composed of Tc(III) metal center coordinated by the tetradentate Schiff base ligand 4,4′-[(1E,1′E)-[ethane-1,2-diylbis(azanylylidene)]bis(methanylylidene)]bis(2,2,5,5-tetramethyl-2,5-dihydrofuran-3-ol) (tmf$_2$enH$_2$) and two tris(3-methoxypropyl)phosphine (TMPP) ligands. Recent work has sought to develop nonradioactive rhenium analogues to [^{99m}Tc]Tc-furifosmin for use as biomodulators for P-glycoprotein.[69-75] Development of a rhenium Q-series could aid in measuring the uptake and washout rates of [^{99m}Tc]Tc-furifosmin. It could also lead to improved image quality and sensitivity for the discrimination of tumors expressing MDR.
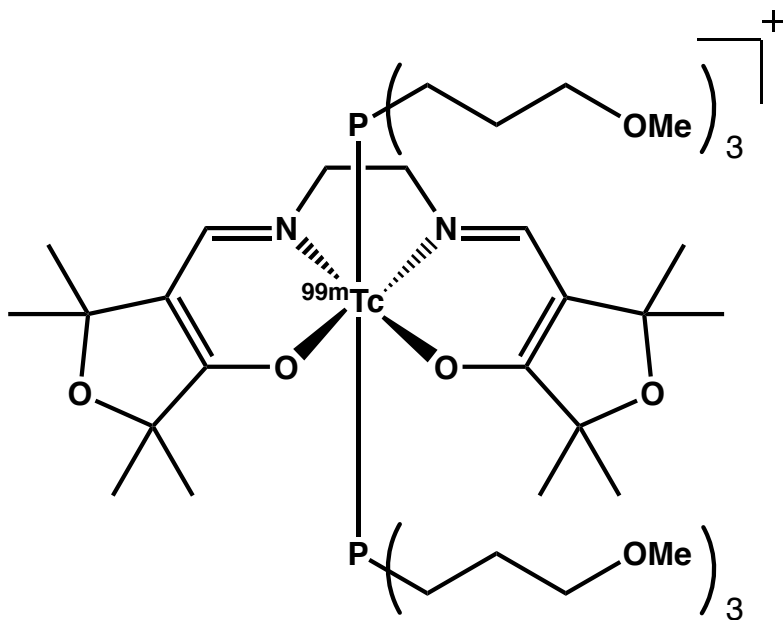
Figure 1.4. Structure of the [^{99m}Tc]Tc-furifosmin cation.

Development of a Rhenium Q-series

The primary motivation for this work was to develop non-radioactive rhenium analogues to [^{99m}Tc]Tc-furifosmin. These compounds have potential application as biomodulators for P-glycoprotein serving to enhance the imaging quality of MDR tumors. Although the synthesis of rhenium Q compounds has been previously investigated, few examples of these compounds are known.[71-73, 75] Syntheses of rhenium Q compounds have suffered from low yields, long reaction times, and complex isolation procedures. Furthermore, no rhenium complexes with H$_2$tmf$_2$en—the N$_2$O$_2$ Schiff base used in [^{99m}Tc]Tc-furifosmin—have been reported.

A secondary motivation for this work was to investigate bifunctional N$_2$O$_2$ Schiff base ligands for developing bifunctional radiopharmaceuticals based on the ^{99m}Tc Q-series. Schiff base ligands are ubiquitous in transition metal chemistry. The chemical and steric properties of N$_2$O$_2$ Schiff base ligands and their metal complexes can be easily tuned. Technetium-99m Q-complexes evaluated for myocardial perfusion imaging have shown excellent stability *in vitro* and *in vivo*. These complexes are easily prepared in high radiochemical yields. In the case of [^{99m}Tc]Tc-furifosmin, a one-step radiopharmaceutical kit was developed obviating the need for complex radiosynthesis. For these reasons, tetradentate Schiff base ligands are a promising building block for bifunctional ^{99m}Tc and $^{186/188}$Re radiopharmaceuticals. The formation and stability of Re(III) Q-complexes has been shown to be impacted by the nature of the Schiff base backbone bone. Development of bifunctional Q-complexes requires strategies for incorporation of targeting vectors that maintain the stability of the metal complex.

1.7 Dissertation Summary

The principal research aim of this dissertation is the development of Re(III) Schiff base compounds analogous to the ^{99m}Tc Q-series. Chapter 2 centers on the synthesis and characterization of Re(III) and Tc(III) compounds with the N_2O_2 Schiff base ligand H_2tmf$_2$en. A novel microwave-assisted synthesis is presented for the preparation of Re(III) Q-compounds that improves upon prior syntheses. The synthesis and characterization of Re(III) and Re(V) compounds with salicylaldehyde-based N_2O_2 Schiff base ligands encompasses Chapter 3. The steric impact of the Schiff base ligand backbone upon Re(III) complex stability is discussed. Chapter 4 involves the influence of N_2O_2 Schiff base backbone functionalization on the radiolabelling of [^{99m}Tc]Tc Q-compounds. A general summary of the results within the dissertation and an outlook for future research is presented in Chapter 5.

CHAPTER 2

Synthesis of Rhenium Analogues to [^{99m}Tc]Tc-Furifosmin[1]

2.1 Introduction

Technetium-99m ($t_{1/2}$ = 6.01 h; E_γ = 140 keV) remains the predominant radionuclide used in diagnostic nuclear medicine because of its favorable nuclear properties and availability from ^{99}Mo/^{99m}Tc generators.[76-79] Radioactive decay of ^{99m}Tc by an isomeric transition produces a 140 keV γ emission that is detected by single photon emission computed tomography (SPECT). With known oxidation states ranging from -1 to +7, technetium has robust redox chemistry and forms an array of coordination compounds. Radiopharmaceuticals incorporating ^{99m}Tc have been used for diagnostic imaging of such diverse biological targets as the brain, lungs, thyroid, skeleton, myocardium, and blood, among others.[28, 80] The chemistry of technetium is closely related to that of its third row congener rhenium. Because technetium has no stable isotopes, natural rhenium is often used as the nonradioactive surrogate for developing technetium chemistry. Differences in substitution kinetics and redox chemistry can cause dissimilar reactivity, however, necessitating thorough investigation of the fundamental inorganic chemistry of the two elements.

Two rhenium radioisotopes have ben investigated for therapeutic nuclear medicine: ^{186}Re [$t_{1/2}$ = 90 h, 1.02 MeV β⁻, 137 keV γ (7%)] and ^{188}Re [$t_{1/2}$ = 17 h, 2.11 MeV β⁻, 155 keV γ (15%)].[81, 82] Each radionuclide emits a therapeutic beta particle in addition to a γ photon suitable for SPECT imaging. High specific- activity ^{188}Re is

---

available from ^{188}W ($t_{1/2}$ = 69.4 days)/^{188}Re radionuclide generators.[55] The short half-life

of ^{188}Re poses a challenge when radiolabeling targeting vectors with long biological half-

lives such as monoclonal antibodies. Because of a longer half-life and lower beta energy,

^{186}Re is seen as more amenable to clinical application. Rhenium-186 has been

conventionally produced in nuclear reactors via the ^{185}Re(n,γ)^{186}Re nuclear reaction,

albeit in low specific activity.[44, 46] Recent work has demonstrated the production of high-

specific-activity ^{186}Re from charged particle reactions on both enriched tungsten targets

and enriched osmium targets.[47, 51-54, 83]

Given the chemical similarity of technetium and rhenium, the rhenium

radioisotopes can serve as a therapeutic compliment to the diagnostic radionuclide ^{99m}Tc.

In principle, one molecular template can be developed incorporating a ^{99m}Tc analogue for

diagnostic imaging and a ^{186}Re or ^{188}Re analogue for targeted radiotherapy. Application

of this principle requires careful attention to the chemical differences between technetium

and rhenium. Rhenium is generally harder to reduce and easier to oxidize and displays

slower substitution kinetics in comparison to technetium.

Technetium-99m complexes with tetradentate N_2O_2 Schiff base ligands have

received much attention in the development of the ^{99m}Tc "Q-series"

($[^{99m}$Tc][Tc(PR$_3$)$_2$(Schiff base)]$^+$).[38, 40, 41, 84, 85] This class of cationic, lipophilic radiometal

complexes has been investigated for myocardial perfusion imaging and multidrug-

resistant (MDR) tumor imaging.[39, 62, 67, 86, 87] The most successful compound in the ^{99m}Tc

Q-series is [^{99m}Tc]Tc-furifosmin (Q 12). This compound consists of a Tc(III) metal center

coordinated by the tetradentate Schiff base ligand 4,4′-[(1E,1′E)-[ethane-1,2-

diylbis(azanylylidene)]bis(methanylylidene)]bis(2,2,5,5-tetramethyl-2,5-dihydrofuran-3-ol) (tmf$_2$enH$_2$) and two tris(3-methoxypropyl)phosphine (TMPP) ligands (**Figure 2.1**).
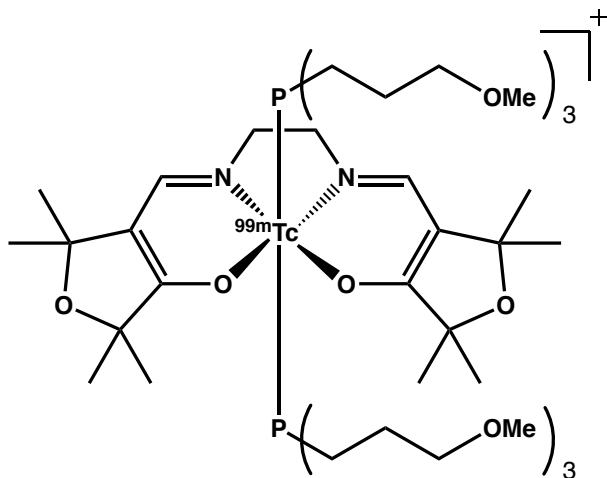
Figure 2.1. Structure of the [^{99m}Tc]Tc-furifosmin cation.

Numerous preclinical and clinical studies established the efficacy of [^{99m}Tc]Tc-furifosmin for myocardial perfusion imaging.[39, 88-90] Similar to [^{99m}Tc]Tc-sestamibi and [^{99m}Tc]Tc-tetrofosmin, [^{99m}Tc]Tc-furifosmin is a substrate for the permeability glycoprotein (P-glycoprotein or Pgp)—a membrane transporter that is overexpressed in MDR tumors—and has been shown to effectively image MDR tumors.[62, 66-68, 87]

The impetus for this work is to develop rhenium analogues to [^{99m}Tc]Tc-furifosmin. Rhenium Q-complexes have application as P-glycoprotein biomodulators. It is predicted that d^4 rhenium(III) complexes will be kinetically inert under biological conditions. Rhenium Q-complexes also have application as a novel platform for bifunctional $^{186/188}$Re radiopharmaceuticals—an application that would require the use of functionalized Schiff base ligands. Despite ongoing efforts, few examples of Re(III) analogues to the ^{99m}Tc Q-series have been reported thus far, testifying to differences in the redox chemistry and substitution kinetics between the two metals.[71-73, 75, 91]

This chapter focuses on the synthesis of the first rhenium analogues to [^{99m}Tc]Tc-furifosmin. The oxorhenium(V) complex *trans*-[ReOCl(tmf$_2$en)], **1**, was synthesized and fully characterized. The Re(III) compounds *trans*-[Re(TMPP)$_2$(tmf$_2$en)]Cl, **2**, *trans*-[Re(PEt$_3$)$_2$(tmf$_2$en)]Cl, **3**, *trans*-[Re(PEt$_2$Ph)$_2$(tmf$_2$en)]Cl, **4**, and *trans*-[Re(PEtPh$_2$)$_2$(tmf$_2$en)]Cl, **5**, were prepared by the *in situ* formation of **1** and subsequent addition of excess tertiary phosphine. Microwave-assisted synthesis was employed in order to overcome the slow substitution kinetics of rhenium. Technetium-99 was used to prepare macroscopic [^{99m}Tc]Tc-furifosmin analogues for a structural comparison between the technetium and rhenium species. The oxotechnetium(V) complex *trans*-[TcOCl(tmf$_2$en)], **6**, was prepared using (*n*Bu$_4$N)[TcOCl$_4$] as the starting material. Unlike the analogous oxorhenium(V) complex, this oxotechnetium(V) compound readily forms under ambient conditions. The Tc(III) species *trans*-[Tc(TMPP)$_2$(tmf$_2$en)]PF$_6$, **7**, and *trans*-[Tc(PEt$_3$)$_2$(tmf$_2$en)]PF$_6$, **8**, were prepared by the *in situ* generation of **6**, followed by the addition of tertiary phosphine. The synthetic and spectroscopic results reported in this chapter lay the foundation for future radiopharmaceutical development utilizing tracer amounts of ^{186}Re or ^{188}Re.

2.2 Experimental

General Considerations.

All common laboratory chemicals were of reagent grade or better. Absolute ethanol was degassed prior to use. Experiments with rhenium were performed under an argon atmosphere, using standard Schlenk techniques for inert syntheses. Experiments with ^{99}Tc were performed under ambient conditions unless otherwise noted. A Centrifan™ PE Personal Evaporator (KD Scientific Inc., Holliston, MA) was used for drying solutions

containing long-lived ^{99}Tc. Microwave reactions were performed using a CEM Discover® SP microwave reactor (CEM Corporation, Matthews, NC). ^{1}H and ^{13}C NMR spectra (including HMQC ^{1}H-^{13}C correlation) were recorded on a Bruker DRX500 or DRX600 at 25 °C in CD_2Cl_2, $CDCl_3$, D_2O or CD_3CN (**Table 2.1**) and calibrated with the respective residual solvent peaks ($CHDCl_2$ at 5.32 ppm; $CHCl_3$ at 7.26 ppm; HOD at 4.79 ppm; CHD_2CN at 1.94 ppm). Infrared spectra were obtained as KBr pellets on a Thermo Nicolet Nexus 670 FT-IR spectrophotometer. Liquid Chromatography Mass Spectroscopy (LC-MS) was performed on a ThermoFisher Scientific LCQ Fleet Ion Trap Mass Spectromeeter. Radio-TLC measurements were conducted using a BioScan 200 Imaging Scanner. Baker-flex Silica Gel IB-F TLC plates (J. T. Baker; 2.5 x 7.5 cm) were used as received. A Shimadzu Prominence HPLC system with a pump, controller, Prominence UV-vis detector (model SPD-20AV) set to 254 nm and coupled to a Beckman 170 NaI(Tl) radioisotope detector with a Phenomenex® Jupiter® LC column (C18, 5 μm, 250 x 4.6 mm) was used to analyze ^{99m}Tc and Re complexes, with a linear gradient from 50% A to 90% B (A = H_2O with 0.1% TFA, and B = MeCN with 0.1% TFA) with a flow rate of 1 mL/min over 20 minutes.

Materials.

Caution! Technetium-99 emits a 0.294 MeV β^-_{max} with a half-life of 2.1×10^5 years. Technetium-99m emits a 140 keV γ-ray with a half-life of 6.01 hours. All operations were carried out in radiochemical laboratories equipped and approved for handling these radionuclides. NMR spectra for ^{99}Tc complexes were recorded using glass NMR tubes equipped with Teflon inserts in order to avoid potential contamination.

Technetium-99m was eluted as sodium pertechnetate from a ^{99}Mo/^{99m}Tc generator (Covidien) using saline.

The tetradentate Schiff base tmf$_2$enH$_2$ and the phosphine ligand TMPP were gifts from Mallinckrodt Medical (St. Louis). (nBu$_4$N)[ReOCl$_4$] and (nBu$_4$N)[TcOCl$_4$] were prepared according to established procedures.[92, 93] The purities of the starting materials were verified by ^{1}H NMR, ^{13}C NMR, and FT-IR spectroscopies.

***trans*-[ReOCl(tmf$_2$en)], 1.** Tmf$_2$enH$_2$ (0.0183 g, 0.05 mmol) and (nBu$_4$N)[ReOCl$_4$] (0.0293 g, 0.05 mmol) were added to a 10 mL microwave reaction vessel, which was purged and backfilled with argon three times. Degassed absolute EtOH (4 mL) was transferred into the vessel via *cannula*. The solution was heated in a microwave reactor at 105 °C, 17 bar (max), and 150 W (max) for 2 min with constant stirring. A deep-red solution resulted. The reaction was dried *in vacuo*. The oily residue was dissolved in a minimal volume of Et$_2$O and filtered through Celite. Crystal of **1**•Et$_2$O suitable for X-ray diffraction were obtained by allowing the solution to sit capped for several days at room temperature. Yield: 78% (23 mg). ^{1}H NMR (500 MHz, CD$_2$Cl$_2$, rt): δ 7.68 (s, 2H, -CH=N-), 4.20 (m, 2H, -CH$_2$-), 3.98 (m, 2H, -CH$_2$-), 1.50 (s, 6H, -CH$_3$), 1.47 (s, 6H, -CH$_3$), 1.46 (s, 6H, -CH$_3$), 1.44 (s, 6H, -CH$_3$). ^{13}C NMR (500 MHz, CD$_2$Cl$_2$, rt): δ204.67 (C-O), 168.64 (-HC=N-), 118.65 (C(CH=N), 82.19, 80.62 (-C(CH$_3$)$_2$), 69.34 (CH$_2$), 32.62, 32.26, 28.18, 27.61 (CH$_3$). FT-IR (KBr pellet, ν in cm^{-1}): 1605 (C=N), 952 (Re≡O). ESI-MS (m/z): 565.16 [calcd 565.17 for [C$_{20}$H$_{30}$N$_2$O$_5$Re]$^+$ (M$^+$)].

***trans*-[Re(TMPP)$_2$(tmf$_2$en)]Cl, 2.** Tmf$_2$enH$_2$ (0.0547 g, 0.15 mmol) and (nBu$_4$N)[ReOCl$_4$] (0.0879 g, 0.15 mmol) were added to a 10 mL microwave reaction vessel that had been purged and backfilled with argon three times. Degassed absolute

EtOH (4 mL) was transferred into the vessel via *cannula*. The solution was heated in a microwave reactor at 105 °C, 17 bar (max), and 150 W (max) for 1 min with constant stirring. A deep-red solution resulted. Tris(3-methoxypropyl)phosphine (TMPP) (0.375 g, 1.5 mmol) was added to the reaction vessel via syringe, and then the mixture was heated at 105 °C, 17 bar (max), and 150 W (max) for 6 min with continued stirring. The resulting bright-red solution was dried *in vacuo*, and then the product-containing residue was dissolved in a minimal volume of CH_2Cl_2 and loaded onto a silica gel column equilibrated with CH_2Cl_2. The column was eluted with CH_2Cl_2, which displaced TMPP and tris(3-methoxypropyl)phosphine oxide. Switching the eluent to acetone eluted an unidentified red band. The desired red product band was eluted from the column using 5% MeOH in MeCN. Yield: 74% (40 mg). ^{1}H NMR (600 MHz, D_2O, rt): δ 77.85 (s, 2H, -CH=N-), 17.60 (s, 4H, -NCH$_2$CH$_2$N-), 8.58 (s, 12H, -CH$_3$), 3.73 (s, 12H, PCH$_2$CH$_2$CH$_2$OCH$_3$), 2.34 (s, 18H, PCH$_2$CH$_2$CH$_2$OCH$_3$), 1.81-1.92 (m, 12H, PCH$_2$CH$_2$CH$_2$OCH$_3$), 1.42-1.48 (m, 12H, PCH$_2$CH$_2$CH$_2$OCH$_3$), 0.41 (s, 12H, -CH3). ^{13}C NMR (600 MHz, D_2O, rt): δ 158.42 (CH$_3$), 84.61 (PCH$_2$CH$_2$CH$_2$OCH$_3$), 59.91 (PCH$_2$CH$_2$CH$_2$OCH$_3$), -17.36 (CH$_3$). ESI-MS (m/z): 1048.88 [calcd 1049.52 for [$C_{44}H_{84}N_2O_{10}P_2Re$]$^+$ (M$^+$)].

trans-[Re(PEt$_3$)$_2$(tmf$_2$en)]Cl, 3. The synthesis of **3** followed the procedure described for **2**, substituting triethylphosphine (1.0 M solution in THF) for TMPP. Crystals suitable for X-ray diffraction were obtained by dissolving the crude product in Et$_2$O, filtering the solution, and allowing it to sit tightly capped for several days. Yield: 56% (69 mg). ^{1}H NMR (600 MHz, CD$_2$Cl$_2$, rt): δ 82.19 (s, 2H, -CH=N-), 17.66 (s, 4H, -NCH$_2$CH$_2$N-), 8.42 (s, 12H, -CH$_3$), 2.75 (br m, PCH$_2$CH$_3$), 2.38 (br t, 18H, PCH$_2$CH$_3$), 0.31 (s, 12H, -

CH$_3$). ^{13}C NMR (600 MHz, CD$_2$Cl$_2$, rt): δ 158.99 (-CH$_3$), -2.95 (PCH$_2$CH$_3$), -21.23 (-CH$_3$). ESI-MS (m/z): 784.99 [calcd 785.00 for [C$_{32}$H$_{60}$N$_2$O$_4$P$_2$Re]$^+$ (M$^+$)].

***trans*-[Re(PEt$_2$Ph)$_2$(tmf$_2$en)]Cl, 4.** The synthesis of **4** followed the procedure described for compound **2**, substituting diethylphenylphosphine (PEt$_2$Ph) for TMPP. Crystals of **4**•0.5H$_2$O suitable for X-ray diffraction were obtained by dissolving the crude product in Et$_2$O, filtering the solution, and allowing it to sit tightly capped for several hours. Yield: 80% (109 mg). ^{1}H NMR (500 MHz, CD$_2$Cl$_2$, rt): δ 82.75 (s, 2H, -CH=N-), 35.03 (s, 4H, -NCH$_2$CH$_2$N-), 11.83 (d, *J* = 7.9 Hz, 4H, o-H), 8.65 (t, *J* = 7.5 Hz, 2H, p-H), 8.58 (s, 12H, -CH$_3$), 7.04 (t, *J* = 7.6 Hz, 4H, m-H), 6.00 (br s, 4H, PCH$_2$CH$_3$), 0.28 (br s, 12H, PCH$_2$CH$_3$), 0.07 (s, 12H, -CH3), -2.62 (br s, 4H, PCH$_2$CH$_3$). ^{13}C NMR (600 MHz, CD$_2$Cl$_2$, rt): δ 166.20 (-CH$_3$), 139.06 (PPh meta), 122.82 (PPh ortho), 122.69 (PPh para), 1.42 (PCH$_2$CH$_3$), -21.46 (-CH$_3$). ESI-MS (m/z): 881.01 [calcd 881.36 for [C$_{40}$H$_{60}$N$_2$O$_4$P$_2$Re]$^+$ (M$^+$)].

***trans*-[Re(PEtPh$_2$)$_2$(tmf$_2$en)]Cl (5).** The synthesis of **5** followed the procedure described for **2**, substituting ethyldiphenylphosphine (PEtPh$_2$) for TMPP. Crystals suitable for X-ray diffraction were obtained by dissolving the crude product in Et$_2$O, filtering the solution, and allowing it to sit tightly capped overnight. Yield: 54% (81 mg). ^{1}H NMR (500 MHz, CD$_2$Cl$_2$, rt): δ 84.88 (s, 2H, -CH=N-), 34.52 (s, 4H, -NCH$_2$CH$_2$N-), 8.79 (s, 12H, -CH3), 8.72 (br s, 6H, PCH$_2$CH$_3$), 7.75 (t, 4H, PPh para), 6.92 (br s, 4H, PCH$_2$CH$_3$), 5.51 (t, 8H, PPh meta), 5.18 (br s, 8H, PPh ortho), -0.56 (s, 12H, -CH$_3$). ^{13}C NMR (500 MHz, CD$_2$Cl$_2$, rt): δ 174.33 (-CH$_3$), 134.79 (PPh meta), 122.93 (PPh para), 109.90 (PPh ortho), 31.02 (PCH$_2$CH$_3$), -25.13 (-CH$_3$). ESI-MS (m/z): 976.86 [calcd 977.36 for [C$_{48}$H$_{60}$N$_2$O$_4$P$_2$Re]$^+$ (M$^+$)].

***trans*-[TcOCl(tmf₂en)] (6).** Tmf₂enH₂ (0.0182 g, 0.050 mmol) was dissolved in 2 mL of absolute EtOH. In a separate vial, (*n*Bu₄N)[TcOCl₄] (0.0243 g, 0.049 mmol) was dissolved in 2 mL of EtOH and then added to the tmf₂enH₂ solution, resulting in a deep-purple solution after 10 min of stirring. The reaction mixture was dried in a Centrifan. The residue was dissolved in CH₂Cl₂ and loaded onto a silica gel column equilibrated in CH₂Cl₂. The column was first flushed with CH₂Cl₂, and then the product was eluted with 30% MeCN in CH₂Cl₂ as a purple band. The product-containing fraction was dried via a Centrifan, dissolved in Et₂O, and then filtered. Crystals of **6**•0.5Et₂O suitable for X-ray diffraction were obtained by allowing the solution to sit loosely capped for several days. Yield: 40% (10 mg). Radiochemical yield: 50% (determined by radio-TLC on silica gel plates performed in MeCN; R_f = 0.25). ¹H NMR (600 MHz, CD₂Cl₂, rt): δ 7.49 (s, 2H, -CH=N-), 4.45 (m, 2H, -CH2-), 4.23 (m, 2H, -CH₂-), 1.54 (s, 6H, -CH₃), 1.49 (s, 6H, -CH₃), 1.48 (s, 6H, -CH₃), 1.42 (s, 6H, -CH3). ¹³C NMR (600 MHz, CD₂Cl₂, rt): δ 200.36 (C-O), 157.37 (-HC=N-), 118.85 (C(CH=N)), 83.07, 80.62 (C(CH₃)₂), 64.17 (CH₂), 32.51, 32.26, 27.60, 27.49 (CH3). FT-IR (KBr pellet, ν in cm⁻¹): 1597 (C=N), 919 (Tc≡O).

***trans*-[Tc(TMPP)₂(tmf₂en)]Cl (7).** Tmf₂enH₂ (0.0295 g, 0.081 mmol) and (*n*Bu₄N)[TcOCl₄] (0.0397 g, 0.080 mmol) were added to a 10 mL microwave reaction vessel, which was then purged and backfilled with argon three times. Degassed absolute EtOH (4 mL) was transferred into the vessel via *cannula*. The solution was heated in a microwave at 105 °C, 17 bar (max), and 150 W (max) for 1 min with stirring. A deep-purple solution resulted. Tris(3-methoxypropyl)-phosphine (TMPP; 0.13 mL, 0.48 mmol) was added to the reaction vessel via a syringe, and then the mixture was heated at 105 °C,

17 bar (max), and 150 W (max) for 6 min with stirring. The resulting blue-green solution was dried via a Centrifan, and then the product containing residue was dissolved in a minimal volume of CH_2Cl_2 and loaded onto a silica gel column equilibrated with CH_2Cl_2. The column was washed with CH_2Cl_2, which displaced no visible bands. Switching the eluent to acetone removed an unidentified yellow band. The blue-green product band was eluted from the column using 20% MeOH in MeCN. Yield: 64% (51 mg). Radiochemical yield: 75% (determined by radio-TLC on silica gel plates in 20% MeCN in MeOH; R_f = 0.31). ^{1}H NMR (600 MHz, CD_3CN, rt): δ 6.21 (s, 12H, -CH3), 3.44 (br s, 6H, $PCH_2CH_2CH_2OCH_3$), 3.22 (br s, 6H, $PCH_2CH_2CH_2OCH_3$), 3.08 (br s, 12H, $PCH_2CH_2CH_2OCH_3$), -0.39 (s, 12H, -CH3), -9.24 (br s, 3H, $PCH_2CH_2CH_2OCH_3$), -15.95 (br s, 9H, $PCH_2CH_2CH_2OCH_3$).

***trans*-[Tc(PEt₃)₂(tmf₂en)]PF₆ (8).** Tmf₂enH₂ (0.0185 g, 0.051 mmol) was dissolved in 2 mL of absolute EtOH. In a separate vial, (nBu₄N)[TcOCl₄] (0.0244 g, 0.049 mmol) was dissolved in 2 mL of absolute EtOH and then added to the tmf₂enH₂ solution, resulting in a deep-purple solution after 15 min. Triethylphosphine (1.0 M solution in THF, 0.3 mL, 0.3 mmol) was added to the reaction via a syringe, and then the reaction was stirred for 1 h at room temperature. The resulting dark-green solution was dried via a Centrifan, dissolved in CH_2Cl_2, and then loaded onto a silica gel column (10 mm diameter; 3 g silica) preequilibrated with CH_2Cl_2. The column was flushed with CH_2Cl_2, which eluted $TcCl_4(PEt_3)_2$ as a bright-blue band. Changing the eluent to acetone removed several unidentified brown bands. The blue green product-containing band was finally eluted with MeOH. Ammonium hexafluorophosphate (0.01 g, 0.06 mmol) was then added to the methanolic solution. Crystals of **8**•H_2O suitable for X-ray diffraction were obtained by

allowing the product to sit for several days in a 1:1 solution of MeOH and water. Yield: 25% (9 mg). Radiochemical yield: 37% (determined by radio-TLC on silica gel plates in 10% MeCN in MeOH; R_f = 0.17). ^{1}H NMR (600 MHz, CDCl$_3$, rt): δ 6.27 (s, 12H, -CH$_3$), 3.47 (br s, 18H, PCH$_2$CH$_3$), -0.33 (s, 12H, -CH$_3$), -12.41 (br s, 12H, PCH$_2$CH$_3$).

[^{99m}Tc][Tc(PEt$_3$)$_2$(tmf$_2$en)]$^+$ ([^{99m}Tc]8). Preparation of the radiotracer [^{99m}Tc][Tc(PEt$_3$)$_2$(tmf$_2$en)]$^+$ complex was based on established procedures for radiolabeling ^{99m}Tc Q-complexes.[38] In the first step, 250 μL of a H$_2$tmf$_2$en stock solution (1 mg/mL in EtOH), 250 μL of a SnCl$_2$ stock solution (8 mg/mL in EtOH), 100 μL of aqueous [^{99m}Tc][NaTcO$_4$] (37-111 MBq), and 30 μL of 1.0 M NaOH were added to a reaction vial. The contents were heated at 75 °C for 10 min. In the second step, 30 μL of 1 M HCl and 300 μL of 1.0 M PEt$_3$ in THF were added to the reaction vial. The contents were heated for an additional 10 min at 75 °C. The reaction mixture was filtered through an Acrodisc 13 mm syringe filter with a 0.2 μm Nylon membrane to remove any precipitates. Complex **3** was used as a nonradioactive standard to confirm the formation of ^{99m}Tc species. Reversed-phase HPLC comparison of **3** (t_R = 14.00 min) and [^{99m}Tc][Tc(PEt$_3$)$_2$(tmf$_2$en)]$^+$ (t_R = 14.78 min) confirmed product formation in 97% radiochemical purity.

Electrochemistry.

Electrochemical data (**Table 2.2**) were obtained with a Bioanalytical Systems Inc. CV-50 (BASi, West Lafayette, IN). Tetraethylammonium perchlorate (TEAP; 0.1 M) in propylene carbonate (Burdick and Jackson, high-purity solvent for gas chromatography and spectrophotometry) was used as the electrolytic solution. A nonaqueous Ag/AgCl electrode (BAS; 0.1 M TEAP in propylene carbonate) was used as the reference

electrode, in addition to a Pt wire auxiliary electrode and a Au working electrode. A scan rate of 100 mV/s was used for all experiments. Formal potentials were standardized against the ferrocenium (Fc^+)/ferrocene (Fc) redox couple. Under these experimental conditions, the Fc^+/Fc redox couple was observed as $E_{1/2}$ = 0.384 V versus Ag/AgCl in propylene carbonate.

X-ray Crystal Structures.

Single-crystal X-ray diffraction (SCXRD) data for **1**•Et_2O were collected on a Bruker X8 Prospector diffractometer equipped with an Apex II CCD area detector using graphite-monochromated Cu Kα radiation from a microfocus source (45 kV, 0.65 mA, λ = 1.54178 Å). SCXRD data for **3**, **5**, and **8**•H_2O were collected on a Bruker D8 Venture diffractometer equipped with a Photon 100 CMOS detector using graphite-monochromated Mo Kα radiation from a microfocus source (50 kV, 1 mA, λ = 0.71073 Å). SCXRD data for **4**•0.5H_2O and **6**•0.5Et_2O were collected on a Bruker SMART diffractometer equipped with an Apex II CCD area detector using graphite-monochromated Mo Kα radiation from a sealed tube source with focusing optics (50 kV, 30 mA, λ = 0.71073 Å). In all cases, hemispheres of unique data were collected using a strategy of scans about the ω and ϕ axes. The intensities were corrected for Lorentz and polarization effects. Equivalent reflections were merged, and empirical absorption corrections were made using the multiscan method. Space groups, lattice parameters, and other relevant information are given in **Table 2.3**. Relevant bond lengths and angles are given in **Table 2.4**. Data collection, unit cell determination, data reduction, absorption correction, scaling, and space group determination were all performed using the Bruker Apex3 software suite.[94] See Appendix A for structure solution details.

2.3 Results and Discussion

Radiopharmaceutical translation into a clinical setting typically requires the development of one-step, one-vial kit formulations. Preparations of this type are simple to use and obviate the need for chromatographic purification prior to patient administration. Thus, ligand systems that quickly and efficiently coordinate radiometals are desirable for radiopharmaceutical development. Technetium-99m furifosmin is one example of a radiopharmaceutical accessible from a one-step kit formulation.

The preparation of Q complexes involves the coordination of dissimilar ligands to a central metal—a tetradentate Schiff base and two tertiary phosphines. Previous work has sought to optimize one-step radiolabeling efficiency for ^{99m}Tc Q complexes by varying the substituents on the Schiff base and tertiary phosphine ligands.[38] Incorporation of a cyclic furanone ring into the Schiff base ligand was found to substantially increase one-step radiolabeling efficiency. One explanation was that the steric constraints imposed by the cyclic furanone ring impart kinetic stability to the labile technetium(V) Schiff base intermediate, leading to increased overall reaction yields. These results led to the creation of radiopharmaceutical kits for ^{99m}Tc Q complexes, including [^{99m}Tc]Tc-furifosmin.[38]

The development of rhenium Q complexes, including potential one-step $^{186/188}$Re kit formulations as potential radiotherapeutic agents, depends primarily on the coordination of the Schiff base ligand to the rhenium center. On the macroscopic level, this coordination is straightforward as rhenium(V) starting materials can be utilized. Translation to the tracer level will be more difficult, however, as [$^{186/188}$Re]ReO$_4^-$, with Re in the 7+ oxidation state, is the only starting material. The necessary reduction of the Re(VII) center prior to Schiff base coordination is nontrivial, requiring significantly more

reducing agent than ^{99m}Tc. The synthesis of $^{186/188}$Re Q complexes would also likely require longer reaction times, additional reducing agents, and higher reaction temperatures and would likely result in lower product yields than those observed for ^{99m}Tc Q complexes. Microwave-assisted synthesis, as reported in this chapter for the macroscopic rhenium complexes, may be a means of avoiding these common challenges in translating technetium-99m chemistry to $^{186/188}$Re.

A series of macroscopic rhenium Q complexes were synthesized to understand the coordination of rhenium with tmf$_2$enH$_2$ and compare it to that observed for technetium. A two-step (one-pot) synthetic methodology was employed because the focus of the present work is to understand the coordination chemistry of rhenium Q complexes rather than to optimize a potential $^{186/188}$Re kit formulation. This methodology also allowed for isolation of the oxorhenium(V) and oxotechnetium(V) Schiff base intermediates.

Synthesis of the *trans*-[Re^{V}OCl(tmf$_2$en)] Complex 1 and the *trans*-[Re^{III}(PR$_3$)$_2$(tmf$_2$en)]$^+$ Complexes 2-5.

Complex **1** was isolated as maroon needlelike crystals from an equimolar reaction of tmf$_2$enH$_2$ with (*n*Bu$_4$N)[ReOCl$_4$] in EtOH under dry, inert conditions (**Scheme 2.1**). Using microwave heating, this reaction proceeds with near-complete rhenium coordination by the Schiff base ligand as determined by ^{1}H NMR. Complex **1** was readily isolated by extraction into and crystallization from Et$_2$O. Purification of **1** by silica gel column chromatography proved difficult, as coordinating solvents such as MeOH, MeCN, or H$_2$O readily displaced the labile chloro ligand. Attempts to isolate **1** by silica gel chromatography yielded the mononuclear *trans*-[ReO(OMe)(tmf$_2$en)] (**A1**) and the dinuclear *trans*-[μ-O(ReO(tmf$_2$en))$_2$] (**A2**) (shown in **Scheme 2.1** and with characterization and structural details in Appendix A). Mononuclear **A1** likely forms by

displacement of the chloro ligand by MeOH, whereas dinuclear **A2** likely forms by hydrolysis facilitated bytrace amounts of water.[71, 75]

Because of the near-quantitative formation of **1**, the Re(III) complexes **2-5** were prepared via a two-step *in situ* approach without isolating the oxorhenium(V) intermediate. Equimolar amounts of tmf$_2$enH$_2$ and (nBu$_4$N)[ReOCl$_4$] were combined forming **1** *in situ*, and then four equivalents of the tertiary phosphine ligand were added in a subsequent step (**Scheme 2.2**). Under these conditions, complexes **2-5** were obtained in 54−80% isolated yield after purification by silica gel column chromatography. These isolated yields using microwave syntheses are an improvement over the synthesis of Re(III) Schiff base phosphine compounds by conventional methods. A similar two-step approach using conventional heating resulted in a 48% isolated yield for *trans*-[Re(PPh$_3$)$_2$(acac$_2$en)]PF$_6$,[73] while a 10% isolated yield was reported by Lane for *trans*-[Re(PPh$_3$)$_2$(sal$_2$phen)]Cl.[72] In addition to low product yields, these conventional heating methods suffer from long reaction times (3-12 h) and the production of various rhenium(V) and ligand side products.[72, 73] The differences between microwave and conventional heating methods are significant because short, high-yielding reactions are preferable for translation to radiotracer syntheses and kit formulations.

The Re(III) complexes are thought to form through a multistep mechanism.[41, 73] An initial tertiary phosphine substitutes for the chloro ligand. A second tertiary phosphine initiates an oxygen-atom-transfer reaction with the oxo group, reducing the metal center from V to III and leaving a vacant coordination site. In the process, phosphine oxide is released as a byproduct and a third tertiary phosphine coordinates *trans* to the initial phosphine to yield the reduced *trans*-[Re^{III}(PR$_3$)$_2$(Schiff base)]$^+$ product. In this manner,

phosphine acts as both a coordinating ligand and a reducing agent. Excess phosphine serves to drive the reaction toward product formation. The *in situ* formation of **1**, as opposed to a *cis*-coordinated product, obviates any rearrangement of the Schiff base about the metal center prior to coordination, as observed for sal₂ibn Schiff base complexes.[71]

The cationic Re(III) species **2-4** are water-soluble and stable under ambient conditions. Each was dissolved in D_2O and analyzed by ^1H NMR. After standing in D_2O for over one week, reanalysis by NMR showed virtually no change in the number or relative intensity of the signals. Complex **5** is only sparingly soluble in water because of the four hydrophobic phenyl rings but is stable in polar organic solvents.

Synthesis of the *trans*-[Tc^{V}OCl(tmf₂en)] Complex 6 and the *trans*-[Tc^{III}(PR₃)₂(tmf₂en)]$^+$ Complexes 7 and 8.

Complex **6** was isolated as purple prismatic crystals from an equimolar reaction of tmf₂enH₂ with (*n*Bu₄N)[TcOCl₄] in absolute EtOH under ambient conditions (**Scheme 2.1**). The reaction was complete in 10 min with a 50% radiochemical yield as determined by radio-TLC. The isolated yield for **6** was 40%. Unlike **1**, complex **6** was easily purified by silica gel chromatography. Despite using reaction conditions similar to those of its rhenium analogue **1**, compound **6** did not lose its Cl⁻ ion or form the μ-oxo dimer. The IR spectrum of the isolated species includes a Tc≡O stretch at 919 cm^{-1} characteristic of technetium(V) oxo complexes.[84, 95] The Tc≡O stretch of **6** is lower in energy than that of the rhenium analogue **1**, which is observed at 952 cm^{-1}. This is tentatively supported by crystallographic data for the two complexes, which indicate that the Tc≡O bond of **6** is longer than the Re≡O bond of **1** (*vide infra*), although the presence of crystallographic disorder makes these distances less reliable indicators. Single crystals of **6** were isolated

by slow evaporation from a solution of the compound in Et_2O. Compound **8** was synthesized by a two-step, in situ approach under ambient conditions (**Scheme 2.2**). Equimolar amounts of tmf_2enH_2 and $(nBu_4N)[TcOCl_4]$ were combined to form **6** *in situ*, followed by the addition of four equivalents of the tertiary phosphine ligands to form the *trans*-$[Tc(PEt_3)_2(tmf_2en)]^+$ species in 37% overall radiochemical yield [74% based on 50% yield for the Tc(V) precursor]. The isolated yield for **8** was 25%.

Compound **7** was prepared analogously to compound **8** only under inert conditions in a microwave reactor. A microwave reactor was used to increase the radiochemical yield, even though the compound readily forms under ambient conditions. A radiochemical yield of 75% (isolated yield of 64%) was achieved when microwave heating was employed. Compounds **7** and **8** were purified by silica gel chromatography. Two common side products were observed during column chromatography: $[TcCl_4(PR_3)_2]$ eluted as a bright-blue band using CH_2Cl_2, while $[TcCl_3(PR_3)_3]$ eluted as an orange-brown band using acetone. These corresponding rhenium byproducts were not observed in the purification of complexes **2-5**.
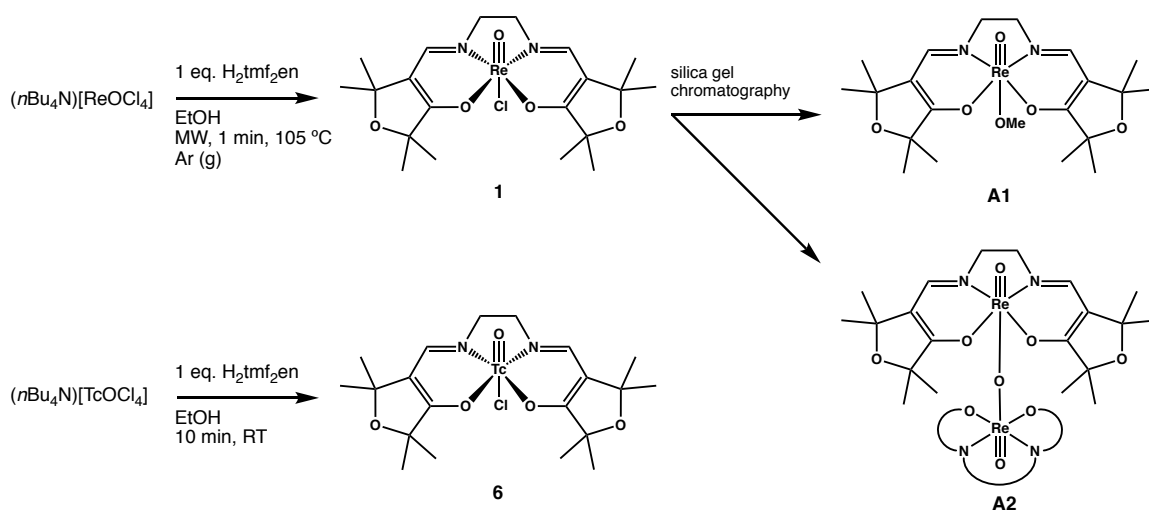
Scheme 2.1 Synthesis of *trans*-$[MOCl(tmf_2en)]$ (M = Tc, **1**; Re, **6**).
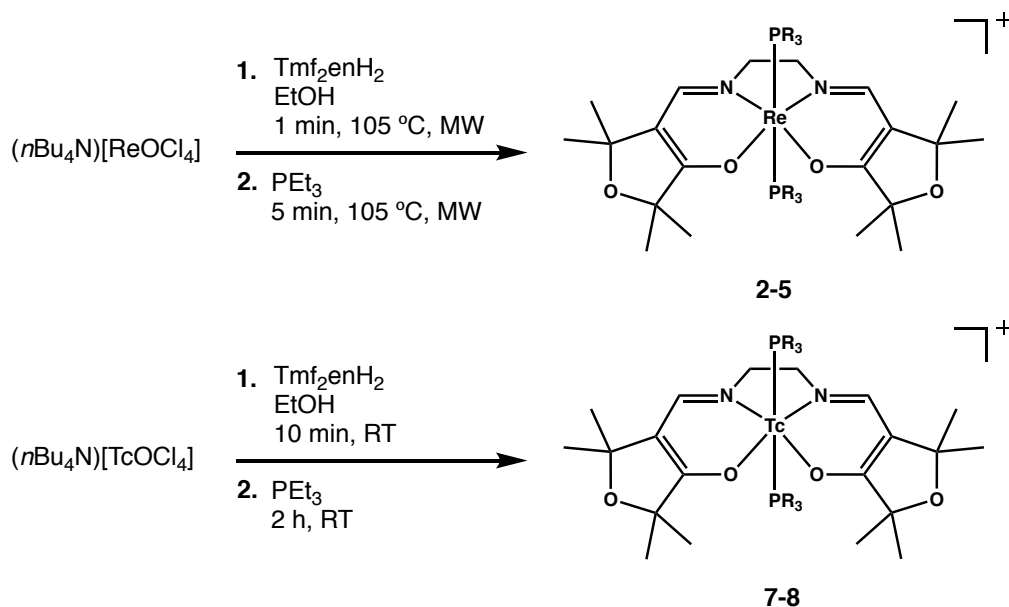
Scheme 2.2. Synthesis of *trans*-[Re(PR$_3$)$_2$(tmf$_2$en)]$^+$ (PR$_3$ = TMPP, **2**; PEt$_3$, **3**; PEt$_2$Ph, **4**; PEtPh$_2$, **5**) and *trans*-[Tc(PR$_3$)$_2$(tmf$_2$en)]$^+$ (PR$_3$ = TMPP, **7**; PEt$_3$, **8**)

Synthesis of [^{99m}Tc][Tc(PEt$_3$)$_2$(tmf$_2$en)]$^+$ ([^{99m}Tc]8) and Comparison to *trans*-[Re(PEt$_3$)$_2$(tmf$_2$en)]$^+$ (3).

The radiotracer principle states that radiolabeled compounds will be chemically identical with their nonradioactive counterparts, but this only holds true when the compounds contain radioactive or non-radioactive isotopes of the same element. Translation of diagnostic ^{99m}Tc radiopharmaceuticals to therapeutic $^{186/188}$Re radiopharmaceuticals relies on the chemical similarity between distinct elements, thus requiring experimental validation. The species [^{99m}Tc]**8** was prepared for comparison with its rhenium congener **3**. A two-step (one-pot) synthesis was followed based on existing procedures for ^{99m}Tc Q complexes.[38] A reversed-phase HPLC comparison of **3** (t_R = 14.004 min) and [^{99m}Tc]**8** (t_R = 14.779 min) confirmed the chemical similarity of the two species (**Figure 2.2**). The difference in the retention times between the ^{99m}Tc and Re species is attributed to the relative positions of the photometric and radiometric detectors in the HPLC system. The radiochemical purity of [^{99m}Tc]**8** was determined to be 97%.
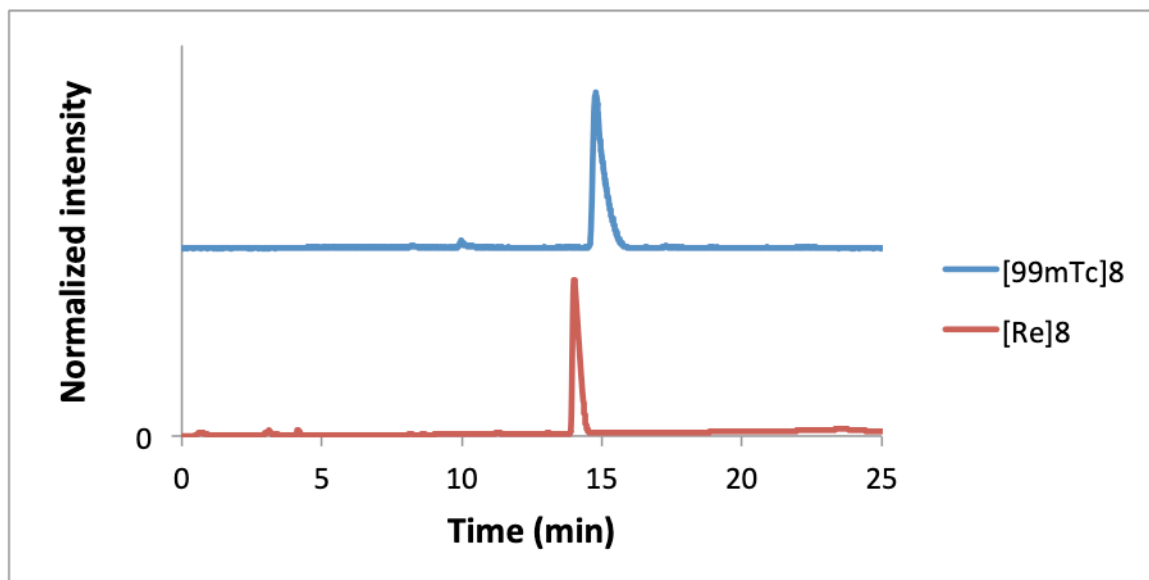
Figure 2.2. Comparison of the HPLC chromatograms for *trans*-[Re(PEt)$_3$(tmf$_2$en)]$^+$ ([Re]**3**, red, t_R = 14.00 min) and [^{99m}Tc][Tc(PEt$_3$)$_2$(tmf$_2$en)]$^+$ ([^{99m}Tc]**8**, blue, t_R = 14.78 min).

General Characterization.

Liquid chromatography-electrospray ionization mass spectrometry (LC-ESI-MS) was used to characterize the rhenium complexes. Molecular ions with the expected rhenium isotope pattern were observed for compounds **2-5** in the positive ESI-MS mode. Fragments of **2-5** with m/z values corresponding to [M - PR$_3$]$^+$ were also observed. Compound **1** was observed as the cation [M - Cl]$^+$. The FT-IR spectrum of **1** displayed a stretch at 952 cm^{-1} indicative of a Re≡O bond. This stretch was absent in all Re(III) complexes. Compound **6** exhibited an intense stretch of 919 cm^{-1} in the FT-IR spectrum indicative of a Tc≡O bond, while Tc(III) compounds **7** and **8** lacked this stretch. Because of the radioactivity of ^{99}Tc, characterization of compounds **6-8** by LC-ESI-MS or elemental analysis was not practical. The ^{99}Tc compounds were characterized by ^{1}H NMR and FT-IR spectroscopies, X-ray crystallography, and radio-TLC.

NMR Characterization.

The M(V) and M(III) complexes are readily identified by their respective ^{1}H NMR chemical shifts (**Table 2.1**). The symmetry of the tmf$_2$en ligand simplifies the NMR spectra. The ^{1}H NMR spectrum for **1** showed four singlets for the furanyl methyl groups (1.44-1.51 ppm), two multiplets for the methylene protons (3.98 and 4.20 ppm), and a singlet for the imine protons (7.68 ppm). This proton splitting pattern is consistent with symmetric coordination of the Schiff base about the metal center and *trans* coordination of the chloro relative to the oxo group. The technetium complex **6** showed a ^{1}H NMR spectrum comparable to that of **1**. Four singlets (1.42-1.54 ppm) indicate the presence of the furanyl groups. Two multiplets (4.23 and 4.45 ppm) correspond to the methylene backbone. A single peak is seen at 7.49 ppm for the two imine protons.

NMR spectra for the Re(III) complexes **2-5** were more complex than those for the rhenium(V) complex **1** because of the influence of the d^4 paramagnetic rhenium center.[96-103] The ^{1}H NMR chemical shifts of **2-5** were sharp and observed in an expanded window (-30 to +85) because of the fast relaxation of the unpaired electrons. This behavior is consistent with previously reported paramagnetic Re(III) Q compounds.[71-73] The two imine protons for **2-5** are observed as singlets far downfield with chemical shifts of 77-85 ppm. The imine peak for complexes **2-5** shifts further downfield as the tertiary phosphine becomes more electronwithdrawing. The imine peak for complex **3** (PR$_3$ = PEt$_3$) was observed at 82.19 ppm, while that for complex **5** (PR$_3$ = PEtPh$_2$) was observed at 84.88 ppm. The backbone methylene protons were shifted downfield to 17−35 ppm for the Re(III) complexes. The furanyl methyl groups were observed as two singlets corresponding to 12 protons each in **2-5**. One singlet was observed in the range -0.6 to

45

+0.4 ppm, while the second singlet was observed in the range of 8.4-8.8 ppm.

For **3**, the methylene and methyl protons of the coordinated PEt$_3$ do not exhibit well-defined quartet−triplet proto coupling. These protons are observed as a broad triplet (2.38 ppm) for the methyl protons and a broad multiplet (2.75 ppm) for the methylene protons. Two-dimensional ^{1}H-^{1}H correlation spectroscopy (COSY) indicates that these two groups are, in fact, coupled. Aromatic protons for the coordinated tertiary phosphines (PEt$_2$Ph and PEtPh$_2$) in complexes **4** and **5** were assigned using ^{1}H-^{1}H COSY NMR. Cross-correlation peaks were observed between the meta protons and both the ortho and para aromatic protons in all cases. In *trans*-[Re(PEt$_2$Ph)$_2$(tmf$_2$en)]$^+$, **4**, the para and meta protons are observed as triplets with coupling constants of 7.5 and 7.1 Hz, respectively. Paramagnetic Re(III) causes rapid relaxation of phosphorus and a resultant loss of coupling. No ^{31}P signals were observed for the phosphorus coordinated to Re(III) in these complexes, consistent with previously reported paramagnetic Re(III) complexes.[71-73]

Spectral assignments for complexes **7** and **8** were challenging because of the influence of the d^4 paramagnetic Tc(III) center. For complex **8**, the methylene and methyl protons of the coordinated triethylphosphine ligand did not exhibit the expected proton coupling. Each group is observed as a broad singlet with chemical shifts of -12.41 and 3.47 ppm for the methylene and methyl protons, respectively. These shifts are similar to those reported by Mazzi et al. for the methylene and methyl protons of TcCl$_3$(PEt$_2$Ph)$_3$.[104, 105] Broad singlets at +6.27 and -0.33 ppm were attributed to the furanyl methyl protons of the tmf$_2$en ligand. The two imine and four ethylene backbone protons of **8** were not observed even after the sample was run overnight in an expanded window (-100 to +100 ppm). Complex **7** displayed furanyl methyl peaks at +6.21 and -

0.39 ppm similar to those for **8**. The methylene protons of the coordinated phosphine ligand have been tentatively assigned chemical shifts of +3.44, +3.22, +3.08, -9.24, and -15.95 ppm.

Table 2.1 ^{1}H NMR Spectral Assignments for **1-8**

Complex	1	2	3	4	5	6	7	8
Metal	Re(V)	Re(III)	Re(III)	Re(III)	Re(III)	Tc(V)	Tc(III)	Tc(III)
Methyl	1.44 (s, 6H)	0.41 (s, 12H)	0.31 (s, 12H)	0.08 (s, 12H)	-0.56 (s, 12H)	1.37 (s, 6H)	-0.39 (s, 12H)	-0.33 (s, 12H)
	1.46 (s, 6H)	8.58 (s, 12H)	8.42 (s, 12H)	8.65 (s, 12H)	8.79 (s, 12H)	1.43 (s, 6H)	6.21 (s, 12H)	6.27 (s, 12H)
	1.49 (s, 6H)					1.49 (s, 6H)		
	1.51 (s, 6H)					1.53 (s, 6H)		
Methylene	3.98 (m, 2H)	17.60 (s, 4H)	17.66 (s, 4H)	35.03 (s, 4H)	34.45 (s, 4H)	4.22 (s, 2H)	Not observed	Not observed
	4.20 (m, 2H)					4.53 (s, 2H)		
Imine	7.68 (s, 2H)	77.85 (s, 2H)	82.19 (s, 2H)	82.75 (s, 2H)	84.88 (s, 2H)	7.54 (s, 2H)	Not observed	Not observed

Electrochemistry.

The electrochemical behavior of the Re(III) and Tc(III) species was studied by cyclic voltammetry. The formal potential of the M^{III}/M^{II} redox couple is of particular interest as an initial gauge of the electrochemical stability *in vivo*. Reduction of cationic $[M^{III}(PR_3)_2(L)]^+$ complexes yields the neutral $[M^{II}(PR_3)_2(L)]$ complexes. Given that the biodistribution of [99m]Tc Q-compounds is dependent on their cationic charge, *in vivo* reduction risks a loss of the target specificity and radiopharmaceutical efficacy. Important cellular reducing agents include glutathione, cysteine, thioredoxin proteins, and $[NADPH]/[NADP^+]$. The potential heart imaging agent, $[^{99m}Tc][TcCl_2(dmpe)_2]^+$, underwent *in vivo* reduction to the neutral $[^{99m}Tc][TcCl_2(dmpe)_2]$ in humans, which led to the initial development of the non-reducible [99m]Tc Q-compounds.[106]

All Re(III) complexes show both reversible Re^{III}/Re^{II} and Re^{III}/Re^{IV} redox couples (**Table 2.2**). A representative cyclic voltammogram for **2** is shown in **Figure 2.3**. Each redox process is sensitive to the substituents of the tertiary phosphine ligand and rationalized by considering the donor/acceptor properties of the various tertiary

phosphine ligands. As the phosphine substituents become more electron-donating, the M(III) center becomes both easier to oxidize and harder to reduce. Phosphines with alkyl substituents are strong σ donors. They can stabilize a relatively electron-poor Re(IV) center through electron donation and, thus, lower the Re^{III}/Re^{IV} formal potential. Phenyl-containing phosphines are strong π acceptors. They can stabilize a relatively electron-rich Re(II) center through π-backbonding and, thus, lower the Re^{III}/Re^{II} potential.
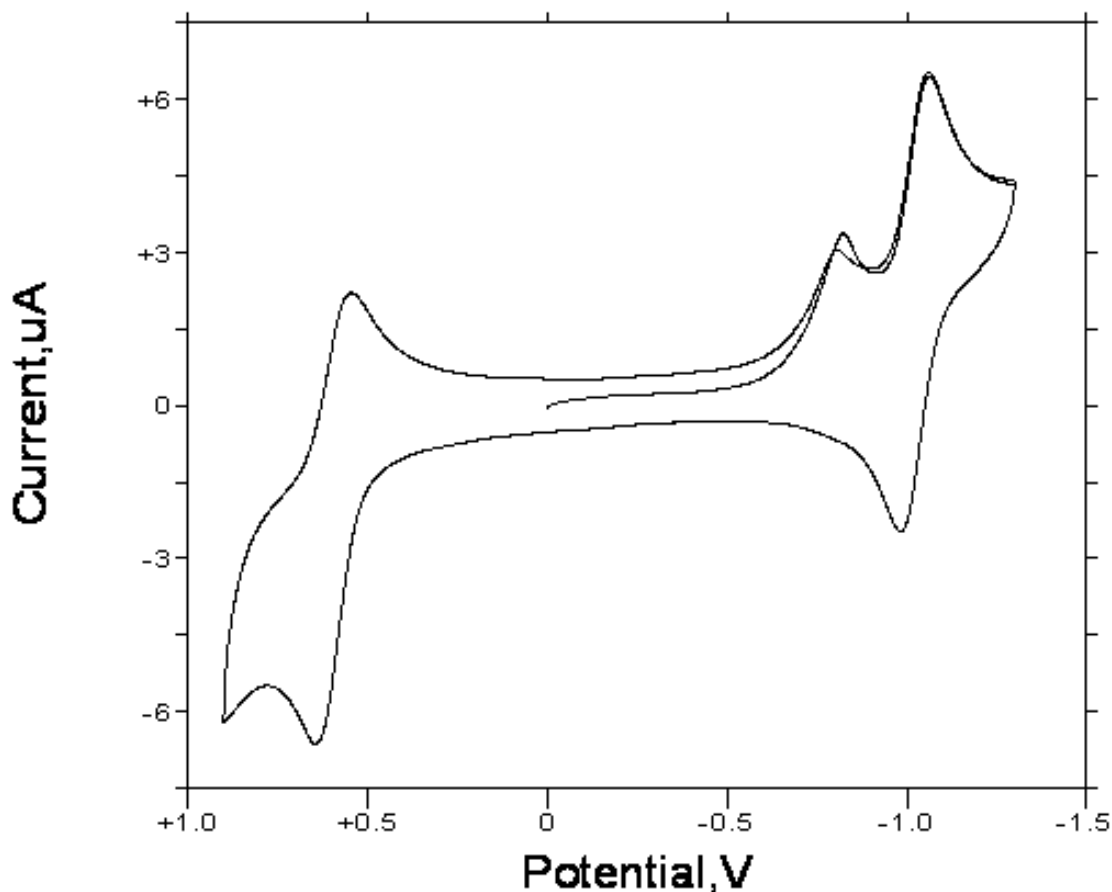
Figure 2.3 Cyclic voltammogram for *trans*-[Re(TMPP)$_2$(tmf$_2$en)]Cl **2**.

The formal potentials observed (**Table 2.2**) are more positive than those for the $Re^{III}acac_2en$ complexes reported by Benny et al.[73] The complex *trans*-[Re(PEt$_2$Ph)$_2$(acac$_2$en)]$^+$ has Re^{III}/Re^{II} and Re^{III}/Re^{IV} reversible redox couples with formal potentials of -1.431 and +0.118 V, respectively. The analogous complex **4**

48

reported herein has a Re^{III}/Re^{II} redox couple at -0.723 V and a Re^{III}/Re^{IV} redox couple at 0.859 V. This behavior is explained by considering the relative electronwithdrawing ability of the tmf$_2$en and acac$_2$en ligands. The tmf$_2$en ligand is more electron-withdrawing than acac$_2$en because of its furanyl substituents. It is a stronger π-acceptor serving to delocalize the electron density from the metal center. By delocalizing the electron density from the metal center, the tmf$_2$en ligand makes the Re(III) center more difficult to oxidize and easier to reduce compared to acac$_2$en. Although complex **4** is easier to reduce than its acac$_2$en counterpart, the Re^{III}/Re^{II} formal potential is still sufficiently negative that *in vivo* reduction is unlikely. Further, the tmf$_2$en ligand renders Re(III) compounds less susceptible to oxidation than acac$_2$en.

Table 2.2 $E°'$ values for Tc(III) and Re(III) complexes[a,b]

complex	III/II	III/IV	$\Delta E°'$
[Re(TMPP)$_2$(tmf$_2$en)]$^+$, **2**	-0.764	0.849	1.613
[Re(PEt$_3$)$_2$(tmf$_2$en)]$^+$, **3**	-0.798	0.848	1.646
[Re(PEt$_2$Ph)$_2$(tmf$_2$en)]$^+$, **4**	-0.713	0.907	1.620
[Re(PEtPh$_2$)$_2$(tmf$_2$en)]$^+$, **5**	-0.654	0.886	1.540
[Tc(TMPP)$_2$(tmf$_2$en)]$^+$, **7**	-0.556	0.817[c]	—
[Tc(PEt$_3$)$_2$(tmf$_2$en)]$^+$, **8**	-0.567	0.826[c]	—

[a]Conditions: cyclic voltammetry in propylene carbonate, 0.1 M TEAP; Au working electrode; Ag/AgCl reference electrode; Pt wire auxiliary electrode. [b]E_{MLCT} values in eV, $E°'$ values in V. [c]This value represent the anoidc $E_{1/2}$ for the oxidation of Tc(III) to Tc(IV). No corresponding cathodic peak was observed.

The Tc(III) complexes **7** and **8** undergo reversible Tc^{III}/Tc^{II} reduction with formal potentials approximately 200 mV more positive than those of their Re(III) congeners **2** and **3**, respectively. This is consistent with previous reports indicating that the Re(III) compounds are more resistant to reduction than the Tc(III) compounds.[73] An irreversible Tc^{III}/Tc^{IV} oxidation was observed for **8** with an anodic peak at 0.826 V. This was

surprising because numerous Tc(III) Schiff base complexes have been reported with reversible Tc^{III}/Tc^{IV} redox couples.[41, 85] Switching the working electrode to platinum or glassy carbon had no effect on the observed behavior. In all cases, a single anodic peak was observed. Complex **7** also displays an irreversible Tc^{III}/Tc^{IV} oxidation with a formal potential of 0.817 V. The irreversibility of the Tc^{III}/Tc^{IV} oxidation in the Tc(III) species compared to the Re(III) species may reflect differences in electron-transfer kinetics between the two metals.

X-ray Structure Analyses.

The metal(V) complexes **6**•$0.5Et_2O$ and **1**•Et_2O and the metal(III) complexes **8**•H_2O, **3**• $0.5H_2O$, **4**•$0.5H_2O$, and **5** were characterized by SCXRD (**Figures 2.4-9**). For all species, the equatorial plane is defined by the two oxygen donors (O1 and O2) and the two nitrogen donors (N1 and N2) of tmf_2en. The metal(III) complexes exhibit octahedral geometries with the Schiff base ligand situated in the equatorial plane and the two phosphine groups coordinated *trans* to each other. In contrast, the *trans*-$[M^VOCl(tmf_2en)]$ complexes **1**•Et_2O and **6**•$0.5Et_2O$ display distorted octahedral geometry with the M≡O positioned above the equatorial plane, consistent with known oxotechnetium(V) and oxorhenium(V) complexes. **Table 2.3** lists the space group, data collection, and refinement information, in addition to other key parameters. Selected bond lengths and bond angles are listed in **Table 2.4**. Crystallographic data for the two oxorhenium(V) compounds **A1** and **A2** are reported in Appendix A.

Table 2.3 X-ray crystal data, data collection parameters, and refinement parameters for **1**•Et$_2$O, **3-5**, **6**•0.5(Et$_2$O), and **8**•H$_2$O.

	1•Et$_2$O	**3**	**4•0.5(H$_2$O)**	**5**	**6•0.5(Et$_2$O)**	**8•H$_2$O**
formula	C$_{24}$H$_{40}$ClN$_2$O$_6$Re	C$_{32}$H$_{62}$ClN$_2$O$_5$P$_2$Re	C$_{40}$H$_{61}$ClN$_2$O$_{4.5}$P$_2$Re	C$_{48}$H$_{60}$ClN$_2$O$_4$P$_2$Re	C$_{22}$H$_{30}$ClN$_2$O$_{5.5}$Tc	C$_{32}$H$_{60}$F$_6$N$_2$O$_5$P$_3$Tc
CCDC #	1848702	1848703	1848704	1848706	1848701	1848705
fw	674.23	838.42	925.49	1012.57	543.93	857.73
cryst system	Monoclinic	Triclinic	Monoclinic	Monoclinic	Triclinic	Monoclinic
space group	C2/*c*	P-1	C2/*c*	P2$_1$/*c*	P-1	P2$_1$/n
a (Å)	25.5582(6)	10.6195(4)	36.136(3)	19.9567(8)	7.714(5)	16.3552(8)
b (Å)	10.8231(3)	11.7923(5)	13.4101(9)	13.1511(5)	10.903(8)	16.1952(8)
c (Å)	21.0843(5)	16.6323(6)	19.982(1)	19.8558(8)	15.35(1)	46.211(2)
α (deg)	90	70.617(1)	90	90	92.70(3)	90
β (deg)	98.952(1)	77.792(1)	121.179(1)	116.854(1)	94.19(2)	95.106(1)
γ (deg)	90	82.208(1)	90	90	98.96(2)	90
V (Å^3)	5761.3(3)	1915.5(1)	8284(1)	4649.2(3)	1269.3(15)	12191.7(1)
Z	8	2	8	4	2	12
ρ (g/cm^3)	1.555	1.454	1.484	1.447	1.423	1.402
T (K)	100	150	100	150	100	100.15
μ (mm^{-1})	9.414	3.363	3.117	2.784	0.707	0.538
λ (Å)	0.71073	0.71073	0.71073	0.71073	0.71073	0.71073
R(F)^a	0.0352	0.0150	0.0257	0.0325	0.0389	0.0482
Rw(F)^2	0.0789	0.0343	0.0483	0.0465	0.0851	0.0987
GoF	1.270	1.140	1.026	1.067	1.063	1.103

Table 2.4 Select bond lengths (Å) and angles (°) for compounds **1•** Et$_2$O, **3, 4•**0.5 H$_2$O, **5, 6•**0.5 Et$_2$O and **8•**H$_2$O.[a]

	1•Et$_2$O	3	4•0.5 H$_2$O	5	6•0.5 Et$_2$O	8•H$_2$O[b]
M(1)-O(1)	2.112(3)	2.047(1)	2.043(2)	2.047(2)	2.123(2)	2.032(2)
M(1)-O(2)	2.103(3)	2.056(1)	2.042(2)	2.048(2)	2.110(2)	2.0355(19)
M(1)-O(3) [oxo]	1.666(15)	—	—	—	1.676(5)	—
M(1)-N(1)	2.037(3)	2.036(1)	2.025(2)	2.033(2)	2.006(2)	2.042(2)
M(1)-N(2)	2.000(3)	2.034(1)	2.040(2)	2.042(2)	2.006(2)	2.041(2)
M(1)-Cl	2.448(3)	—	—	—	2.4853(15)	—
M(1)-P(1)	—	2.4762(4)	2.4713(7)	2.4721(7)	—	2.4901(8)
M(1)-P(2)	—	2.4627(4)	2.4745(7)	2.4750(7)	—	2.4909(8)
O(1)-M(1)-O(2)	91.8(1)	96.40(4)	94.10(7)	97.23(7)	92.51(9)	98.19(8)
O(1)-M(1)-N(1)	91.5(1)	91.39(5)	91.99(8)	90.91(8)	92.0(1)	90.22(9)
O(2)-M(1)-N(1)	164.02(15)	172.15(5)	173.91(7)	171.81(8)	166.55(9)	171.11(9)
O(1)-M(1)-N(2)	164.44(16)	172.15(5)	173.89(8)	171.05(8)	165.56(9)	171.41(9)
O(2)-M(1)-N(2)	92.9(1)	91.33(5)	91.87(7)	90.58(8)	91.72(9)	89.86(9)
N(1)-M(1)-N(2)	80.1(1)	80.91(5)	82.05(8)	81.31(9)	80.95(10)	81.9(1)
O(1)-M(1)-Cl(1)	81.29(13)	—	—	—	79.42(8)	—
O(2)-M(1)-Cl(1)	79.0(1)	—	—	—	80.72(8)	—
O(3)-M(1)-Cl(1)	167.4(6)	—	—	—	164.5(2)	—
N(1)-M(1)-Cl(1)	86.0(1)	—	—	—	87.69(8)	—
N(2)-M(1)-Cl(1)	85.05(13)	—	—	—	87.66(9)	—
N(2)-M(1)-P(2)	—	93.66(4)	89.35(6)	93.60(7)	—	95.08(8)
N(1)-M(1)-P(2)	—	91.65(4)	91.01(6)	91.41(6)	—	91.86(7)
O(1)-M(1)-P(2)	—	88.06(3)	89.43(5)	88.19(6)	—	88.56(6)
O(2)-M(1)-P(2)	—	87.68(3)	88.72(5)	87.92(5)	—	85.51(6)
N(2)-M(1)-P(1)	—	91.05(4)	90.29(6)	92.10(7)	—	93.40(8)
N(1)-M(1)-P(1)	—	93.68(4)	91.56(6)	92.88(6)	—	95.66(7)
O(1)-M(1)-P(1)	—	87.89(3)	91.20(5)	86.64(6)	—	83.93(6)
O(2)-M(1)-P(1)	—	87.57(3)	88.65(5)	88.55(5)	—	88.14(6)
P(1)-M(1)-P(2)	—	173.38(1)	177.33(2)	173.33(2)	—	169.38(3)

[a]M(1) = Re(1) or Tc(1) [b]Only the data for **8•**H$_2$O molecule a is listed. Data for molecules b and c are given in Appendix A.

1·Et₂O

Complex **1** (**Figure 2.4**) displays distorted octahedral coordination with the chloride ligand oriented trans to the oxo group. The central O≡Re-Cl axis is disordered by 18% because of the partial occupancy of these atoms in two orientations with respect to the equatorial plane. In the principal occupancy, rhenium sits 0.26 Å above the ligand equatorial plane toward the oxo group. The minor occupancy features an inversion of the oxo and chloro moieties with a concomitant shift of rhenium below the equatorial plane. The two moieties are related by an approximate 180° rotation about an axis passing directly through the ligand but above (or below) the metal. The axial bond angle is 167.4°, indicating a deviation from linearity. This arises because the chloro ligand is directed away from the backbone methylene protons. The structure of **1**•Et₂O is similar to that of *trans*-[ReOCl(acac₂pn)] reported by Benny et al.[75] The Re≡O bond length of 1.666 Å is slightly shorter than the 1.676 Å Tc≡O bond length observed for complex **6**•0.5Et₂O. This difference in the bond length is reflected in the IR spectrum of the two complexes. Complex **1**·Et₂O displays a Re≡O stretch at 952 cm⁻¹, while the longer, lower energy Tc≡O stretch of **6**•0.5Et₂O is observed at 919 cm⁻¹. The Re-O (2.103-2.112 Å) and Re-N (2.000-2.037 Å) bond distances are also consistent with other oxorhenium(V) Schiff base complexes.[71, 75, 107-110] The bond lengths and angles between the rhenium and technetium complexes are nearly identical.
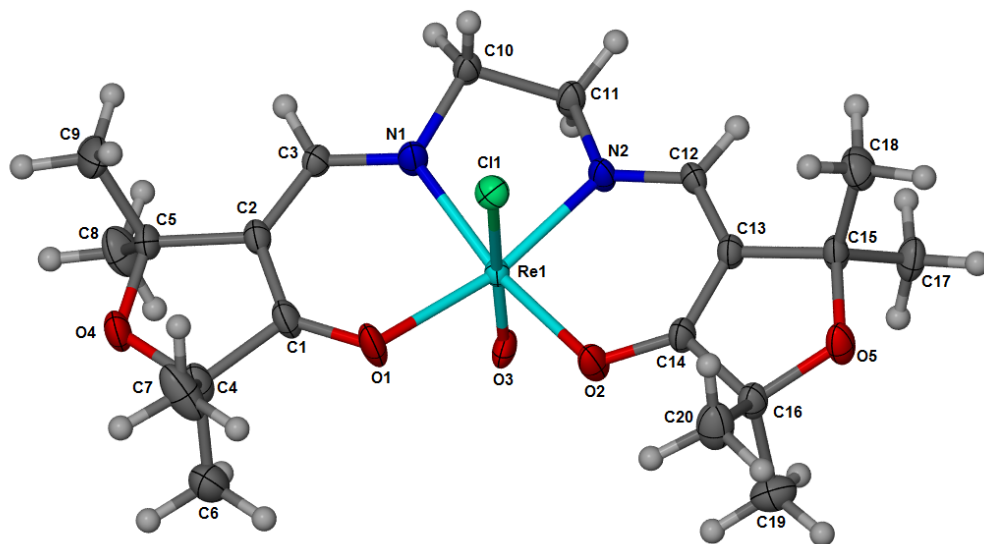
Figure 2.4 X-ray crystal structure of *trans*-[ReOCl(tmf$_2$en)]•Et$_2$O, **1**•Et$_2$O, with 50% probability thermal ellipsoids (CCDC # 1848702).

3, 4·0.5H$_2$O, and 5.

Complexes **3-5** (**Figures 2.5-7**) demonstrate octahedral coordination geometry with the two tertiary phosphine ligands orientated *trans* to one another. All bond angles about the metal center lie within the expected range with the angles for the cis and trans ligands at 88-94° and 173-177°, respectively. The Re-P (2.4627-2.4750 Å) bond distances are similar to other Re(III) bis-(phosphine) species[72, 73] and show that rhenium lies equidistant to each phosphine. The average Re-P bond distance is shortest for **3** and longest for **5**, consistent with the observation that PEt$_3$ is the strongest σ donor of the tertiary phosphine series while PEtPh$_2$ is the weakest. Complex **3** is the third-row congener of complex **8**•H$_2$O. The Re-P bond lengths in **3** (2.4627−2.4762 Å) are shorter than those for Tc-P in **8**•H$_2$O (2.4852−2.5022 Å).
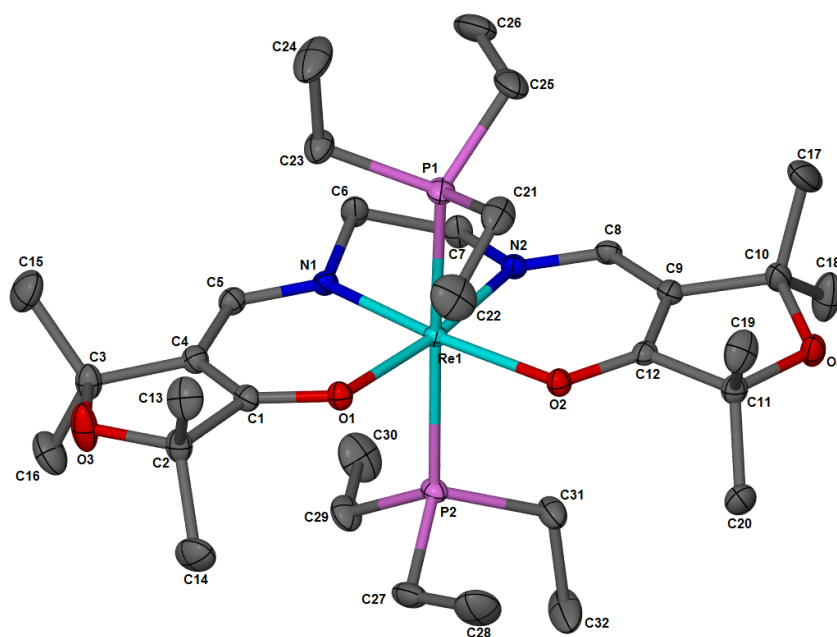
Figure 2.5 X-ray crystal structure of *trans*-[Re(PEt₃)₂(tmf₂en)]Cl, **3**, with 50% probability thermal ellipsoids (CCDC # 1848703).
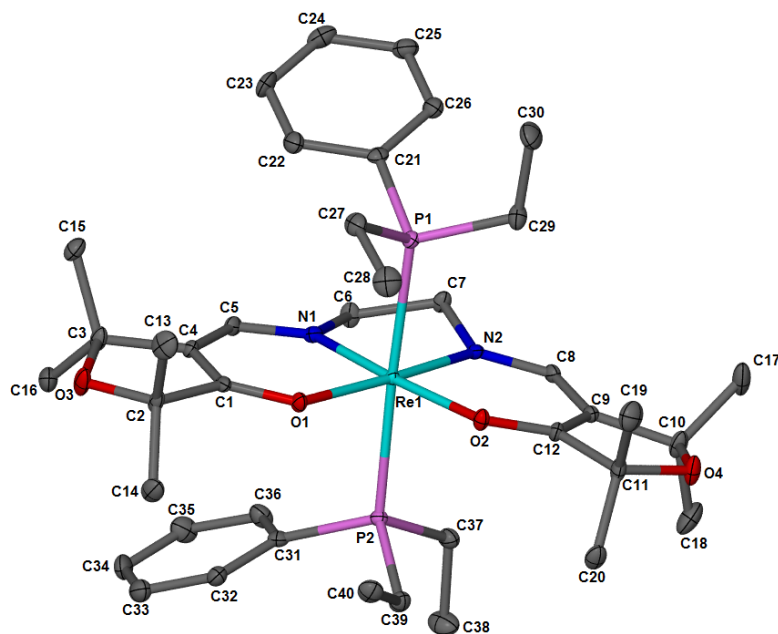
Figure 2.6 X-ray crystal structure of *trans*-[Re(PEt₂Ph)₂(tmf₂en)]Cl•0.5(H₂O), **4**•0.5(H₂O), with 50% probability thermal ellipsoids (CCDC # 1848704).
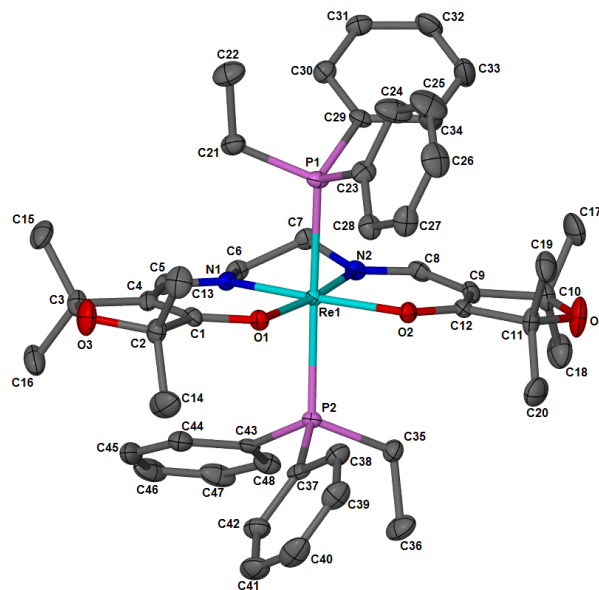
Figure 2.7 X-ray crystal structure of *trans*-[Re(PEtPh$_2$)$_2$(tmf$_2$en)]Cl, **5**, with 50% probability thermal ellipsoids (CCDC # 1848706).

6•0.5Et$_2$O.

The X-ray crystal structure of **6•0.5Et$_2$O** shows a Tc^V(tmf$_2$en) complex with a chloride ligand coordinated *trans* relative to the oxo group (**Figure 2.8**). The structure of **6•0.5Et$_2$O** exhibits coordination similar to that of *trans*-[TcOCl(sal$_2$en)] and *trans*-[TcO(H$_2$O)(acac$_2$en)]$^+$ reported previously by Jurisson et al.[84] The Tc center of **6•0.5Et$_2$O** is pulled 0.23 Å above the equatorial plane toward the oxo group. Bond angles about the metal center fall within expected ranges, with *cis* and *trans* bond angles of 79-106° and 166°, respectively. The axial O≡Tc-Cl bond angle is 164.53° with the oxo and chloro groups oriented away from the ethylene backbone with respect to the technetium center. The Tc≡O bond length of 1.676 Å is comparable to those of known oxotechnetium(V) species and indicative of a formal triple bond.[41, 107] The Tc-Cl bond length of 2.4853 Å lies within the expected range for similar compounds.[41, 107] The Tc-N (2.006 Å) and Tc-O (2.110-2.123 Å) bond lengths fall within expected ranges for related species.[41, 84, 107-110]
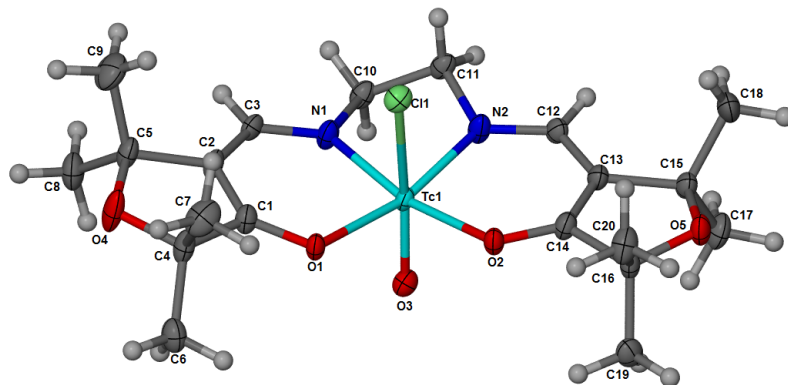
Figure 2.8 X-ray crystal structure of *trans*-[TcOCl(tmf$_2$en)]•0.5(Et$_2$O), **6**•0.5(Et$_2$O), with 50% probability thermal ellipsoids (CCDC # 1848701).

8·3H$_2$O.

Crystallographic data for **8**•3H$_2$O shows a Tc^{III}(tmf$_2$en) complex with two triethylphosphine substituents coordinated *trans* to each other (**Figure 2.9**). Each technetium metal center sits in the equatorial plane equidistant from the two coordinated phosphines. The central P-Tc-P bond angle is nonlinear at 168.34°. The Tc-N (2.039-2.041 Å), Tc-O (2.035-2.036 Å), and Tc-P (2.485-2.502 Å) bond lengths are consistent with known Tc(III) Schiff base complexes.[41, 107, 108, 111, 112] Three crystallographically unique molecules are observed in the unit cell of **8**•3H$_2$O along with three PF$_6^-$ anions for charge balance. In the extended structure, the metal complexes hydrogen bond to each other with the aid of water molecules (three per unit cell), to form zigzag chains, and the PF$_6^-$ anions sit between the zigzags. Two of the unique formula units are in one layer, and the third formula unit forms its own exclusive layer. The layers stack along B in an ABBA fashion, and all of the molecules have their P−Tc−P bond axes roughly parallel to B. The layers interface mainly through the ethyl groups of the PEt$_3$ ligands, possibly mediated by very weak C-H···interactions.
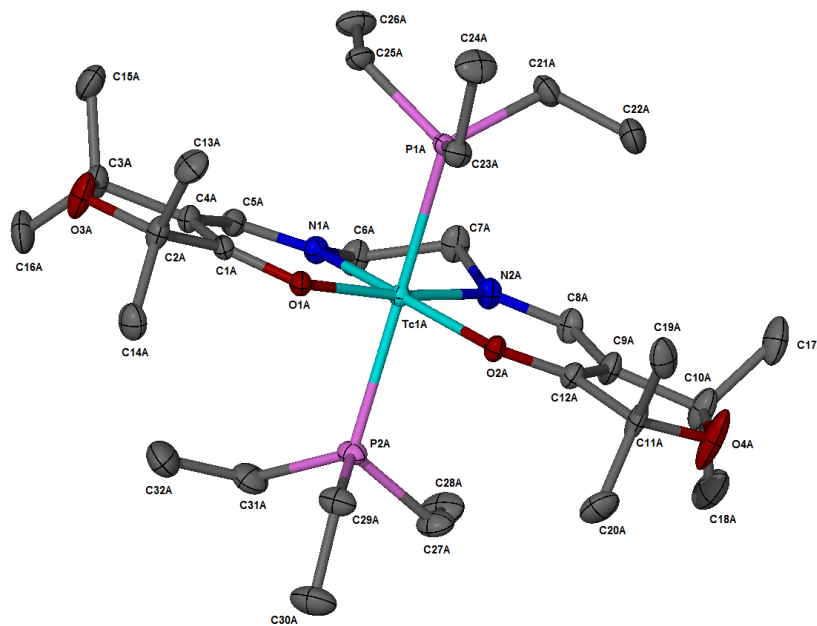
Figure 2.9 X-ray crystal structure of *trans*-[Tc(PEt$_3$)$_2$(tmf$_2$en)]PF$_6$•H$_2$O, **8**•H$_2$O, with 50% probability thermal ellipsoids (CCDC # 1848705).

2.4 Conclusion

Mononuclear oxorhenium(V) and Re(III) Schiff base complexes are readily prepared by microwave-assisted synthesis. The oxorhenium(V) compound **1** can be isolated via crystallization or used as an *in situ* intermediate in the formation of *trans*-[Re(PR$_3$)$_2$(tmf$_2$en)]$^+$ species. As expected, microwave-assisted synthesis produced higher yields and shorter reaction times compared to conventional synthesis methods for Re(III) Q-compounds and significantly fewer byproducts, making purification and isolation much simpler. The oxotechnetium(V) complex **6** was prepared under ambient conditions and isolated by column chromatography. *In situ* formation of **6** followed by reduction with triethylphosphine yields the Tc(III) complexes **7** and **8**. Complexes **2**-**5** all undergo reversible Re^{III}/Re^{II} and Re^{III}/Re^{IV} redox processes. The position of the Re^{III}/Re^{II} redox

couple for each is sufficiently negative that in vivo reduction should not be accessible. In contrast, complexes **7** and **8** display reversible Tc^{III}/Tc^{II} redox couples and irreversible Tc^{III}/Tc^{IV} redox couples. This result correlates well with the observed tendency of **8** to oxidize and disproportionate in solution to TcO_2 and TcO_4^-. The Re(III) complexes **2-5** readily dissolve in water and are resistant to degradation over more than one week, as determined by ^1H NMR. The Re(III) complexes reported herein are the first rhenium analogues to the imaging agent $[^{99m}Tc]$Tc-furifosmin (Tc Q12). These results highlight some of the differences in rhenium and technetium chemistry and demonstrate the potential of Re(III) Schiff base compounds for use as P-glycoprotein biomodulators.

CHAPTER 3

Steric Influence of Salicylaldehyde-based Schiff Base Ligands in

the Formation of *trans*-[Re(PR$_3$)$_2$(Schiff Base)]$^+$ Complexes[2]

3.1 Introduction

Rhenium and technetium complexes with Schiff base ligands have garnered much attention in the fields of nuclear medicine and commercial catalysis. High oxidation state rhenium oxo (Re^{VII} and Re^V) complexes have found application as catalysts for oxygen atom transfer (OAT)[113-118] and hydrosilylation.[119, 120] Schiff base complexes of methyltrixoxrhenium (MTO) have also been investigated as epoxidation catalysts.[121-123] Although technetium has been the subject of numerous catalytic studies[124-130], any application of technetium towards commercial catalysis is hampered as all isotopes of this element are radioactive. The chemistry of technetium with Schiff base ligands has focused instead on the development of diagnostic imaging agents. Technetium-99m complexes of the type *trans*-[^{99m}Tc][Tc(PR$_3$)$_2$(N$_2$O$_2$-Schiff base)]$^+$, commonly known as the ^{99m}Tc "Q-series", have been investigated for single-photon emission computed tomography (SPECT) imaging of both myocardial perfusion and multi-drug resistant (MDR) tumors.[39, 62, 67, 68, 88, 131] The prototypical example of the Tc Q-series is ^{99m}Tc-furifosmin (Tc Q12), which has been evaluated in humans for myocardial perfusion imaging (**Figure 3.1**).[39]

Recent work has sought to translate Tc Q-series chemistry to rhenium for the development of therapeutic radiopharmaceuticals.[70-75] Development of isostructural Re and Tc complexes requires careful attention to the chemical differences between the two elements. Rhenium generally displays slower substitution kinetics than Tc and is harder to reduce. In the case of Re Q-compounds, attention must also be paid to the distinct roles played by the N_2O_2 Schiff base and tertiary phosphine ligands in Re Q-complex formation.
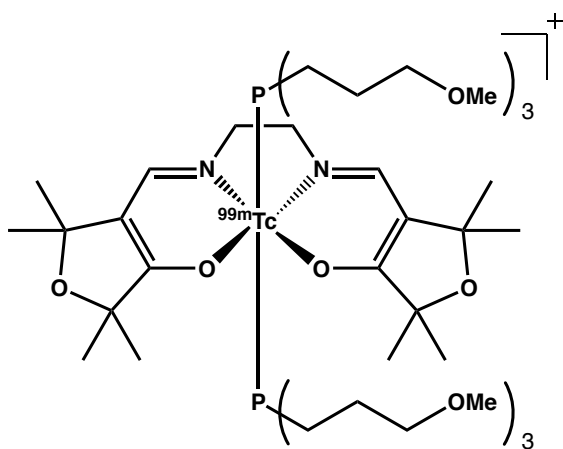
Figure 3.1. Structure of the [^{99m}Tc]Tc-furifosmin cation

The factors that direct the formation of *trans*-[Re(PR$_3$)$_2$(Schiff base)]$^+$ species have been previously investigated using a sterically hindered N_2O_2 Schiff base ligand (sal$_2$ibn).[71] This led to the isolation of the novel Re(V) complexes *cis*-[ReOCl(sal$_2$ibn)], *trans*-[μ-O(ReO(sal$_2$ibn))$_2$], and *cis*-[ReO(NCS)(sal$_2$ibn)], the Re(III) monomer *trans*-[Re(NCS)(PPh$_3$)(sal$_2$ibn)], and the Re(IV) dimer *trans*-[μ-O(Re(NCS)(sal$_2$ibn))$_2$].[71] Despite this progress, no true Re Q-compounds were made with the sal$_2$ibn ligand suggesting potential steric impedance to their formation. The few previously reported Re Q-compounds incorporate the N_2O_2 Schiff base ligands acac$_2$en, sal$_2$phen, or tmf$_2$en ligands, which all possess the sterically unencumbering ethylene (en) backbone. These

three ligands (acac$_2$en, sal$_2$phen, tmf$_2$en) all form *trans*-coordinated Re(V)-oxo intermediates, in contrast to the *cis*-coordinated sal$_2$ibn intermediate *cis*-[ReOCl(sal$_2$ibn)].[70, 72, 73] Formation of *trans*-[Re(PR$_3$)$_2$(sal$_2$ibn)]$^+$ complexes, thus, requires rearrangement of the Schiff base about the metal center. This chapter describes the synthesis and characterization of novel *trans*-[Re(PR$_3$)$_2$(Schiff base)]$^+$ species incorporating salicylaldehyde based N$_2$O$_2$ Schiff base ligands (sal$_2$ibn and sal$_2$en). By utilizing tertiary phosphine ligands with varying degrees of steric hindrance, an improved understanding of the steric factors influencing the formation of stable *trans*-[Re(PR$_3$)$_2$(Schiff base)]$^+$ species is developed.

Both sal$_2$en and sal$_2$ibn were found to form *trans*-[Re(PR$_3$)$_2$(Schiff base)]$^+$ complexes. The *trans*-[Re(PR$_3$)$_2$(sal$_2$ibn)]$^+$ complexes form through the *cis*-coordinated intermediate *cis*-ReOCl(sal$_2$ibn), whereas the *trans*-[Re(PR$_3$)$_2$(sal$_2$en)]$^+$ complexes form through a *trans*-coordinated intermediate. The *trans*-[Re(PR$_3$)$_2$(sal$_2$ibn)]$^+$ complexes were observed to rearrange and oxidize in solution over time to the corresponding *cis*-[ReO(PR$_3$)(sal$_2$ibn)]$^+$ products. Similar reactivity was not observed for their *trans*-[Re(PR$_3$)$_2$(sal$_2$en)]$^+$ analogues. The Re(III) and Re(V) complexes were fully characterized, including by single crystal X-ray crystallography and cyclic voltammetry.

3.2 Experimental

Materials

Unless otherwise noted, all common laboratory chemicals were of reagent grade or better. Absolute ethanol was degassed prior to use. All syntheses with rhenium were performed under an atmosphere of argon using standard Schlenk techniques. Microwave reactions were performed using a CEM Discover® SP microwave reactor (CEM Corporation,

Matthews, NC). ^{1}H and ^{13}C NMR spectra were recorded on a Brüker DRX500 or DRX600 at 25°C in CD_2Cl_2 or CD_3CN and calibrated with the respective residual solvent peaks ($CHDCl_2$ at 5.32 ppm; CHD_2CN at 1.94 ppm). ^{31}P NMR spectra were recorded on a Brüker DRX300 at 25 °C and calibrated using 85% aqueous H_3PO_4 as an external standard (0.00 ppm). Infrared spectra were obtained as KBr pellets on a Thermo Nicolet Nexus 670 FT-IR spectrometer. Liquid Chromatography Mass Spectroscopy (LC-MS) was performed on a ThermoFisher Scientific LCQ Fleet Ion Trap Mass Spectrometer. A Shimadzu Prominence HPLC system with a pump, controller, Prominence UV-vis detector (model SPD-20AV) set to 254 nm and coupled to a Beckman 170 NaI(Tl) radioisotope detector with a Phenomenex® Jupiter® LC column (C18, 5 μm, 250 x 4.6 mm) was used to analyze ^{99m}Tc and Re complexes, with a linear gradient from 50% A to 90% B (A = H_2O with 0.1% TFA, and B = MeCN with 0.1% TFA) with a flow rate of 1 mL/min over 20 minutes.

(nBu$_4$N)[ReOCl$_4$] was prepared according to established procedures.[92, 93] Salicylaldehyde, ethylenediamine, 1,2-diamino-2-methylpropane, triethylphosphine (1.0 M solution in THF), diethylphenylphosphine, ethyldiphenylphosphine, and triphenylphosphine were purchased from Sigma Aldrich and used as received. The tetradentate N_2O_2 Schiff base ligands *N,N'*-(1,1-dimethylethylene)bis(salicylaldimine) (sal$_2$ibnH$_2$) and *N,N'*-bis(salicylidene)ethylenediamine (sal$_2$enH$_2$) (**Figure 3.2**) were prepared as previously reported through condensation of two equivalents of salicylaldehyde with one equivalent of the respective diamine in absolute ethanol.[132] Each Schiff base ligand was recrystallized from absolute ethanol prior to use. ^{1}H NMR and FT-IR spectroscopies were used to verify the chemical purity of the starting materials.
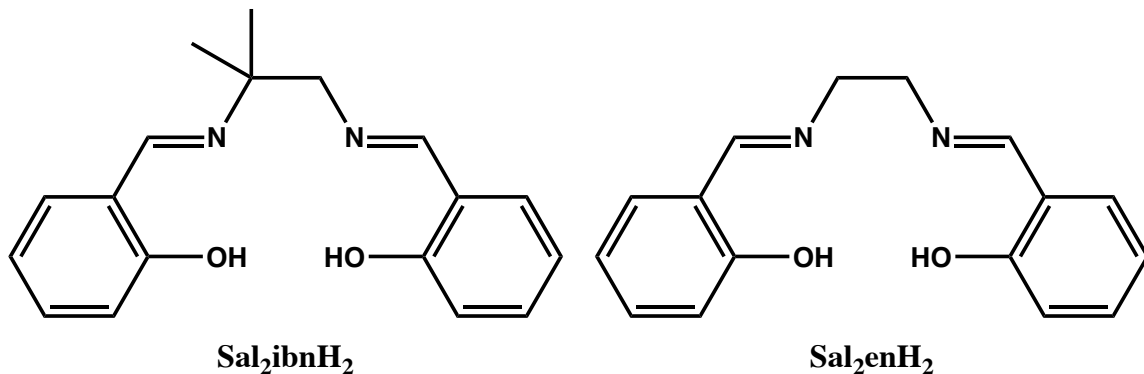
Figure 3.2. Structures of the N_2O_2 tetradentate Schiff base ligands sal$_2$ibnH$_2$ and sal$_2$enH$_2$

cis-ReOCl(sal₂ibn) , 9. Complex **9** was prepared by a modification to the literature method.[71] (nBu$_4$N)[ReOCl$_4$] (100.3 mg, 0.171 mmol) and H$_2$sal$_2$ibn (103.3 mg, 0.348 mmol) were added to a 10-mL microwave reaction vessel, which was purged and backfilled with argon three times. Degassed absolute ethanol (2 mL) was added to the vessel via *cannula*. The mixture was heated in a microwave reactor at 105 °C, 17 bar (max), and 150 W (max) for 1 min with stirring to yield a Kelly green precipitate and a brown supernatant. The precipitate was isolated by centrifugation and then washed with absolute ethanol (2 x 5 mL) and diethyl ether (2 x 5 mL). Yield 68.2% (62.0 mg). ^{1}H NMR [600 MHz, CD$_3$CN, r.t., δ (ppm)]: 8.85 (s, 1H, -**CH**=N-); 8.09 (s, 1H, -**CH**=N-); 7.85-7.75 (m, 8H, Ar**H**); 4.60, 4.63 (d, 1H, -**CH₂-**); 4.23, 4.26 (d, 1H, -**CH₂-**); 1.71 (s, 3H, -**CH₃**); 1.06 (s, 3H, -**CH₃**). ^{13}C NMR [600 MHz, CD$_3$CN, r.t., δ (ppm)]: 176.62, 175.07 (-H**C**=N-); 140.10, 139.47, 139.45, 135.77, 122.37, 120.89, 120.50, 120.21, 119.53, 119.24 (**Ar**); 138.95, 139.03 (**Ar**-O); 82.67 (-N**C**H$_2$-C(CH$_3$)$_2$); 79.17 (-NCH$_2$-**C**(CH$_3$)$_2$); 27.10, 23.56 (-**C**H$_3$). FT-IR (KBr pellet, ν in cm^{-1}): 1601 (C=N); 945 (Re=O).

trans-[Re(PEt₃)₂(sal₂en)][PF₆] , 10. (nBu$_4$N)[ReOCl$_4$] (50.24 mg, 0.086 mmol) and H$_2$sal$_2$en (24.57 mg, 0.092 mmol) were added to a 10-mL microwave reaction vessel,

which was purged and backfilled with argon three times. Degassed absolute ethanol (3 mL) was added to the vessel via *cannula*. The reaction solution was heated in a microwave reactor at 105 °C, 17 bar (max), and 150 W (max) for 1 min with stirring, resulting in a dark green solution. Triethylphosphine (1.0 M solution in THF, 350 μL, 0.34 mmol) was added to the reaction vessel via syringe, and the mixture was then heated (105 °C, 17 bar (max), and 150 W (max)) for 5 min with stirring. The resultant bright red solution was taken to dryness *in vacuo*. The oily red residue was dissolved in a minimal volume of CH_2Cl_2 and then loaded onto a silica gel column (8 g silica, 15 mm i.d.) pre-equilibrated in CH_2Cl_2. Elution with CH_2Cl_2 displaced triethylphosphine and triethylphosphine oxide from the column as a faint pink band. Switching the eluent to MeCN eluted several unidentified red bands. The red product-containing band was eluted with 20% MeOH in MeCN. This solution was brought to dryness by rotary evaporation to yield a dark red solid. Yield: 85% (53 mg). X-ray quality crystals of **10** were obtained by adding ammonium hexafluorophosphate (14.02 mg, 0.086 mmol) to a methanolic solution of the product, adding MilliQ H_2O, filtering the solution through Celite®, and then allowing the solution to sit loosely capped for several days. ^{1}H NMR [600 MHz, CD_3CN, r.t., δ (ppm)]: 60.06 (s, 2H, -**H**C=N-); 27.68 (d, J = 8.3 Hz, 2H, Ar**H**); 17.08 (t, J = 7.5 Hz, 2H, Ar**H**); 1.91 (t, J = -7.4 Hz, 18H, PCH$_2$C**H$_3$**); 1.76 (q, J = 7.3 Hz, 12H, PC**H$_2$**CH$_3$); -7.15 (t, J = 8.3 Hz, 2H, Ar**H**); -19.10 (d, J = 7.4 Hz, 2H, Ar**H**); -26.35 (s, 4H, -NC**H$_2$**C**H$_2$**N-). ^{13}C NMR [600 MHz, CD_3CN, r.t., δ (ppm)]: 172.47 (-**H**C=N-); 138.30, 134.63, 121.19, 121.03 (**Ar**); 67.72 (-NCH$_2$-CH$_2$N-); 16.39 (PCH$_2$**C**H$_3$); -6.16 (P**C**H$_2$CH$_3$). ESI MS (*m/z*): 688.94 (calcd. 689.24 for $[C_{28}H_{44}N_2O_2P_2Re]^+$ (M$^+$-PF$_6$)).

***trans*-[Re(PEtPh₂)₂(sal₂en)][Cl] , 11.** The synthesis of **11** followed the synthesis of **10** substituting ethyldiphenylphosphine for triethylphosphine. Yield: 32% (59 mg). X-ray quality crystals of **11**•CH₃OH were obtained by dissolving the product in methanol, filtering the solution through Celite®, and then allowing the solution to sit loosely capped for several days. ^{1}H NMR [500 MHz, CD₃CN, r.t., δ (ppm)]: 61.16 (s, 2H, -**H**C=N-); 27.00 (d, J = 8.2 Hz, 2H, Ar**H**); 16.45 (t, J = 7.3 Hz, 2H, Ar**H**); 8.11 (t, J = 7.4 Hz, 4H, P**Ph** *para*); 7.13 (t, J = 6.7 Hz, 6H, PCH₂C**H₃**); 6.61 (d, J = 7.7, 8H, P**Ph** *ortho*); 6.56 (br s, 8H, P**Ph** *meta*); 2.10 (q, J = 7.2 Hz, 4H, PC**H₂**CH₃); -7.84 (t, J = 8.0 Hz, 2H, Ar**H**); -19.70 (d, J = 7.8 Hz, 2H, Ar**H**); -20.28 (s, 4H, -NC**H₂**C**H₂**N-). ^{13}C NMR [600 MHz, CD₃CN, r.t., δ (ppm)]: 175.19 (-H**C**=N-); 136.06 (P**Ph** *meta*); 134.99, 134.93, 129.85, 129.78 (**Ar**); 128.99 (P**Ph** *para*); 125.17 (P**Ph** *ortho*) ; 67.13 (-N**C**H₂-**C**H₂N-)). ESI MS (*m/z*): 881.02 (calcd. 881.24 for [C₄₄H₄₄N₂O₂P₂Re]$^+$ (M$^+$-PF₆)).

***trans*-[Re(PPh₃)₂(sal₂en)][PF₆] , 12.** H₂sal₂en (41.44 mg, 0.15 mmol) and (*n*Bu₄N)[ReOCl₄] (88.22 mg, 0.15 mmol) were added to a 10-mL microwave reaction vessel. The vessel was backfilled and purged with Ar(g) three times and then 3 mL of degassed absolute ethanol was added via *cannula*. The mixture was heated in a microwave at 105 °C, 17 bar (max), and 150 W (max) for 1 min with stirring producing a green-brown slurry. In the second step, triphenylphosphine (238 mg, 0.91 mmol) dissolved in 0.5 mL CH₂Cl₂ was added to the reaction vessel via syringe. The mixture was heated in a microwave at 105 °C, 17 bar (max), and 150 W (max) for 6 min yielding a red-brown solution. The product was isolated by silica gel column chromatography as described for compound **10**. Yield: 50% (77 mg). ^{1}H NMR [600 MHz, CD₃CN, r.t., δ (ppm)]: 59.37 (s, 2H, -**H**C=N-); 26.54 (d, J = 7.8 Hz, 2H, Ar**H**); 15.75 (t, J = 7.5 Hz, 2H,

Ar**H**); 8.20 (t, *J* = 7.6 Hz, 6H, P**Ph** *para*); 7.24 (t, *J* = 7.1 12H, P**Ph** *meta*); 6.44 (br s, 12H, P**Ph** *ortho*); -9.30 (t, *J* = 8.1 Hz, 2H, Ar**H**); -19.51 (s, 4H, -NC**H₂**C**H₂**N-); -20.94 (d, *J* = 7.5 Hz, 2H, Ar**H**). ^{13}C NMR [600 MHz, CD₃CN, r.t., δ (ppm)]: 175.19 (-H**C**=N-); 136.06 (P**Ph** *meta*); 134.99, 134.93, 129.85, 129.78 (**Ar**); 128.99 (P**Ph** *para*); 125.17 (P**Ph** *ortho*) ; 67.13 (-N**C**H₂-**C**H₂N-)). ESI MS (*m/z*): 976.92 (calcd. 977.24 for $[C_{52}H_{44}N_2O_2P_2Re]^+$ (M⁺-PF₆)).

trans-[Re(PEt₃)₂(sal₂ibn)][PF₆] , **13**. Compound **9** (71.0 mg, 0.133 mmol) was added to a 10-mL microwave reaction vessel, which was backfilled and purged with argon three times. Degassed absolute ethanol (3 mL) was transferred to the vessel via *cannula*. Triethylphosphine (1.0 M in THF, 800 μL, 0.80 mmol) was added to the vessel via syringe. The mixture was heated in a microwave reactor at 105 °C, 17 bar (max), and 150 W (max) for 5 min with stirring to produce a bright red solution. This solution was evaporated under reduced pressure, dissolved in a minimal volume of CH₂Cl₂, and then loaded onto a silica gel column (8 g silica, 15 mm dia.) preequilibrated with CH₂Cl₂. The column was washed with CH₂Cl₂, which displaced a faint yellow band (PEt₃ and P(O)Et₃). The eluent was switched to acetonitrile (MeCN), which eluted an unidentified brown band. The product was finally eluted with 20% MeOH in MeCN. The product-containing solution was evaporated to dryness to yield a dark red solid. Yield: 79% (79 mg). X-ray quality crystals of **13** were obtained by the addition of ammonium hexafluorophosphate to a MeOH/H₂O solution of the product that was filtered through Celite® and left to sit for several days. ^{1}H NMR [600 MHz, CD₃CN, r.t., δ (ppm)]: 84.49 (s, 1H, -**H**C=N-); 56.59 (s, 1H, -**H**C=N-); 28.75 (d, 1H, Ar**H**); 27.75 (d, 1H, Ar**H**); 18.03 (t, 1H, Ar**H**); 17.25 (t, 1H, Ar**H**); 1.65 (s, 18H, P(C**H₂**C**H₃**)₃); 0.64-0.54 (br m, 6H,

P(C**H₂**CH₃)₃); 0.34-0.25 (br m, 6H, P(C**H₂**CH₃)₃); -1.65 (s, 6H, -C(C**H₃**)₂CH₂-); -6.66 (t, 1H, Ar**H**); -6.95 (t, 1H, Ar**H**); -18.96 (d, 1H, Ar**H**); -19.75 (d, 1H, Ar**H**); -31.06 (s, 2H, -C(CH₃)₂C**H₂**-). ^{13}C NMR [600 MHz, CD₃CN, r.t., δ (ppm)]: 167.71 (-H**C**=N-); 139.29, 138.88, 131.02, 129.92, 123.24, 122.65, 122.22, 121.35, 120.58, 119.89 (**Ar**) ; 73.31 (-N**C**H₂-C(CH₃)₂)); 67.72 (-NCH₂-**C**(CH₃)₂)); 19.32 (P**C**H₂CH₃); 7.29 (PCH₂**C**H₃); -6.29 ((**C**H₃)₂). ESI MS (*m/z*): 716.90 (calcd. 717.27 for [C₃₀H₄₈N₂O₂P₂Re]⁺ (M⁺-PF₆)).

trans-[Re(PEt₂Ph)₂(sal₂ibn)][Cl] , 14. The synthesis of 14 followed the synthesis of 13 substituting neat diethylphenylphosphine for triethylphosphine. Yield: 57% (65 mg). ^{1}H NMR [600 MHz, CD₃CN, r.t., δ (ppm)]: 83.34 (s, 1H, -C**H**=N-); 55.92 (s, 1H, -C**H**=N-); 27.94 (d, 1H, Ar**H**); 27.64 (d, 1H, Ar**H**); 17.48 (t, 1H, Ar**H**); 17.15 (t, 1H, Ar**H**); 13.62 (d, 4H, P**Ph** *ortho*); 9.20 (t, 2H, P**Ph** *para*); 8.42 (t, 4H, P**Ph** *meta*); 3.41 (q, 8H, PC**H₂**CH₃); 1.12 (t, 12H, PCH₂C**H₃**); -2.53 (s, 6H, -C(C**H₃**)₂CH₂-); -6.41 (t, 1H, Ar**H**); -7.57 (t, 1H, Ar**H**); -18.51 (d, 1H, Ar**H**); -20.29 (d, 1H, Ar**H**); -28.65 (s, 2H, -C(CH₃)₂C**H₂**-). ^{13}C NMR [600 MHz, CD₃CN, r.t., δ (ppm)]: 140.1 (P**Ph** *meta*); 132.3 (**C**(CH₃)₂CH₂-); 131.6 (P**Ph** *ortho*); 125.2 (P**Ph** *para*); 48.31 (C(CH₃)₂**C**H₂-). ESI MS (*m/z*): 812.93 (calcd. 813.27 for [C₃₈H₄₈N₂O₂P₂Re]⁺ (M⁺-Cl)).

trans-[Re(PEtPh₂)₂(sal₂ibn)][PF₆] , 15. The synthesis of 15 followed the synthesis of 13 substituting neat ethyldiphenylphosphine for triethylphosphine. Yield: 67% (89 mg). X-ray quality crystals of 15•2.333CH₃OH were obtained by the addition of ammonium hexafluorophosphate into a MeOH/H₂O solution of the product that was filtered and left to sit for several days. ^{1}H NMR [600 MHz, CD₃CN, r.t., δ (ppm)]: 81.68 (s, 1H, -C**H**=N-); 57.17 (s, 1H, -C**H**=N-); 27.78 (d, 1H, Ar**H**); 27.50 (d, 1H, Ar**H**); 16.91 (t, 1H, Ar**H**); 16.71 (t, 1H, Ar**H**); 8.43, 8.36 (d of t, 4H, P**Ph** *para*); 7.93 (br s, 4H, P**Ph**

ortho); 7.84 (br s, 4H, **PPh** *ortho*); 7.18, 7.01 (d of t, 8H, **PPh** *meta*); 5.54 (t, 6H, PCH$_2$C**H$_3$**); 0.72 (br s, 2H, PC**H$_2$**CH$_3$); 0.31 (br s, 2H, PC**H$_2$**CH$_3$); -2.39 (s, 6H, -C(C**H$_3$**)$_2$CH$_2$-); -6.59 (t, 1H, Ar**H**); -8.46 (t, 1H, Ar**H**); -18.85 (d, 1H, Ar**H**); -20.92 (d, 1H, Ar**H**); -26.39 (s, 2H, -C(CH$_3$)$_2$C**H$_2$**-). ^{13}C NMR [600 MHz, CD$_3$CN, r.t., δ (ppm)]: 137.46, 136.00 (**PPh** *meta*); 127.27, 126.52 (**PPh** *para*); 123.90, 122.12 (**PPh** *ortho*); 50.57 (C(**C**H$_3$)$_2$CH$_2$-); 0.35 (P**C**H$_2$CH$_3$). ESI MS (*m/z*): 908.74 (calcd. 909.27 for [C$_{46}$H$_{48}$N$_2$O$_2$P$_2$Re]$^+$ (M$^+$-PF$_6$)).

cis-[ReO(PEt$_3$)(sal$_2$ibn)][PF$_6$] , 16. Compound **9** (37.5 mg, 0.071 mmol) was added to a 10-mL microwave reaction vessel, which was backfilled and purged with argon three times. Degassed absolute ethanol (3 mL) was transferred to the vessel via *cannula*. Triethylphosphine (1.0 M in THF, 75 μL, 0.075 mmol) was added to the vessel via syringe. The reaction solution was heated in a microwave reactor at 105 °C, 17 bar (max), and 150 W (max) for 2 min with stirring to produce a golden brown solution. This solution was dried down *in vacuo*, dissolved in a minimal volume of CH$_2$Cl$_2$, and then loaded onto a silica gel column (2 g silica, 5 mm i.d.) preequilibrated in CH$_2$Cl$_2$. The column was eluted subsequently with CH$_2$Cl$_2$ and then MeCN. The product was finally eluted with 20% MeOH in MeCN. Yield: 80% (43 mg). X-ray quality crystals of **16** were obtained by the addition of ammonium hexafluorophosphate into a MeOH/H$_2$O solution of the product that was filtered and left to sit for several days. ^{1}H NMR [600 MHz, CD$_3$CN, r.t., δ (ppm)]: 9.04 (d, *J* = 9.7 Hz, 1H, -**H**C=N-); 8.60 (s, 1H, -**H**C=N-); 7.52-7.55 (t, Ar**H,** 1H); 7.35 (d, Ar**H**, 1H); 7.24 (t, Ar**H**, 1H); 7.09 (t, Ar**H**, 1H); 6.98 (d, Ar**H**, 1H); 4.86 (d, *J* = 11 Hz, 1H, -NC**H$_2$**-C(CH$_3$)); 4.30 (d, *J* = 11 Hz, 1H, -NC**H$_2$**-C(CH$_3$)); 1.77-1.85 (m, 3H, PC**H$_2$**CH$_3$); 1.41-1.46 (m, 1H, PC**H$_2$**CH$_3$); 1.75 (s, 3H, -**CH$_3$**); 1.06-

1.11 (d of t, $J = 7.5$ Hz, 9H, PCH$_2$C**H$_3$**) 1.02 (s, 3H, -C**H$_3$**). ^{13}C NMR [600 MHz, CD$_3$CN, r.t., δ (ppm)]: 175.37, 171.19 (-H**C**=N-); 139.92, 139.51, 138.89, 135.95, 133.51, 122.38, 122.19, 121.83, 120.63 (**Ar**); 81.97 (-N**C**H$_2$-C(CH$_3$)$_2$)); 72.84 (-NCH$_2$-**C**(CH$_3$)$_2$)); 27.29, 23.65 (C(**C**H$_3$)); 17.26, 17.45 (P**C**H$_2$CH$_3$); 7.31, 7.29 (PCH$_2$**C**H$_3$). ^{31}P NMR: -8.72. FT-IR (KBr pellet v/cm^{-1}): 1606 (C=N st); 960 (Re≡O st). ESI MS (*m/z*): 614.96 (calcd. 615.18 for [C$_{24}$H$_{33}$N$_2$O$_3$PRe]$^+$ (M$^+$)).

cis-[ReO(PEt$_2$Ph)(sal$_2$ibn)][PF$_6$] , 17. Complex **17** was formed indirectly through the degradation of **14** in solution. A MeOH/H$_2$O solution of **14** with one molar equivalent of ammonium hexafluorophosphate was prepared to attempt to crystallize **14**. Over the course of several days, the solution changed color from red to brown and crystals of **17** began to form. ^{1}H NMR [600 MHz, CD$_3$CN, r.t., δ (ppm)]: 8.94 (d, 1H, -**H**C=N-); 8.05 (s, 1H, -**H**C=N-); 7.82 (m, $J = 1.4$, 7.7 Hz, 1H, Ar**H**); 7.72, 7.70 (dd, $J = 1.8$, 7.9 Hz, 1H, Ar**H**); 7.50, 7.49 (d, J =8.4 Hz, 1H, Ar**H**); 7.47-7.45 (m, 1H, P**Ph** *para*); 7.37-7.35 (m, 4H, P**Ph**); 7.43, 7.42 (dd, $J = 1.7$, 8.0 Hz, 1H, Ar**H**); 7.20 (m, $J = 1.7$, 6.3 Hz, 1H, Ar**H**); 7.12 (m, $J = 1.1$, 7.5 Hz, 1H, Ar**H**); 7.05 (m, $J = 1.0$, 7.5 Hz, 1H, Ar**H**); 6.31, 6.29 (d, $J = 8.5$ Hz, 1H, Ar**H**); 4.75, 4.73 (d, $J = 11$ Hz, 1H, -NC**H$_2$**-C(CH$_3$)); 4.33, 4.31 (d, $J = 11$ Hz, 1H, -NC**H$_2$**-C(CH$_3$)-); 2.20-2.08 (m, 4H, PC**H$_2$**CH$_3$); 1.76 (s, 3H, -C**H$_3$**); 1.15-1.02 (d of d of t, $J = 7.5$ Hz, 6H, PCH$_2$C**H$_3$**); 1.01 (s, 3H, -C**H$_3$**). ^{13}C NMR [600 MHz, CD$_3$CN, r.t., δ (ppm)]: 174.45, 171.12 (-H**C**=N-); 140.04, 138.97, 138.80, 122.50, 121.86, 121.75, 120.23 (**Ar**); 135.51, 132.18, 132.12, 129.69, 129.62 (PEt$_2$**Ph**); 81.61 (-N**C**H$_2$-C(CH$_3$)$_2$)); 73.31 (-NCH$_2$-**C**(CH$_3$)$_2$)); (27.10, 23.47 ((**C**H$_3$)$_2$); 19.32, 19.13, (P**C**H$_2$CH$_3$); 7.66, 7.15 (PCH$_2$**C**H$_3$). ^{31}P NMR: -14.80. FT-IR (KBr pellet v/cm^{-1}): 1608 (C=N st); 955 (Re≡O st).

cis-[ReO(PEtPh₂)(sal₂ibn)][PF₆] , **18.** Complex **18** was formed indirectly through the degradation of **15** in solution. The red MeOH/H₂O crystallization solution of **15** was allowed to sit for several days producing a few X-ray quality crystals of **15**. Over time, the solution color changed from red to brown and crystals of **18** began to form. ^{1}H NMR [500 MHz, CD₃CN, r.t., δ (ppm)]: 8.95 (d, *J* = 10 Hz, 1H, -**H**C=N-); 8.20 (s, 1H, -**H**C=N-); 7.87-6.99 (m, Ar**H,** 8H); 7.53-7.36 (m, P**Ph**, 10H); 4.69 (d, *J* = 11 Hz, 1H, -NC**H₂**-C(CH₃)); 4.33 (d, *J* = 11 Hz, 1H, -NC**H₂**-C(CH₃)); 2.68-2.58 (m, 1H, PC**H₂**CH₃); 2.25-2.15 (m, 1H, PC**H₂**CH₃); 1.73 (s, 3H, -**CH₃**); 1.15-1.02 (d of t, *J* = 7.5 Hz, 3H, PCH₂**CH₃**) 0.96 (s, 3H, -**CH₃**). ^{13}C NMR [500 MHz, CD₃CN, r.t., δ (ppm)]: 174.22, 171.38 (-H**C**=N-); 140.30, 139.16, 138.95, 135.83, 133.51, 133.44, 132.20, 130.01, 129.993, 129.80, 129.72, 122.70, 122.13, 121.95, 121.86, 120.32, 1199.93 (**Ar**); 81.74 (-N**C**H₂-C(CH₃)₂)); 74.07 (-NCH₂-**C**(CH₃)₂)); 27.16, 23.63 (C(**C**H₃)); 20.17 (P**C**H₂CH₃); 7.94 (PCH₂**C**H₃). ^{31}P NMR: -13.01. FT-IR (KBr pellet *v*/cm^{-1}): 1602 (C=N st); 962 (Re≡O st). ESI MS (*m/z*): 497.23 (calcd. 497.09 for [C₁₈H₁₈N₂O₃Re]$^+$ (M$^+$-PEtPh₂)).

cis-[ReO(PPh₃)(sal₂ibn)][PF₆] , **19.** Triphenylphosphine (12.20 mg, 0.054 mmol) and compound **9** (25.99 mg, 0.049 mmol) were added to a 10-mL microwave reaction vessel, which was backfilled and purged with argon three times. Degassed absolute ethanol (3 mL) was transferred to the vessel via *cannula*. The reaction solution was heated in a microwave reactor at 105 °C, 17 bar (max), and 150 W (max) for 1 min with stirring. A brown supernatant formed with a green precipitate. The precipitate was isolated and found to be a small amount of compound **9**. The supernatant was dried down *in vacuo* and then redissolved in a minimal volume of methanol. Ammonium hexafluorophosphate (8.02 mg, 0.049 mmol) was added to the methanolic solution.

71

Yield: 75% (33 mg). X-ray quality crystals of **19** were obtained by allowing the solution to sit loosely capped for several days. ^{1}H NMR [600 MHz, CD$_3$CN, r.t., δ (ppm)]: 8.96 (d, J = 10 Hz, 1H, 8.22 (-H**C**=N-); 7.84-7.74, 7.34-6.44 (m, 8H, Ar**H**); 7.52-7.39 (m, P**Ph**, 15H); 4.67 (d, J = 11 Hz, 1H, -NC**H$_2$**-C(CH$_3$)); 4.34 (d, J = 11 Hz, 1H, -NC**H$_2$**-C(CH$_3$)); 1.73 (s, 3H, -C**H$_3$**); 1.00 (s, 3H, -C**H$_3$**). ^{13}C NMR [600 MHz, CD$_3$CN, r.t., δ (ppm)]: 174.32, 171.59 (-H**C**=N-); 81.78 (-N**C**H$_2$-C(CH$_3$)$_2$)); 74.07 (-NCH$_2$-**C**(CH$_3$)$_2$)); 27.21, 23.74 (C(**C**H$_3$)). ^{31}P NMR: -13.98. FT-IR (KBr pellet v/cm^{-1}): 1605 (C=N st); 961 (Re≡O st). ESI MS (m/z): 497.21 (calcd. 497.09 for [C$_{18}$H$_{18}$N$_2$O$_3$Re]$^+$ (M$^+$-PPh$_3$)).

Radiochemical Preparations

Preparation of the radiolabelled [^{99m}Tc][Tc(PEt$_3$)$_2$(Schiff base)]$^+$ complexes, [^{99m}Tc]**10** and [^{99m}Tc]**13**, was based on established procedures for radiolabeling ^{99m}Tc Q-complexes. In the first step, 500 μL of N$_2$O$_2$ Schiff base stock solution (4 mg/mL in EtOH), 100 μL of a SnCl$_2$ stock solution (100 mg/mL in EtOH), 100 μL of aqueous [^{99m}Tc]TcO$_4$$^-$ (37-111 MBq), and 50 μL of 1.0 M NaOH were added to a 2 mL reaction vial. The contents were heated at 75 °C for 15 min. In the second step, 50 μL of 1.0 M HCl and 300 μL of PEt$_3$ (1.0 M in THF) were added to the reaction vial. The contents were heated for an additional 15 min at 75 °C. The reaction mixture was filtered through an Acrodisc 13 mm syringe filter with a 0.2 μm Nylon membrane to remove any precipitates. Reversed-phase HPLC was used to identify and purify the complexes. The Re(III) complexes **10** and **13** were used as nonradioactive HPLC standards to confirm the formation of their analogous ^{99m}Tc complexes. A linear gradient from 50% A to 90% B (A = H$_2$O with 0.1% TFA, and B = MeCN with 0.1% TFA) with a flow rate of 1 mL/min over 20 minutes was used for all HPLC analyses.

Technetium-99m Stability Study

Reversed-phase HPLC was used to purify [^{99m}Tc]**10** and [^{99m}Tc]**13**. A portion of the crude reaction mixture was injected onto the HPLC and then the fraction of the HPLC eluent corresponding to the retention time of ^{99m}Tc Q-complex was collected. The purified fractions of [^{99m}Tc]**10** and [^{99m}Tc]**13** (3-4 MBq in ~1 mL HPLC eluent) were incubated under ambient conditions. At various time points, a portion of the purified fraction (50-150 µL) was reinjected on the HPLC to assess the radiochemical purity.

Electrochemistry

Electrochemical data (**Table 3.3**) were obtained with a Bioanalytical Systems Inc. (BAS) CV-50. Tetraethylammonium perchlorate (TEAP; 0.1 M) in propylene carbonate (Burdick and Jackson, high-purity solvent for GC and spectrophotometry) was used as the electrolytic solution. A non-aqueous Ag/AgCl reference electrode (BAS) (0.1 M TEAP in propylene carbonate) was used, along with a platinum wire auxiliary electrode and a glassy carbon working electrode. A scan rate of 100 mV s^{-1} was used for all experiments. Ferrocene (3 mM in propylene carbonate) was used as a reference standard with a Ag/AgCl aqueous reference electrode. Under these experimental conditions, the Fc$^+$/Fc redox couple was observed as E$_{1/2}$ = 0.384 V vs Ag/AgCl in propylene carbonate. Formal potentials ($E°'$) are reported versus Ag/AgCl in 3M NaCl (aq).

X-ray crystal structures

Single crystal X-ray diffraction (SCXRD) data for all structures were collected using Mo-Kα radiation (λ = 0.71073 Å). Compounds **10**, **13**, **15**, and **17-19** were measured on a Bruker SMART diffractometer equipped with an Apex II CCD area detector and a sealed tube source with TRIUMPH focusing optics (50 kV, 30 mA, λ = 0.71073 Å). Compound

11 was measured on a Bruker APEX II diffractometer with a CCD area detector and a sealed tube X-ray source. Compound **16** was measured on a Bruker D8 Venture diffractometer equipped with a Photon 100 CMOS detector and a microfocus source (50 kV, 1 mA, λ = 0.71073 Å) using shutterless scans. In all cases, hemispheres of unique data were collected using a strategy of scans about the omega and phi axes. Intensities were corrected for Lorentz and polarization effects. Equivalent reflections were merged, and empirical absorption corrections were made using the multiscan method. Space group, lattice parameters, and other relevant information are given in **Table 3.4** for the Re(III) complexes and **Table 3.5** for the Re(V) complexes. Relevant bond lengths and angles are given in **Table 3.6** for the Re(III) complexes and **Table 3.7** for the Re(V) complexes. Data collection, unit cell determination, data reduction, absorption correction, scaling, and space group determination were all performed using the Bruker Apex3 software suite.[94] See Appendix B for structure solution details.

3.3 Results and Discussion

The synthesis of *trans*-[Re(PR$_3$)$_2$(Schiff base)]$^+$ complexes (Q compounds) involves the coordination of two dissimilar ligands—a monodentate tertiary phosphine and a tetradentate N$_2$O$_2$ Schiff base—to a common metal center. Electronic and steric factors on the part of each ligand type affect the formation of Q compounds. Previous reports on the preparation of Re Q-compounds have used sterically unencumbering Schiff base ligands, which form symmetric, *trans*-coordinated Re(V) intermediates (i.e., *trans*-Re^{V}OCl(tmf$_2$en)], *trans*-[Re^{V}O(OH$_2$)(acac$_2$en)]$^+$ and *trans*-[Re^{V}OCl(sal$_2$phen)]).[70, 72, 73] The reactions of symmetric Re(V) complexes with phosphine ligands were observed to produce either a reduced, disubstituted *trans*-[Re^{III}(PR$_3$)$_2$(Schiff base)]$^+$ product, or a rearranged, monosubstituted *cis*-[Re^{V}O(PR$_3$)(Schiff base)]$^+$ product. The nature of the product was dependent on both the rigidity of the Schiff base and the relative nucleophilicity of the phosphine ligand.[72, 73] The use of sal$_2$enH$_2$ and sal$_2$ibnH$_2$ in this chapter allowed the formation of *trans*-[Re^{III}(PR$_3$)$_2$(Schiff base)]$^+$ species from both a symmetric Re(V) intermediate and an asymmetric Re(V) intermediate to be investigated.

Synthesis of the Re(III)-sal$_2$en complexes 10-12

Complexes **10-12** were synthesized via a one-pot, two-step approach adapted from the literature.[70] Microwave irradiation of (*n*Bu$_4$N)[ReOCl$_4$] with sal$_2$enH$_2$ in ethanol under dry, inert conditions yields the intermediate *trans*-[ReOCl(sal$_2$en)]. The presence of *trans*-[ReOCl(sal$_2$en)] was observed by ^{1}H NMR and LC-MS of the crude reaction mixture, however, no attempt was made to isolate this intermediate, which has been previously reported by several groups.[133, 134] Subsequent addition of excess tertiary phosphine (PEt$_3$, PEtPh$_2$ or PPh$_3$) to the reaction mixture yields a reduced and

disubstituted *trans*-[Re(PR$_3$)$_2$(sal$_2$en)]$^+$ product (**Scheme 3.1**). The Re(III) products are readily isolated by silica gel column chromatography in moderate yields (32-85%). The Re(III) complexes are thought to form by a multistep mechanism.[38, 41, 73] In the first step, a phosphine ligand coordinates *trans* to the oxo group. A second phosphine ligand then reduces the metal center through oxygen atom abstraction resulting in an open coordination site on the metal and the production of the phosphine oxide. In the last step, a third phosphine ligand coordinates to the open site *trans* to the first phosphine ligand. A number of unidentified byproducts were removed during the chromatographic separation of the products. These are likely Re(IV) or Re(V) chloro-phosphine complexes formed through the reaction of tertiary phosphine with unreacted (*n*Bu$_4$N)[ReOCl$_4$]. No evidence was observed of the formation of rearranged Re(V)-sal$_2$en species.

The formation of *trans*-[Re(PEt$_3$)$_2$(sal$_2$en)]$^+$, **10**, is rather surprising. Benny *et al*. found that the reaction of triethylphosphine with *trans*-[ReO(OH$_2$)(acac$_2$en)]$^+$ exclusively produced *cis*-[ReO(PEt$_3$)(acac$_2$en)]$^+$.[73] It was hypothesized that the reaction was subject to kinetic control with rearrangement being favored over oxygen atom abstraction for the nucleophilic triethylphosphine ligand.[73] Complex **10** likely represents the thermodynamic product in the reaction of triethylphosphine with *trans*-[ReOCl(sal$_2$en)] accessible by the use of microwave irradiation and an increased reaction temperature compared to the work of Benny *et al*.[73]

Synthesis of the Re(III)-sal$_2$ibn complexes 13-15, and the Re(V)-sal$_2$ibn complexes 16-19

cis-[ReOCl(sal$_2$ibn)], **9**, was synthesized in 68% yield by the microwave irradiation of (*n*Bu$_4$N)[ReOCl$_4$] and sal$_2$ibnH$_2$ in ethanol under dry, inert conditions. This

synthesis is faster and higher yielding than the previously reported method.[71] Complex **9** was used as a starting material to study the formation of *trans*-[Re^{III}(PR$_3$)$_2$(sal$_2$ibn)]$^+$ species upon reaction with tertiary phosphines. Two products are possible upon reaction of **9** with phosphine ligands. Ligand substitution of PR$_3$ for Cl$^-$ can lead to a *cis*-[Re^{V}O(PR$_3$)(sal$_2$ibn)]$^+$ product. The *trans*-[Re^{III}(PR$_3$)$_2$(sal$_2$ibn)]$^+$ species can be formed through a complex process involving ligand substitution, oxygen atom abstraction, and intramolecular rearrangement. Detailed mechanistic studies of these processes are beyond the scope of this work.

10-12
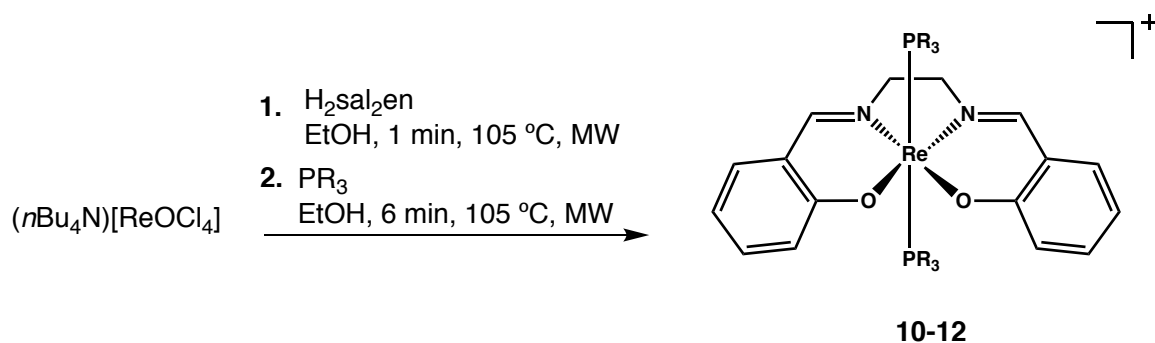
Scheme 3.1. Synthesis of *trans*-[Re(PR$_3$)$_2$(sal$_2$en)]$^+$ (PR$_3$ = PEt$_3$, **10**; PEtPh$_2$, **11**; PPh$_3$, **12**)

The reaction of **9** with tertiary phosphine ligands generated mixed results (**Scheme 3.2**). Reaction of **9** with the nucleophilic triethylphosphine yielded a mixture of *trans*-[Re(PEt$_3$)$_2$(sal$_2$ibn)]$^+$, **13**, and *cis*-[ReO(PEt$_3$)(sal$_2$ibn)]$^+$, **16**. This mixture of products was observed even after increasing the amount of triethylphosphine and increasing reaction time to force formation of **13**. Diethylphenylphosphine reacts with **9** to produce the Re(III) product *trans*-[Re(PEt$_2$Ph)$_2$(sal$_2$ibn)]$^+$, **14**. A small amount of the Re(V) product *cis*-[Re(PEt$_2$Ph)(sal$_2$ibn)]$^+$, **17**, was observed in the initial reaction mixture. Ethyldiphenylphosphine reacts with **9** to give *trans*-[Re(PEtPh$_2$)$_2$(sal$_2$ibn)]$^+$, **15**, as the sole product. The results with PEt$_2$Ph and PEtPh$_2$ were consistent with the

observation by Benny *et al*. that the electrophilic phosphines (PPh$_3$ and PEtPh$_2$) yielded reduced, disubstituted Re(III) upon reaction with Re(V) precursors. Pure solutions of complexes **10-12** were all observed to convert in solution to their respective *cis*-[ReO(PR$_3$)(sal$_2$ibn)]$^+$ species **16-18** over time (**Scheme 3.3**). Conversion is nearly quantitative as observed by ^{1}H NMR. This conversion involves ligand dissociation, oxidation of the Re(III) metal center, and rearrangement of the N$_2$O$_2$ Schiff base ligand. It is hypothesized that the geminal dimethyl substituents of the sal$_2$ibn backbone experience steric crowding with the bulky ethyldiphenylphosphine ligand. Dissociation of the tertiary phosphine and rearrangement to form the Re(V) complex reduces steric crowding by orienting the phosphine ligand away from the dimethyl substituents as seen in the X-ray crystal structures of **16-18** (*vide infra*).
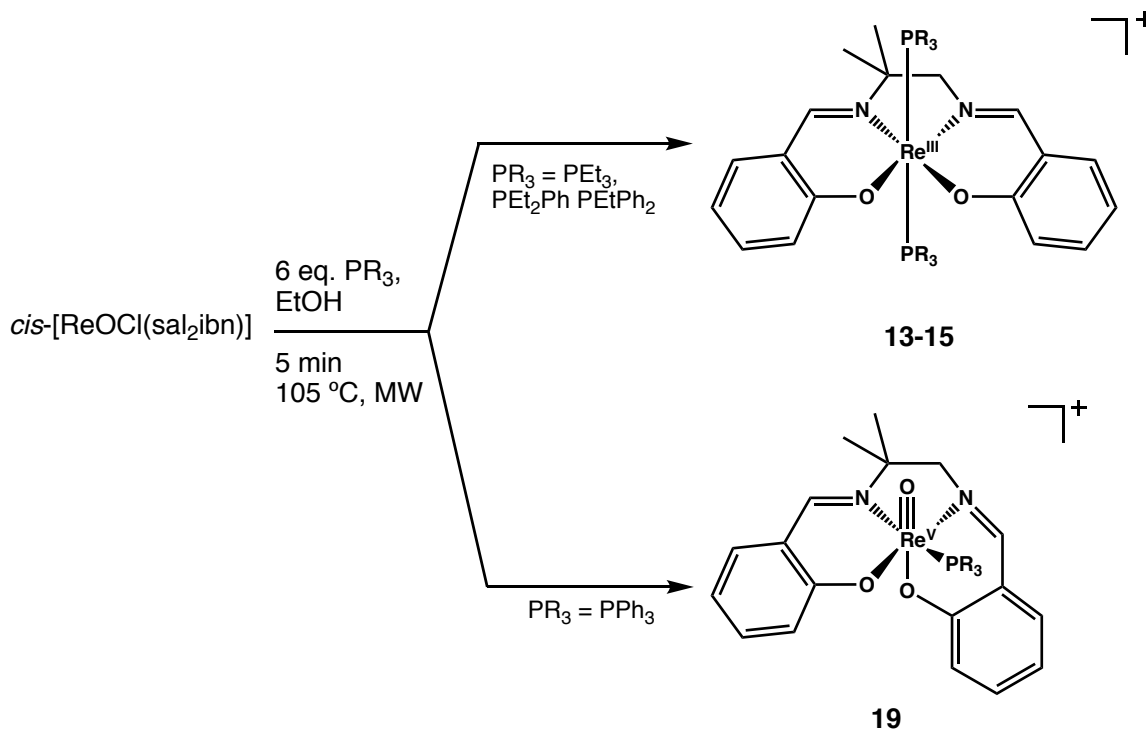
Scheme 3.2. Synthesis of *trans*-[Re(PR$_3$)$_2$(sal$_2$ibn)]$^+$ (PR$_3$ = PEt$_3$, **13**; PEt$_2$Ph, **14**; PEtPh$_2$, **15**) and *cis*-[ReO(PPh$_3$)(sal$_2$ibn)]$^+$, **19**.

Reaction of the electrophilic triphenylphosphine with **9** solely produced *cis*-[ReO(PPh$_3$)(sal$_2$ibn)]$^+$, **19**, with no indication of the Re(III) product (**Scheme 3.2**). Increasing reaction time and molar equivalents of triphenylphosphine had no effect on product identity. One explanation for this result is that triphenylphosphine lacks the reducing power to induce oxygen atom abstraction. The previously reported compounds *trans*-[Re(PPh$_3$)$_2$(acac$_2$en)]PF$_6$] and *trans*-[Re(PPh$_3$)$_2$(sal$_2$phen)][Cl],[72, 73] and *trans*-[Re(PPh$_3$)$_2$(sal$_2$en)][PF$_6$] reported herein, however, demonstrate that triphenylphosphine is sufficiently reducing to produce Re(III) complexes from Re(V) Schiff base precursors. The formation of **19** appears to be sterically driven by the interaction of the geminal methyl groups of sal$_2$ibn with the bulky triphenylphosphine ligand.
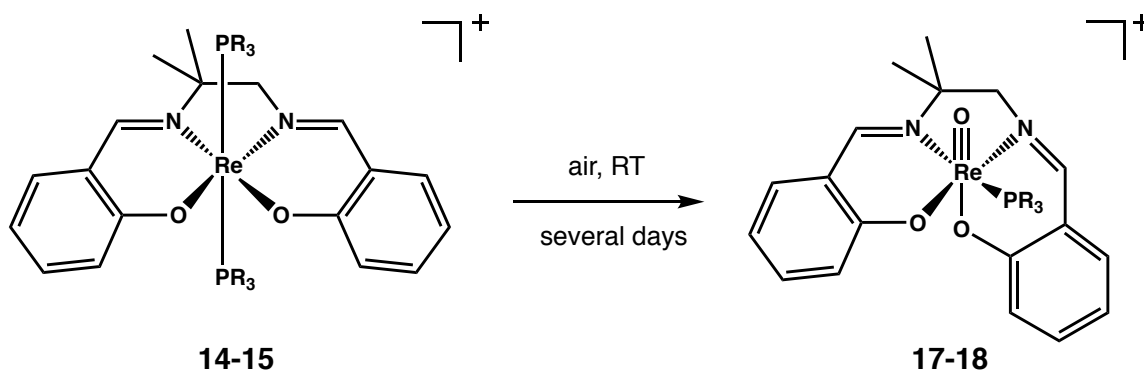
Scheme 3.3. Conversion of *trans*-[Re(PR$_3$)$_2$(sal$_2$ibn)]$^+$ species (**14-15**) to *cis*-[ReO(PR$_3$)(sal$_2$ibn)]$^+$ (**17-18**) (PR$_3$ = PEt$_2$Ph, PEtPh$_2$).

Conversion of *trans*-[Re(PR$_3$)$_2$(sal$_2$ibn)]$^+$ species to *cis*-[ReO(PR$_3$)(sa$_2$libn)]$^+$ species

The solution stability of the *trans*-[Re(PR$_3$)$_2$(sal$_2$ibn)]$^+$ complexes **13-15** was monitored by HPLC-UV/Vis. A pure sample of each complex was dissolved in a 50/50 mixture of MeCN and MilliQ water and then allowed to stand under ambient conditions for several days. The conversion of the Re(III) species to the Re(V) species was assessed by measuring the disappearance of the 280 nm UV peak for the Re(III) product over time.

Complex **13**, *trans*-[Re(PEt$_3$)$_2$(sal$_2$ibn)]$^+$, was stable in solution over seven days (**Figure 3.3**), and no conversion to *cis*-[ReO(PEt$_3$)(sal$_2$ibn)]$^+$, **16,** was observed. Complex **14**, *trans*-[Re(PEt$_2$Ph)$_2$(sal$_2$ibn)]$^+$, was observed to degrade to **9** over time. After seven days, 66% of the Re(III) species remained. The sterically hindered *trans*-[Re(PEtPh$_2$)$_2$(sal$_2$ibn)]$^+$, **15**, underwent a more rapid and complete degradation to **18** after four days of incubation. These results are in agreement with the trend of increasing steric bulk of the PEt$_3$, PEt$_2$Ph and PEtPh$_2$ ligands. Additionally, only the Re(V) analogue with PPh$_3$ was observed and not the Re(III) complex, further supporting steric hindrance of the bulkier phosphines.
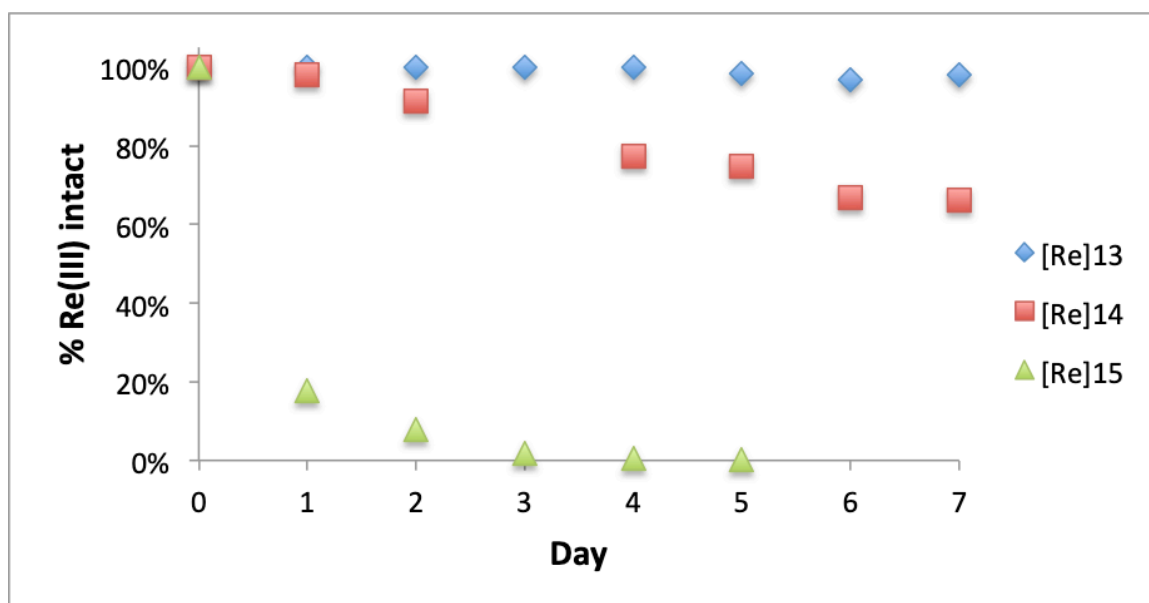
Figure 3.3. Stability of Re(III)-sal$_2$ibn species **13-15** in 50/50 MeCN/H$_2$O over seven days.

General Characterization

The FT-IR spectra of all complexes showed the expected Schiff base C=N stretches between 1597—1605 cm^{-1}. The monomeric oxo-rhenium(V) complexes showed the presence of the Re≡O stretches between 935—962 cm^{-1}.[41, 71, 74, 75, 107, 135] Electrospray

ionization mass spectrometry (ESI-MS) of the Re complexes **10-19** confirmed their product identities. Molecular ions with the expected rhenium isotope pattern were observed for compounds **10-19** in the positive ESI-MS mode. Fragments of **10-15** with *m/z* corresponding to $[Re(PR_3)(L)]^+$ were observed indicating loss of one tertiary phosphine ligand. Fragments of **16-19** with *m/z* corresponding to $[ReO(L)]^+$ were observed indicating loss of the tertiary phosphine ligand. All species were evaluated by ^{1}H and ^{13}C NMR (*vide infra*).

NMR Characterization

The asymmetric Re(V) complexes **9** and **16-19** can be clearly distinguished by their ^{1}H-NMR chemical shifts (**Table 3.1**). The coordination of the ancillary ligand *cis* with respect to the oxo center leads to NMR spectra in which all protons and carbons are unique. The ^{1}H spectra for **9** and **16-19** displayed two singlets for the backbone geminal methyl protons, two distinct doublets for the backbone methylene protons, and aromatic protons in the characteristic region (6.29-7.87 ppm). While the imine protons in **9** were observed as two unique singlets, the imine protons in the phosphine coordinated species **16-19** were observed as a singlet and a doublet corresponding to a single proton each. Two-dimensional NMR techniques were used to identify the alkyl and aryl protons of the various phosphine ligands (PEt_3, PEt_2Ph, $PEtPh_2$, PPh_3) and to distinguish the aryl protons of the sal$_2$ibn ligand from those of the phosphine ligands (PEt_2Ph, $PEtPh_2$, PPh_3). The ^{31}P NMR chemical shifts for the Re(V) complexes **16-19** were observed as singlets falling between -9 and -14 ppm, consistent with previously reported Re(V) complexes with *cis*-coordinated phosphines.[73, 136] This range is narrower than that of the free phosphine ligands, which vary from -5 ppm for triphenylphosphine to -20 ppm for

triethylphosphine. The chemical shifts of metal-coordinated phosphine ligands are determined by a combination of factors including the metal oxidation state, coordination geometry, steric bulk of the phosphine ligand, and the electron-withdrawing ability of the free ligand. As a general rule, highly shielded ligands become less shielded upon metal coordination, whereas deshielded ligands tend to increase their shielding.[137]

Table 3.1 ^{1}H Spectral Assignments for the Re(V) complexes **9** and **16-19**

Complex	9	16	17	18	19
gem-methyl	1.71 (s, 3H)	1.75 (s, 3H)	1.76 (s, 3H)	1.73 (s, 3H)	1.73 (s, 3H)
	1.06 (s, 3H)	1.02 (s, 3H)	1.01 (s, 3H)	0.96 (s, 3H)	1.00 (s, 3H)
Methylene	4.62 (d, 1H)	4.86 (d, 1H)	4.74 (d, 1H)	4.69 (d, 1H)	4.67 (d, 1H)
	4.25 (d, 1H)	4.30 (d, 1H)	4.32 (d, 1H)	4.33 (d, 1H)	4.34 (d, 1H)
Imine	8.85 (s, 1H)	9.04 (d, 1H)	8.94 (d, 1H)	8.95 (d, 1H)	8.96 (d, 1H)
	8.09 (s, 1H)	8.60 (s, 1H)	8.05 (s, 1H)	8.20 (s, 1H)	8.22 (s, 1H)
Aromatic	7.85-7.75 (m, 8H)	7.55-6.98 (m, 8H)	7.82-6.29 (m, 8H)	7.87-6.99 (m, 8H)	7.84-6.44 (m, 8H)

The ^{1}H NMR spectra for **10-15** were much more complex owing to the paramagnetic d^4 Re(III) center (**Table 3.2**). Sharp chemical shifts were observed within an expanded window of approximately -30 to +90 ppm, consistent with known paramagnetic Re(III) complexes.[96-99, 102, 103, 138-141] Dramatic differences were observed in the ^{1}H NMR chemical shifts of the sal$_2$en and sal$_2$ibn ligand substituents between the Re(V) and Re(III) complexes. The imine protons in the diamagnetic Re(V) species ranged from 8.05 to 9.04 ppm, while the imine protons in the paramagnetic Re(III) species ranged from 56 to 84 ppm. Aromatic protons were observed in the narrow range of 6.29 to 7.87 ppm for the Re(V) species, while a broad range of -21 to +29 ppm was observed for the Re(III) species. No ^{31}P coupling was observed as coordination of phosphorus to the paramagnetic Re(III) center leads to rapid relaxation and subsequent loss of coupling.[70, 73, 96-103, 139] Phosphine ligands coordinated to a paramagnetic Re(III) center were not observed by ^{31}P NMR, consistent with known paramagnetic Re(III) compounds.[97, 98, 139, 140]

Table 3.2 ^{1}H Spectral Assignments for the Re(III) complexes **10-15**

Complex	10	11	12	13	14	15
gem-methyl	—	—	—	-1.30 (s, 6H)	-2.53 (s, 6H)	-2.39 (s, 6H)
Methylene	-26.47 (s, 4H)	-20.28 (s, 4H)	-19.51 (s, 4H)	-31.06 (s, 2H)	-28.65 (s, 2H)	-26.39 (s, 2H)
Imine	60.06 (s, 2H)	61.16 (s, 2H)	59.37 (s, 2H)	56.59 (s, 1H)	55.92 (s, 1H)	57.17 (s, 1H)
				84.49 (s, 1H)	83.34 (s, 1H)	81.68 (s, 1H)
Aromatic	27.71 (d, 2H)	27.01 (d, 2H)	26.54 (d, 2H)	-19.75 (d, 1H)	-20.29 (d, 1H)	-20.92 (d, 1H)
	17.09 (t, 2H)	16.45 (t, 2H)	15.75 (t, 2H)	-18.96 (d, 1H)	-18.51 (d, 1H)	-18.85 (d, 1H)
	-7.14 (t 2H)	-7.84 (t, 2H)	-9.30 (t, 2H)	-6.94 (t, 1H)	-7.57 (t, 1H)	-8.46 (t, 1H)
	-19.14 (d, 2H)	-19.70 (d, 2H)	-20.94 (d, 2H)	-6.66 (t, 1H)	-6.41 (t, 1H)	-6.59 (t, 1H)
				17.25 (t, 1H)	17.15 (t, 1H)	16.71 (t, 1H)
				18.02 (t, 1H)	17.48 (t, 1H)	16.91 (t, 1H)
				27.75 (d, 1H)	27.64 (d, 1H)	27.50 (d, 1H)
				28.75 (d, 1H)	27.94 (d, 1H)	27.78 (d, 1H)

Electrochemistry

Complexes **10-15** were analyzed by cyclic voltammetry for comparison with analogous Re(III) and Tc(III) complexes, which are known to exhibit both chemically reversible M(III)/M(IV) and M(III)/M(II) redox couples.[41, 70, 73] The formal potential for the Re(III)/Re(II) process is of particular interest as a preliminary gauge of *in vivo* stability. Reduction of cationic *trans*-[Re^{III}(PR$_3$)$_2$(L)]$^+$ yields the neutral species *trans*-[Re^{II}(PR$_3$)$_2$(L)]. As the *in vivo* behavior of Tc Q-complexes is dependent on their cationic charge, stability against *in vivo* reduction by cellular reducing agents such as glutathione and NADPH is required for potential Re Q-complexes.

Table 3.3 $E°'$ values for the Re(III) complexes **10-15**^{a,b}

complex	IV/III		III/II	
	$E°'$ (V)	ΔE_p (V)	$E°'$ (V)	ΔE_p (V)
[Re(PEt$_3$)$_2$(sal$_2$en)]$^+$, **10**	0.359	0.074	-1.017	0.087
[Re(PEtPh$_2$)$_2$(sal$_2$en)]$^+$, **11**	0.396	0.080	-0.906	0.080
[Re(PPh$_3$)$_2$(sal$_2$en)]$^+$, **12**	0.443	0.084	-0.861	0.088
[Re(PEt$_3$)$_2$(sal$_2$ibn)]$^+$, **13**	0.369	0.134	-1.043	0.137
[Re(PEt$_2$Ph)$_2$(sal$_2$ibn)]$^+$, **14**	0.392	0.075	-0.962	0.076
[Re(PEtPh$_2$)$_2$(sal$_2$ibn)]$^+$, **15**	0.412	0.090	-0.929	0.094

^{a}Conditions: cyclic voltammetry in propylene carbonate, 0.1 M TEAP; glassy-carbon working electrode; Ag/AgCl reference electrode; Pt wire auxiliary electrode. ^{b}$E°'$ is vs. Ag/AgCl/NaCl (3M).

Each of the Re(III) complexes undergoes a chemically reversible Re(IV)/Re(III) and a chemically reversible Re(III)/Re(II) process. The $E°'$ values listed in **Table 3.3** are calculated as the average of the cathodic (E_{pc}) and anodic (E_{pa}) peak potentials. Under the conditions measured, the redox processes do not meet the technical requirements for electrochemical reversibility. In an electrochemically reversible process, the separation between the anodic and cathodic peaks (ΔE_p) will equal the theoretical value of 0.059 V given by the Nernst equation. The complexes reported herein, however, exhibit ΔE_p values of 0.075 to 0.134 V. **Figure 3.4** shows the repetitive cyclic voltammogram of **11**. The strongly negative potentials of the Re(III)/Re(II) redox couples exhibited by **10-15** suggest *in vivo* reduction will not be accessible, as these values are more negative than those of Tc^{III} species, which have been evaluated for human use.[38-41, 85, 87]
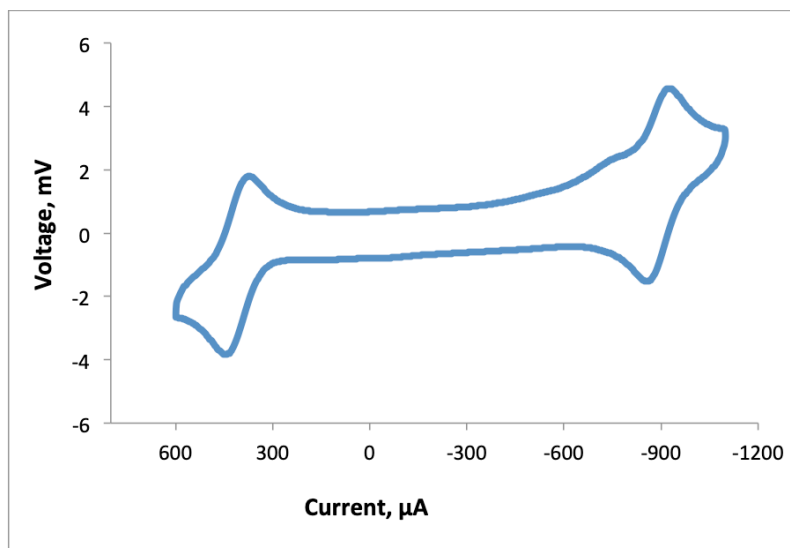
Figure 3.4 Cyclic voltammogram of *trans*-[Re(PEtPh$_2$)$_2$(sal$_2$en)][PF$_6$], **11**.

Formal potential values for the Re(III)/Re(II) and the Re(IV)/Re(III) couples are sensitive to the substituents on both the phosphine ligand and the Schiff base ligand. As the phosphine ligands become stronger reducing agents, the Re(III) center becomes easier

to oxidize to Re(IV), but harder to reduce to Re(II). Phosphine ligands with alkyl substituents are better σ-donors than π-acceptors, and, thus, stabilize rhenium in higher oxidation states. As a corollary, phosphine ligands with aryl substituents are strong π-acceptors and stabilize rhenium in low oxidation states. This trend is seen most apparently in the 0.084 V lower Re(IV)/Re(III) formal potential of *trans*-$[Re(PEt_3)_2(sal_2en)]^+$ in comparison to *trans*-$[Re(PPh_3)_2(sal_2en)]^+$. Elucidating the effect of the different Schiff base ligand substituents was difficult given the similarity of sal_2en and sal_2ibn. For compounds with identical phosphine ligands, the sal_2ibn complex was slightly more difficult to reduce and slightly more difficult to oxidize. This behavior can be understood as sal_2ibn stabilizing the Re(III) metal center over a slightly broader potential range. The geminal dimethyl substituents of sal_2ibn are electron-donating groups and would thus be expected to stabilize the Re(III) metal center against reduction. Regardless, the electrochemical differences between the sal_2en and sal_2ibn species are small and support the hypothesis that the instability of the Re(III)-sal_2ibn complexes is not electrochemically driven.

The cyclic voltammogram for *trans*-$[Tc(PEtPh_2)_2(sal_2en)]^+$, the Tc analogue to **11**, has been previously reported allowing for direct comparison between the two species.[41, 85] Complex **11** exhibits a chemically reversible Re(IV)/(III) redox couple with a potential of 0.443 V, while the Tc(IV)/Tc(III) process for *trans*-$[Tc(PEtPh_2)_2(sal_2en)]^+$ is observed at 0.787 V. For the M(III)/M(II) redox process, the Tc(III) and Re(III) complexes exhibit potentials of -0.693 and -0.861 V, respectively.[41] These results show the Re(III) complex is easier to oxidize and harder to reduce than its analogous Tc(III) complex in agreement with periodic trends and prior studies of Tc and Re analogues.[142]

X-ray crystal structures

The rhenium complexes **10**, **11•**CH$_3$OH, **13**, **15•**2.333CH$_3$OH, and **16-19** were characterized by SCXRD (**Figures 3.5-12**). All seven complexes exhibit distorted octahedral geometry about the rhenium center. In the Re(III) complexes (**10**, **11•**CH$_3$OH, **13**, and **15**), the Schiff base ligand occupies the equatorial plane and the two tertiary phosphine ligands are coordinated *trans* to each other. The Re(V) complexes (**16-19**) have a single tertiary phosphine ligand coordinated *cis* to the oxo, while a phenolic oxygen from sal$_2$ibn occupies the *trans* position. Two distinct molecules were observed in the unit cell of **13** with similar bond angles and distances between the two. Space group, lattice parameters, and data collection information are given in **Table 3.4** for the Re(III) complexes and **Table 3.5** for the Re(V) complexes. Relevant bond lengths and angles are given in **Table 3.6** for the Re(III) complexes and **Table 3.7** for the Re(V) complexes.

10, and 11•CH$_3$OH. The X-ray crystal structures of **10** (**Figure 3.5**) and **11•**CH$_3$OH (**Figure 3.6**) each show a Re(III)-sal$_2$en complex with two tertiary phosphine ligands coordinated *trans* to each other. The Re metal center is situated in the equatorial plane defined by the nitrogen and phenolic oxygen donors of the Schiff base ligand. The Re-O (2.005-2.0206 Å), and Re-N (2.025-2.043 Å) bond distances fall within the expected range for similar complexes.[71-73, 75, 113] Each triethylphosphine ligand in complex **10** lies equidistant from the Re center with Re-P bond lengths of 2.4700-2.4713 Å. Complex **11•**CH$_3$OH displays longer Re-P bond lengths (2.4854-2.4862 Å) than **10** owing to the enhanced σ-donating ability of triethylphosphine compared to ethyldiphenylphosphine. Bite angles for Schiff base ligands coordinated equatorially to a

Re metal center (i.e., N1-Re-N2, N1-Re-O1, N2-Re-O2) vary from 81.53 to 89.49°. The ethylene backbone constrains the structure resulting in a reduction in the N1-Re-N2 angles (81.53-82.17°) and an expansion of the N1-Re-O1 (88.65-89.49°) and N2-Re-O2 (89.07-89.16°) bond angles. Complex **10** displays a slightly contracted P-Re-P bond angle of 172.23°, while complex **11**•CH$_3$OH has a nearly linear P-Re-P bond angle of 176.21°. The longer Re-P bonds and expanded P-Re-P bond angle in **11**•CH$_3$OH compared to **10** are consistent with **11**•CH$_3$OH having a more sterically demanding phosphine ligand.

13, and 15•2.333CH$_3$OH. The X-ray crystal structures for **13** (**Figure 3.7**) and **15**•2.333CH$_3$OH (**Figure 3.8**) highlight the steric influence of the asymmetric sal$_2$ibn ligand. Each structure shows a Re(III)-sal$_2$ibn complex with the two tertiary phosphine ligands coordinated *trans* to each other, and the sal$_2$ibn ligand occupying the equatorial plane. The sal$_2$ibn backbone contains two geminal methyl substituents, with one adopting a pseudo-axial orientation with respect to the central P-Re-P axis, while the other adopts a pseudo-equatorial orientation. All Re-O (2.0058-2.0213 Å), Re-N (2.0299-2.106 Å), and Re-P (2.4632-2.5071 Å) bond distances for complexes **13** and **15**•2.333CH$_3$OH fall within expected ranges for similar complexes.[70, 71, 73, 76] The P-Re-P bond angles in **13** and **15**•2.333CH$_3$OH deviate from linearity with values ranging from 165.88 to 168.43°. Complexes **13** and **10** each contain two triethylphosphine ligands, but they are coordinated by different Schiff base ligands The contracted P-Re-P bond found in **13** (165.88 and 168.43° for molecules **13a** and **13b**) compared to **10** (172.23°) reveals the steric influence of the sal$_2$ibn geminal dimethyl substituents in the former. The pseudo-axial methyl group constrains the P-Re-P bond angle through its interaction with one of

the triethylphosphine ligands. A similar contraction is observed when comparing the P-Re-P bond angles in the ethyldiphenylphosphine containing compounds **11**•CH$_3$OH and **15**•2.333CH$_3$OH. Complex **15**•2.333CH$_3$OH has a substantially more acute P-Re-P bond angle at 166.703° than **11**•CH$_3$OH at 176.21°. The steric influence of the sal$_2$ibn ligand is further seen by comparing the P-Re bond lengths in the sal$_2$en complexes with those in the sal$_2$ibn complexes. Whereas the P-Re bond lengths in **10** and **11**•CH$_3$OH are statistically identical (Δ = 0.0013 and 0.0008 Å, respectively), the P-Re bond lengths for **13** and **15**•2.333CH$_3$OH display much larger differences (0.0206-0.0439 Å). In each case, the P-Re bond adjacent (P2-Re) to the pseudo-axial methyl substituent is elongated compared to the P-Re bond (P1-Re) transverse to the pseudo-axial methyl substituent.

16-19. Complexes **16-19** (**Figures 3.9-3.12**) exhibit distorted octahedral coordination geometry with the phosphine ligands coordinated *cis* with respect to the oxo group. The rhenium center lies above the equatorial plane (0.2 Å) towards the oxo group. The equatorial plane is defined by the two imine nitrogen donors, one of the phenolic oxygen donors, and the lone phosphorus donor. The second phenolic oxygen donor is bound *trans* to the oxo group. Bond angles about the rhenium center fall within the expected ranges for the *cis* (77-105°) and *trans* (160-178°) ligands, respectively. Bond lengths for the Re-N (2.083-2.111 Å) and Re-O (1.9495-1.9990 Å) fall within expected ranges. The Re≡O bond lengths (1.6929-1.6994 Å) are comparable to known Re(V) oxo compounds. The Re≡O bond length for **19** (1.6994 Å) is slightly longer than that for **16** (1.696 Å) owing to the increased electron-withdrawing ability of PPh$_3$ compared to PEt$_3$. The Re-P bond distances (2.4743-2.4856 Å) lie within the expected range for *cis* coordinated oxorhenium(V) phosphine compounds.
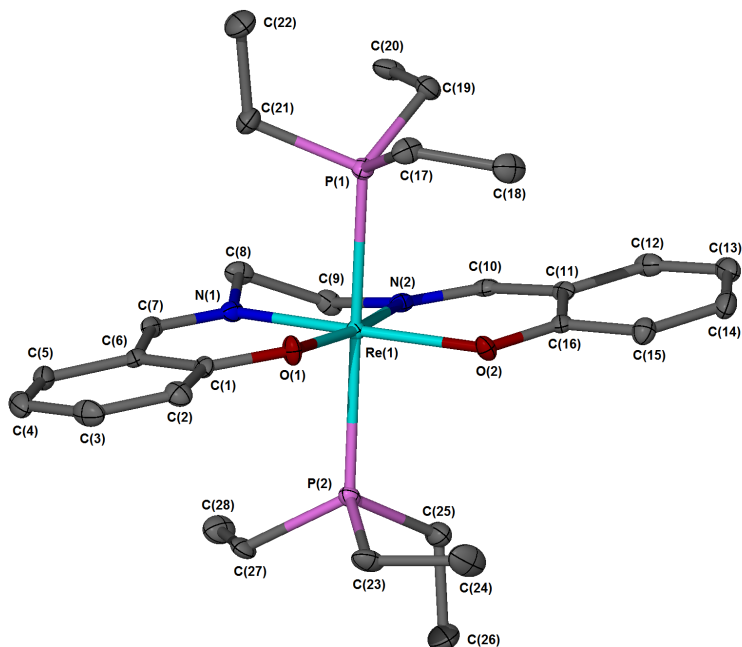
Figure 3.5 X-ray crystal structure of *trans*-[Re(PEt$_3$)$_2$(sal$_2$en)]PF$_6$, **10**, with 50% probability thermal ellipsoids (CCDC # 1910610).
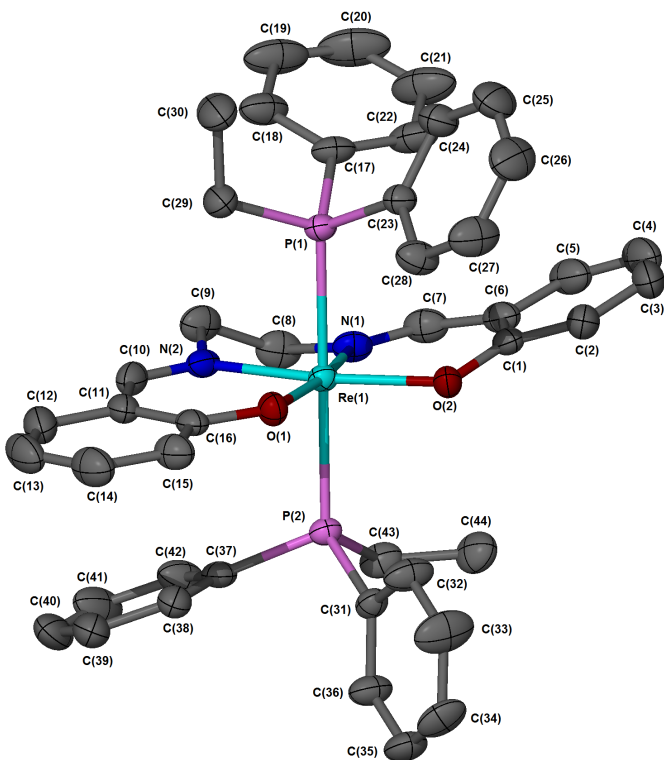
Figure 3.6 X-ray crystal structure of *trans*-[Re(PEtPh$_2$)$_2$(sal$_2$en)]Cl•CH$_3$OH, **11**•CH$_3$OH, with 50% probability thermal ellipsoids (CCDC # 1910611).
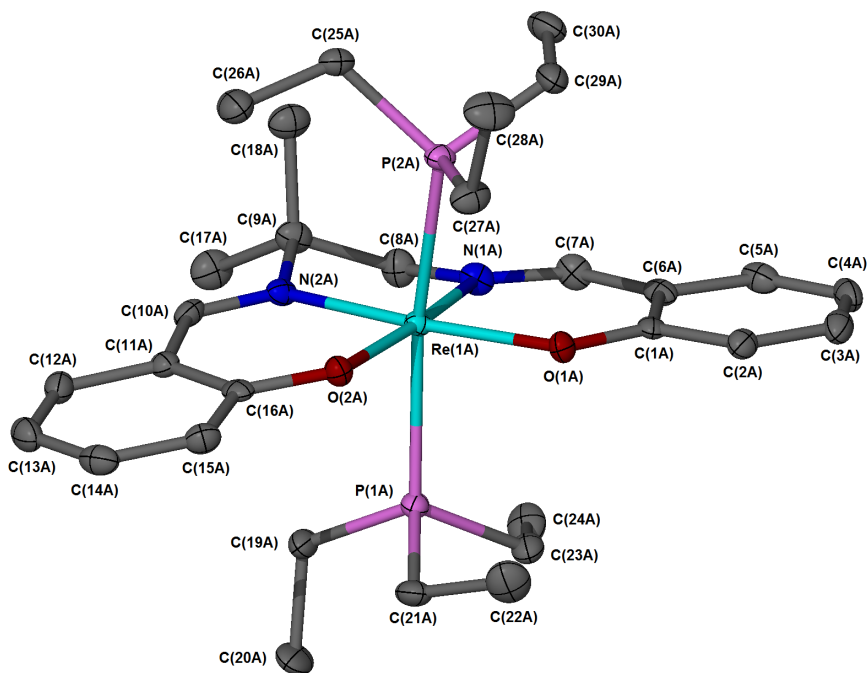
Figure 3.7 X-ray crystal structure of *trans*-[Re(PEt$_3$)$_2$(sal$_2$ibn)]PF$_6$, **13**, with 50% probability thermal ellipsoids (CCDC # 1910612).
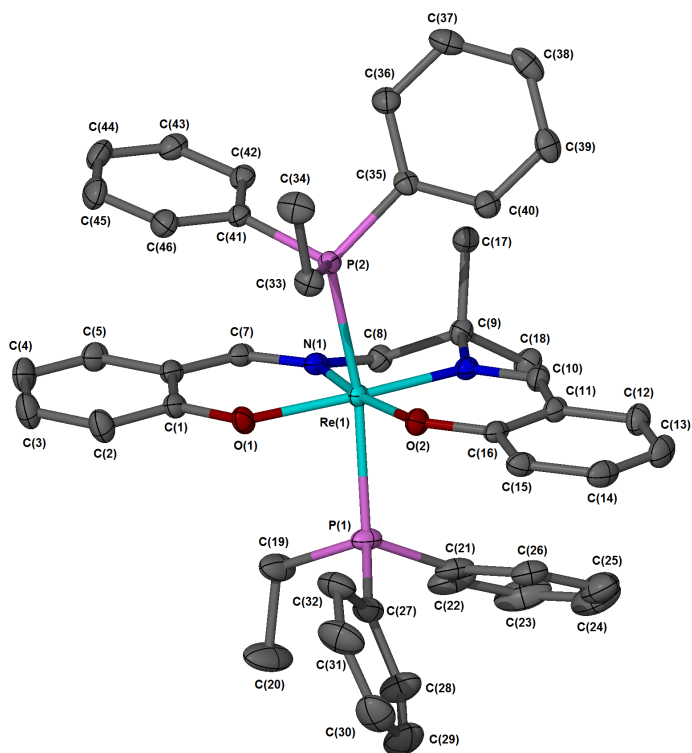
Figure 3.8 X-ray crystal structure of *trans*-[Re(PEtPh$_2$)$_2$(sal$_2$ibn)]PF$_6$•2.333CH$_3$OH, **15**•2.333CH$_3$OH, with 50% probability thermal ellipsoids (CCDC # 1910613).
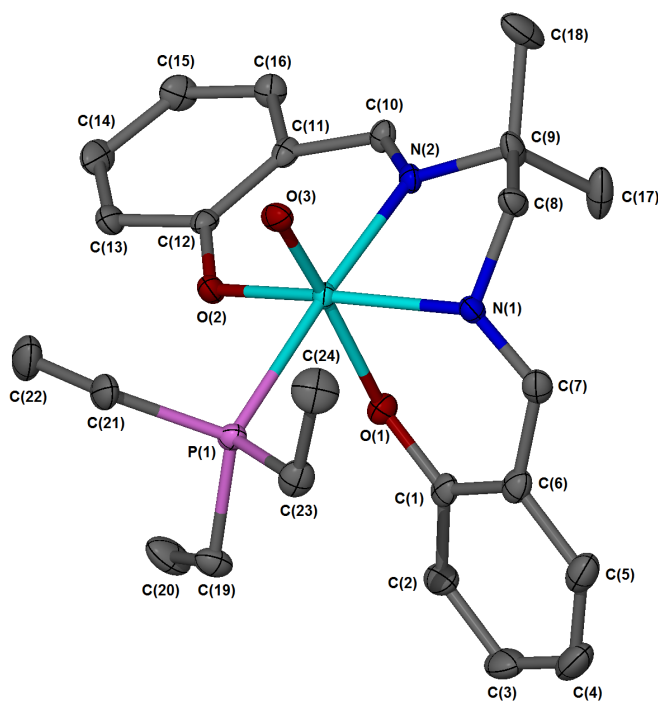
Figure 3.9 X-ray crystal structure of *cis*-[Re(PEt$_3$)(sal$_2$ibn)]PF$_6$, **16**, with 50% probability thermal ellipsoids (CCDC # 1910614).
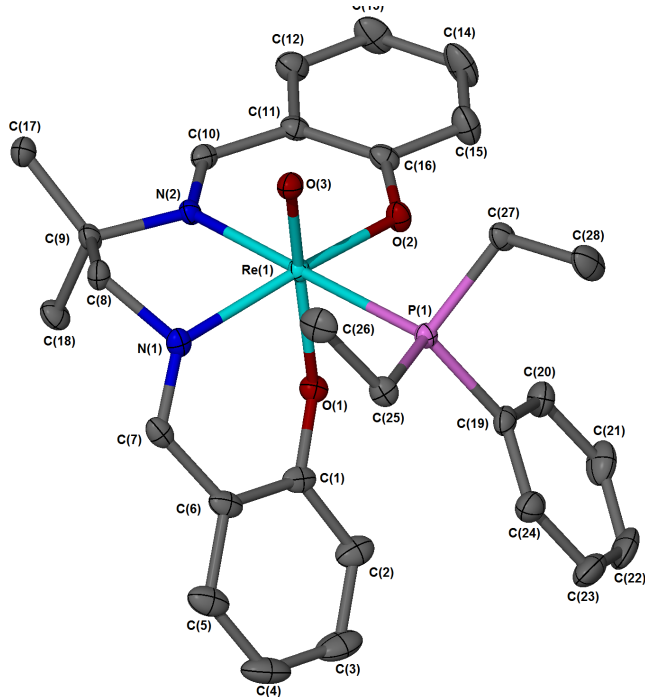
Figure 3.10 X-ray crystal structure of *cis*-[Re(PEt$_2$Ph)(sal$_2$ibn)]PF$_6$, **17**, with 50% probability thermal ellipsoids (CCDC # 1910615).
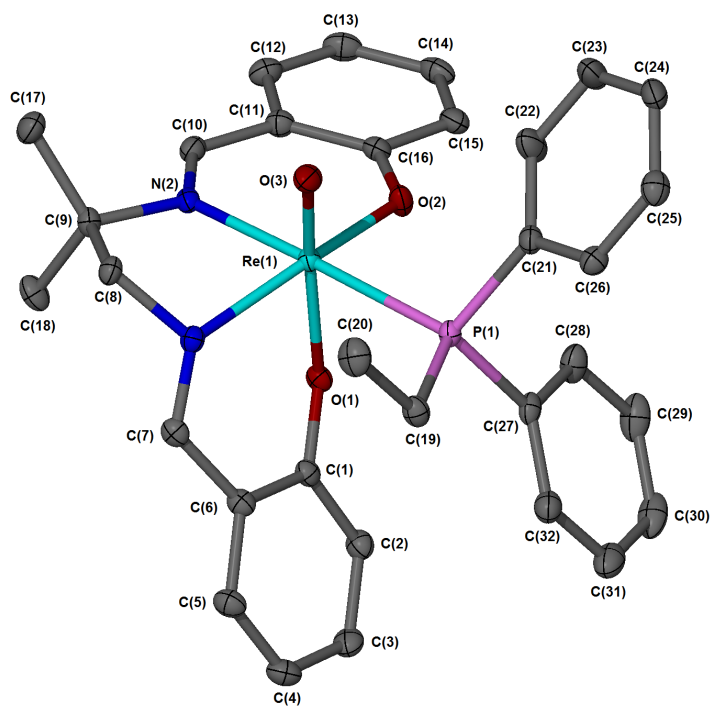
Figure 3.11 X-ray crystal structure of *cis*-[Re(PEtPh$_2$)(sal$_2$ibn)]PF$_6$, **18**, with 50% probability thermal ellipsoids (CCDC # 1910616).
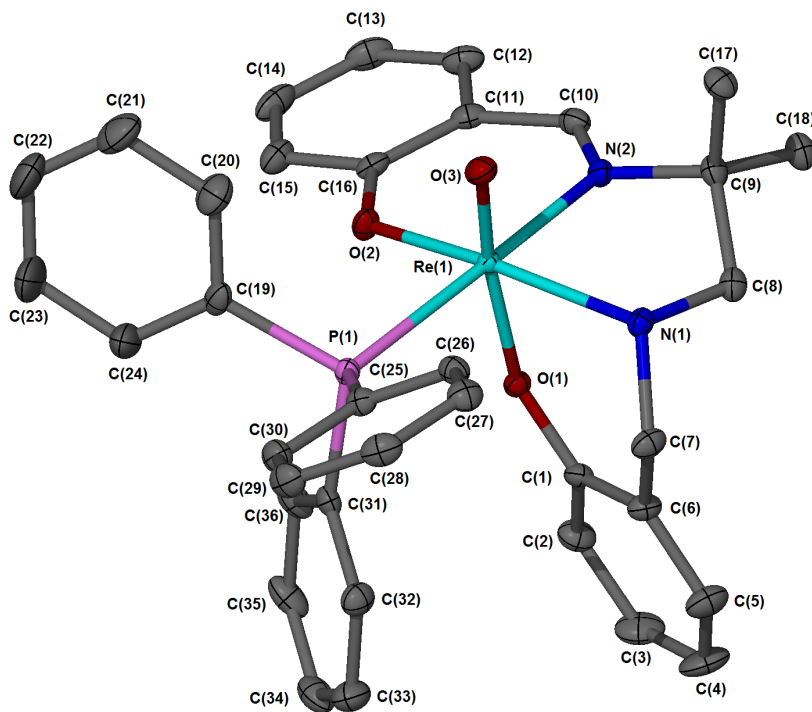
Figure 3.12 X-ray crystal structure of *cis*-[Re(PPh$_3$)(sal$_2$ibn)]PF$_6$, **19**, with 50% probability thermal ellipsoids (CCDC # 1912253).

Table 3.4 X-ray crystal data, data collection parameters, and refinement parameters for **10**, **11**•CH_3OH, **13**, and **15**•$2.333CH_3OH$

	10	**3•CH_3OH**	**13**	**15•$2.333CH_3OH$**
CCDC	1910610	1910611	1910612	1910613
formula	$C_{28}H_{44}F_6N_2O_2P_3Re$	$C_{46}H_{52}ClN_2O_4P_2Re$	$C_{30}H_{48}F_6N_2O_2P_3Re$	$C_{46}H_{48}F_6N_2O_2P_3Re$
fw	833.76	980.48	861	1053.97
cryst system	Monoclinic	Triclinic	Monoclinic	Monoclinic
space group	$P2_1/c$	P-1	$P2_1/c$	C2/c
a (Å)	10.462(1)	10.5691(6)	23.173(2)	42.450(4)
b (Å)	15.724(2)	12.4434(8)	15.547(1)	10.1296(9)
c (Å)	19.766(3)	17.083(1)	21.324(2)	30.348(3)
α (deg)	90	100.042(1)	90	90
β (deg)	98.111(3)	91.437(1)	117.133(1)	130.284(1)
γ (deg)	90	106.144(1)	90	90
V (Å^3)	3219.2(7)	2118.6(2)	6836.9(9)	9955(2)
Z	4	2	8	8
ρ (g/cm^3)	1.720	1.537	1.675	1.406
T (K)	100	223	100	100
μ (mm^{-1})	3.988	3.052	3.758	2.596
λ souce (Å)	0.71073	0.71073	0.71073	0.71073
R(F)^a	0.0289	0.0326	0.0263	0.0196
Rw(F)^2	0.0459	0.0667	0.0473	0.0426
GoF	1.005	1.017	0.944	1.025

Table 3.5 X-ray crystal data, data collection parameters, and refinement parameters for Re(V) complexes **16-19.**

	16	17	18	19
CCDC	1910614	1910615	1910616	1912253
formula	$C_{24}H_{33}F_6N_2O_3$ P_2Re	$C_{28}H_{33}F_6N_2O_3$ P_2Re	$C_{32}H_{33}F_6N_2O_3$ P_2Re	$C_{39.5}H_{38}F_6N_2O_3$ P_2Re
fw	759.66	807.70	855.74	950.86
cryst system	Monoclinic	Triclinic	Monoclinic	Triclinic
space group	$P2_1/n$	P-1	$P2_1/n$	P-1
a (Å)	8.7506(3)	10.7455(9)	9.327(1)	10.0028(6)
b (Å)	10.9321(4)	12.292(1)	19.497(2)	11.2585(7)
c (Å)	29.4316(11)	13.353(1)	17.659(2)	17.187(1)
α (deg)	90	65.584(1)	90	94.487(2)
β (deg)	90.9445(12)	70.251(1)	94.463(2)	94.223(2)
γ (deg)	90	83.092(1)	90	98.847(2)
V (Å^3)	2815.1(2)	1511.1(2)	3201.5(6)	1899.4(2)
Z	4	2	4	2
ρ (g/cm^3)	1.792	1.775	1.775	1.663
T (K)	100	100	100	100
μ (mm^{-1})	4.499	4.197	3.967	3.353
λ souce (Å)	0.71073	0.71073	0.71073	0.71073
R(F)^a	0.0307	0.0180	0.0208	0.0170
Rw(F)^2	0.0643	0.0391	0.0421	0.0376
GoF	1.390	1.036	1.350	1.085

Table 3.6 Select bond lengths (Å) and angles (°) for **10**, **11**•CH$_3$OH, **15**, and **15**•2.333CH$_3$OH

	10	**11**•CH$_3$OH	**13a**	**13b**	**15**•2.333CH$_3$OH
Re(1)-O(1)	2.005(2)	2.021(2)	2.012(2)	2.0058(19)	2.021(1)
Re(1)-O(2)	2.016(2)	2.011(2)	2.016(2)	2.1028(18)	2.010(1)
Re(1)-N(1)	2.037(3)	2.029(2)	2.106(2)	2.037(2)	2.030(2)
Re(1)-N(2)	2.025(3)	2.043(2)	2.049(2)	2.044(2)	2.049(2)
Re(1)-P(1)	2.4700(9)	2.4854(7)	2.4632(7)	2.4664(8)	2.4654(5)
Re(1)-P(2)	2.4713(9)	2.4862(7)	2.5071(7)	2.4870(9)	2.4895(5)
O(1)-Re(1)-O(2)	99.22(9)	100.77(8)	98.83(8)	99.77(8)	99.88(5)
O(1)-Re(1)-N(1)	89.5(1)	170.16(8)	89.33(9)	88.90(8)	88.91(6)
O(1)-Re(1)-N(2)	171.5(1)	88.65(9)	171.25(9)	169.69(8)	170.17(6)
O(1)-Re(1)-P(1)	84.78(7)	87.90(6)	88.29(6)	87.60(6)	86.05(4)
O(1)-Re(1)-P(2)	88.51(7)	88.61(6)	81.60(6)	87.00(6)	83.00(4)
O(2)-Re(1)-N(1)	171.19(10)	89.07(9)	171.40(9)	171.19(9)	171.20(6)
O(2)-Re(1)-N(2)	89.16(10)	170.25(8)	89.92(9)	90.52(9)	89.86(6)
O(2)-Re(1)-P(1)	89.96(7)	88.97(6)	86.62(6)	86.84(6)	89.60(4)
O(2)-Re(1)-P(2)	87.25(6)	90.23(6)	85.24(6)	84.01(6)	84.89(4)
N(1)-Re(1)-N(2)	82.2(1)	81.5(1)	81.9 (1)	80.83(9)	81.36(6)
N(1)-Re(1)-P(1)	92.16(8)	92.58(7)	90.93(7)	95.13(7)	91.43(5)
N(1)-Re(1)-P(2)	91.69(8)	91.11(7)	98.73(7)	94.99(7)	95.87(5)
N(2)-Re(1)-P(1)	93.60(7)	88.88(6)	92.08(6)	92.36(7)	92.75(5)
N(2)-Re(1)-P(2)	93.60(7)	92.52(6)	99.42(6)	94.78(7)	99.31(4)
P(1)-Re(1)-P(2)	172.23(3)	176.21(2)	165.88(3)	168.43(3)	166.70(2)

Table 3.7 Select bond lengths (Å) and angles (°) for Re(V) complexes **16-19.**

	16	**17**	**18**	**19**
Re(1)-O(1)	1.993(3)	1.979(2)	1.996(2)	1.949(1)
Re(1)-O(2)	1.998(3)	1.994(2)	1.999(2)	1.987(1)
Re(1)-O(3) [oxo]	1.696(3)	1.697(2)	1.693(2)	1.699(1)
Re(1)-N(1)	2.083(3)	2.088(2)	2.085(2)	2.182(1)
Re(1)-N(2)	2.111(3)	2.107(2)	2.100(2)	2.097(1)
Re(1)-P(1)	2.465(1)	2.4732(5)	2.4856(6)	2.4734(5)
O(1)-Re(1)-O(2)	84.4(1)	85.73(6)	84.16(7)	87.01(5)
O(1)-Re(1)-N(1)	80.5(1)	80.95(7)	81.06(7)	79.68(5)
O(1)-Re(1)-N(2)	92.7(1)	95.90(6)	95.30(7)	87.10(5)
O(1)-Re(1)-O(3)	168.2(1)	165.86(6)	165.68(7)	167.63(5)
O(1)-Re(1)-P(1)	85.88(8)	85.12(4)	84.29(5)	89.59(4)
O(2)-Re(1)-N(1)	160.6(1)	161.63(6)	160.15(7)	165.11(5)
O(2)-Re(1)-N(2)	91.3(1)	91.33(6)	91.29(7)	92.81(5)
O(2)-Re(1)-O(3)	102.9(1)	102.94(7)	104.72(8)	104.87(6)
O(2)-Re(1)-P(1)	91.28(8)	89.17(4)	90.47(5)	82.63(4)
N(1)-Re(1)-N(2)	77.3(1)	77.61(7)	77.03(7)	79.96(6)
N(1)-Re(1)-O(3)	94.1(1)	92.71(7)	92.51(8)	88.88(6)
N(1)-Re(1)-P(1)	99.71(9)	102.15(5)	101.11(5)	103.76(4)
N(2)-Re(1)-O(3)	96.4(1)	95.05(7)	95.69(8)	95.57(6)
N(2)-Re(1)-P(1)	176.90(9)	178.90(5)	178.15(5)	174.51(4)
O(3)-Re(1)-P(1)	84.74(9)	83.88(5)	84.43(6)	88.58(4)

Technetium-99m radiolabelling

The ^{99m}Tc complexes [^{99m}Tc]**10** and [^{99m}Tc]**13** were prepared for comparison with their non-radioactive rhenium analogues. A two-step (one-pot) synthesis was followed based on existing procedures for ^{99m}Tc Q-complexes (**Scheme 3.4**).[38] Radiochemical yields ranged from 75-90% using non-optimized conditions. The identity of the ^{99m}Tc complexes [^{99m}Tc]**10** and [^{99m}Tc]**13** was confirmed by HPLC comparison with the well characterized Re analogues **10** and **13** using parallel radiometric and photometric detection. **Figure 3.13** shows the comparison of the HPLC chromatograms for *trans*-[Re(PEt$_3$)$_2$(sal$_2$en)]$^+$, **10**, and HPLC-purified [^{99m}Tc]**10**. The similar retention times observed for [^{99m}Tc]**10** (t_R = 16.45 min) and **10** (t_R = 15.81 min) indicate that the two species are chemically analogous. The earlier retention time for **10** compared to [^{99m}Tc]**10** reflects the relative positions of the photometric and radiometric detectors in the HPLC system.
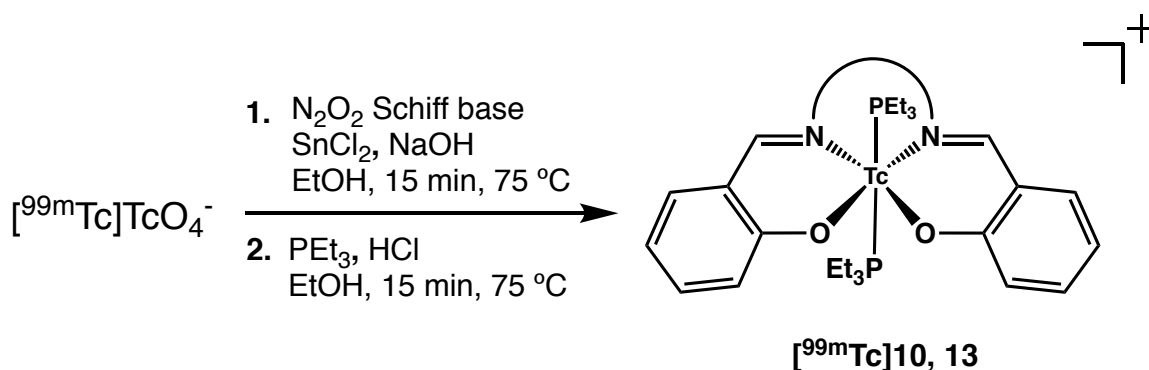
Scheme 3.4. Synthesis of [^{99m}Tc]**10** and [^{99m}Tc]**13**.

A preliminary assessment of the stability of the ^{99m}Tc complexes was performed by incubation in aqueous solution. After HPLC purification, each ^{99m}Tc complex was incubated in HPLC eluent (70-80% MeCN in H$_2$O) under ambient conditions. The radiochemical purity of each complex was measured by radio-HPLC for several time

points out to a maximum of twenty-four hours. [^{99m}Tc]**10** was observed to be stable at all time points measured (**Figure 3.14**). No indications of reoxidation of Tc(III) to Tc(V) species or [^{99m}Tc]TcO$_4^-$ were observed. This result agrees with previous studies of ^{99m}Tc Q-compounds incorporating sterically unencumbering Schiff base ligands.
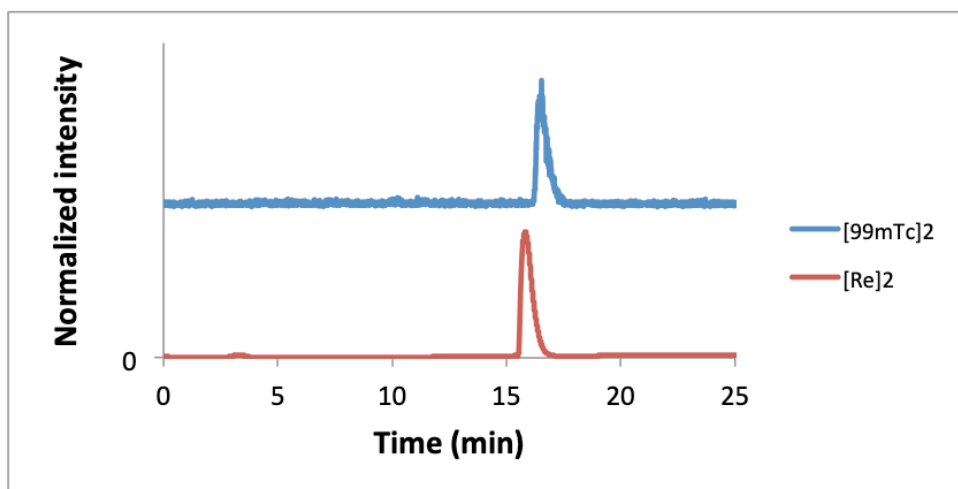
Figure 3.13. Overlay of HPLC chromatograpm of **10** (red, t_R = 15.81 min) and [^{99m}Tc]**10** (blue, t_R = 16.45 min).
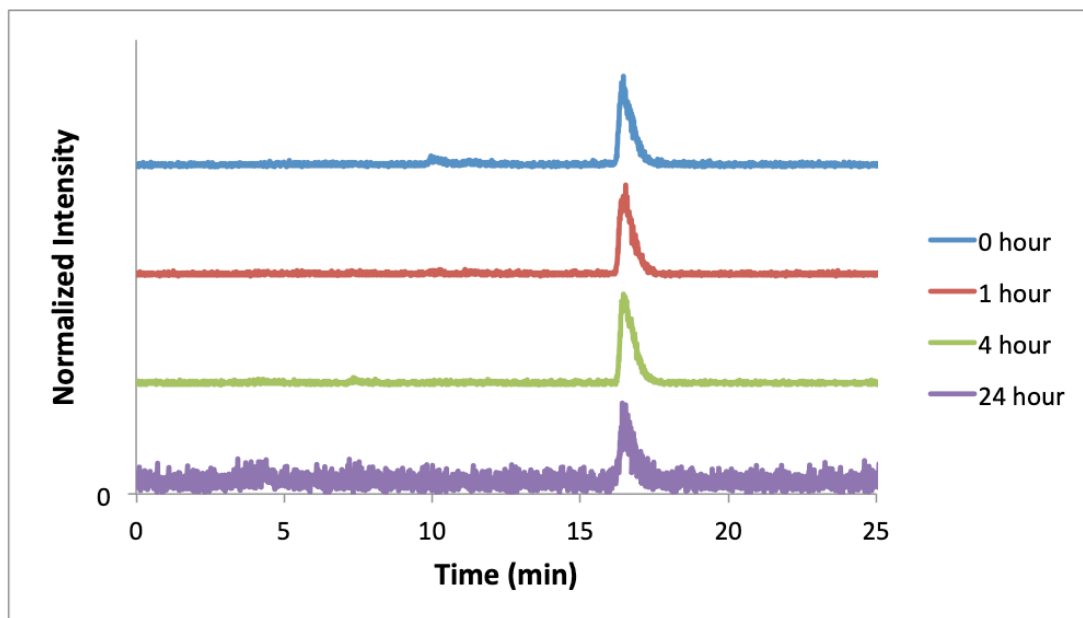
Figure 3.14. Overlay HPLC chromatograph of [^{99m}Tc][Tc(PEt$_3$)$_2$(sal$_2$en)]$^+$, [^{99m}Tc]**10**, stability at 0, 1, 4, and 24 hours.

[^{99m}Tc]**13**, incorporating the sterically hindering sal$_2$ibn ligand, underwent rapid and complete degradation in solution. **Figure 3.15** shows a comparison of the radiometric HPLC chromatogram for the crude reaction mixture of [^{99m}Tc]**13** with the photometric HPLC chromatogram of *trans*-[Re(PEt$_3$)$_2$(sal$_2$ibn)]$^+$, **13**. A major peak is observed with a retention time of 17.73 minutes in the HPLC chromatogram of the crude [^{99m}Tc]**13** reaction solution. This major peak for [^{99m}Tc]**13** aligns with that for **13** suggesting the ^{99m}Tc and Re species are chemically analogous.
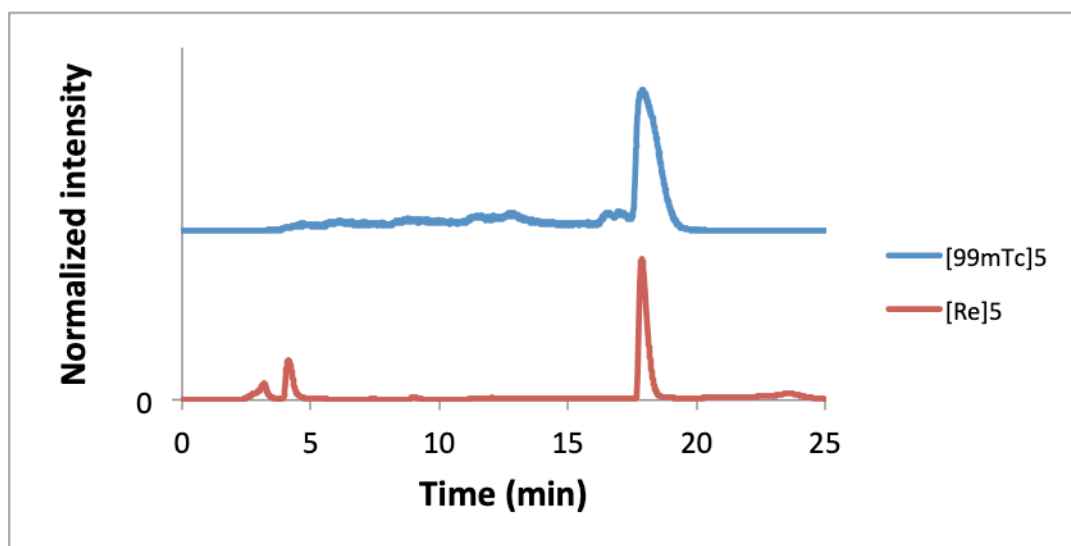
Figure 3.15. Overlay of HPLC chromatograpm of *trans*-[Re(PEt$_3$)$_2$(sal$_2$ibn)]$^+$ (red, t_R = 17.80 min) and [^{99m}Tc]**13** (blue, t_R = 17.73 min).

The radiolabelled complex [^{99m}Tc]**13** was purified by collecting the peak at 17.73 minutes. After collection, a portion of the purified solution was immediately reinjected onto the HPLC in order to start the stability study. The radiochemical purity of [^{99m}Tc]**13** was 72% in the initial injection of the purified complex (**Figure 3.16**). This indicates [^{99m}Tc]**13** underwent significant degradation in the time between collection of the purified complex and reinjection to initiate the stability study (~15 minutes). A secondary peak was observed with a retention time of 8.38 minutes. As the stability study

progressed, the secondary peak at 8.38 minutes became the major species. The radiochemical purity of [^{99m}Tc]**13** was 22% after 1 hour and a mere 6% after 2 hours. The new peak was identified as [^{99m}Tc][TcO(PEt)(sal$_2$ibn)]$^+$, [^{99m}Tc]**16**.
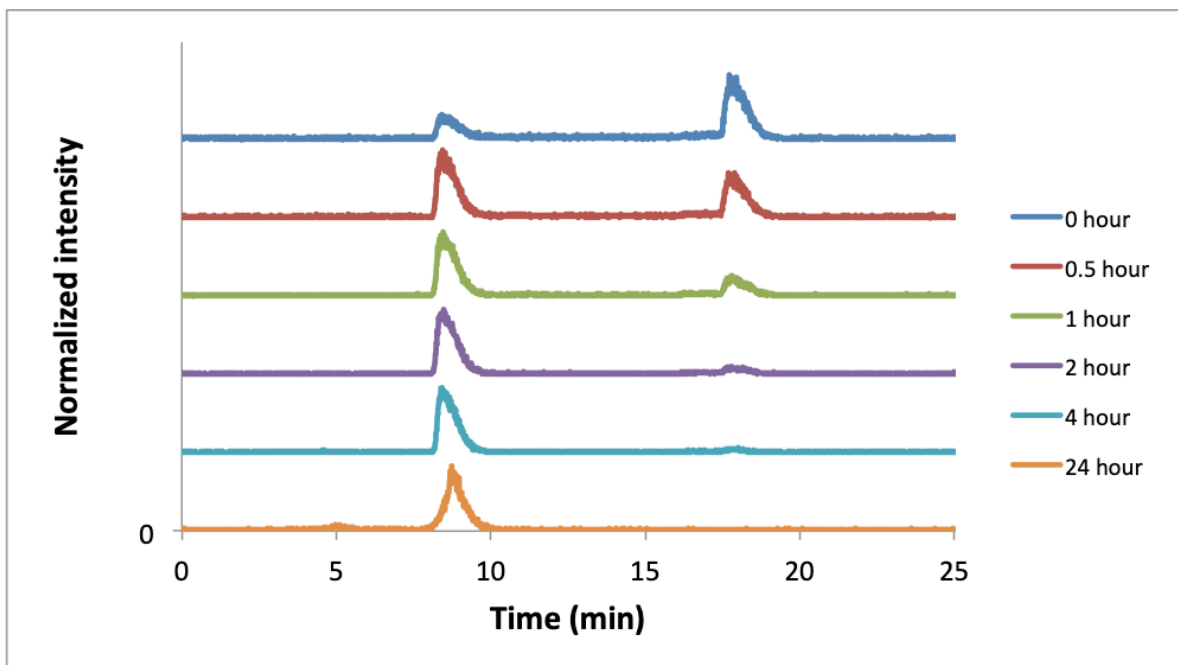
Figure 3.16. Overlay HPLC chromatograph of [^{99m}Tc][Tc(PEt$_3$)$_2$(sal$_2$ibn)]$^+$, [^{99m}Tc]**13**, stability at 0, 0.5, 1, 2, 4, and 24 hours.

Figure 3.17 shows a comparison of the initial radiometric HPLC chromatogram (t = 0 h) for [^{99m}Tc]**13** with the photometric chromatograms for the Re complexes *trans*-[Re(PEt$_3$)$_2$(sal$_2$ibn)]$^+$, **13,** and *cis*-[ReO(PEt$_3$)(sal$_2$ibn)]$^+$, **16**. The retention time of the secondary peak aligns with that of [Re]**16** suggesting the two species are chemically analogous. The peak for [^{99m}Tc]**16** was not observed in the HPLC chromatogram of the crude reaction mixture (**Figure 3.15**). It is hypothesized that excess PEt$_3$ in the reaction solution stabilizes [^{99m}Tc]**13** by preventing oxidation to Tc(V) species. Complex [^{99m}Tc]**16** likely forms by multi-step process involving ligand dissociation, metal

oxidation, and Schiff base ligand rearrangement. In this regard, the degradation of [^{99m}Tc]**13** mirrors that of the Re congener **13**.
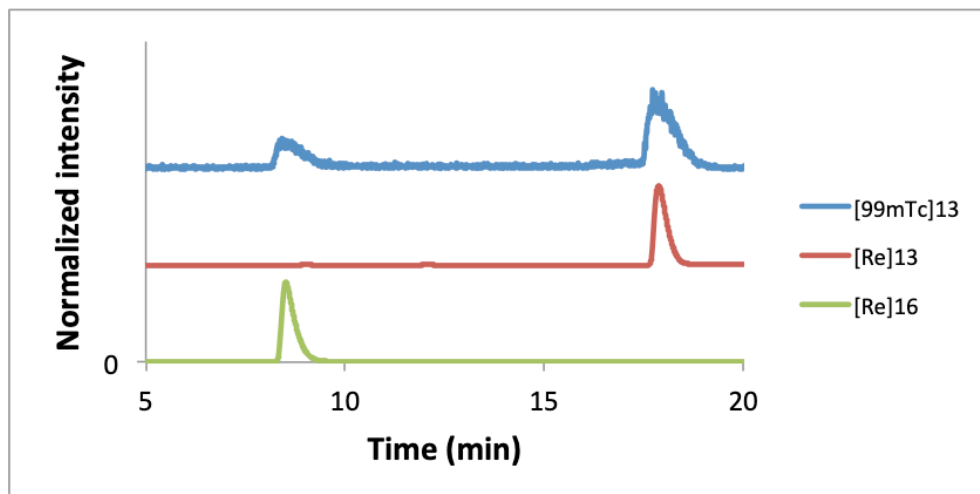
Figure 3.17. Overlay HPLC comparison of the Re-sal$_2$ibn complexes **13** (red, t_R = 17.80 min) and **16** (green, t_R = 8.45 min) with [^{99m}Tc]**13** (blue, t_R = 17.63 min) after HPLC purification

Although [^{99m}Tc]**13** was observed to oxidize to [^{99m}Tc]**16**, there was no evidence of [^{99m}Tc]TcO$_4^-$ formation. The Tc metal center remained coordinated by the Schiff base ligand throughout the stability study. The conversion of [^{99m}Tc]**13** to [^{99m}Tc]**16** (**Figure 3.18**) is likely driven by steric interactions between the bulky backbone *gem*-diemthyl groups of the sal$_2$ibn ligand and the PEt$_3$ ligand.
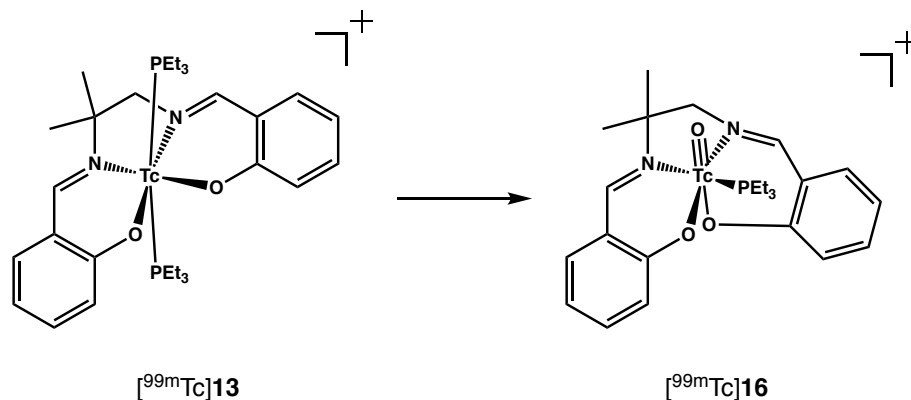
Figure 3.18. Conversion of [^{99m}Tc]**13** to [^{99m}Tc]**16**.

3.4 Conclusion

Rhenium complexes of the type *trans*-[Re(PR$_3$)$_2$(Schiff base)]$^+$ were prepared under anerobic conditions using the Schiff base ligands sal$_2$ibnH$_2$ and sal$_2$enH$_2$. The isolated *trans*-[Re(PR$_3$)$_2$(sal$_2$en)]$^+$ species **10-12** were found to be stable in solution under aerobic conditions. The stability of the the *trans*-[Re(PR$_3$)$_2$(sal$_2$ibn)]$^+$ species **13-15** under aerobic conditions was dependent on the tertiary phosphine used. Complex **13** incorporating triethylphosphine was found to be stable in solution, while complexes **14** and **15** (incorporating diethylphenyl phosphine and ethyldiphenylphosphine, respectively) were observed to decompose over time to their respective *cis*-[ReO(PR$_3$)(Schiff base)]$^+$ species. Decomposition of the *trans*-[Re(PR$_3$)$_2$(sal$_2$ibn)]$^+$ species involves oxidation from Re(III) to Re(V), and loss of one tertiary phosphine ligand. The decomposition appears to be driven by steric rather than electronic factors. Technetium-99m complexes [^{99m}Tc][Tc(PEt$_3$)$_2$(sal$_2$en)]$^+$, [^{99m}Tc]**10**, and [^{99m}Tc][Tc(PEt$_3$)$_2$(sal$_2$ibn)]$^+$, [^{99m}Tc]**13**, were prepared in order to evaluate their solution stability and for comparison with their non-radioactive rhenium analogues. [^{99m}Tc]**10** was found to be stable in solution. [^{99m}Tc]**13** was observed to oxidize in solution to form [^{99m}Tc][TcO(PEt$_3$)(sal$_2$ibn)]$^+$, [^{99m}Tc]**16**. This data will be useful in ligand selection for translating Re Q-chemistry to the radiotracer level with ^{186}Re and ^{188}Re, and will aid in the design of bifunctional derivatives of the Re Q series.

CHAPTER 4

Synthesis and Radiolabelling of Q-compounds with Backbone-Functionalized N_2O_2 Schiff Base Ligands

4.1 Introduction

The development of peptide-based radiopharmaceuticals for tumor imaging and radiotherapy has been an emphasis of nuclear medicine for the past two decades. Radiopharmaceuticals of this type use receptor-specific peptides labeled with a radionuclide to target receptor sites on diseased tissues. Design of peptide-based radiopharmaceuticals varies greatly by the type of peptide and the radiolabelling strategy employed. The pharmacological properties of radiolabelled peptides are strongly influenced by the appended radionuclide complex. When designing peptide-based radiopharmaceuticals, it is advantageous to have as many available radiolabeling strategies as possible. In an effort to develop novel peptide labeling strategies, the "Q-series" mixed-ligand complexes of Tc(III) and Re(III) were explored as a framework for peptide-based radiopharmaceuticals.

Mixed ligand technetium "Q-compounds", *trans*-[^{99m}Tc][Tc(PR$_3$)$_2$(L)]$^+$, where Tc(III) is coordinated by two tertiary phosphine ligands and a tetradentate N_2O_2 Schiff base ligand, have been previously investigated as single photon emission computed tomography (SPECT) imaging agents for myocardial perfusion and multidrug resistant (MDR) tumors.[38-40, 62, 67, 68, 86-88] Recent work has sought to develop a Re(III) Q-series analogous to the Tc(III) Q-series for use as biomodulators in MDR tumor imaging.[69-73, 75] The archetypal example of the Tc Q-series is [^{99m}Tc]Tc-furifosmin (Tc Q12), which has

been evaluated in humans for myocardial perfusion imaging.[39] Technetium-99m Q-compounds are easily prepared in high radiochemical yield. In the case of [^{99m}Tc]Tc-furifosmin, a one-step kit formulation was developed in which tris(3-methoxypropyl)phosphine (TMPP) is used as both a coordinating ligand and the sole reducing agent.[38] The stability of the Tc(III) Q-series against *in vivo* ligand exchange reactions and their accessibility from a one-step kit formulation make them attractive building blocks for peptide-based radiopharmaceuticals.
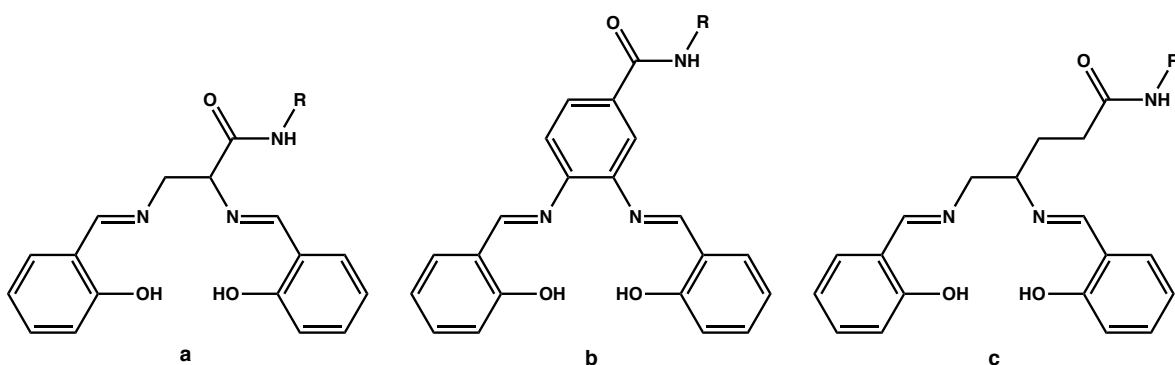
Figure 4.1. Design strategies for bifunctional N$_2$O$_2$ Schiff base ligands based on incorporation of propanamide (a), benzamide (b), or pentanamide (c) backbones.

Development of a bifunctional Tc "Q-series" requires attaching a receptor-specific peptide to the N$_2$O$_2$ Schiff base ligand. Tetradentate N$_2$O$_2$ Schiff base ligands incorporating peptides have been previously reported.[143-146] The most common way to attach peptides into tetradentate Schiff base ligands has been through the use of a propanamide linker in the ligand backbone.[144-146] Benzamide linkers have similarly been used to incorporate biomolecules into the backbone of tetradentate Schiff base ligands.[147, 148] Another potential strategy for functionalizing tetradentate Schiff base ligands is through the use of a pentanamide linker. In the pentanamide linker, two carbons atoms separate the Schiff base backbone and the amide moiety. This spacing could be beneficial

for reducing steric interactions near the coordinated metal center in a bifunctional Tc Q-series. **Figure 4.1** illustrates the general strategies for incorporating propanamide, benzamide, or pentanamide linkers into tetradentate Schiff base ligands.

Technetium Q-compounds developed for myocardial perfusion imaging and MDR tumor imaging have exclusively used non-functionalized ethylene backbones. Incorporation of propanamide, benzamide, or pentanamide linkers into N_2O_2 Schiff base ligands necessarily changes the steric and electronic properties of the ligands themselves and their metal complexes. Previous reports on the synthesis of Re(III) Q-compounds have shown that additional substituents on the N_2O_2 Schiff base backbone impact both the formation and stability of Re(III) Q-compounds.[69, 71-75] In Chapter 3, it was shown that *trans*-[Re(PR$_3$)$_2$(sal$_2$ibn)]$^+$ (PR$_3$ = PEt$_3$, PEt$_2$Ph, PEtPh$_2$) complexes undergo oxidation and rearrangement in solution to form the corresponding *cis*-[ReO(PR$_3$)(sal$_2$ibn)]$^+$ species. Similarly, the radiolabelled complex [^{99m}Tc][Tc(PEt$_3$)$_2$(sal$_2$ibn)]$^+$ was observed to rapidly oxidize and rearrange to form [^{99m}Tc][TcO(PEt$_3$)(sal$_2$ibn)]$^+$. In this chapter, mixed-ligand complexes of the type *trans*-[M(PEt$_3$)$_2$(Schiff base)]$^+$ (M = Re, ^{99m}Tc) were prepared using a series of salicylaldehyde-based Schiff base ligands (**Figure 4.2**). The substituents on the Schiff base ligand backbone were varied in order to assess the influence of backbone functionalization on the formation and stability of these complexes. Two bifunctional model ligands—H$_2$sal$_2$ppa-Bn and H$_2$sal$_2$bza-Bn—were included in order to assess the use of propanamide and benzamide linkers for incorporation of targeting biomolecules into Q-compounds.
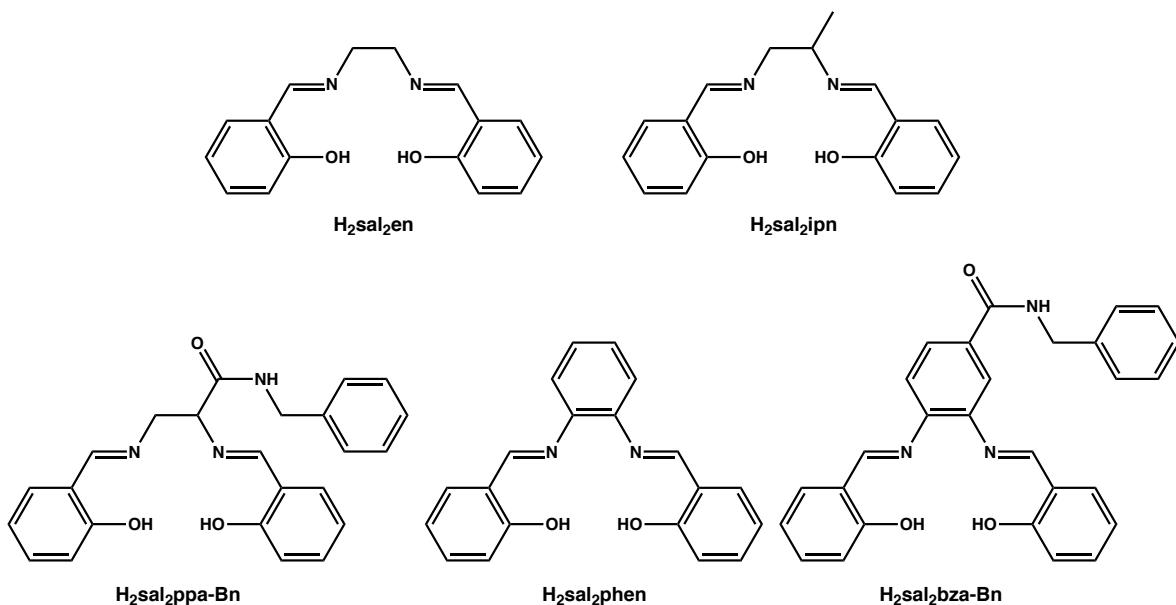
Figure 4.2. Structures of the N_2O_2 Schiff base ligands used in this study.

4.2. Experimental

General Considerations. Unless otherwise noted, all common laboratory chemicals were of reagent grade or better. Absolute ethanol (EtOH) was degassed prior to use. Experiments with rhenium were performed under an argon atmosphere using standard Schlenk techniques for inert syntheses. Microwave reactions were performed using a CEM Discover® SP microwave reactor (CEM Corporation, Matthews, NC). ^{1}H and ^{13}C NMR spectra (including HMQC ^{1}H-^{13}C correlation) were recorded on a Bruker DRX500 or DRX600 at 25 °C in CD_2Cl_2, $CDCl_3$, or CD_3CN and calibrated with the respective residual solvent peaks ($CHDCl_2$ at 5.32 ppm; $CHCl_3$ at 7.26 ppm; CHD_2CN at 1.94 ppm). ^{31}P NMR spectra were recorded on a Brüker DRX300 at 25 °C and calibrated using 85% aqueous H_3PO_4 as an external standard (0.00 ppm). Liquid Chromatography Mass Spectroscopy (LC-MS) was performed on a ThermoFisher Scientific LCQ Fleet Ion Trap Mass Spectrometer. A Shimadzu Prominence HPLC system with a pump, controller, Prominence UV-vis detector (model SPD-20AV) set to 254 nm and coupled to a

Beckman 170 NaI(Tl) radioisotope detector with a Phenomenex® Jupiter® LC column (C18, 5 μm, 250 x 4.6 mm) was used to analyze ^{99m}Tc and Re complexes. A linear gradient from 50% A to 90% B (A = H_2O with 0.1% TFA, and B = MeCN with 0.1% TFA) with a flow rate of 1 mL/min over 20 minutes was used for all HPLC analyses.

Materials.

Caution! Technetium-99m emits a 140 keV γ-ray with a half-life of 6.01 hours. All operations were carried out in radiochemical laboratories equipped and approved for handling this radionuclide. Technetium-99m was eluted as sodium pertechnetate from a ^{99}Mo/^{99m}Tc generator (Covidien) using saline.

Salicylaldehyde, *o*-phenylenediamine, triethylphosphine (1.0 M in THF), tin(II) chloride, DL-2,3-diaminopropionic acid monohydrochloride (**L1**), di-tert butyl dicarbonate (Boc$_2$O), 3,4-diamino-N-benzylbenzamide, 4-dimethylaminopyridine (DMAP), *N*-(3-dimethylaminopropyl)-*N'*-ethylcarbodiimide hydrochloride (EDC•HCl), and *N,N'*-bis(salicylidene)-1,2-propanediamine (sal$_2$ipnH$_2$) were purchased from commercial sources and used as received. (*n*Bu$_4$N)[ReOCl$_4$] was prepared according to established procedures.[92] The Re(III) complex *trans*-[Re(PEt$_3$)$_2$(sal$_2$en)]Cl, **10**, was prepared according to the methods described in Chapter 3. The N$_2$O$_2$ Schiff base sal$_2$phenH$_2$ and sal$_2$enH$_2$ were prepared by the condensation of the appropriate diamine with two equivalents of salicylaldehyde. The purities of the starting materials were verified by ^{1}H NMR, ^{13}C NMR, and FT-IR spectroscopies.

(*R,S*)-2,3-bis((*tert*-butoxycarbonyl)amino)propanoic acid, L2. Compound **L2** was prepared from DL-2,3-diaminopropionic acid monohydrochloride (**L1**, 5.0 g) according

to a literature method.[149] Yield: 75%. ESI MS (*m/z*): 327.07 (calcd. 327.15 for [$C_{13}H_{24}N_2NaO_6$]$^+$ [M+Na]).

(*R,S*)-*N*-benzyl-2,3-bis(*tert*-butoxycarbonyl)aminopropionamide , **L3**. Compound **L2** (4.00 g, 13.1 mmol) was added to 40 mL of dichloromethane. Benzylamine (1600 μL, 15.2 mmol), EDC•HCl (3.02 g, 15.8 mmol), and DMAP (1.93 g, 15.8 mmol) were added to the slurry, which quickly dissolved. The reaction was stirred for 18 h under ambient conditions, after which time the solvent was removed by rotary evaporation yielding the crude product as a viscous yellow oil. Recrystallization from 50:50 ethyl acetate/hexanes at -13 °C afforded the pure product as a white solid. Yield 63% (3.26 g). ^{1}H NMR [600 MHz, CDCl$_3$, r.t., δ (ppm)]: 7.31-7.23 (m, 5H, C$_6$**H$_5$**); 7.08 (br s, 1H, N**H**CH$_2$Ph); 5.92 (s, 1H, (CH$_3$)COC(O)N**H**)); 5.27 (s, 1H, (CH$_3$)COC(O)N**H**)); 4.37-4.52 (m, 2H, NHC**H$_2$**Ph); 4.24 (s, 1H, **CH**); 3.46-3.53 (m, 2H, C**H$_2$**NH); 1.42 (s, 9H, C(C**H$_3$**)$_3$); 1.41 (s, 9H, C(C**H$_3$**)$_3$). ^{13}C NMR [600 MHz, CDCl$_3$, r.t., δ (ppm)]: 170.56 (**C**(O)NHCH$_2$Ph); 157.18, 156.20 (2 **C**(O)OC(CH$_3$)$_3$); 137.85, 137.64, 128.61, 128.43, 127.27, 127.17 (**C$_6$**H$_5$); 80.30, 79.92 (2 **C**(CH$_3$)$_3$); 55.79 (**CH**); 43.31 (**CH$_2$**NH); 42.32 (NH**CH$_2$**Ph); 28.26, 28.21 (2 C(**CH$_3$**)$_3$). ESI MS (*m/z*): 416.12 (calcd. 416.22 for [$C_{20}H_{31}N_3NaO_5$]$^+$ [M+Na]).

2,3-diamino-*N*-benzylpropanamide, L4. Compound **L3** (2.026 g, 5.14 mmol) was dissolved in 20 mL of CH$_2$Cl$_2$. Trifluoroacetic acid (15 mL) was added to the solution. The reaction mixture was stirred overnight at room temperature and then the solvent was evaporated *in vacuo*. The crude product was dissolved in CH$_2$Cl$_2$ and extracted with 1 M HCl (3 x 50 mL). The combined aqueous layers were washed with CH$_2$Cl$_2$ (2 x 50 mL), basified with 3 M NaOH, and extracted with CH$_2$Cl$_2$ (3 x 50 mL). The combined organic

layers were washed with brine (2 x 50 mL), dried over MgSO$_4$, and evaporated *in vacuo* to yield the product as a light yellow oil. Yield 20% (200 mg). ^{1}H NMR [600 MHz, CD$_3$OD, r.t., δ (ppm)]: 7.20-7.31 (m, 5H, Ar**H**); 4.36 (2H, s, -NHC**H$_2$**Ph-); 3.27 (m, 1H, C**H**); 2.85, 2.69 (m, 2H, -NC**H$_2$**CH(CO)). ^{13}C NMR [600 MHz, CD$_3$OD, r.t., δ (ppm)]: ^{13}C NMR [600 MHz, CD$_3$OD, r.t., δ (ppm)]: 176.06 (-**C**(O)NCH$_2$-); 162.50, 161.94 (**C**H=N); 141.72, 139.87, 129.58, 128. 61, 128.33 (Ar); 57.92 (**C**H); 46.98, 46.22 (-NCH$_2$**C**H(CO)); 44.00 (-NH**C**H$_2$Ph). ESI MS (*m/z*): 194.12 (calcd. 194.13 for [C$_{10}$H$_{16}$N$_3$O]$^+$ [M+H]).

N-benzyl-2,3-bis(((*E*)-2-hydroxybenzylidene)amino)propanamide, H$_2$sal$_2$ppa-Bn.

Compound **L4** (190 mg, 0.98 mmol) was dissolved in 5 mL of absolute EtOH. Salicylaldehyde was added to the reaction mixture, which immediately turned bright yellow. The reaction mixture was stirred for 2 hours under ambient conditions during which time a yellow precipitate formed. The precipitate was isolated by centrifugation and then washed sequentially with cold EtOH (2 x 5 mL) and diethyl ether (1 x 10 mL). Yield: 80% (316 mg). ^{1}H NMR [600 MHz, CD$_3$OD, r.t., δ (ppm)]: 8.55 (s, 1H, -**C**H=N-); 8.45 (s, 1H, -**C**H=N-); 7.30-7.38 (m, 4H, Ar**H**); 7.15-7.22 (m, 5H, -CH$_2$(C$_6$**H$_5$**)); 6.85-6.91 (m, 4H, **ArH**); 4.43 (s, 2H, -C**H$_2$**(C$_6$H$_5$)); 4.39 (t, 1H, C**H**), 4.05-4.20 (m, 2H, C**H$_2$**). ^{13}C NMR [600 MHz, CD$_3$OD, r.t., δ (ppm)]: 172.19 (-**C**(O)NCH$_2$-); 162.50, 161.94 (**C**H=N); 139.56, 134.15, 133.78, 133.40, 133.10, 129.48, 128.37, 128.13, 120.11, 119.78, 117.84, 117.77 (Ar); 74.36 (**C**H); 63.08 (-N**C**H$_2$CH(CO)); 44.15 (-NH**C**H$_2$-). ESI MS (*m/z*): 402.19 (calcd. 402.18 for [C$_{24}$H$_{24}$N$_3$O$_3$]$^+$ [M+H]).

N-benzyl-3,4-bis(((E)-2-hydroxybenzylidene)amino)benzamide, H$_2$sal$_2$bza-Bn. 3,4-diamino-*N*-benzylbenzamide (52.85 mg, 0.219 mmol) was dissolved in 5 mL of absolute

EtOH. Salicylaldehyde (46 μL, 0.438 mmol) was added and then the reaction mixture was stirred for 2 hours at 50 °C. The reactive mixture was dried down via rotary evaporation to yield a bright orange solid. The ligand was used without further purification. Yield: 95% (93.5 mg). ^{1}H NMR [600 MHz, CD$_3$OD, r.t., δ (ppm)]: 8.87 (s, 1H, -C**H**=N-); 8.84 (s, 1H, -C**H**=N-); 7.90-6.95 (m, 16H, Ar**H**); 4.62 (s, 2H, -C**H$_2$**-). ^{13}C NMR [600 MHz, CD$_3$OD, r.t., δ (ppm)]: 168.92 (**C**=O); 166.70, 166.45 (**C**H=N); 134.89, 134.64, 134.03, 133.94, 129.58, 128.64, 128.51, 128.26, 127.85, 121.14, 120.74, 120.43, 119.93, 117.99 (**Ar**); 44.46 (**C**H$_2$). ESI MS (*m/z*): 450.13 (calcd. 450.18 for [C$_{28}$H$_{24}$N$_3$O$_3$]$^+$ [M+H]).

trans-[Re(PEt$_3$)$_2$(sal$_2$ipn)]Cl, 20. (*n*Bu$_4$N)[ReOCl$_4$] (50.07 mg, 0.085 mmol) and H$_2$sal$_2$ipn (48.16 mg, 0.171 mmol) were added to a 10-mL microwave reaction vessel, which was purged and backfilled with argon three times. Degassed absolute ethanol (3 mL) was added to the vessel via *cannula*. The reaction mixture was heated in a microwave reactor at 105 °C, 17 bar (max), and 150 W (max) for 1 min with stirring, resulting in a dark green solution. Triethylphosphine (1.0 M solution in THF, 350 μL, 0.34 mmol) was added to the reaction vessel via syringe, and the mixture was then heated (105 °C, 17 bar (max), and 150 W (max)) for 5 min with stirring. The resultant bright red solution was taken to dryness *in vacuo*. The oily red residue was dissolved in a minimal volume of CH$_2$Cl$_2$ and then loaded onto a silica gel column (8 g silica, 15 mm i.d.) pre-equilibrated in CH$_2$Cl$_2$. Elution with CH$_2$Cl$_2$ displaced triethylphosphine and triethylphosphine oxide from the column as a faint pink band. Switching the eluent to MeCN eluted two unidentified red bands. The red product-containing band was eluted with 20% MeOH in MeCN. This solution was brought to dryness by rotary evaporation

to yield a dark red solid. Yield: 75% (47 mg). X-ray quality crystals of **20** were obtained by the addition of ammonium hexafluorophosphate into a MeOH/H_2O solution of the product that was filtered and left to sit for several days. ^{1}H NMR [600 MHz, CDCl$_3$, r.t., δ (ppm)]: 73.31 (s, 1H, -**CH**=N-); 51.92 (s, 1H, -**CH**=N-); 27.47 (d, J = 8.3 Hz, 1H, Ar**H**); 27.32 (d, J = 8.3 Hz, 1H, Ar**H**); 17.26 (t, J = 7.3 Hz, 1H, Ar**H**); 16.57 (t, J = 7.3 Hz, 1H, Ar**H**); 1.89 (t, 9H, PCH$_2$**CH$_3$**); 1.80 (t, 9H, PCH$_2$**CH$_3$**); 1.46 (m, 6H, P**CH$_2$**CH$_3$); 1.25 (s, 1H, -NCH$_2$CH(**CH$_3$**)N-); 1.15 (m, 3H, -NCH$_2$CH(**CH$_3$**)N-); 1.12 (m, 6H, P**CH$_2$**CH$_3$); -6.41 (t, J = 8.3 Hz, 1H, Ar**H**); -7.25 (t, J = 8.1 Hz, 1H, Ar**H**); -8.11 (s, 1H, -N**CH$_2$**CH(CH$_3$)N-); -18.45 (d, J = 6.8 Hz, 1H, Ar**H**); -19.15 (d, J = 6.0 Hz, 1H, Ar**H**); -19.23 (s, 1H, -N**CH$_2$**CH(CH$_3$)N-). ESI MS (*m/z*): 702.96 (calcd. 703.26 for [C$_{29}$H$_{46}$N$_2$O$_2$P$_2$Re]$^+$ [M]).

***trans*-[Re(PEt$_3$)$_2$(sal$_2$ppa-Bn)]Cl, 21.** Complex **21** was synthesized according to the methods described for complex **20** substituting H$_2$sal$_2$ppa-Bn for H$_2$sal$_2$ipn. Yield: 59% (43 mg). Crystals suitable for X-ray diffraction were obtained as the ReO$_4^-$ salt by slow evaporation from a solution of 25% MeCN in H$_2$O. ^{1}H NMR [600 MHz, CDCl$_3$, r.t., δ (ppm)]: 77.88 (s, 1H, -**CH**=N-); 63.90 (s, 1H, -**CH**=N-); 28.97 (d, 1H, Ar**H**); 28.90 (d, 1H, Ar**H**); 17.96 (m, 2H, Ar**H**); 6.59 (t, 1H, Bz**H** *para*); 6.37 (t, 2H, Bz**H** meta); 4.61 (d, 2H, Bz**H** ortho); 1.92, 1.75 (d of t, 18H, P(CH$_2$**CH$_3$**)$_3$); 1.28 (m, 5H, P(**CH$_2$**CH$_3$)$_3$); 0.67 (m, 4H, P(**CH$_2$**CH$_3$)$_3$); 0.25 (m, 3H, P(**CH$_2$**CH$_3$)$_3$); -0.47 (s, 1H, -NCH$_2$C(CH$_2$Bz)**H**-); -7.52 (t, 1H, Ar**H**); -8.06 (s, 1H, -NCH$_2$C(CH$_2$Bz)H-); -8.26 (t, 1H, Ar**H**); -8.76 (s, 1H, -N**CH$_2$**C(CH$_2$Bz)H-); -19.28 (d, 1H, Ar**H**); -21.16 (d, 1H, ArH). ESI MS (*m/z*): 704.05 (calcd. 704.21 for [C$_{36}$H$_{51}$N$_3$O$_3$P$_2$Re]$^+$ (M$^+$-PEt$_3$)).

***trans*-[Re(PEt₃)₂(sal₂phen)]Cl, 22.** Complex **22** was synthesized according to the methods described for complex **20** substituting H₂sal₂phen for H₂sal₂ipn. Yield: 69% (45 mg). ¹H NMR [600 MHz, CDCl₃, r.t., δ (ppm)]: 31.45 (d, $J = 8.0$ Hz, 2H, Ar**H**); 21.36 (t, $J = 7.2$ Hz, 2H, Ar**H**); 2.74 (m, 2H, Ar**H**); 1.99 (m, 18H, PCH₂C**H₃**); 1.89 (m, 12H, PC**H₂**CH₃); -7.14 (d, $J = 7.3$ Hz, 2H, Ar**H**); -7.33 (t, $J = 8.3$ Hz, 2H, Ar**H**); -20.75 (m, 2H, Ar**H**). ESI MS (*m/z*): 619.11 (calcd. 619.15 for [C₃₂H₄₄N₂O₂P₂Re]⁺ (M⁺-PEt₃)).

***trans*-[Re(PEt₃)₂(sal₂bza-Bn)]Cl, 23.** Complex **23** was synthesized following the methods described for **20** substituting H₂sal₂bza-Bn for H₂sal₂ipn. Yield: 80% (62 mg). ¹H NMR [600 MHz, CD₃CN, r.t., δ (ppm)]: 31.96 (d, $J = 9.1$ Hz, 1H, Ar**H**); 31.85 (d, $J = 8.2$ Hz, 1H, Ar**H**); 22.19 (t, $J = 7.0$ Hz, 1H, Ar**H**); 21.58 (t, $J = 6.8$ Hz, 1H, Ar**H**); 6.61 (d, $J = 7.4$ Hz, 1H, Bn**H**); 6.49 (t, $J = 7.5$ Hz, 2H, Bn**H**); 5.61 (d, $J = 7.3$ Hz, 2H, Bn**H**); -6.94 (t, $J = 8.5$ Hz, 1H, Ar**H**); -7.19 (t, $J = 8.4$ Hz, 1H, Ar**H**); -20.07 (d, $J = 6.6$ Hz, 1H, Ar**H**); -20.96 (d, $J = 6.5$ Hz, 1H, Ar**H**). ESI MS (*m/z*): 870.01 (calcd. 870.30 for [C₄₀H₅₁N₃O₃P₂Re]⁺ [M]).

***cis*-[ReO(PEt₃)(sal₂ppa-Bn)]Cl, 24.** (*n*Bu₄N)[ReOCl₄] (40.41 mg, 0.069 mmol) and H₂sal₂pa-Bn (42.21 mg, 0.105 mmol) were added to a 10-mL microwave reaction vessel, which was purged and backfilled with argon three times. Degassed absolute ethanol (2 mL) was added to the vessel via *cannula*. The reaction mixture was heated in a microwave reactor at 105 °C for 2 min with stirring, resulting in the formation of a bright green precipitate and a red-brown supernatant. Triethylphosphine (1.0 M solution in THF, 69 μL, 0.069 mmol) was added to the reaction mixture via syringe. The reaction mixture was heated in a microwave reactor at 90 °C for 1 min with stirring, resulting in the formation of a brown solution. The crude reaction mixture was brought to dryness

under reduced pressure. The oily brown residue was dissolved in a minimal volume of CH_2Cl_2 and then loaded onto a silica gel column (4 g silica, 15 mm i.d.) pre-equilibrated in CH_2Cl_2. Elution with CH_2Cl_2 displaced triethylphosphine and triethylphosphine oxide from the column as a faint pink band. The brown product-containing band was eluted with 20% MeOH in MeCN. This solution was brought to dryness by rotary evaporation to yield the product as a dark brown solid. Yield: 62% (32 mg). ^{1}H NMR [600 MHz, $CDCl_3$, r.t., δ (ppm)]: 9.56 (br s, 1H, -**CH₂CH(C(O)NH-**); 9.06 (d, 1H, -**CH**=N-); 8.36 (s, 1H, -**CH**=N-); 6.94-7.72 (m, 13H, Ar**H**); 5.51 (d, J = 11.8 Hz, 1H, -**CH₂**-(C₆H₅)); 5.38 (d, J = 5.9 Hz, 1H, -**CH₂**-(C₆H₅)); 4.52 (m, 1H, -**CH₂CH(C(O)NH-**); 4.32 (m, 1H, -**CH₂CH(C(O)NH-**); 4.13 (m, 1H, -**CH₂CH(C(O)NH-**); 1.72-1.78 (m, 3H, PC**H₂**CH₃); 1.38-1.43 (m, 3H, PC**H₂**CH₃); 1.10-1.12 (m, 9H, PC**H₂**CH₃). ^{13}C NMR [600 MHz, $CDCl_3$, r.t., δ (ppm)]: 174.66, 173.83 (C-O); 170.26 (C=O); 166.54, 164.00 (-**C**H=N-); 139.16, 138.24, 138.18, 137.98, 134.63, 128.60, 128.34, 127.99, 127.90, 127.07, 121.82, 121.29, 121.11, 120.93, 120.00, 119.04 (**Ar**); 72.48 (-N**C**H₂CH(C(O)NH-); 71.25 (-N**C**H₂CH(C(O)NH-); 43.94 (-NH**C**H₂(C₆H₅); 16.68 (PCH₂**C**H₃); 7.02 (P**C**H₂CH₃). ^{31}P NMR: -11.17. ESI MS (m/z): 719.66 (calcd. 720.20 for $[C_{30}H_{36}N_3O_4PRe]^+$ (M^+)).

Electrochemistry

Electrochemical data (**Table 4.1**) were obtained with a Bioanalytical Systems Inc. (BAS) CV-50. Tetraethylammonium perchlorate (TEAP; 0.1 M) in propylene carbonate (Burdick and Jackson, high-purity solvent for GC and spectrophotometry) was used as the electrolytic solution. An aqueous Ag/AgCl reference electrode (BAS; 3 M NaCl) was used, along with a platinum wire auxiliary electrode and a glassy carbon working electrode. A scan rate of 100 mV s^{-1} was used for all experiments. Ferrocene (3 mM in

propylene carbonate) was used as a reference standard with an aqueous Ag/AgCl reference electrode. Under these experimental conditions, the Fc^+/Fc redox couple was observed as $E_{1/2}$ = 0.384 vs Ag/AgCl in propylene carbonate. Formal potentials are reported *versus* Ag/AgCl in 3M NaCl (aq).

X-ray crystal structures

Single crystal X-ray diffraction (SCXRD) data for all structures were collected using Mo-Kα radiation (λ = 0.71073 Å). Compounds **20** and **21** were measured on a Bruker D8 Venture diffractometer equipped with a Photon 100 CMOS detector and a microfocus source (50 kV, 1 mA, λ = 0.71073 Å) using shutterless scans. In all cases, hemispheres of unique data were collected using a strategy of scans about the omega and phi axes. Intensities were corrected for Lorentz and polarization effects. Equivalent reflections were merged, and empirical absorption corrections were made using the multiscan method. Space group, lattice parameters, and other relevant information are given in **Table 4.2**. Relevant bond lengths and angles are given in **Table 4.3.** Data collection, unit cell determination, data reduction, absorption correction, scaling, and space group determination were all performed using the Bruker Apex3 software suite.[94]

Radiochemical Preparations

Preparation of the radiolabelled [^{99m}Tc][Tc(PEt$_3$)$_2$(Schiff base)]$^+$ complexes, [^{99m}Tc]**20-24**, was based on established procedures for radiolabeling ^{99m}Tc Q-complexes. In the first step, 500 μL of N_2O_2 Schiff base stock solution (4 mg/mL in EtOH), 100 μL of a $SnCl_2$ stock solution (100 mg/mL in EtOH), 100 μL of aqueous [^{99m}Tc]TcO$_4^-$ (37-111 MBq), and 50 μL of 1.0 M NaOH were added to a 2 mL reaction vial. The contents were heated at 75 °C for 15 min. In the second step, 50 μL of 1.0 M HCl and 300 μL of PEt$_3$ (1.0 M in

THF) were added to the reaction vial. The contents were heated for an additional 15 min at 75 °C. The reaction mixture was filtered through an Acrodisc 13 mm syringe filter with a 0.2 μm Nylon membrane to remove any precipitates. Reversed-phase HPLC was used to identify and purify the complexes. The rhenium complexes **20-24** were used as nonradioactive HPLC standards to confirm the formation of their analogous ^{99m}Tc complexes. A linear gradient from 50% A to 90% B (A = H_2O with 0.1% TFA, and B = MeCN with 0.1% TFA) with a flow rate of 1 mL/min over 20 minutes was used for all HPLC analyses. The retention times (t_R) for the Re compounds **20-24** and their ^{99m}Tc congeners [^{99m}Tc]**21-24** are listed in **Table 4.4**.

Technetium-99m Stability Study

Reversed-phase HPLC was used to purify [^{99m}Tc]**20-23.** A portion of the crude reaction mixture was injected onto the HPLC and then the fraction of the HPLC eluent corresponding to the retention time of [^{99m}Tc]**20-23** (**Table 4.4**) was collected. The purified fractions of [^{99m}Tc]**20-23** (3-4 MBq in ~1 mL HPLC eluent) were incubated under ambient conditions. At various time points, a portion of the purified fraction was reinjected on the HPLC to assess the radiochemical purity.

4.3 Results and Discussion

Synthesis of H$_2$sal$_2$ppa-Bn and H$_2$sal$_2$bza-Bn

Two novel Schiff base ligands—H$_2$sal$_2$ppa-Bn and H$_2$sal$_2$bza-Bn—were synthesized as model compounds for the evaluation of potential bifunctional Re and [99mTc] Q-compounds. The H$_2$sal$_2$ppa-Bn ligand contains a *N*-benzylpropanamide backbone in order to model the incorporation of a targeting biomolecule through a propanamide linker. The H$_2$sal$_2$bza-Bn ligand contains a *N*-benzylbenzamide backbone to model the use of a benzamide linker. These linkers were chosen for evaluation because they have been previously used to attach biomolecules to N$_2$O$_2$ Schiff base ligands.[144-148] Each ligand can be prepared in four steps from inexpensive, commercially available starting materials.

The bifunctional model ligand H$_2$sal$_2$ppa-Bn was synthesized according to **Scheme 4.1**. A modified literature procedure was used to prepare (*R,S*)-2,3-bis((*tert*-butoxycarbonyl)amino)propanoic acid, **L2**, in 70% overall yield.[149] Reaction of **L2** with benzylamine, DMAP, and EDC•HCl in CH$_2$Cl$_2$ yielded **(*R,S*)-*N*-benzyl-2,3-bis(*tert*-butoxycarbonyl)aminopropionamide, **L3**, in 63% yield. Deprotection of **L3** in TFA/CH$_2$Cl$_2$ afforded 2,3-diamino-*N*-benzylpropanamide, **L4**, as an amine salt. The amine salt could be converted to the free amine using aqueous NaOH. While conversion of **L4** to the free amine resulted in poor isolated yields (20%), the free amine proved to be a more facile reactant in the subsequent reaction step. Direct condensation of **L4** with salicylaldehyde afforded H$_2$sal$_2$ppa-Bn in 80% yield. Proton NMR, mass spectrometry, and IR confirmed the chemical identity of the ligand.
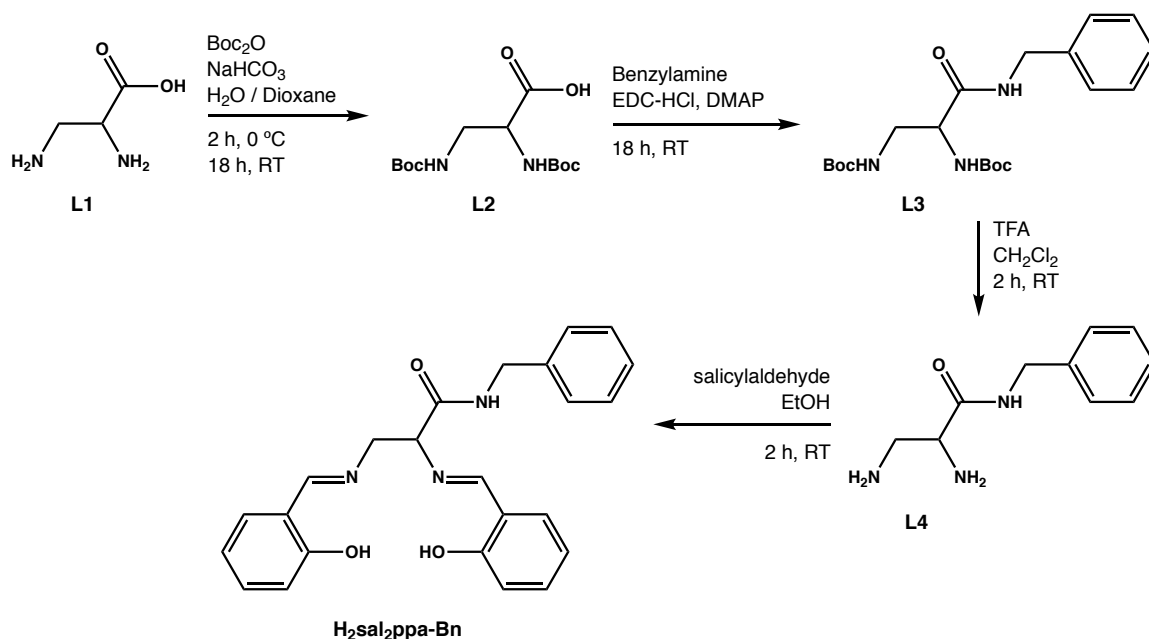
Scheme 4.1. Synthesis of H$_2$sal$_2$ppa-Bn.

The bifunctional N$_2$O$_2$ Schiff base model ligand H$_2$sal$_2$bza-Bn was prepared by direct condensation of 3,4-diamino-*N*-benzylbenzamide with salicylaldehyde in absolute ethanol in 95% overall yield (**Scheme 4.2**). The H$_2$sal$_2$bza-Bn ligand can also be prepared by the route illustrated in **Scheme 4.1** substituting 3,4-diaminobenzoic acid for 2,3-diaminopropionic acid monohydrochloride. Proton NMR, mass spectrometry, and IR confirmed the chemical identity of the ligand.
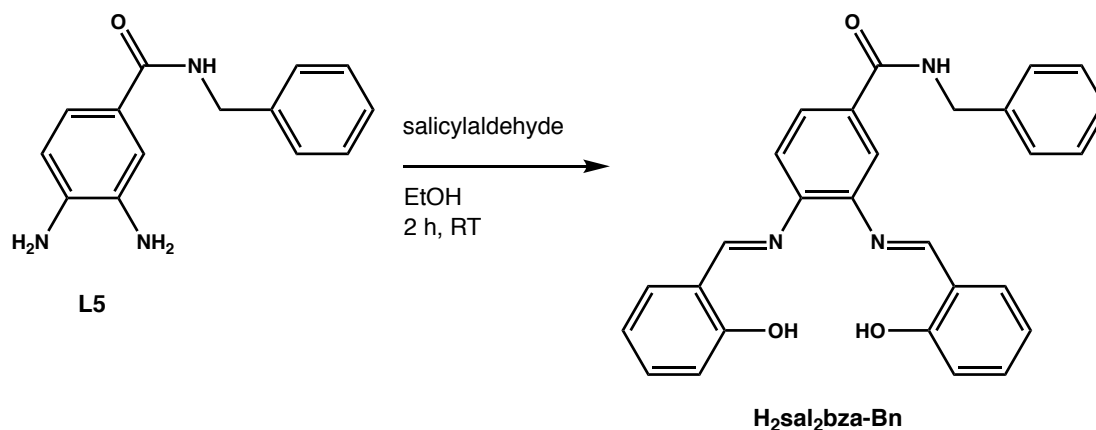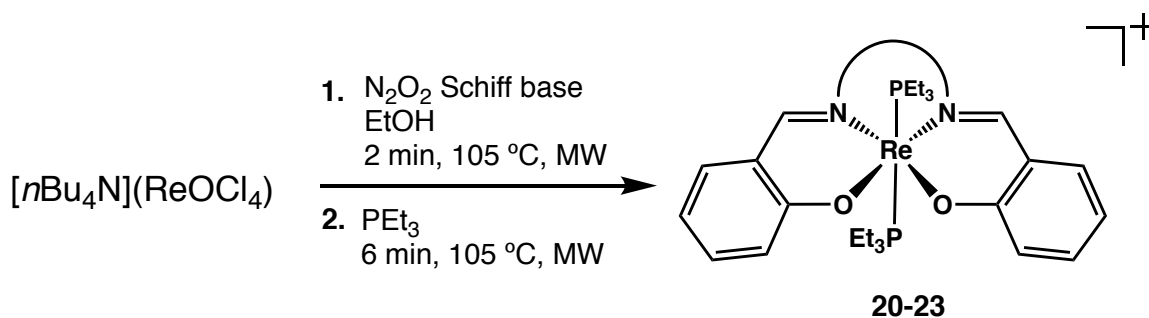

Scheme 4.2. Synthesis of H$_2$sal$_2$bza-Bn.

Synthesis of Re(III) and Re(V) Q-complexes

Rhenium complexes **20-23** were prepared by a one-pot, two-step procedure according to previously reported methods (**Scheme 4.3**).[69, 70] Microwave irradiation of (nBu$_4$N)[ReOCl$_4$] with an equimolar amount of Schiff base affords an *in situ* oxorhenium(V) intermediate. Subsequent addition of excess triethylphosphine produces the reduced and disubstituted *trans*-[Re(PEt$_3$)$_2$(Schiff base)]$^+$ product. Complexes were obtained in isolated yields of 59-85% after purification by silica gel chromatography. For the Schiff base ligands H$_2$sal$_2$en and H$_2$sal$_2$phen, the oxorhenium(V) intermediate adopts a *trans* configuration in which the chloro group is situated *trans* with respect to the oxo group.[72, 133, 134]

Scheme 4.3 Synthesis of Re(III) Q compounds **20-23.**

The oxorhenium(V) intermediates with the ligands H$_2$sal$_2$ipn, H$_2$sal$_2$ppa-Bn and H$_2$sal$_2$bza-Bn were not isolated and have not been previously reported. Given the rigidity of H$_2$sal$_2$bza-Bn, the *in situ* ReOCl(sal$_2$bza-Bn) intermediate likely adopts a *trans* coordination. The structural similarity of H$_2$sal$_2$ipn and H$_2$sal$_2$ppa-Bn to H$_2$sal$_2$ibn suggests these ligands will form oxorhenium(V) intermediates with *cis* coordination as observed for *cis*-ReOCl(sal$_2$ibn).[69, 71]

The N$_2$O$_2$ Schiff base ligand H$_2$sal$_2$phen has been previously investigated for the formation of Re(III) Q-compounds. The complex *trans*-[Re(PPh$_3$)$_2$(sal$_2$phen)]Cl, **22**, was reported in 10% yield from the reaction of PPh$_3$ with *trans*-ReOCl(sal$_2$phen) in refluxing ethanol.[72] The formation of *trans*-[Re(PPh$_3$)$_2$(sal$_2$phen)]Cl suffered from low isolated yields and complex purification procedures. The isolation of *trans*-[Re(PEt$_3$)$_2$(sal$_2$phen)]Cl in 80% isolated yield highlights the advantage of using microwave assisted synthesis for the preparation of Re(III) Q-compounds.

The oxorhenium(V) complex *cis*-[ReO(PEt$_3$)(sal$_2$ppa-Bn)]Cl, **24**, was prepared by a two-step procedure similar to that used for the Re(III) species **20-23** (**Scheme 4.4**). One molar equivalent of triethylphosphine was used to ensure the formation of the monophosphine product. Complex **24** was used alongside the Re(III) complex **21** as a nonradioactive HPLC standard to evaluate the degradiation of [^{99m}Tc]**21** (*vide infra*).
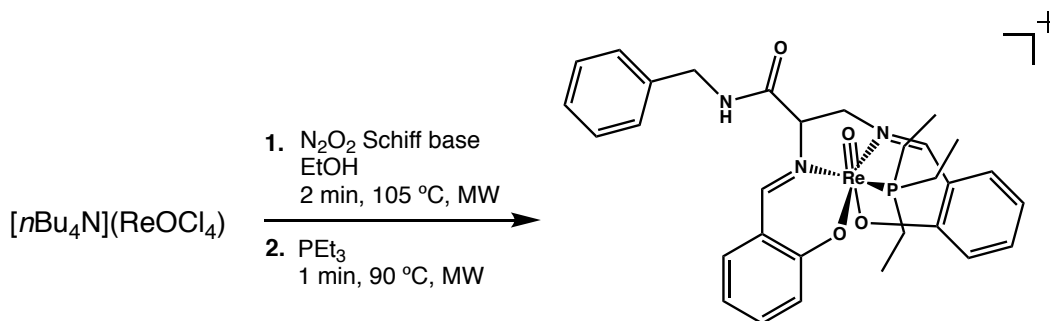
Scheme 4.4. Synthesis of *cis*-[ReO(PEt$_3$)(sal$_2$ppa-Bn)]Cl, **24**.

Electrochemistry

The rhenium complexes **20-23** were evaluated by cyclic voltammetry for comparison with previously reported Tc(III) and Re(III) species, which are known to exhibit chemically reversible M(III)/M(II) and M(III)/M(IV) redox couples. Technetium Q-compounds are lipophilic, cationic compounds. Their efficacy towards myocardial perfusion imaging and MDR tumor imaging depends on their overall cationic charge.

Reduction of cationic $[Tc^{III}(PR_3)_2(L)]^+$ complexes produces neutral $[Tc^{II}(PR_3)_2(L)]$ species. Electrochemical stability against *in vivo* reduction is imperative for the use of Tc(III) Q-compounds as imaging agents for myocardial perfusion and MDR tumors. While the use of Q-compounds as bifunctional agents for peptide-based radiopharmaceuticals does not depend on their cationic charge, electrochemical stability against *in vivo* reduction remains important. Changes to the overall charge of a radiometal chelate can potentially change the pharmacological properties of radiolabelled peptides.

Table 4.1. Formal potential values for compound **10** and **20-23.**

complex	III/II	III/IV	$\Delta E^{\circ\prime}$
$[Re(PEt_3)_2(sal_2en)]^+$, **10**	-1.017	0.359	1.376
$[Re(PEt_3)_2(sal_2ipn)]^+$, **20**	-0.931	0.458	1.389
$[Re(PEt_3)_2(sal_2ppa-Bn)]^+$, **21**	-0.918	0.479	1.379
$[Re(PEt_3)_2(sal_2phen)]^+$, **22**	-0.855	0.505	1.360
$[Re(PEt_3)_2(sal_2bza-Bn)]^+$, **23**	-0.812	0.528	1.340

[a]Conditions: Cyclic voltammetry in propylene carbonate, 0.1 M TEAP; glassy-carbon working electrode; Ag/AgCl reference electrode; Pt wire auxiliary electrode. [b]$E^{\circ\prime}$ is vs Ag/AgCl (3M NaCl).

Complexes **20-23** each contain a Re(III) metal center coordinated to two triethylphosphine (PEt$_3$) ligands and a tetradentate Schiff base. All of the Re(III) species exhibited the expected chemically reversible Re(IV)/Re(III) and Re(III)/Re(II) redox couples (**Table 4.1**). The Re(III) complexes containing better π-accepting Schiff base ligands are easier to reduce and harder to oxidize. Of the complexes investigated, *trans*-$[Re(PEt_3)_2(sal_2bza-Bn)]^+$ was the easiest to reduce and the most difficult to oxidize. Schiff base ligands with phenylene-type backbones (i.e., sal$_2$phen and sal$_2$bza-Bn) appear to provide the maximum amount of π-electron delocalization in these systems.
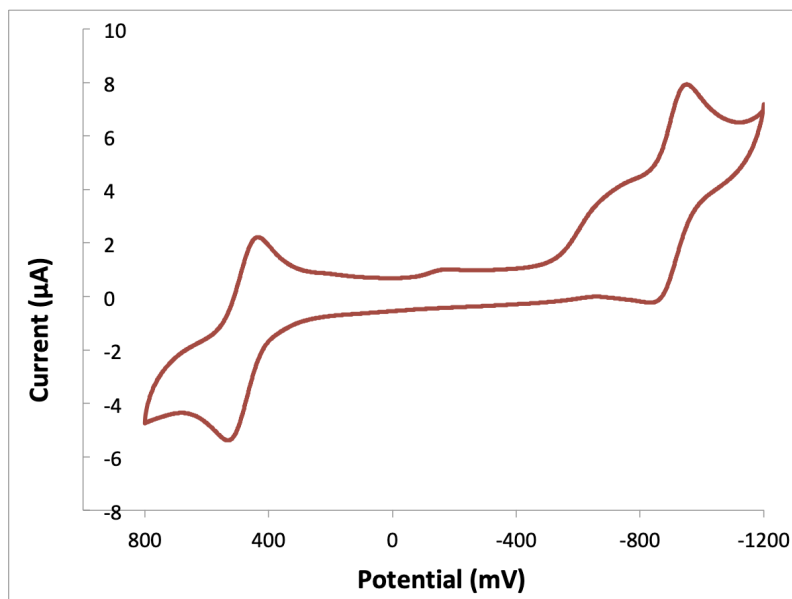
Figure 4.3. Cyclic voltammogram of *trans*-[Re(PEt$_3$)$_2$(sal$_2$ppa-Bn)]$^+$, **21.**

X-ray crystal structures

The rhenium complexes **20** (**Figure 4.4**) and **21** (**Figure 4.5**) were characterized by SCXRD. Each complex exhibits distorted octahedral geometry about the rhenium center. The N$_2$O$_2$ Schiff base ligand occupies the equatorial plane, while the two tertiary phosphine ligands are coordinated *trans* to each other. Space group, lattice parameters, and data collection information are given in **Table 4.2**. Relevant bond lengths and angles are given in **Table 4.3**.

The crystal structure of **20** indicates that approximately 5% of the molecules correspond to the isoelectronic oxorhenium(V) complex, *cis*-[ReO(PEt$_3$)(sal$_2$ipn)]PF$_6$, where one of the triethylphosphine ligands has been replaced with an oxo ligand. Whereas the Re(III) ion is effectively perfectly coplanar with the equatorial atoms, the alternate Re(V) atoms are either above or below the plane of the ligand, a form of disorder observed in other Re(V) and Tc(V) complexes.[70] The sal$_2$ipn ligand is disordered

with the methyl group situated on each carbon atom. This disorder is via 180° rotation, so the chirality of the ligand is fixed. The methyl substituent adopts a pseudo-equatorial orientation with respect to the central P-Re-P axis. All bond angles about the metal center lie within the expected range with the angles for the *cis* and *trans* ligands at 82.1-98.6° and 170.70-171.8°, respectively. All Re-O (2.006-2.017 Å) and Re-N (2.017-2.042 Å) bond distances fall within expected ranges for similar complexes. The Re-P bond distances (2.471(2) and 2.473(2) Å) are similar to other Re(III) bis-(phosphine) species and show that the metal center lies equidistant to each phosphine.[69-71, 73]

The crystal structure of **21** contains a Re(III)-sal$_2$ppa-Bn complex cation balanced by an [ReO$_4$]$^-$ anion. Complex **21** is octahedrally coordinated with the two triethylphosphine ligands coordinated *trans* to each other and the sal$_2$ppa-Bn ligand occupying the equatorial plane. The structure packs by forming hydrogen-bonded clusters composed of a racemic pair of two cations linked by two [ReO$_4$]$^-$ anions around a center of symmetry. These clusters interact through an assortment of weaker hydrogen bonds between C-H groups and aromatic π-rings or carbonyl oxygen atoms. All Re-O (2.001-2.003 Å) and Re-N (2.045-2.051 Å) bond distances fall within the expected ranges for similar compounds. The Re-P bond distances (2.462(3) and 2.470(3) Å) are similar to other Re(III) bis-phosphine species.[69-73] Whereas the P-Re bond lengths in **20** are statistically identical (Δ = 0.002(2) Å), the P-Re bond lengths of **21** display a much larger difference (Δ = 0.008(3) Å). This could be due to the influence of the sterically encumbering propanamide backbone.

**Table 4.2** X-ray crystal data, data collection parameters, and refinement parameters for **20** and **21**

	20	21
formula	$C_{29}H_{46}F_6N_2O_2P_3Re$	$C_{36}H_{51}N_3O_7P_2Re_2$
fw	847.79	1072.13
cryst system	Monoclinic	Orthorhombic
space group	$P2_1/c$	Pbca
a (Å)	10.5553(8)	20.167(1)
b (Å)	15.834(1)	18.894(1)
c (Å)	20.257(1)	20.231 (1)
α (deg)	90	90
β (deg)	98.057(3)	90
γ (deg)	90	90
V (Å^3)	3352.1(4)	7708.7(8)
Z	4	8
ρ (g/cm^3)	1.680	1.848
T (K)	100	100
μ (mm^{-1})	3.831	6.409
λ souce (Å)	0.71073	0.71073
R(F)^a	0.0470	0.0627
Rw(F)^2	0.1053	0.1133
GoF	1.078	1.115

Table 4.3 Select bond lengths (Å) and angles (°) for **20** and **21.**

	20	21
Re(1)-O(1)	2.006(4)	2.003(7)
Re(1)-O(2)	2.017(4)	2.001(7)
Re(1)-N(1)	2.042(5)	2.045(8)
Re(1)-N(2)	2.031(5)	2.051(8)
Re(1)-P(1)	2.471(2)	2.462(3)
Re(1)-P(2)	2.473(2)	2.470(3)
O(1)-Re(1)-O(2)	98.6(2)	102.4(3)
O(1)-Re(1)-N(1)	89.6(2)	88.5(3)
O(2)-Re(1)-N(1)	171.8(2)	168.7(3)
O(1)-Re(1)-N(2)	171.6(2)	168.8(3)
O(2)-Re(1)-N(2)	89.8(2)	88.1(3)
N(1)-Re(1)-N(2)	82.1(2)	81.4(3)
N(2)-Re(1)-P(2)	95.0(2)	90.9(2)
N(1)-Re(1)-P(2)	92.1(2)	94.4(2)
O(1)-Re(1)-P(2)	85.5(2)	85.1(3)
O(2)-Re(1)-P(2)	88.3(1)	89.8(2)
N(2)-Re(1)-P(1)	93.2(2)	97.7(2)
N(1)-Re(1)-P(1)	93.4(2)	91.8(2)
O(1)-Re(1)-P(1)	87.1(2)	87.3(3)
O(2)-Re(1)-P(1)	87.4(1)	85.7(2)
P(1)-Re(1)-P(2)	170.70(6)	170.1(1)
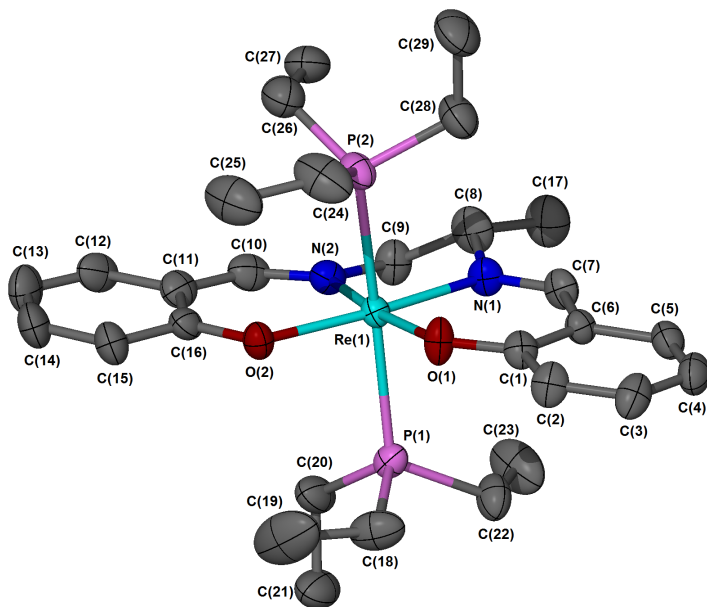
Figure 4.4 X-ray crystal structure of *trans*-[Re(PEt₃)₂(sal₂ipn)]PF₆, **20**, with 50% probability thermal ellipsoids.
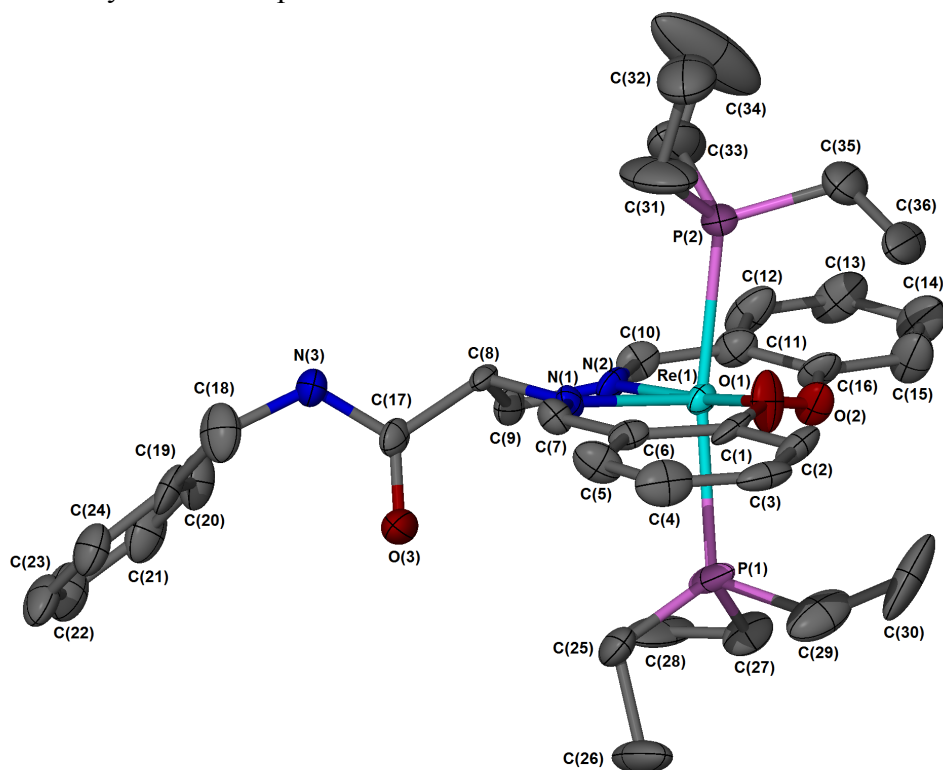

Figure 4.5 X-ray crystal structure of *trans*-[Re(PEt₃)₂(sal₂ppa-Bn)]ReO₄, **21**, with 50% probability thermal ellipsoids.

Technetium-99m radiolabelling

The ^{99m}Tc complexes [^{99m}Tc]**20-23** were prepared by a two-step (one-pot) synthesis (**Scheme 4.5**) adapted from previously reported procedures.[38] Radiochemical yields ranged from 70-90% using non-optimized conditions. The identity of the ^{99m}Tc complexes was confirmed by HPLC comparison with the well characterized Re analogues using parallel radiometric and photometric detection (**Table 4.4**). The rhenium complexes consistently show earlier retention times (0.3-0.6 min) than their analogous ^{99m}Tc complexes. This is a result of the relative positions of the photometric and radiometric detectors in the HPLC system. **Figure 4.6** displays a comparison of the HPLC chromatograms for [^{99m}Tc]**21** (t_R = 18.48 min) and [Re]**21** (t_R = 18.13 min). The nearly identical chromatographic profiles of the [^{99m}Tc]**21** and [Re]**21** complexes indicate that the two species are chemically analogous. Using this method, all of the ^{99m}Tc complexes [^{99m}Tc]**20-23** were found to be analogous to their Re congeners [Re]**20-23**.

A preliminary assessment of the stability of the ^{99m}Tc complexes over time in aqueous solution was performed after HPLC purification, with the ^{99m}Tc complexes incubated in HPLC eluent (70-80% MeCN in H_2O). The radiochemical purity of each complex was reassessed by HPLC following one, four, and twenty-four hours of incubation times. The complex [^{99m}Tc][Tc(PEt$_3$)$_2$(sal$_2$en)]$^+$, [^{99m}Tc]**10**, was included as a positive control in the stability study. All of the ^{99m}Tc Q-compounds evaluated for myocardial perfusion and MDR tumor imaging used Schiff base ligands with sterically unencumbering ethylene backbones. The complex [^{99m}Tc][Tc(PEt$_3$)$_2$(sal$_2$en)]$^+$, [^{99m}Tc]**10**, was observed to be stable at all time points measured (**Figure 4.7**). There was no indication of oxidation to any oxotechnetium(V) species or [^{99m}Tc]TcO$_4^-$.
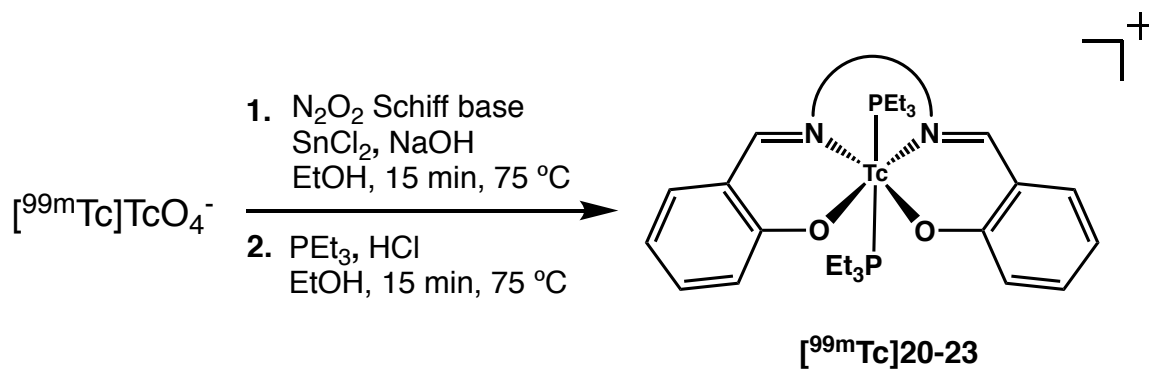
Scheme 4.5. Synthesis of [^{99m}Tc]**20-23**.

Table 4.4. HPLC retention times (t_R) for the Re and ^{99m}Tc complexes

complex	t_R (min)	
	[Re]	[^{99m}Tc]
[M(PEt$_3$)$_2$(sal$_2$en)]$^+$, **10**	15.81	16.45
[M(PEt$_3$)$_2$(sal$_2$ipn)]$^+$, **20**	16.74	17.15
[M(PEt$_3$)$_2$(sal$_2$ppa-Bn)]$^+$, **21**	18.13	18.48
[M(PEt$_3$)$_2$(sal$_2$phen)]$^+$, **22**	16.15	16.73
[M(PEt$_3$)$_2$(sal$_2$bza-Bn)]$^+$, **23**	16.24	16.83
[MO(PEt$_3$)$_2$(sal$_2$ppa-Bn]$^+$, 24	7.94	8.56
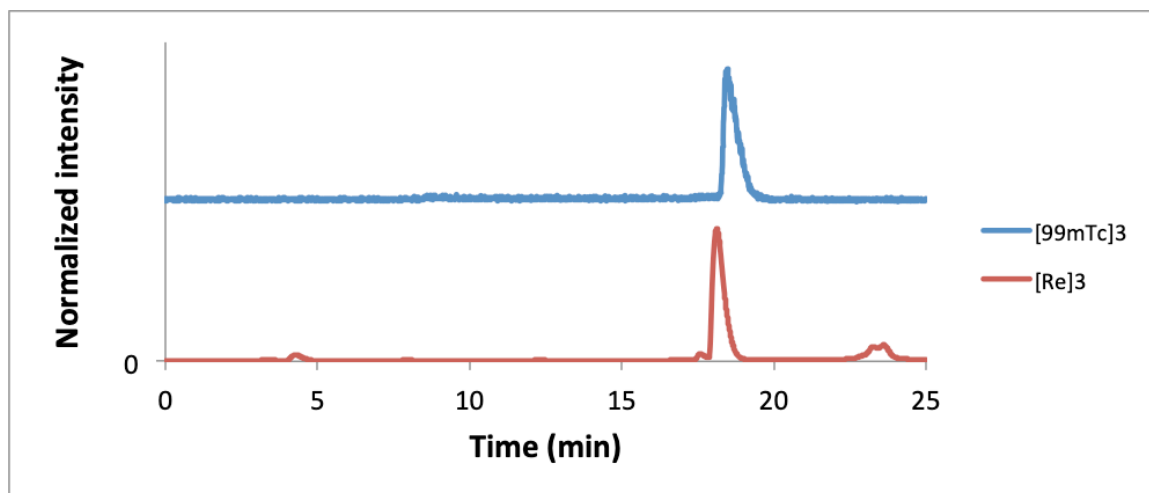
Figure 4.6. Overlay of HPLC chromatogram of [^{99m}Tc][Tc(PEt$_3$)$_2$(sal$_2$ppa-Bn)]$^+$ ([^{99m}Tc]**21**; t_R = 18.48 min) and *trans*-[Re(PEt$_3$)$_2$(sal$_2$ppa-Bn)]$^+$ ([Re]**21**; t_R = 18.13 min).

The complex $[^{99m}Tc][Tc(PEt_3)_2(sal_2ppa\text{-}Bn)]^+$, $[^{99m}Tc]\textbf{21}$, incorporating the bifunctinoal model ligand sal$_2$ppa-Bn, was observed to degrade over time (**Figure 4.8**). The radiochemical purity of $[^{99m}Tc]\textbf{21}$ (t_R = 18.48 min) was 94% after one hour and 70% after four hours. After 24 hours of incubation, radiochemical purity of $[^{99m}Tc]\textbf{3}$ was only 9%. A single new peak was observed to grow in at 8.56 minutes. The radiometric HPLC chromatogram of $[^{99m}Tc]\textbf{21}$ after four hours of incubation was compared to the photometric chromatograms for [Re]**21** and *cis*-$[ReO(PEt_3)(sal_2ppa\text{-}Bn)]^+$ ([Re]**24**, t_R = 7.94 min) (**Figure 4.9**). The similar retention times for [Re]**24** and the new ^{99m}Tc species (t_R = 8.56 min) suggest that the two complexes are chemically analogous. Thus, the radiometric peak at 8.56 minutes likely represents $[^{99m}Tc][TcO(PEt_3)(sal_2ppa\text{-}Bn)]^+$ ($[^{99m}Tc]\textbf{24}$). The conversion of $[^{99m}Tc]\textbf{21}$ to $[^{99m}Tc]\textbf{24}$ mirrors the conversion of $[^{99m}Tc][Tc(PEt_3)_2(sal_2ibn)]^+$ to $[^{99m}Tc][TcO(PEt_3)(sal_2ibn)]^+$ observed in Chapter 3. Formation of $[^{99m}Tc]\textbf{24}$ occurs *via* a process involving ligand dissociation, rearrangement of the Schiff base, and oxidation of the metal center. Despite the near complete conversion of $[^{99m}Tc]\textbf{21}$ to $[^{99m}Tc]\textbf{24}$, there was no observed formation of $[^{99m}Tc]TcO_4^-$ (t_R = 4.50 min) All of the ^{99m}Tc remained coordinated by sal$_2$ppa-Bn throughout the stability study. The instability of $[^{99m}Tc]\textbf{21}$ indicates that the use of a propanamide linker is a poor strategy for incorporation of targeting biomolecules into Q-complexes. Given the electrochemical similarity of [Re]**10** and [Re]**21** (**Table 4.4**), the instability of $[^{99m}Tc]\textbf{21}$ compared to $[^{99m}Tc]\textbf{10}$ is likely driven by steric rather than electronic factors.
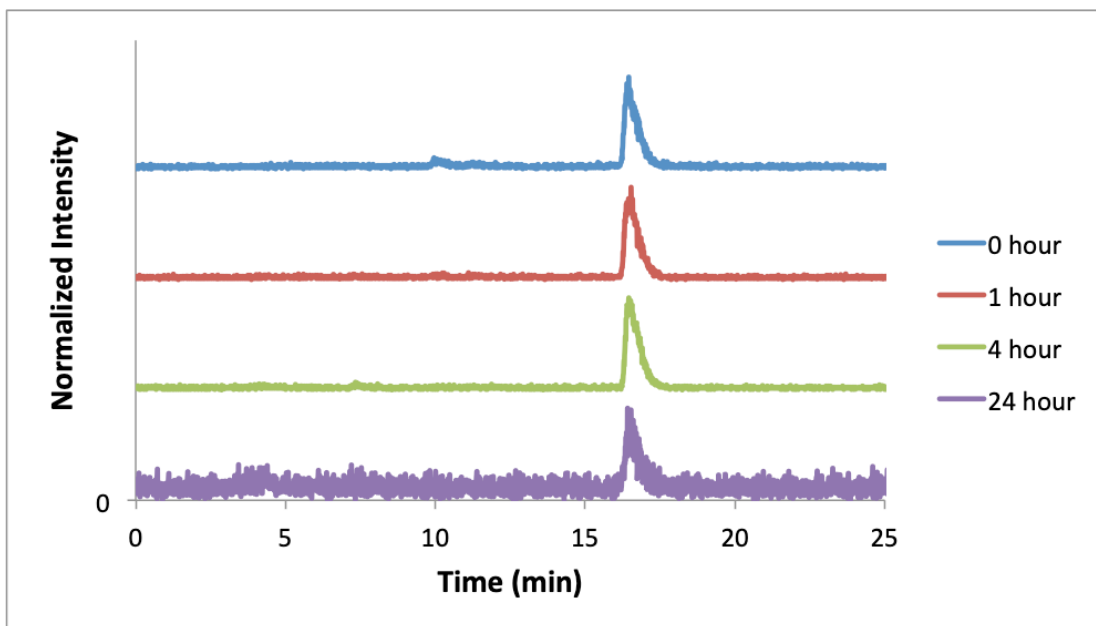
Figure 4.7 Overlay HPLC chromatograph of [^{99m}Tc][Tc(PEt$_3$)$_2$(sal$_2$en)]$^+$, [^{99m}Tc]**10**, stability at 0, 1, 4, and 24 hours.
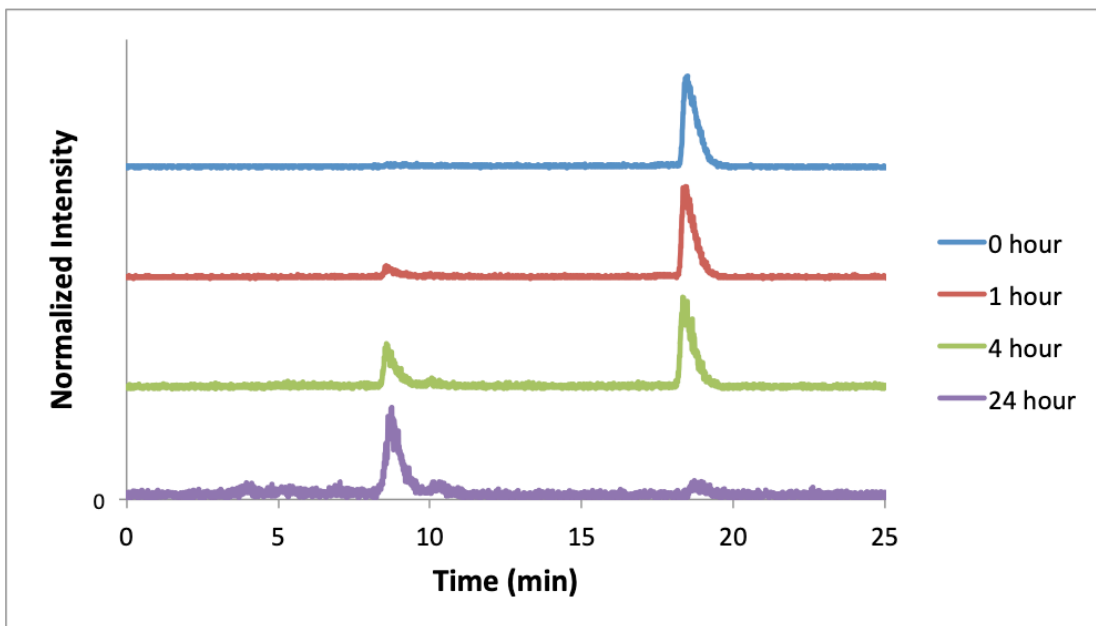
Figure 4.8 Overlay HPLC chromatograph of [^{99m}Tc][Tc(PEt$_3$)$_2$(sal$_2$ppa-Bn)]$^+$, [^{99m}Tc]**21**, stability at 0, 1, 4, and 24 hours.
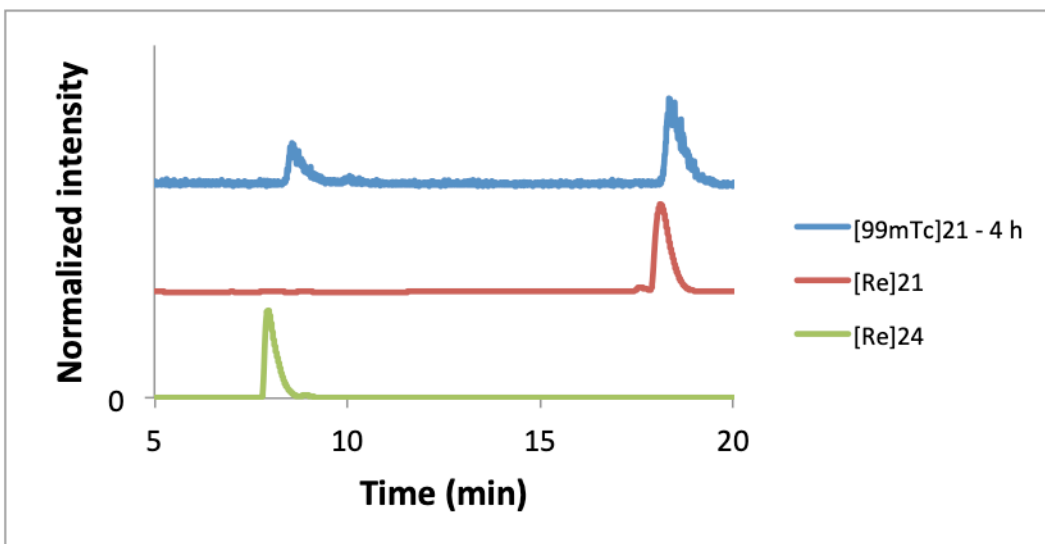
Figure 4.9 Overlay HPLC comparison of the Re-sal$_2$ppa-Bn complexes **21** (red, t_R = 18.13 min) and **24** (green, t_R = 7.94 min) with [^{99m}Tc]**21** (blue, t_R = 8.56 min, 18.48 min) after 4 hours of incubation.

One potential strategy to reduce the steric-driven instability in ^{99m}Tc Q-complexes is to lengthen the linker such that the amide moiety is situated further from the metal center. The use of a pentanamide linker (**Figure 4.1**) would accomplish this by inserting two carbon atoms between the Schiff base backbone and the amide moiety. In order to further evaluate the steric factors governing the stability of functionalized ^{99m}Tc Q-complexes, the complex [^{99m}Tc][Tc(PEt$_3$)$_2$(sal$_2$ipn)]$^+$, [^{99m}Tc]**20**, was included in the stability study. The methyl substituent of sal$_2$ipn represents the smallest unit of steric bulk that can be added to the N$_2$O$_2$ Schiff base backbone. [^{99m}Tc]**20** (t_r = 17.17 min) was observed to degrade over time. The radiochemical purity was 92% after four hours and 56% after 24 hours (**Figure 4.10**). A single new peak was observed with a retention time of 7.87 minutes. The new ^{99m}Tc peak was not definitively identified by comparison to a known Re complex, however, the similarity of the stability chromatograms for [^{99m}Tc]**20** and [^{99m}Tc]**21** suggest the two complexes are degrading through the same process. The

new peak at 7.87 minutes likely corresponds to $[^{99m}Tc][TcO(PEt_3)(sal_2ipn)]^+$, in which one of the triethylphosphine ligands has dissociated from the metal center and the Tc(III) core has been oxidized to Tc(V). The instability of $[^{99m}Tc]$**20** indicates that even small backbone substituents reduce the stability of ^{99m}Tc Q-complexes.

A model Schiff base ligand incorporating a pentanamide linker was not assessed in this study, however, the results with $[^{99m}Tc]$**20** suggest that a pentanamide linker would yield a similarly unstable complex. Even though the methyl substituent of sal$_2$ipn is relatively small, the flexibility of the isopropylene backbone allows the methyl substituent to interact with the triethylphosphine ligands bound to the metal center. A pentanamide linker would be just as flexible as the isopropylene backbone of sal$_2$ipn. The added steric bulk of a pentanamide linker compared to an isopropylene backbone (sal$_2$ipn) would likely render a pentanamide complex less stable than an analogous sal$_2$ipn complex.

The use of a benzamide linker proved to be an attractive alternative to propanamide or pentanamide linkers for bifunctional ^{99m}Tc Q-complexes. A benzamide linker inserts two carbon atoms between the Schiff base backbone and the amide moiety, similar to a pentanamide linker. The rigidity of the benzamide linker, in contrast to the flexibility of a pentanamide linker, reduces steric interaction between backbone substituents and the triethylphosphine ligands attached to the metal center.

The complex $[^{99m}Tc][Tc(PEt_3)_2(sal_2phen)]^+$, $[^{99m}Tc]$**22**, was evaluated as a baseline to evaluate the impact of a rigid backbone on ^{99m}Tc Q-complex stability without an appended substituent. No degradation was observed after one or four hours of incubation (**Figure 4.11**). The radiochemical purity of $[^{99m}Tc]$**22** (t_r = 16.73 min) after 24

hours was 86%. A new peak was observed after 24 hours with a retention time of 8.28 minutes. Based on the similarity of the stability chromatograms for [^{99m}Tc]**22** (**Figure 4.11**) and [^{99m}Tc]**21** (**Figure 4.8**), the two complexes are likely degrading through the same process. This suggests the new peak at 8.28 minutes corresponds to [^{99m}Tc][TcO(PEt$_3$)(sal$_2$phen)]$^+$, in which one of the triethylphosphine ligands has dissociated from the metal center and the Tc(III) core has been oxidized to Tc(V). The slight instability of [^{99m}Tc]**22** compared to [^{99m}Tc]**10** shows that the phenylene backbone (sal$_2$phen) does result in a decrease in ^{99m}Tc Q-complex stability. The rigidity of the phenylene backbone does not fully eliminate steric-induced instability.
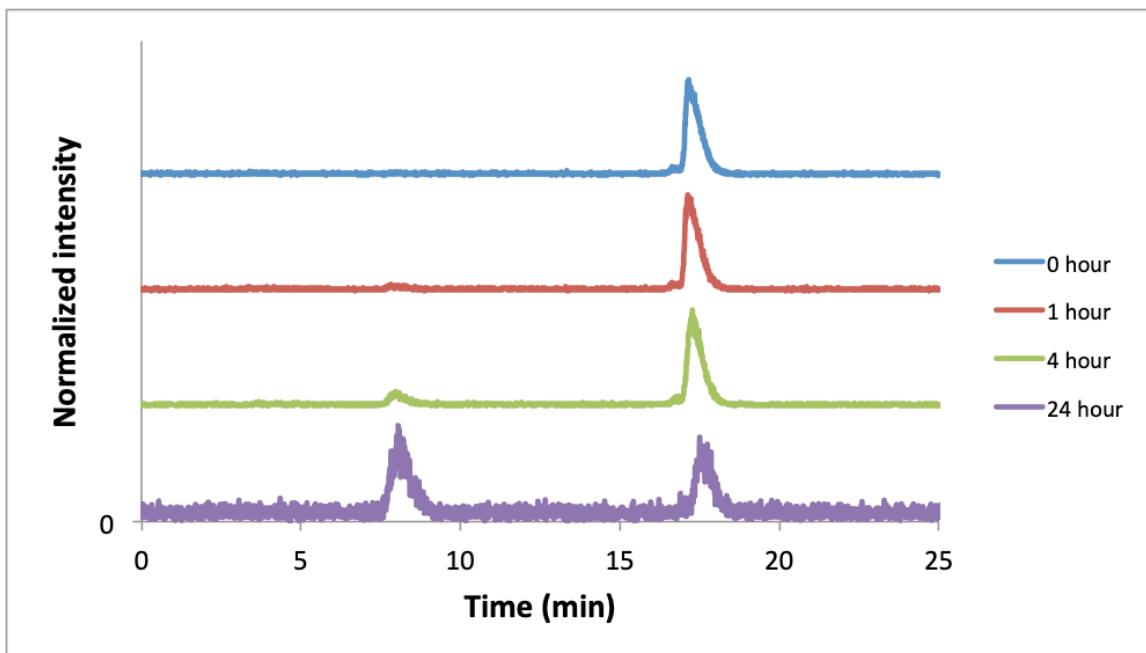
Figure 4.10 Overlay HPLC chromatograph of [^{99m}Tc][Tc(PEt$_3$)$_2$(sal$_2$ipn)]$^+$, [^{99m}Tc]**20**, stability at 0, 1, 4, and 24 hours.
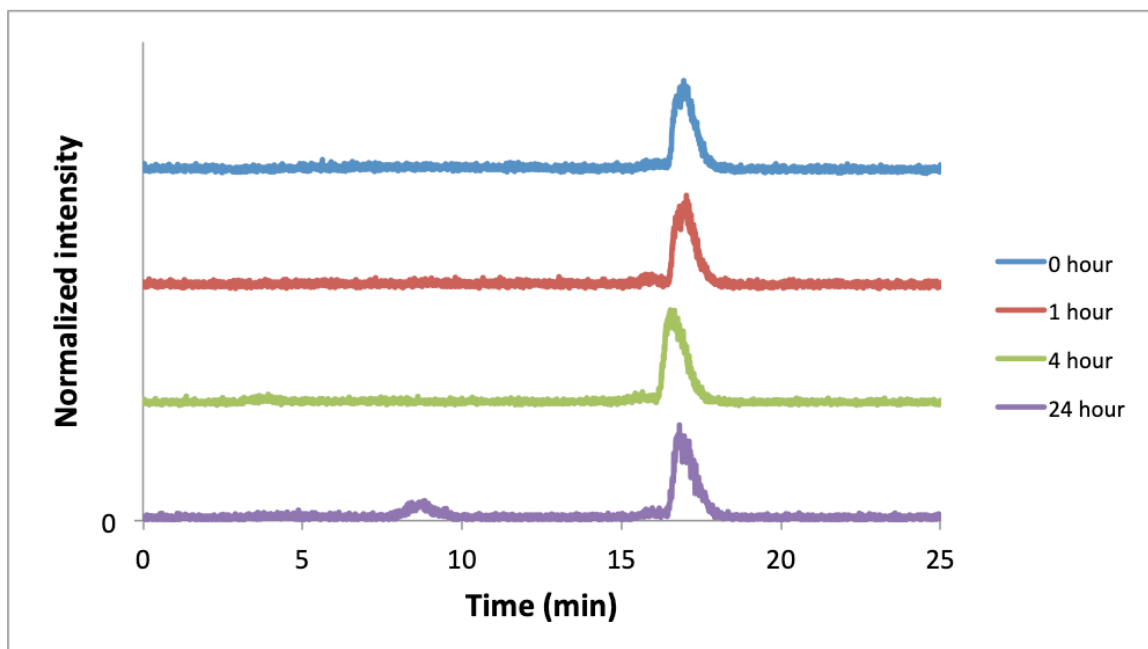
Figure 4.11 Overlay HPLC chromatograph of $[^{99m}Tc][Tc(PEt_3)_2(sal_2phen)]^+$, $[^{99m}Tc]$**22**, stability at 0, 1, 4, and 24 hours.
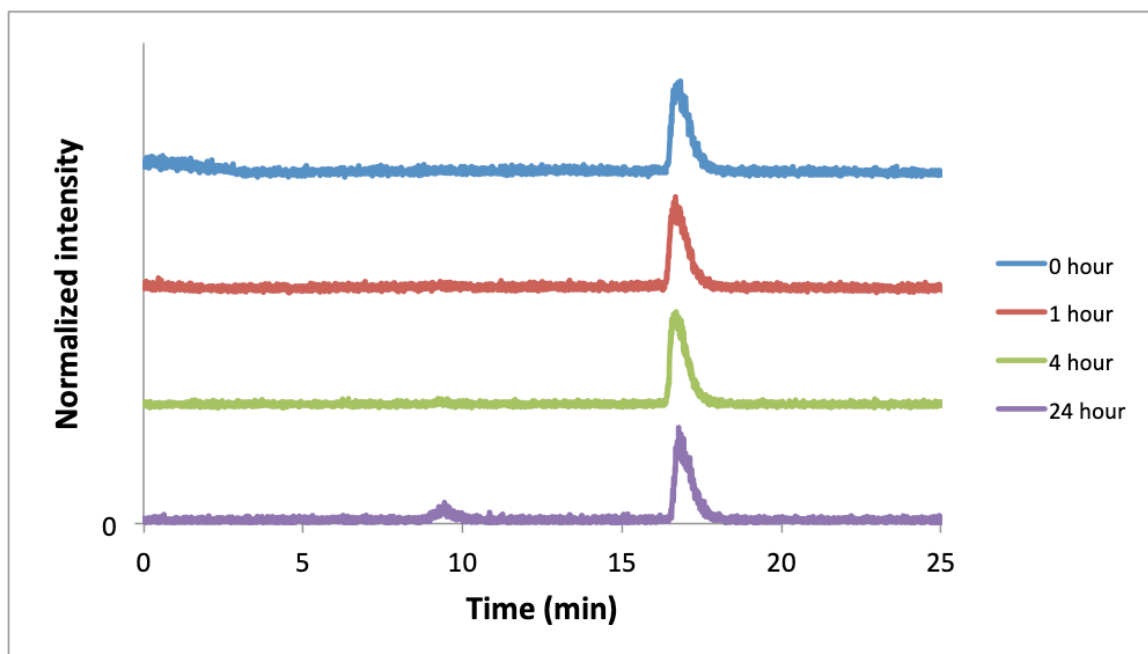
Figure 4.12 Overlay HPLC chromatograph of $[^{99m}Tc][Tc(PEt_3)_2(sal_2bza-Bn)]^+$, $[^{99m}Tc]$**23**, stability at 0, 1, 4, and 24 hours.

The complex $[^{99m}Tc][Tc(PEt_3)_2(sal_2bza-Bn)]^+$, $[^{99m}Tc]$**23**, incorporating the bifunctional model ligand sal$_2$bza-Bn, exhibited remarkable stability in solution (**Figure 4.12**). The radiochemical purity of $[^{99m}Tc]$**23** (t_r = 16.73 min) was 98% after four hours and 88% after 24 hours. A single new peak was observed to grow in at 9.08 minutes. The radiometric chromatogram for $[^{99m}Tc]$**23** parallels that of the other radiolabelled complexes. The new peak observed at 9.08 minutes likely corresponds to $[^{99m}Tc][TcO(PEt_3)(sal_2bza-Bn)]^+$. The sal$_2$bza-Bn ligand is bulkier than the sal$_2$phen ligand due to the presence of the *N*-benzyl moiety. If the stability of functionalized ^{99m}Tc Q-complexes were solely determined by the bulk of backbone substituents, $[^{99m}Tc]$**23** would be expected to be less stable than $[^{99m}Tc]$**22**. However, $[^{99m}Tc]$**23** and $[^{99m}Tc]$**22** display equivalent stability under the measured conditions. The added steric bulk of the sal$_2$bza-Bn ligand compared to the sal$_2$phen ligand had no effect on the stability of their respective ^{99m}Tc Q-complexes. The rigidity and spacing of the benzamide linker in $[^{99m}Tc]$**23** appears to situate the appended benzyl moiety in a way that minimizes steric interaction with the triethylphosphine ligands attached to the metal center. It remains to be seen whether this observation holds true when larger substituents are incorporated into the benzamide linker. Further investigation is needed in order to assess the efficacy of benzamide linkers for the inclusion of targeting biomolecules into potential bifunctional ^{99m}Tc Q-complexes.

4.4 Conclusions

Mixed-ligand complexes of the type *trans*-$[M(PEt_3)_2(Schiff\ base)]^+$ (M = Re, ^{99m}Tc) were prepared using a series of salicylaldehyde-based Schiff base ligands. The substituents on the Schiff base ligand backbone were varied in order to assess the

influence of backbone functionalization on the formation and stability of these complexes. The model bifunctional Schiff base ligands H_2sal_2ppa-Bn and H_2sal_2bza-Bn were prepared in order to investigate strategies for incorporation of targeting vectors into Schiff base ligand backbones. The *trans*-[Re(PEt_3)_2(Schiff base)]$^+$ complexes **20-23** were synthesized in high yield by microwave-assisted synthesis. The analogous ^{99m}Tc complexes [^{99m}Tc]**20-23** were prepared at no-carrier-added levels in high radiochemical yields. The stability of the ^{99m}Tc complexes over time was assessed in aqueous solution. [^{99m}Tc]**10**, incorporating the non-functionalized Schiff base ligand sal_2en, was observed to be stable over all time points measured. The bifunctional model complex [^{99m}Tc]**21**, incorporating a propanamide linker in the ligand backbone, was observed to oxidize to [^{99m}Tc]**24** over time. In contrast, the bifunctional model complex [^{99m}Tc]**23**, incorporating a benzamide linker in the ligand backbone, displayed superior stability with a radiochemical purity of 98% after four hours and 88% after 24 hours. There was no indication of [^{99m}Tc]TcO$_4^-$ formation for any of the ^{99m}Tc complexes evaluated.

Tetradentate Schiff base ligands facilitate facile modification in order to fine-tune the pharmacological properties of their metal complexes or conjugate to targeting biomolecules. Mixed-ligand ^{99m}Tc complexes with tetradentate Schiff base ligands are easily prepared in high radiochemical yields. Preliminary results with model bifunctional Schiff base ligands indicate that the use of a benzamide linker in the ligand backbone allows for incorporation of targeting biomolecules while maintaining complex stability. Therefore, mixed-ligand technetium "Q-compounds" are proposed as a novel tool in the design of bifunctional ^{99m}Tc or $^{186}Re/^{188}Re$ radiopharmaceuticals.

CHAPTER 5

Conclusions

5.1 Summary

This dissertation has investigated the synthesis of rhenium and technetium Schiff base complexes for applications in nuclear medicine. Mixed-ligand technetium "Q-compounds", $[^{99m}Tc][Tc(PR_3)_2(Schiff\ base)]^+$, have been previously investigated as single photon emission computed tomography (SPECT) imaging agents for myocardial perfusion and multidrug resistant (MDR) tumors. The development of rhenium analogues to existing ^{99m}Tc Q-compounds has been an ongoing effort at the University of Missouri-Columbia. Rhenium Q-compounds have potential application as biomodulators for P-glycoprotein serving to enhance the quality of tumor imaging by ^{99m}Tc SPECT agents. Additionally, this work proposes Tc(III) and Re(III) Q-compounds as a novel platform for the design of bifunctional radiopharmaceuticals. Despite ongoing efforts to synthesize Re(III) Q-compounds, few examples have been reported. Syntheses of Re(III) Q-compounds have suffered from low-yields, long reaction times, and complex isolation procedures. This work addresses these issues by using microwave-assisted synthesis to develop a facile protocol for the synthesis of Re(III) Q-compounds.

In Chapter 2, a series of Re(III) complexes of the form $trans$-$[Re(PR_3)_2(tmf_2en)]^+$ were prepared by microwave assisted synthesis. A two-step (one-pot) procedure was utilized. In the first step, the Re(V) precursor $(nBu_4N)[ReOCl_4]$ is reacted with the Schiff base ligand forming $trans$-$[ReOCl(tmf_2en)$ $in\ situ$. In the second step, a tertiary phosphine ligand is added yielding the reduced $trans$-$[Re(PR_3)_2(tmf_2en)]^+$ species. The preparation of these Re(III)-tmf_2en complexes by microwave assisted synthesis resulted in higher

reaction yields and shorter reaction times compared to syntheses of similar Re(III) Q-complexes. A general methodology was developed, which could be used to synthesize Re(III) Q-compounds with a diverse range of Schiff base ligands and tertiary phosphines.

Chapter 3 investigated the steric influence of salicylaldehyde-based N_2O_2 Schiff base ligands on the formation and stability of Re(III) and Tc(III) Q-compounds. A series of Re(III) complexes of the form *trans*-[Re(PR$_3$)$_2$(L)]$^+$ were prepared with the Schiff base ligands sal$_2$en and sal$_2$ibn. Rhenium(III) complexes with the sterically unencumbering sal$_2$en ligand were observed to be stable in solution, while complexes with the sterically encumbering sal$_2$ibn ligand were observed to oxidize to isoelectronic oxorhenium(V) species. The conversion rate of the *trans*-[Re(PR$_3$)$_2$(sal$_2$ibn)]$^+$ species to their respective *cis*-[ReO(PR$_3$)(sal$_2$ibn)]$^+$ products increased as the steric bulk of the tertiary phosphine suggesting the conversion was sterically driven. The ^{99m}Tc compounds [^{99m}Tc][Tc(PEt$_3$)$_2$(sa$_2$len)]$^+$ and [^{99m}Tc][Tc(PEt$_3$)$_2$(sa$_2$libn)]$^+$ were prepared for an assessment of their stability in aqueous solution. The [^{99m}Tc][Tc(PEt$_3$)$_2$(sa$_2$len)]$^+$ species were stable in solution. The [^{99m}Tc][Tc(PEt$_3$)$_2$(sa$_2$libn)]$^+$ species underwent rapid degradation in solution. The degradation product was identified as [^{99m}Tc][TcO(PEt$_3$)(sal$_2$ibn)]$^+$ indicating that conversion of the ^{99m}Tc(III)-sal$_2$ibn species mirrored that of the Re(III)-sal$_2$ibn species.

Chapter 4 examined the formation and stability of Q-complexes with model bifunctional Schiff base ligands. A series of backbone-functionalized Schiff base ligands was used to prepare Re(III) complexes of the form *trans*-[Re(PEt$_3$)$_2$(L)]$^+$ in order to assess strategies for incorporating biomolecules into Q-complexes. The two primary strategies under investigation for biomolecule incorporation were the use of propanamide

linkers or benzamide linkers in the Schiff base backbone. The ^{99m}Tc(III) compounds [^{99m}Tc][Tc(PEt$_3$)$_2$(L)]$^+$ were prepared for comparison with their Re(III) analogues. A preliminary stability study of the various ^{99m}Tc(III) complexes was performed in aqueous solution. Technetium-99m complexes with the flexible propanamide linker were observed to oxidize in solution, whereas ^{99m}Tc complexes with the rigid benzamide linker displayed superior stability in solution. Rhenium and technetium Q-compounds incorporating benzamide-linked targeting biomolecules are proposed as a novel class of bifunctional radiopharmaceuticals.

5.2 Future Outlook

The results reported herein indicate mixed-ligand Q-complexes of the form *trans*-[M(PR$_3$)$_2$(L)]$^+$ (M = Tc, Re) may have application as a ligand framework for bifunctional radiopharmaceuticals. The use of Q-complexes for potential peptide-based radiopharmaceuticals represents a significant change in application for these complexes. Technetium-99m Q-complexes were originally developed as small molecules for myocardial perfusion imaging and multidrug resistant tumor imaging. The cationic and lipophilic nature of ^{99m}Tc Q-complexes made them ideally suited for such applications. The lipophilic nature of Q-complexes could be a potential problem for a bifunctional Q-series. Lipophilic radiopharmaceuticals tend to accumulate in the liver. Accumulation of radiopharmaceuticals in the liver can lead to poor image quality for diagnostic procedures due to high background. Large radiation doses to the liver can also cause radiation-induced liver disease. This is not an issue for the ^{99m}Tc Q-complexes as they have been shown to clear from the liver rapidly. Further, the radiation burden from ^{99m}Tc is only minor. The attachment of a large peptide to a Q-complex could adversely affect the

ability of bifunctional Q-complexes to clear from the liver. Future bifunctional Q-complexes incorporating peptides should utilize water-soluble phosphine ligands as a means of decreasing the overall lipophilicity of these complexes.

Another obstacle for the development of peptide-based bifunctional Q-complexes is synthesizing Schiff base ligands incorporating peptides. Peptides incorporating radiometal chelators are typically synthesized through solid-phase peptide-synthesis (SPPS). In this process, radiometal chelates are appended to the peptide in the penultimate step of SPPS prior to resin cleavage by trifluoroacetic acid. Schiff base ligands cannot be appended because they are subject to acid-catalyzed hydrolysis. Previous reports have shown a two-step approach can be used form peptide-linked Schiff base ligands (**Scheme 5.1**).[146] In the first step, a proto-peptide with a terminal diamine is synthesized through SPPS and then cleaved from the resin. In the second step, an aldehyde is reacted with the terminal diamine of the proto-peptide to form the Schiff base. Future development of peptide-based Q-complexes will need to optimize this process for incorporating peptides relevant to ^{99m}Tc and $^{186/188}$Re radiopharmaceuticals.
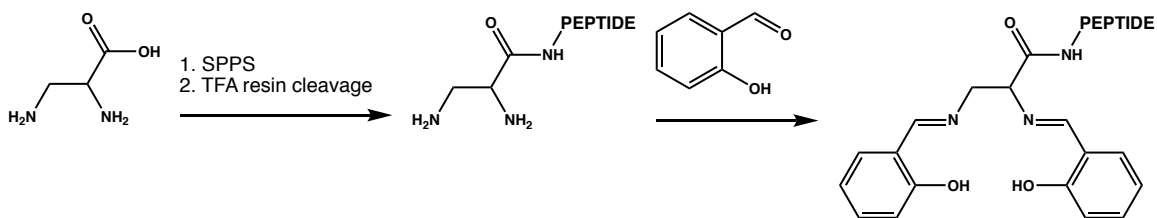
Scheme 5.1. Two-step approach for the formation of peptide-linked Schiff base ligands

The most significant challenge to the development of peptide-based bifunctional Q-complexes is the radiosynthesis of $^{186/188}$Re Q-complexes. Although [^{99m}Tc]Tc-furifosmin can be prepared in high yield from a one-step radiopharmaceutical, there have been no reports of $^{186/188}$Re Q-compounds. Future research will need to develop novel

methods for the synthesis of $^{186/188}$Re(III) Q-compounds. The ideal radiosynthesis would be a one-step kit formulation analogous to that developed for [^{99m}Tc]Tc-furifosmin. It remains to be seen whether such a formulation is possible. The radiosynthesis of $^{186/188}$Re radiopharmaceuticals is typically more difficult than that for analogous ^{99m}Tc radiopharmaceuticals. Rhenium is harder to reduce than technetium. Rhenium radiosyntheses typically require longer reaction times, higher temperatures, and greater amounts of reducing agents. Microwave assisted synthesis of $^{186/188}$Re Q-compounds could be one means of overcoming these challenges.

APPENDIX A

Supporting Information for CHAPTER 2

Synthesis of Rhenium Analogues to [^{99m}Tc]Tc-Furifosmin

A1. Structure details for compounds **1**, **3-6**, and **8**.

A2. ^{1}H-NMR spectra of compounds **1-8**.

A3. ^{1}H- and ^{13}C-NMR, and FT-IR spectral details, and x-ray crystal structures of compounds **A1** and **A2**.

A4. Cyclic voltammograms for compounds **2-5, 7** and **8.**

A1. *Structure details for compounds 1, 3-6, and 8*.

The crystal structures of **1** and **3-5** were solved by an iterative dual space algorithm as implemented in SHELXT.[1] The structure of **8** was solved by direct methods. Non-hydrogen atoms were located from the difference map and refined by full-matrix least squares refinement using SHELXL 2014[2] as implemented in Olex2.[3] Hydrogen atoms bonded to carbon atoms were placed in calculated positions, and their coordinates and thermal parameters were constrained to ride on the carrier atom. Hydrogen atoms on methyl groups were constrained to ideal angles but allowed to rotate about the C-C bond axis.

In the crystal structure of **1**, the metal complex was found to be disordered by two-fold rotation passing through the axis of symmetry of the ligand. Since the metal ion sits above this axis, it is disordered in two positions, and the Cl and O ligands are also disordered over positions that overlap heavily. These conformations were refined at 82% and 18% occupancies. The minor occupancy oxygen atom was refined isotropically as its thermal parameters were affected by its overlap with the major occupancy chlorine atom. The lattice diethyl ether molecule was also found to be disordered and was allowed to refine at full occupancy. The resulting large thermal parameters and unusual geometry reflect the fact that the positions are averaged over multiple conformations.

The crystal structure of **6** is disordered in a manner similar to **1.** However because of the V-shaped geometry of the ligand the coordinating oxygen atoms are also disordered. The occupancies of the two conformations were allowed to refine and converged to approximately 92% and 8%. The atoms in the minor conformation were refined isotropically. The large thermal ellipsoids associated with this disorder lead to an

unusually wide range of thermal parameters for this moiety. This is an artifact due to the difficulty of accurately refining thermal ellipsoids of partial occupancy light atoms that are near much heavier atoms and does not indicate any incorrect element assignments in this case. A diethyl ether molecule was found residing on a crystallographic center of inversion, located on the C-O bond. To model this, the three unique atom sites were modeled as a 50% occupancy -CH$_3$ group, a 100% occupancy -CH$_2$- group, and either an O or C atom at 50% occupancy each, constrained to occupy the same site and have the same thermal parameters. This model generates a false A-level CheckCIF alert where the two symmetry-related fragments are interpreted as an unrealistically close O-O intermolecular contact, when in fact that distance corresponds to a C-O bond 100% of the time.

The crystal structure of **8** was solved with three symmetry inequivalent formula units which are related by pseudo-translation. The structure can be solved in a unit cell with a *c* axis of 1/3 the length, but an attempt at anisotropic refinement of this solution results in non-positive definite thermal ellipsoids and anomalous difference map peaks. Furthermore, there are sets of peaks in the X-ray diffraction photographs that cannot be indexed to the smaller unit cell, which indicates that the misorientations of pseudo-translation related formula units are ordered. Two the of [PF$_6$]$^-$ ions were modeled as being disordered by rotation about one of the F-P-F axes, and one of the P(Et)$_3$ ligands was modeled as being disordered over two orientations related by rotation about the P-Tc bond axis. The residual difference map after locating all non-hydrogen atoms was too noisy to allow the location of hydrogen atoms for the lattice water molecules. The large ellipsoids of the water molecules indicate that they are likely also disordered over closely

143

overlapping positions, probably a consequence of the anion disorder. An anomalously large difference map peak is located next to one of the Tc ions, and the most disagreeable reflections are all systematically higher in intensity than F_c^2. These problems are likely consequences of systematic errors in the data caused by the pseudo-symmetric relationship of the heavy atoms and do not appear to indicate problems with the model.

References

1. Sheldrick, G. M. SHELXT – Integrated space-group and crystal-structure determination. *Acta Cryst. Sect. A. Found. Adv.* **2015**, *71*, 3-8.
2. Sheldrick, G. M. Crystal structure refinement with *SHELXL. Acta Cryst. Sect. C. Struct. Chem.* **2015**, *71*, 3-8.
3. Dolomanov, O.V.; Bourhis, L.J.; Gildea, R.J.; Howard, J.A.K.; Puschmann, H. OLEX2: A complete structure solution, refinement and analysis program. *J. Appl. Cryst.* **2009**, *42*, 339-341.

Table A1 Select bond lengths (Å) and angles (°) for *trans*-[Tc(PEt$_3$)$_2$(tmf$_2$en)]PF$_6$•H$_2$O, **8**•H$_2$O.

	8•H$_2$O		
	molecule a	molecule b	molecule c
Tc(1)-O(1)	2.032(2)	2.035(2)	2.0376(19)
Tc(1)-O(2)	2.0355(19)	2.036(2)	2.0367(19)
Tc(1)-N(1)	2.042(2)	2.042(2)	2.045(2)
Tc(1)-N(2)	2.041(2)	2.042(2)	2.039(2)
Tc(1)-P(1)	2.4901(8)	2.4887(8)	2.4883(9)
tc(1)-P(2)	2.4909(8)	2.4961(8)	2.4899(8)
O(1)-Tc(1)-O(2)	98.19(8)	98.75(8)	98.37(8)
O(1)-Tc(1)-N(1)	90.22(9)	89.72(9)	89.66(9)
O(2)-Tc(1)-N(1)	171.11(9)	171.04(9)	171.73(9)
O(1)-Tc(1)-N(2)	171.41(9)	170.75(9)	170.98(9)
O(2)-Tc(1)-N(2)	89.86(9)	90.09(9)	90.24(9)
N(1)-Tc(1)-N(2)	81.90(10)	81.60(10)	81.85(10)
N(2)-Tc(1)-P(2)	95.08(8)	96.05(7)	93.72(7)
N(1)-Tc(1)-P(2)	91.86(7)	93.64(7)	94.04(8)
O(1)-Tc(1)-P(2)	88.56(6)	87.64(6)	83.82(6)
O(2)-Tc(1)-P(2)	85.51(6)	83.88(6)	88.84(6)
N(2)-Tc(1)-P(1)	93.40(8)	92.76(7)	93.68(8)
N(1)-Tc(1)-P(1)	95.66(7)	95.88(7)	90.08(8)
O(1)-Tc(1)-P(1)	83.93(6)	84.92(6)	89.34(6)
O(2)-Tc(1)-P(1)	88.14(6)	87.80(6)	88.02(6)
P(1)-Tc(1)-P(2)	169.38(3)	167.87(3)	171.98(3)

A2. *1H-NMR spectra of compounds 1-8*.
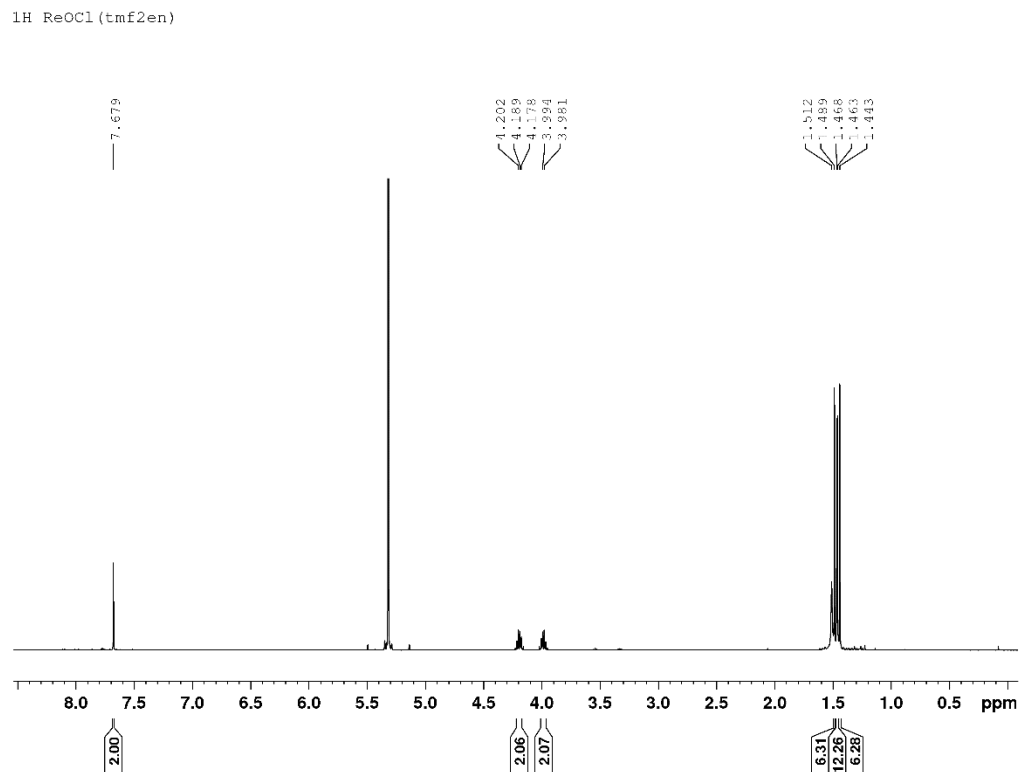
1H ReOCl(tmf2en)

Figure A.1. Full-view for ^{1}H NMR of **1** *trans*-[ReOCl(tmf$_2$en)] in CD$_2$Cl$_2$ (500 MHz, calibrated to residual CHDCl$_2$ at 5.32 ppm).
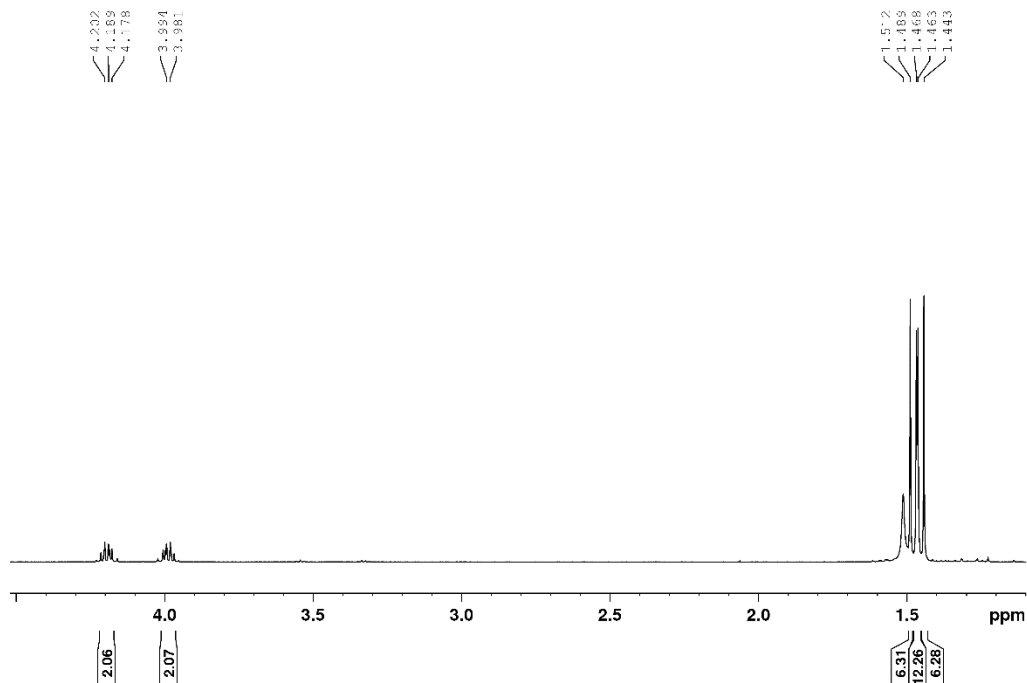
Figure A.2 Narrow-view for ^{1}H NMR of **1**, *trans*-[ReOCl(tmf$_2$en)], in CD$_2$Cl$_2$ (500 MHz, calibrated to residual CHDCl$_2$ at 5.32 ppm).

^{1}H NMR [500 MHz, CD$_2$Cl$_2$, r.t., δ (ppm)]: 7.68 (s, 2H, **-CH**=N-); 4.20 (m, 2H, **-CH$_2$-**); 3.98 (m, 2H, **-CH$_2$-**); 1.50 (s, 6H, **-CH$_3$**); 1.47 (s, 6H, **-CH$_3$**); 1.46 (s, 6H, **CH$_3$**); 1.44 (s, 6H, **-CH$_3$**). A singlet at 1.512 ppm is observed characteristic for residual H$_2$O in CD$_2$Cl$_2$. The solvent peak for CD$_2$Cl$_2$ was calibrated to 5.32 ppm.
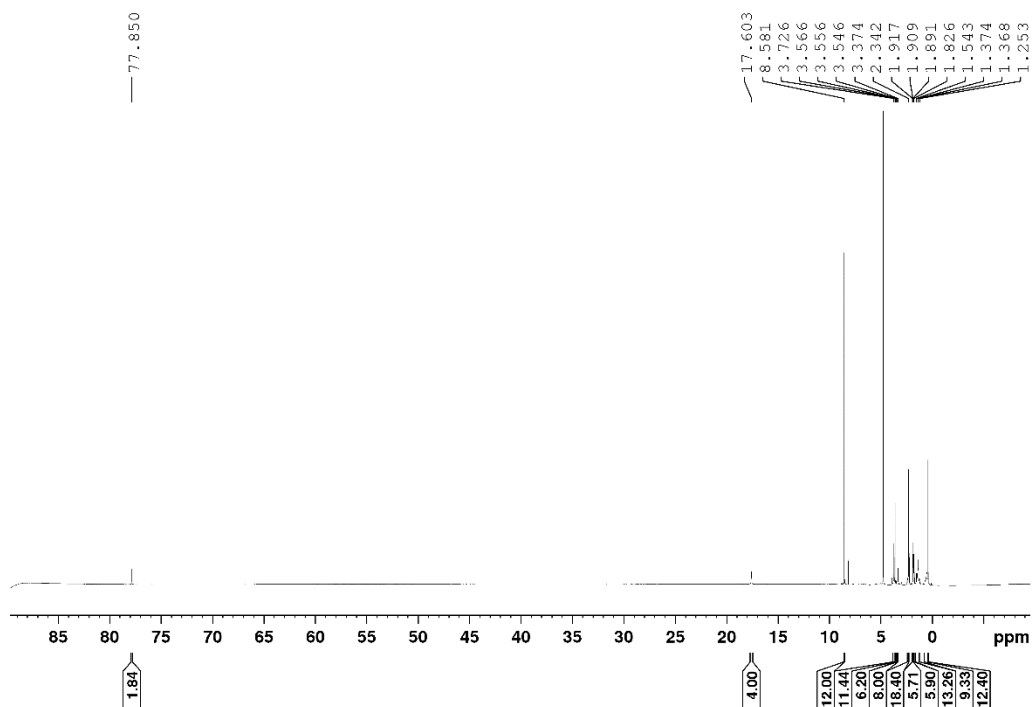
Figure A.3. ^{1}H NMR of **2**, *trans*-[Re(TMPP)$_2$(tmf$_2$en)]PF$_6$, in D$_2$O (600 MHz, calibrated to residual HOD at 4.79 ppm).
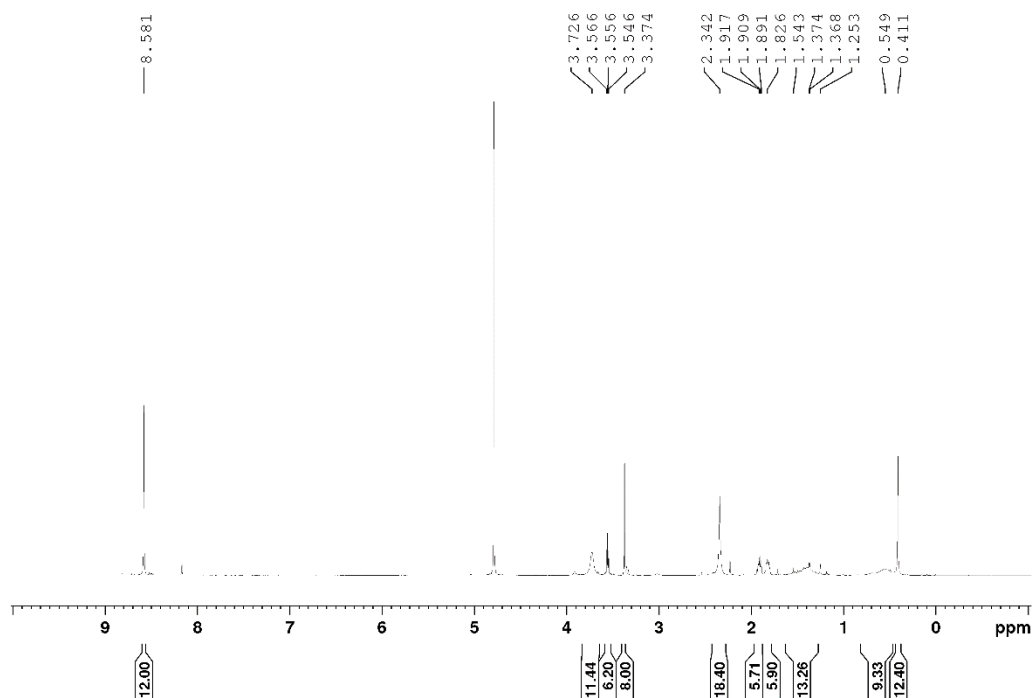
Figure A.4. ^{1}H NMR of **2**, *trans*-[Re(TMPP)$_2$(tmf$_2$en)]PF$_6$, in D$_2$O (600 MHz, calibrated to residual HOD at 4.79 ppm).

^{1}H NMR [600 MHz, D$_2$O, r.t., δ (ppm)]: 77.85 (s, 2H, -**CH**=N-); 17.60 (s, 4H, -NC**H$_2$**C**H$_2$**N-); 8.58 (s, 12H, -C**H$_3$**); 3.73 (s, 12H, PCH$_2$CH$_2$CH$_2$OC**H$_3$**); 2.34 (s, 18H, PCH$_2$CH$_2$CH$_2$OC**H$_3$**); 1.81-1.92 (m, 12H, PC**H$_2$**CH$_2$CH$_2$OCH$_3$); 1.42-1.48 (m, 12H, PCH$_2$C**H$_2$**CH$_2$OCH$_3$); 0.41 (s, 12H, -C**H$_3$**).

1H [Re(PEt3)2(tmf2en)][PF6]
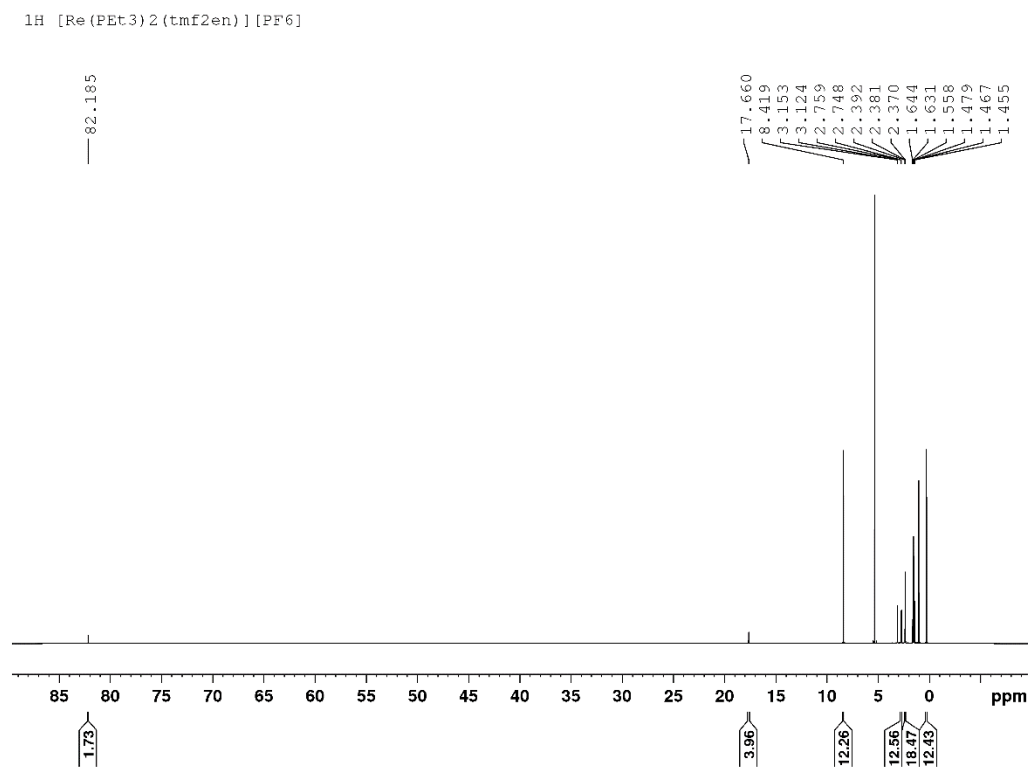
Figure A.5. Full-view of ^{1}H NMR of **3**, *trans*-[Re(PEt$_3$)$_2$(tmf$_2$en)]PF$_6$, in CD$_2$Cl$_2$ (600 MHz, calibrated to residual CHDCl$_2$ at 5.32 ppm).
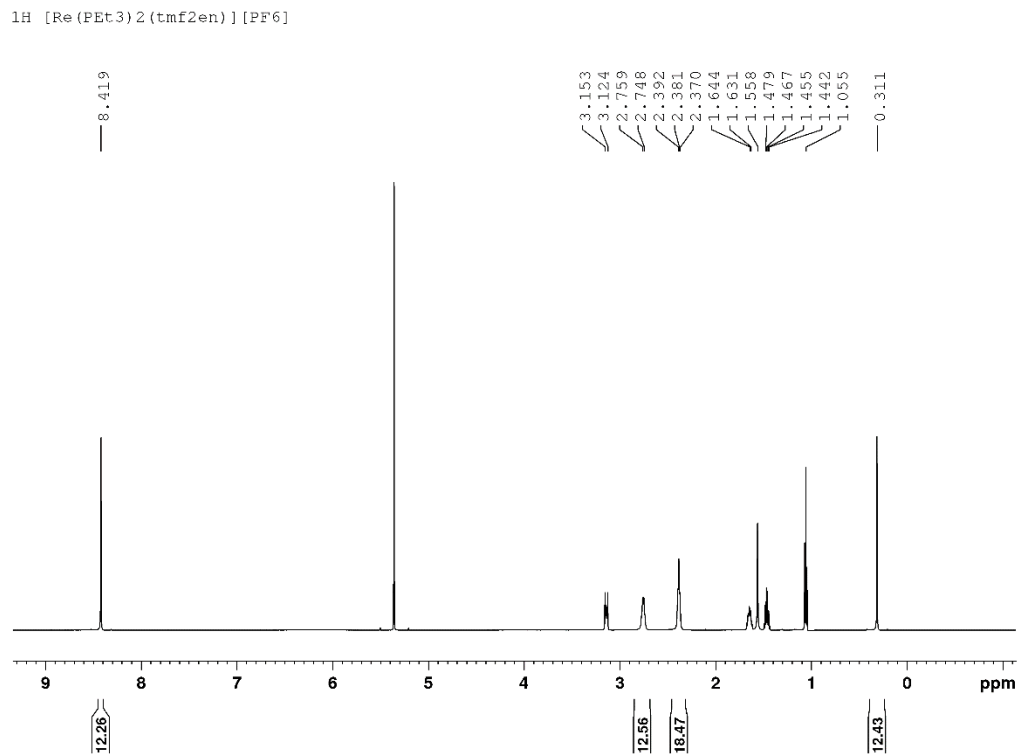
Figure A.6. Narrow-view of ^{1}H NMR of **3**, *trans*-[Re(PEt$_3$)$_2$(tmf$_2$en)]PF$_6$, in CD$_2$Cl$_2$ (600 MHz, calibrated to residual CHDCl$_2$ at 5.32 ppm).

^{1}H NMR [600 MHz, CD$_2$Cl$_2$, r.t., δ (ppm)]: 82.19 (s, 2H, -C**H**=N-); 17.66 (s, 4H, -NC**H$_2$**C**H$_2$**N-); 8.42 (s, 12H, -C**H$_3$**); 2.75 (br m, PC**H$_2$**CH$_3$); 2.38 (br t, 18H, PCH$_2$C**H$_3$**); 0.31 (s, 12H, -C**H$_3$**).

The ^{1}H NMR spectrum in **S4** shows a singlet at 1.56 ppm corresponding to residual H$_2$O in CD$_2$Cl$_2$. The multiplets observed at 3.13, 1.64, 1.46, and 1.06 ppm correspond to the tetrabutylammonium cation. The solvent peak for CD$_2$Cl$_2$ was calibrated to 5.32 ppm.

151
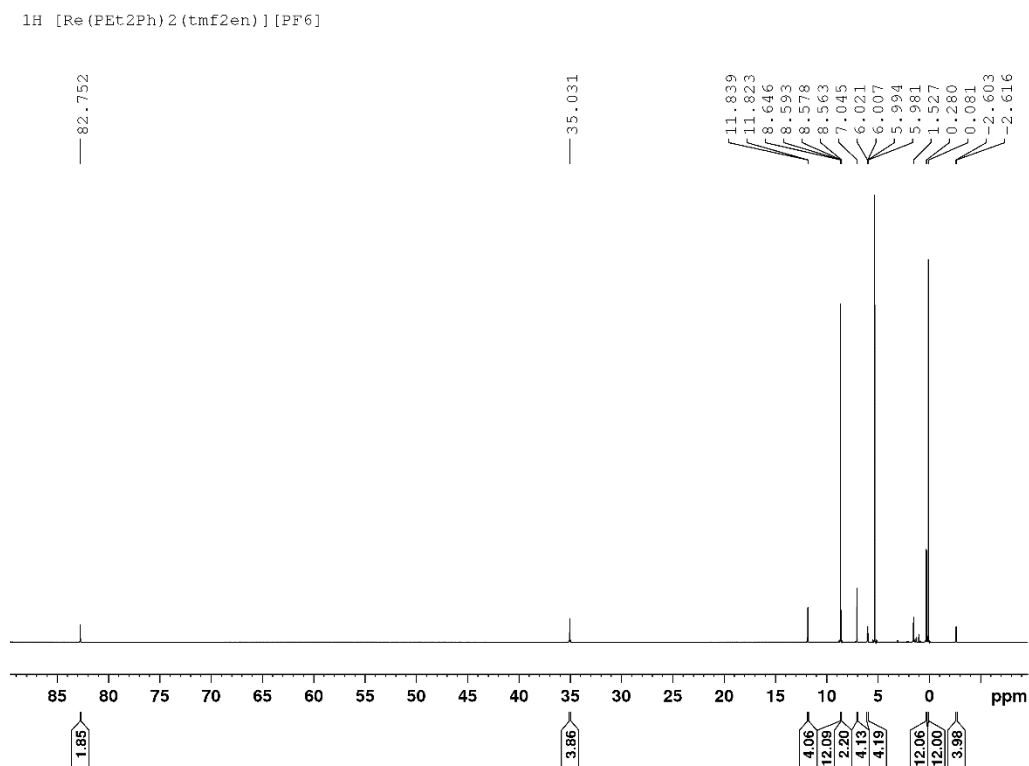
Figure A.7. Full-view for ¹H NMR of **4**, *trans*-[Re(PEt₂Ph)₂(tmf₂en)]PF₆, in CD₂Cl₂ (600 MHz, calibrated to residual CHDCl₂ at 5.32 ppm).
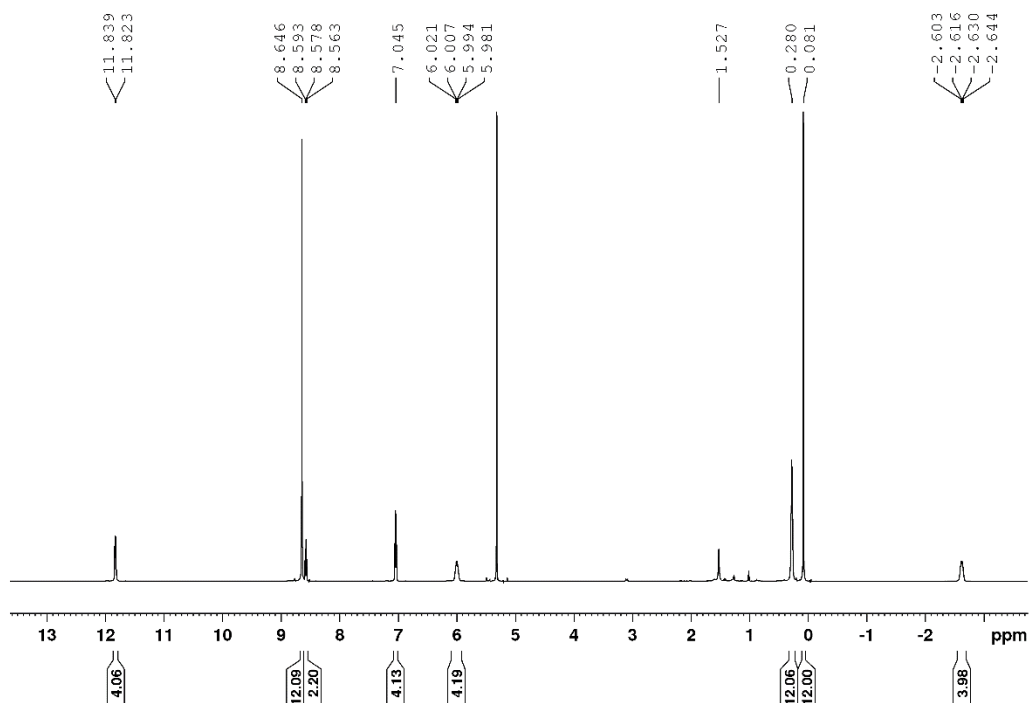
Figure A.8. Narrow-view for ^{1}H NMR of **4**, *trans*-[Re(PEt$_2$Ph)$_2$(tmf$_2$en)]PF$_6$, in CD$_2$Cl$_2$ (600 MHz, calibrated to residual CHDCl$_2$ at 5.32 ppm).

^{1}H NMR [500 MHz, CD$_2$Cl$_2$, r.t., δ (ppm)]: 82.75 (s, 2H, -C**H**=N-); 35.03 (s, 4H, -NC**H$_2$CH$_2$**N-); 11.83 (d, J = 7.9 Hz, 4H, ortho H); 8.65 (t, J = 7.5 Hz, 2H, para H); 8.58 (s, 12H, -CH$_3$); 7.04 (t, J = 7.6 Hz, 4H, meta H); 6.00 (br s, 4H, PC**H$_2$**CH$_3$); 0.28 (br s, 12H, PCH$_2$C**H$_3$**); 0.07 (s, 12H, -C**H$_3$**); -2.62 (br s, 4H, PC**H$_2$**CH$_3$).

A singlet is observed at 1.527 ppm corresponding to residual H$_2$O. The solvent peak for CD$_2$Cl$_2$ was calibrated to 5.32 ppm.
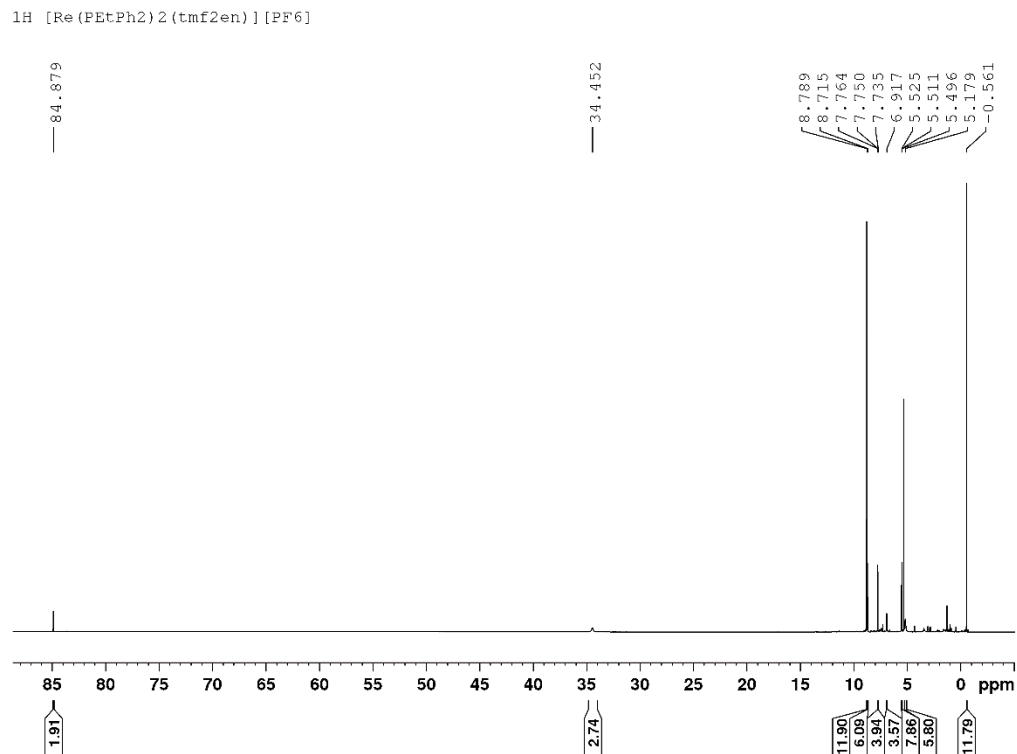
Figure A.9. Full-view for ^{1}H NMR of **5**, *trans*-[Re(PEtPh$_2$)$_2$(tmf$_2$en)]Cl, in CD$_2$Cl$_2$ (500 MHz, calibrated to residual CHDCl$_2$ at 5.32 ppm).
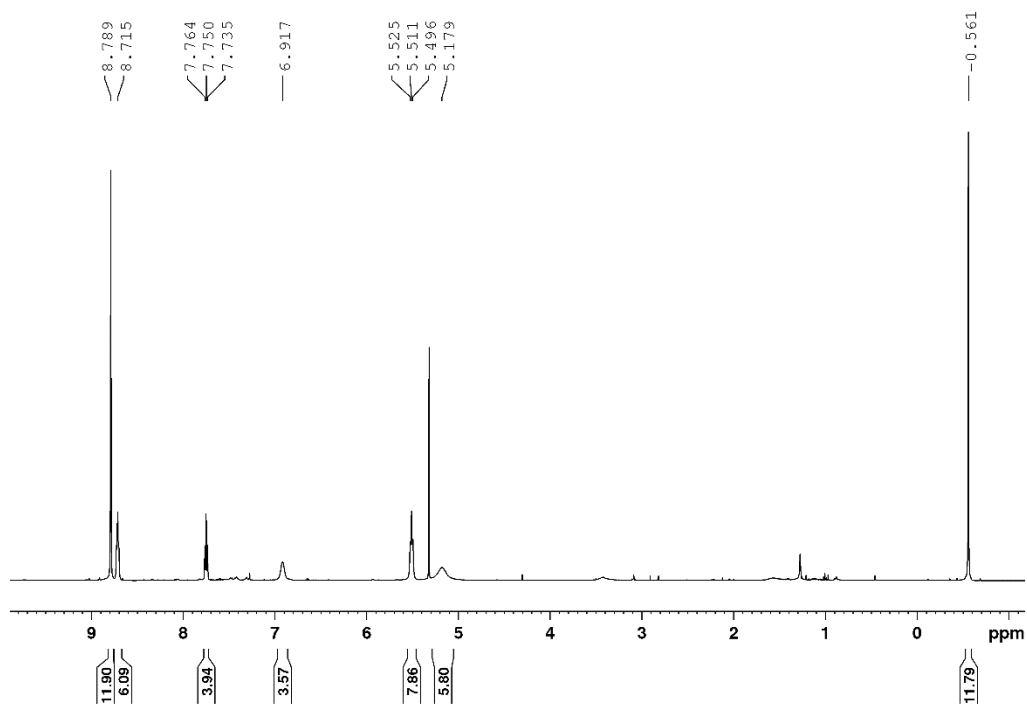
Figure A.10. Narrow-view for ^{1}H NMR of **5**, *trans*-[Re(PEtPh$_2$)$_2$(tmf$_2$en)]Cl, in CD$_2$Cl$_2$ (500 MHz, calibrated to residual CHDCl$_2$ at 5.32 ppm).

^{1}H NMR [500 MHz, CD$_2$Cl$_2$, r.t., δ (ppm)]: 84.88 (s, 2H, -C**H**=N-); 34.52 (s, 4H, -NC**H$_2$CH$_2$**N-); 8.79 (s, 12H, -C**H$_3$**); 8.72 (br s, 6H, PCH$_2$C**H$_3$**); 7.75 (t, 4H, P**Ph** para); 6.92 (br s, 4H, PC**H$_2$**CH$_3$); 5.51 (t, 8H, P**Ph** meta); 5.18 (br s, 8H, P**Ph** ortho); -0.56 (s, 12H, -C**H$_3$**).

The solvent peak for CD$_2$Cl$_2$ was calibrated to 5.32 ppm.
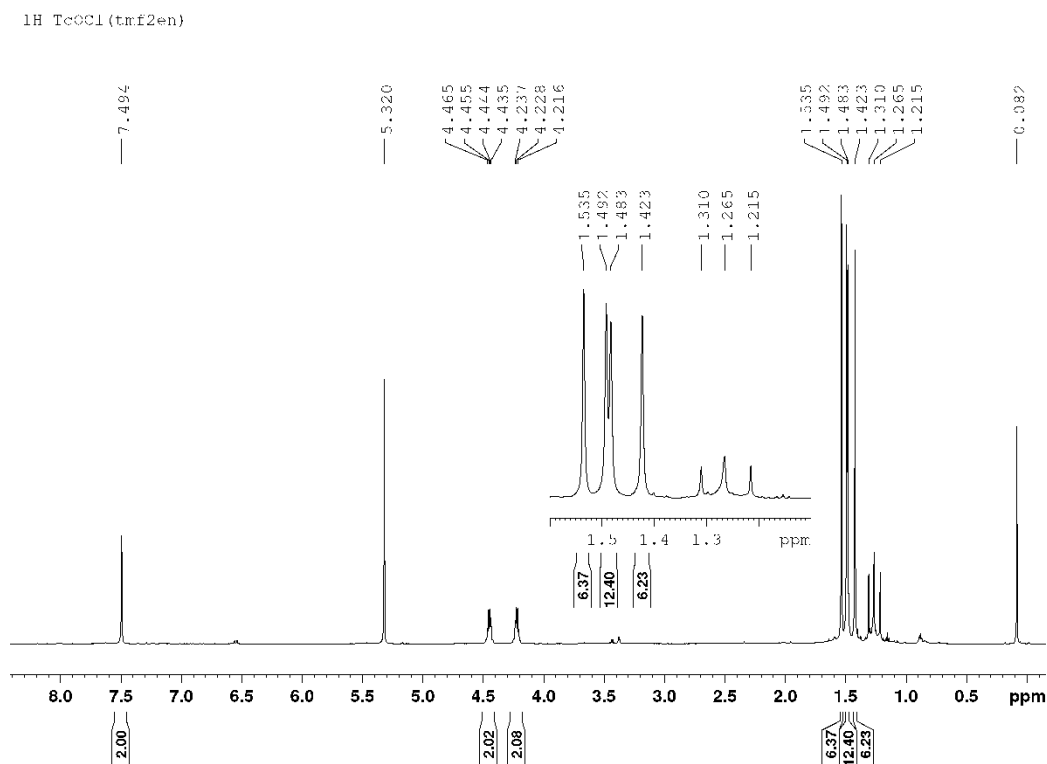
Figure A.11. ^{1}H NMR of **6**, *trans*-[TcOCl(tmf$_2$en)], in CD$_2$Cl$_2$ (600 MHz, calibrated to residual CHDCl$_2$ at 5.32 ppm).

^{1}H NMR [600 MHz, CD$_2$Cl$_2$, r.t., δ (ppm)]: 7.49 (s, 2H, **-CH=N-**); 4.45 (m, 2H, **-CH$_2$-**); 4.23 (m, 2H, **-CH$_2$-**); 1.54 (s, 6H, **-CH$_3$**); 1.49 (s, 6H, **-CH$_3$**); 1.48 (s, 6H, **CH$_3$**); 1.42 (s, 6H, **-CH$_3$**).

A broad singlet is observed at 1.265 ppm that is attributed to residual H grease. The singlet observed at 0.082 ppm is attributed to silicone grease. The singlets observed at 1.310 and 1.215 ppm are attributed the methyl substituents on unreacted H$_2$tmf$_2$en. The solvent peak for CD$_2$Cl$_2$ was calibrated to 5.32 ppm.
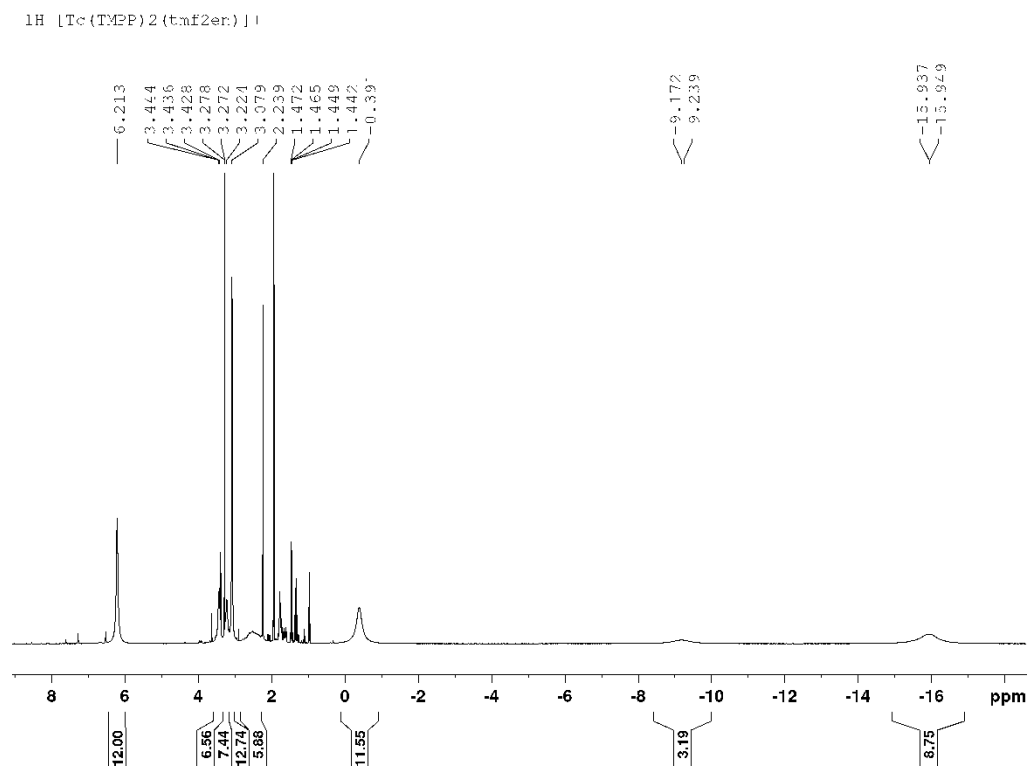
Figure A.12. ^{1}H NMR of **7**, *trans*-[Tc(TMPP)$_2$(tmf$_2$en)]Cl, in CD$_3$CN (600 MHz, calibrated to residual CHD$_2$CN at 1.94 ppm).

^{1}H NMR [600 MHz, CD$_3$CN, r.t., δ (ppm)]: 6.21 (s, 12H, -CH$_3$); 3.44 (br s, 6H, PCH$_2$CH$_2$**CH$_2$**OCH$_3$); 3.22 (br s, 6H, PCH$_2$CH$_2$**CH$_2$**OCH$_3$); 3.08 (br s, 12H, PCH$_2$**CH$_2$**CH$_2$OCH$_3$); -0.39 (s, 12H, -**CH$_3$**); -9.24 (br s, 3H, PC**H$_2$**CH$_2$CH$_2$OCH$_3$); -15.95 (br s, 9H, PC**H$_2$**CH$_2$CH$_2$OCH$_3$).
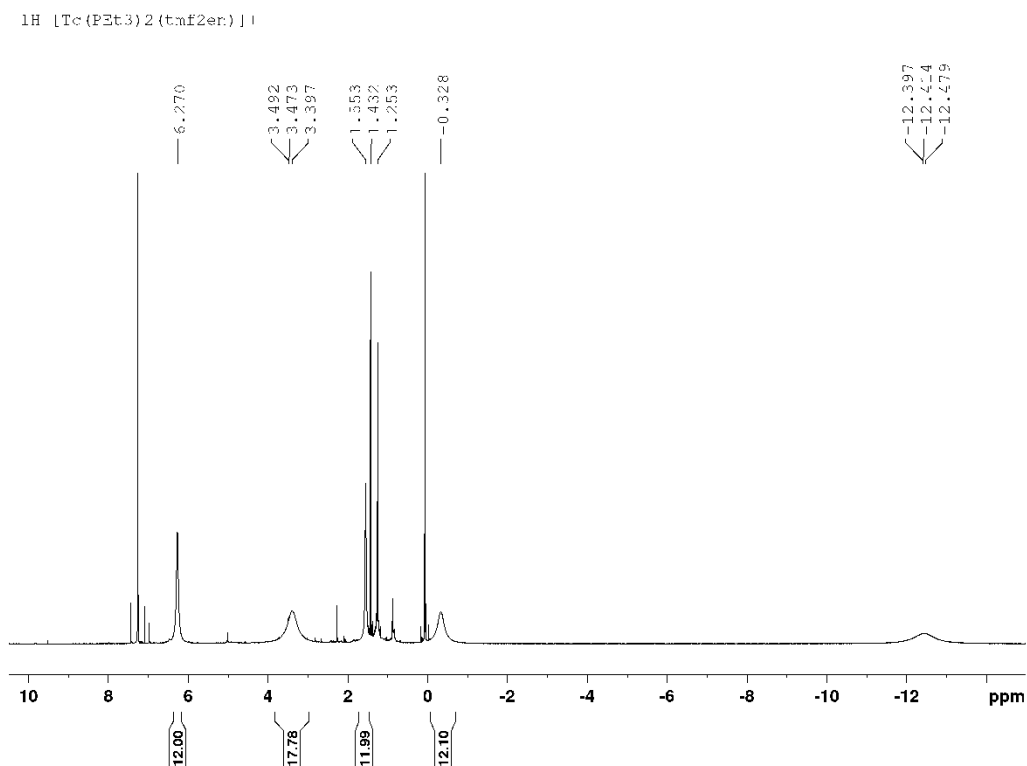
Figure A.13. ^{1}H NMR of **8**, *trans*-[Tc(PEt$_3$)$_2$(tmf$_2$en)]Cl, in CDCl$_3$ (600 MHz, calibrated to residual CHCl$_3$ at 7.26 ppm).

^{1}H NMR [600 MHz, CDCl$_3$, r.t., δ (ppm)]: 6.27 (s, 12H, -CH$_3$); 3.47 (br s, 18H, PCH$_2$**CH$_3$**); -0.33 (s, 12H, -**CH$_3$**); -12.41 (br s, 12H, PC**H$_2$**CH$_3$).

A broad singlet is observed at 1.265 ppm that is attributed to residual H grease. The singlet observed at 0.082 ppm is attributed to silicone grease. A single is observed at 1.56 that is attributed to residual H$_2$O. The solvent peak for CDCl$_3$ was calibrated to 7.26 ppm.

A3. *^{1}H- and ^{13}C-NMR, and FT-IR spectral details, and x-ray crystal structures of compounds S1 and S2.*

trans-[ReO(OMe)(tmf₂en)] , A1. ^{1}H NMR [500 MHz, CDCl₃, r.t., δ (ppm)]: 7.40 (s, 2H, -**CH**=N-); 3.93 (m, 2H, -**CH₂-**); 3.86 (m, 2H, -**CH₂-**); 1.53 (s, 6H, -**CH₃**); 1.49 (s, 6H, -**CH₃**); 1.47 (s, 6H, **CH₃**); 1.46 (s, 6H, -**CH₃**); 1.26 (s, 3H, O-**CH₃**). ^{13}C NMR [500 MHz, CDCl₃, r.t., δ (ppm)]: 200.65 (**C**-O); 163.88 (-H**C**=N-); 118.59 (**C**(CH=N); 82.35, 80.38 (**C**H₂); 66.67 (O-**C**H₃); 32.51, 32.46, 28.24, 27.62 (**C**H₃). FT-IR (KBr pellet, v/cm^{-1}): 1607 (C=N); 932 (Re≡O); 704 (Re-O).
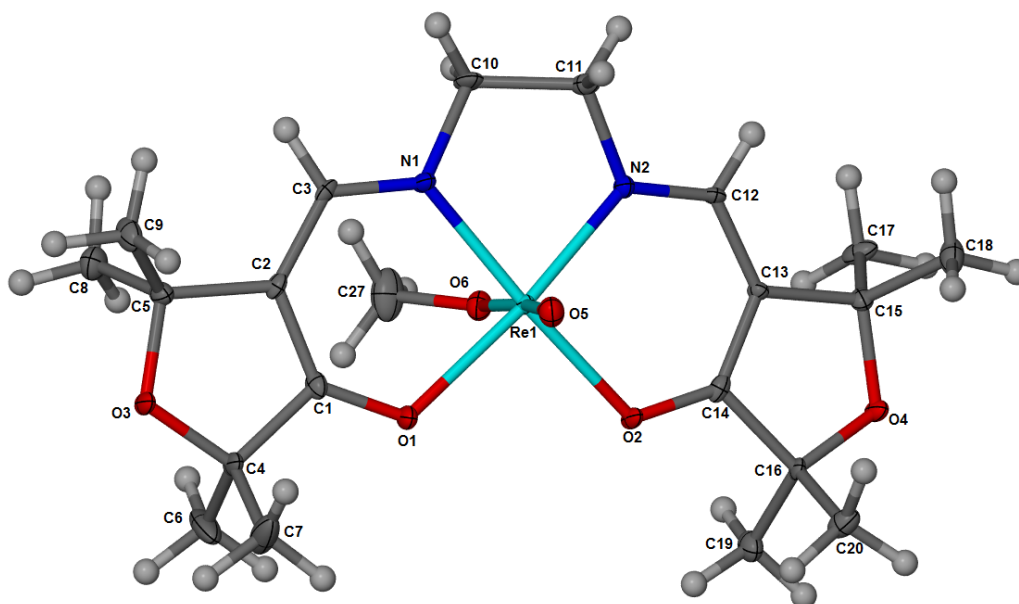
Figure A.14: X-ray crystal structure of *trans*-[ReO(OMe)(tmf₂en)], A**1**, with 50% probability thermal ellipsoids (CCDC # 1848708).

***trans*-[μ-O(ReO(tmf₂en))₂] , A2.** ¹H NMR [500 MHz, CDCl₃, r.t., δ (ppm)]: 7.63 (s, 2H, -CH=N-); 4.23 (m, 2H, -**CH₂**-); 4.02 (m, 2H, -**CH₂**-); 1.57 (s, 6H, -**CH₃**); 1.54 (s, 6H, -**CH₃**); 1.50 (s, 6H, **CH₃**); 1.46 (s, 6H, -**CH₃**). ¹³C NMR [500 MHz, CDCl₃, r.t., δ (ppm)]: 198.59 (**C**-O); 165.81 (-H**C**=N-); 114.99 (**C**(CH=N); 81.66, 80.39 (**CH₂**); 33.55, 32.06, 27.90, 27.67 (**CH₃**). FT-IR (KBr pellet, *υ*/cm⁻¹): 1606 (C=N); 931 (Re≡O); 707 (Re-O).
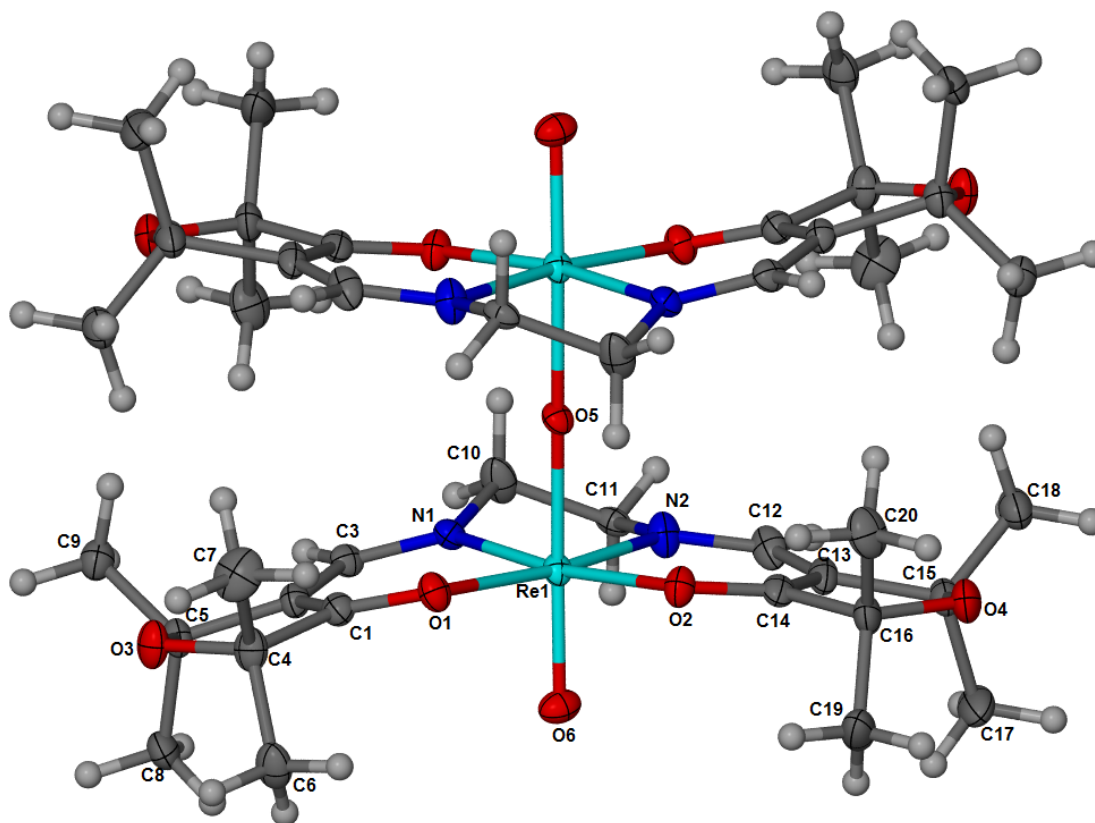
Figure A.15: X-ray crystal structure of *trans*-[μ-O(ReO(tmf₂en))₂], **A2**, with 50% probability thermal ellipsoids (CCDC # 1848707).

Table A.2: X-ray crystal data, data collection and refinement parameters for **A1** and **A2**

	A1	**A2**
formula	$C_{21}H_{33}N_2O_6Re$	$C_{40}H_{61.31}N_4O_{11.65}Re_2$
fw	595.69	1157.03
cryst system	Orthorhombic	Monoclinic
space group	Pbca	P2$_1$/c
a (Å)	8.9813(5)	11.7433(6)
b (Å)	13.5423(7)	10.8202(6)
c (Å)	37.7946(19)	17.2256(10)
α (deg)	90	90
β (deg)	90	95.8080(10)
γ (deg)	90	90
V (Å^3)	4596.9(4)	2177.5(2)
Z	8	2
ρ (g/cm^3)	1.721	1.765
T (K)	100	100
μ (mm^{-1})	5.325	5.617
λ souce (Å)	0.71073	0.71073
R(F)^a	0.0596	0.0166
Rw(F)^2	0.0693	0.0365
GoF	1.264	1.063

Table A.3: Select bond lengths (Å) and angles (°) for compounds **A1** and **A2**

	S1	S2
Re(1)-O(5)	1.705(3)	1.7114(17)
Re(1)-O(6)	1.912(3)	1.92417(12)
Re(1)-N(2)	2.031(4)	2.033(2)
Re(1)-N(1)	2.049(4)	2.0280(19)
Re(1)-O(2)	2.106(3)	2.1079(16)
Re(1)-O(1)	2.128(3)	2.1106(16)
O(5)-Re(1)-O(6)	172.51(15)	175.47(6)
O(5)-Re(1)-N(2)	96.342(16)	88.71(6)
O(6)-Re(1)-N(2)	90.72(16)	94.13(9)
O(5)-Re(1)-N(1)	93.78(13)	88.42(5)
O(6)-Re(1)-N(1)	84.74(16)	95.49(8)
N(2)-Re(1)-N(1)	81.18(16)	81.33(8)
O(5)-Re(1)-O(2)	96.43(16)	85.67(5)
O(6)-Re(1)-O(2)	85.73(15)	90.61(7)
N(2)-Re(1)-O(2)	93.04(15)	93.94(7)
N(1)-Re(1)-O(2)	168.77(15)	172.52(7)
O(5)-Re(1)-O(1)	88.48(15)	87.57(5)
O(6)-Re(1)-O(1)	84.29(14)	89.95(8)
N(2)-Re(1)-O(1)	172.98(15)	173.18(7)
N(1)-Re(1)-O(1)	93.42(14)	92.84(7)
O(2)-Re(1)-O(1)	91.51(13)	91.48(6)
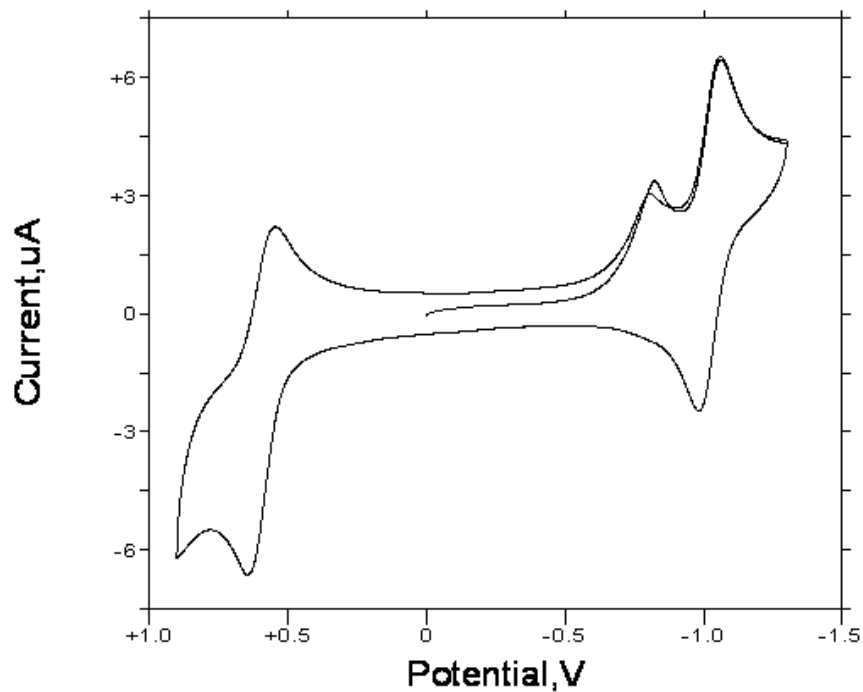
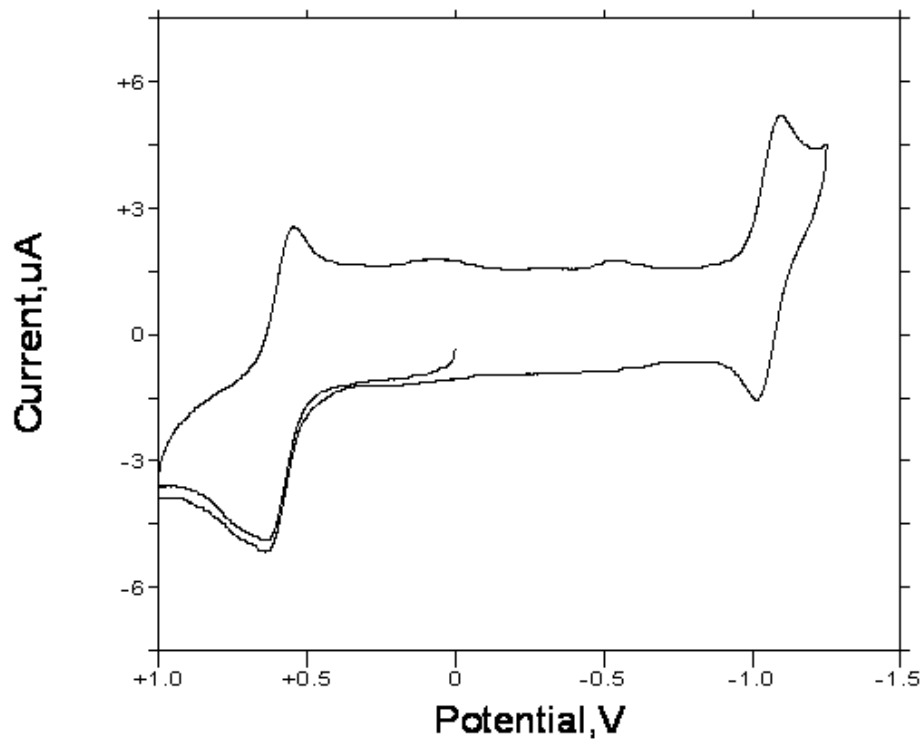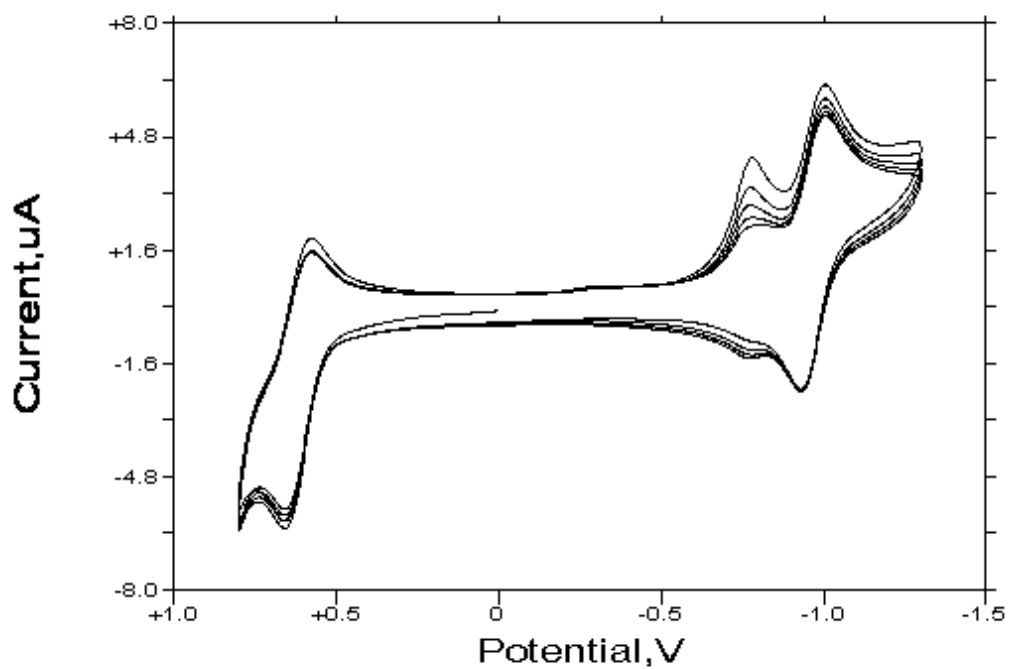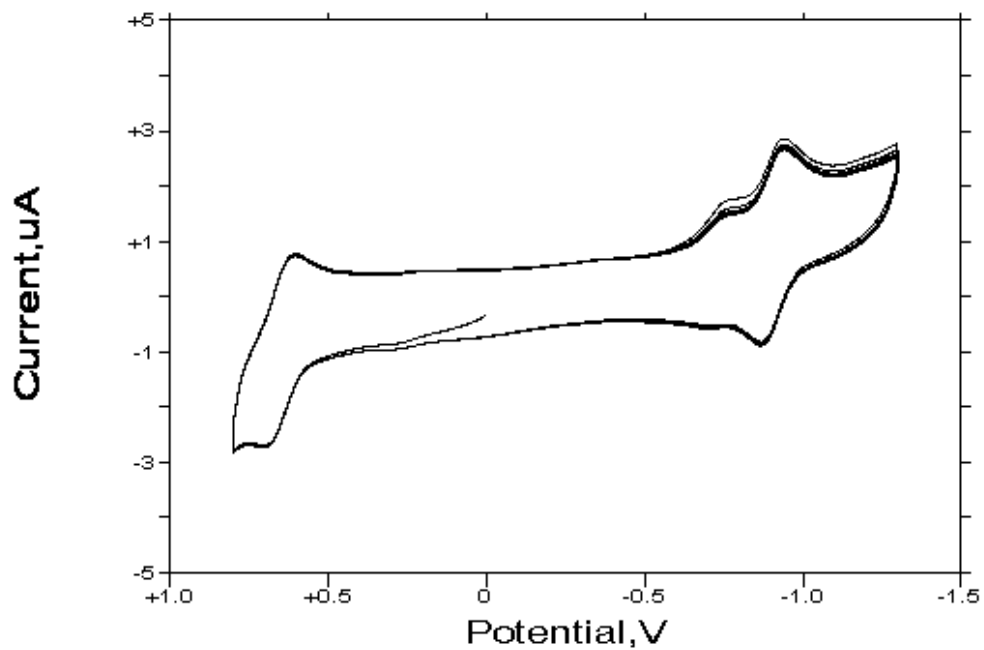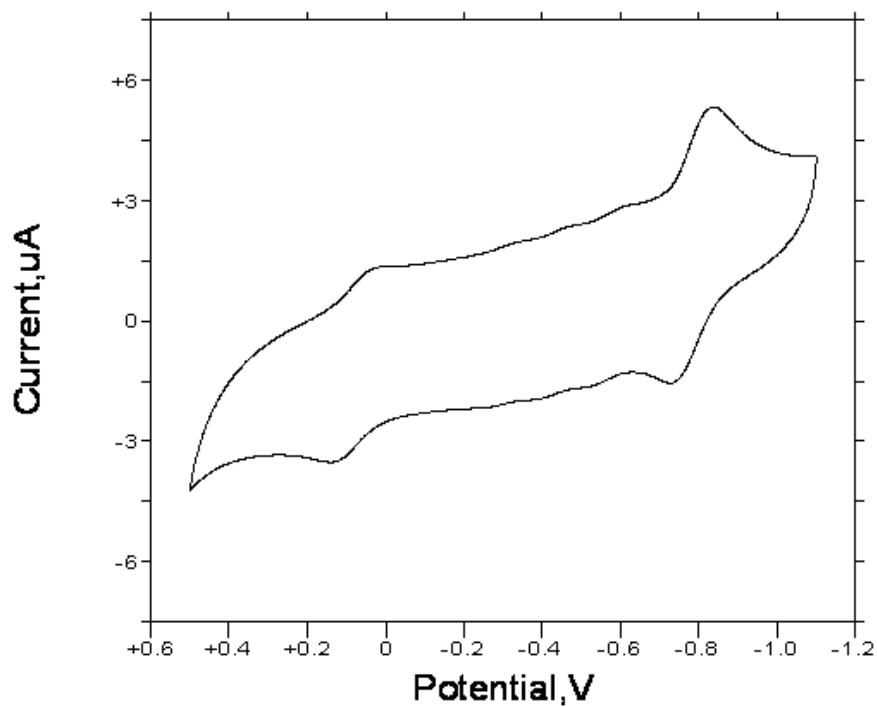**Figure A.16**: Cyclic voltammogram (CV) for *trans*-[Re(TMPP)$_2$(tmf$_2$en)][Cl] **2**.

Figure A.17: Cyclic voltammogram (CV) for *trans*-[Re(PEt$_3$)$_2$(tmf$_2$en)][Cl] **3**.
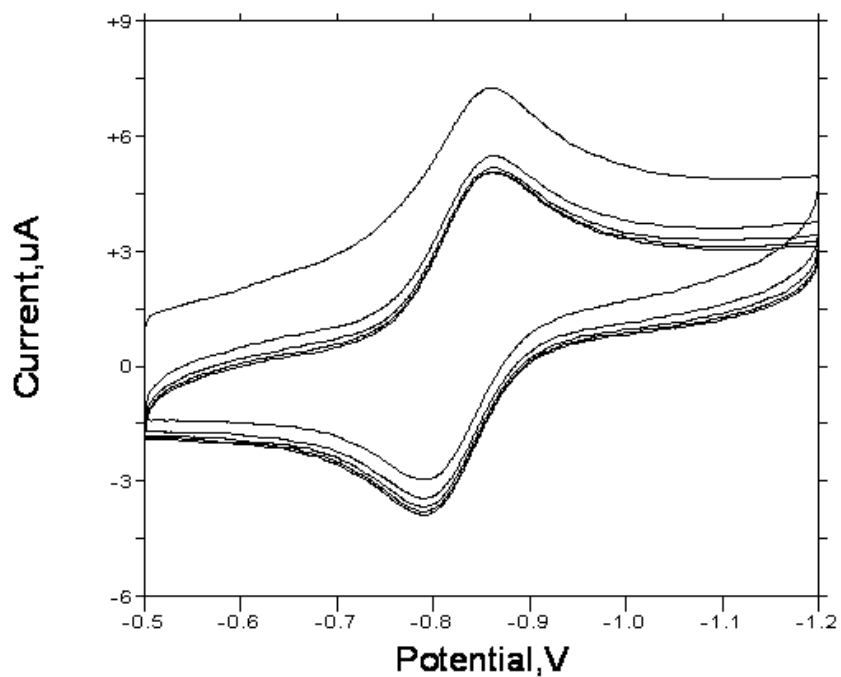
Figure A.18: Cyclic voltammogram (CV) for *trans*-[Re(PEt$_2$Ph)$_2$(tmf$_2$en)][Cl] **4**.

Figure A.19: Cyclic voltammogram (CV) for *trans*-[Re(PEtPh$_2$)$_2$(tmf$_2$en)][Cl] **5**.

Figure A.20: Cyclic voltammogram (CV) for *trans*-[Tc(TMPP)$_2$(tmf$_2$en)][Cl] **7**.

Figure A.21: Repetitive cyclic voltammogram (CV) for *trans*-[Tc(PEt$_3$)$_2$(tmf$_2$en)][Cl] **8** from -0.5 to -1.2 V.

APPENDIX B

Supporting Information for CHAPTER 3

Steric Influence of Salicylaldehyde-based Schiff Base Ligands in the Formation of *trans*-[Re(PR$_3$)$_2$(Schiff Base)]$^+$ Complexes

B1. SCXRD refinement details for compounds **10**, **11**•CH$_3$OH, **13**, **15**•2.333CH$_3$OH, and **16-19**.

**B2.** ^{1}H-NMR spectra for compounds **10-19**.

B3. Cyclic voltammograms for compounds **10-15**.

S1. *SCXRD refinement details for compounds **10**, **11•CH$_3$OH**, **13**, **15•2.333CH$_3$OH**, and **16-19**.*

Compounds **10**, **11•CH$_3$OH**, **13**, and **19** were solved by iterative dual space recycling as implemented in SHELXT v. 2014/5.[150] Compounds **15•2.333CH$_3$OH**, **16**, **17**, and **18** were solved by direct methods as implemented in SHELXS.[151] All structures were refined by full-matrix least squares refinement against F^2 using SHELXL v. 2017/1.[152] Full occupancy non-hydrogen atoms were refined anisotropically to convergence. Hydrogen atoms were placed in calculated positions and constrained to ride on the carrier atoms; a riding-rotating model was used for methyl group hydrogen atoms. [PF$_6$]$^-$ ions in **10** and **13** and two ethyl groups from a P(Et)$_3$ ligand in **13** were found to be disordered over two positions; the relative occupancies were constrained to add to 1 and refined to values of 87.5%, 69.3%, 53.2%, and 54.3% for the major parts of all four groups, respectively. A total of five distance restraints were used to keep the disordered groups in **13** near reasonable values. Due to systematic errors in the intensities for **19** caused by satellite crystals, rigid group restraints were used to keep the anisotropic thermal ellipsoids for the terminal Re≡O oxygen atom within reasonable values.[153] For compounds **11•CH$_3$OH** and **15•2.333CH$_3$OH**, contributions to scattering from highly disordered solvent molecules were determined and removed using PLATON SQUEEZE.[154] The structure of **11•CH$_3$OH** was found to contain 70 electrons per unit cell distributed across 256 Å^3 of void space, in good agreement with the expected values for four methanol molecules (72 electrons). For **15•2.333CH$_3$OH**, 336 electrons were found distributed through a total void volume of 1902 Å^3, equivalent to 18.667 methanol molecules per unit cell (7 methanol molecules per 3 molecules of the metal complex).

For Compound **10**, the thermal ellipsoid of the Cl⁻ ion is significantly greater than the average values for other non-hydrogen atoms in the structure; greater thermal motion is chemically reasonable for this moiety as it is situated within the disordered solvent void. Compounds **16** and **19** contain significant difference map peaks in chemically unreasonable positions, which are likely caused by extra intensity from diffraction by unremovable satellite crystals. This is supported by the fact that $|F_{obs}| > |F_{calc}|$ for the most disagreeable reflections. For compound **19**, which crystallized in the form of highly intergrown clumps, this problem is especially severe; nearly complete powder diffraction rings are observed on almost every frame of the data. Nevertheless, the data that was able to be obtained for **19** could be reliably indexed to a single unit cell and refined anisotropically as a structure fully consistent with the NMR data. Since both morphological inspection and the appearance of the diffraction data suggested the crystal of **19** is likely a single crystal core heavily coated in smaller, randomly oriented satellites, improving the model with de-twinning was not feasible.
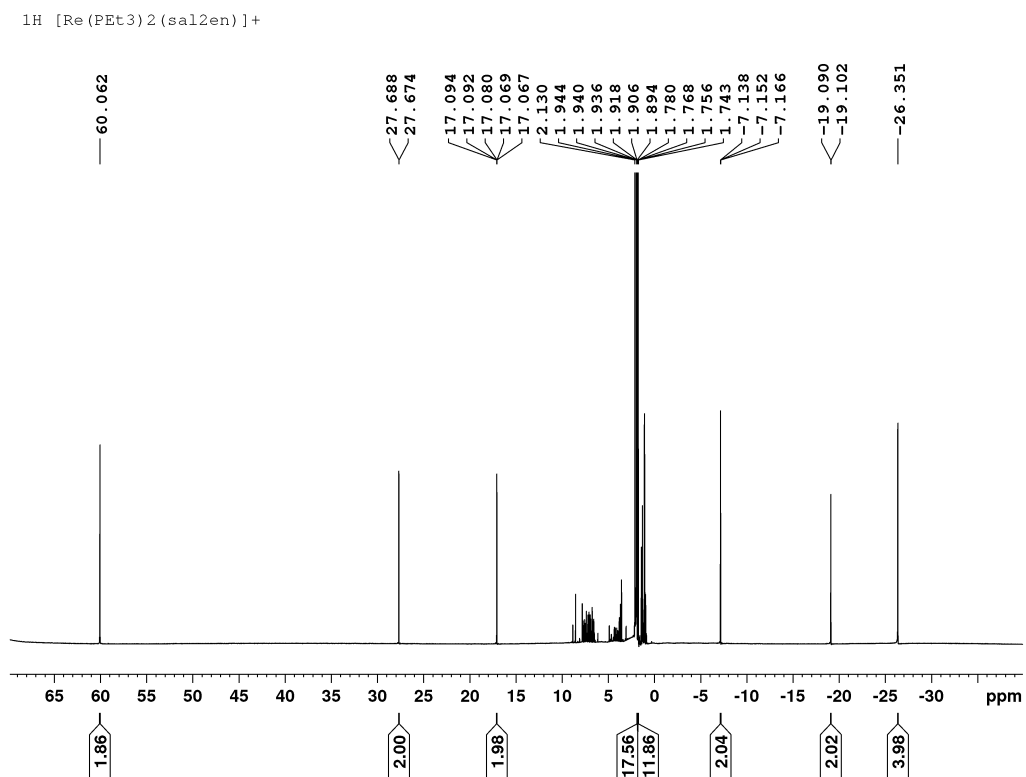
1H [Re(PEt3)2(sal2en)]+

Figure B.1. Full view of ¹H NMR of **10** *trans*-[Re(PEt$_3$)$_2$(sal$_2$en)][PF$_6$] in CD$_3$CN (600 MHz, calibrated to residual CHD$_2$CN at 1.94 ppm).
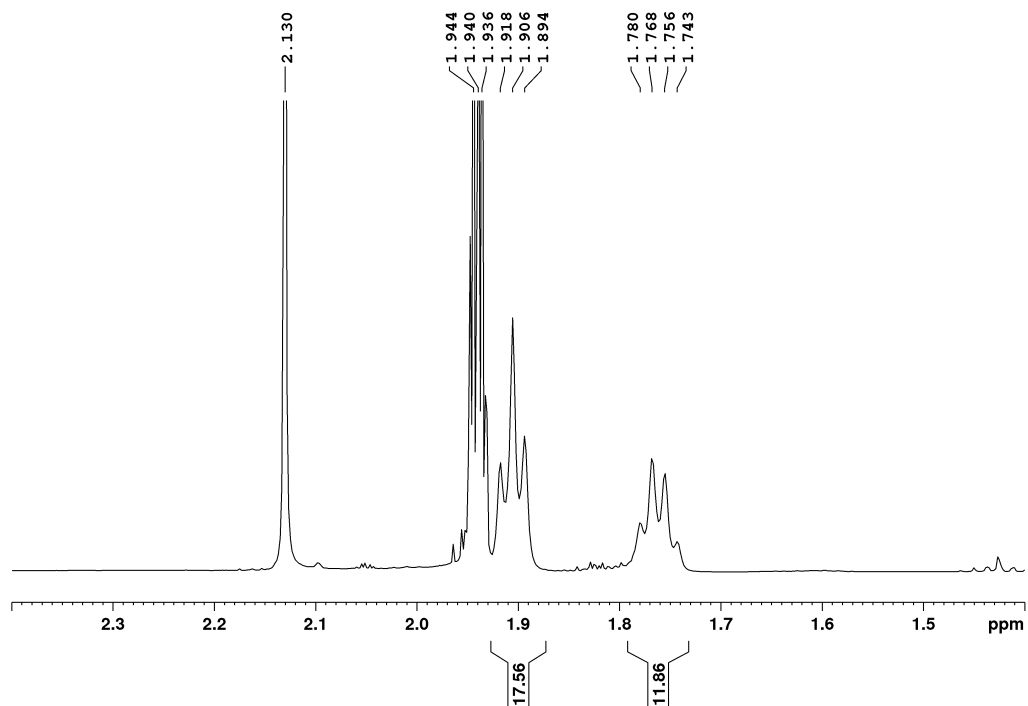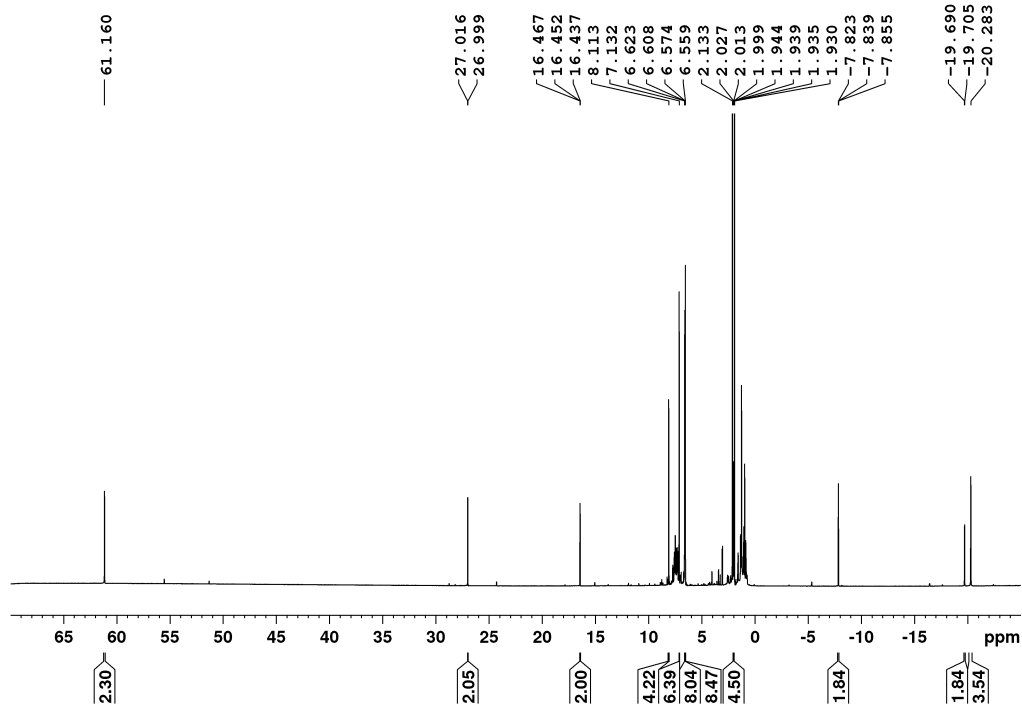
Figure B.2. Narrow view of ^{1}H NMR of **10** *trans*-[Re(PEt$_3$)$_2$(sal$_2$en)][PF$_6$] in CD$_3$CN (600 MHz, calibrated to residual CHD$_2$CN at 1.94 ppm).
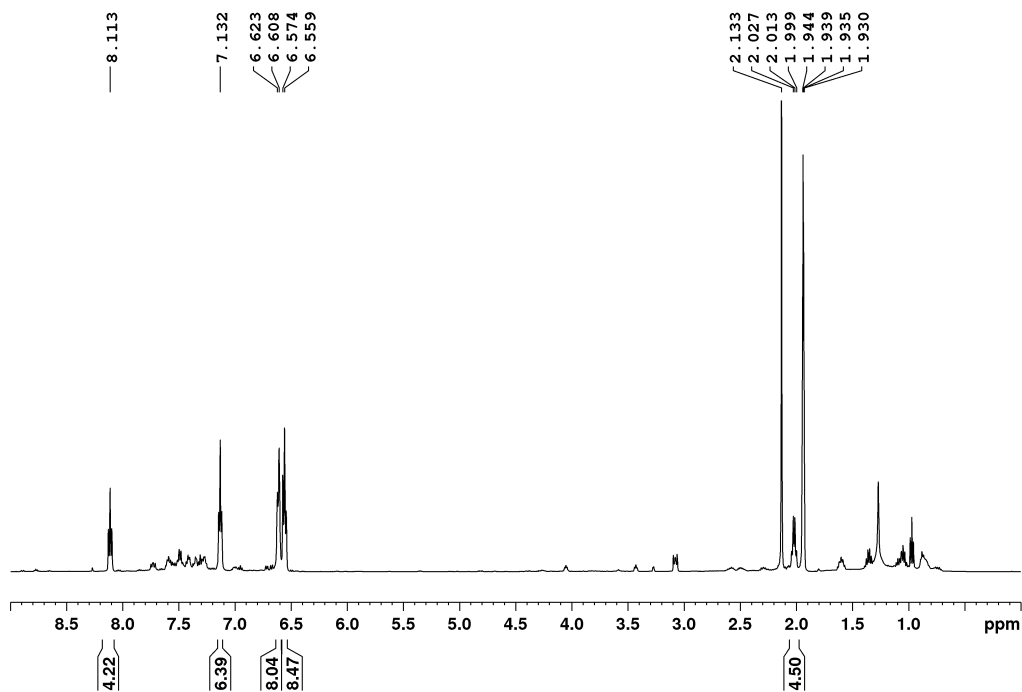
^{1}H NMR [600 MHz, CD$_3$CN, r.t., δ (ppm)]: 60.06 (s, 2H, -**H**C=N-); 27.68 (d, *J* = 8.3 Hz, 2H, Ar**H**); 17.08 (t, *J* = 7.5 Hz, 2H, Ar**H**); 1.91 (t, *J* = 7.4 Hz, 18H, PCH$_2$C**H$_3$**); 1.76 (q, *J* = 7.3 Hz, 12H, PC**H$_2$**CH$_3$); -7.15 (t, *J* = 8.3 Hz, 2H, Ar**H**); -19.10 (d, *J* = 7.4 Hz, 2H, Ar**H**); -26.35 (s, 4H, -NC**H$_2$**C**H$_2$**N-).

Figure B.3. Full view of ¹H NMR of **11** *trans*-[Re(PEtPh₂)₂(sal₂en)][Cl] in CD₃CN (500 MHz, calibrated to residual CHD₂CN at 1.94 ppm).

Figure B.4. Narrow view of ^{1}H NMR of **11** *trans*-[Re(PEtPh$_2$)$_2$(sal$_2$en)][Cl] in CD$_3$CN (500 MHz, calibrated to residual CHD$_2$CN at 1.94 ppm).

^{1}H NMR [500 MHz, CD$_3$CN, r.t., δ (ppm)]: 61.16 (s, 2H, -**H**C=N-); 27.00 (d, *J* = 8.2 Hz, 2H, Ar**H**); 16.45 (t, *J* = 7.3 Hz, 2H, Ar**H**); 8.11 (t, *J* = 7.4 Hz, 4H, P**Ph** para); 7.13 (t, *J* = 6.7 Hz, 6H, PCH$_2$C**H$_3$**); 6.61 (d, *J* = 7.7, 8H, P**Ph** ortho); 6.56 (br s, 8H, P**Ph** meta); 2.10 (q, J = 7.2 Hz, 4H, PC**H$_2$**CH$_3$); -7.84 (t, *J* = 8.0 Hz, 2H, Ar**H**); -19.70 (d, *J* = 7.8 Hz, 2H, Ar**H**); -20.28 (s, 4H, -NC**H$_2$**C**H$_2$**N-).

Figure B.5. Full view of ^{1}H NMR of **12** *trans*-[Re(PPh$_3$)$_2$(sal$_2$en)][PF$_6$] in CD$_3$CN (600

MHz, calibrated to residual CHD$_2$CN at 1.94 ppm).
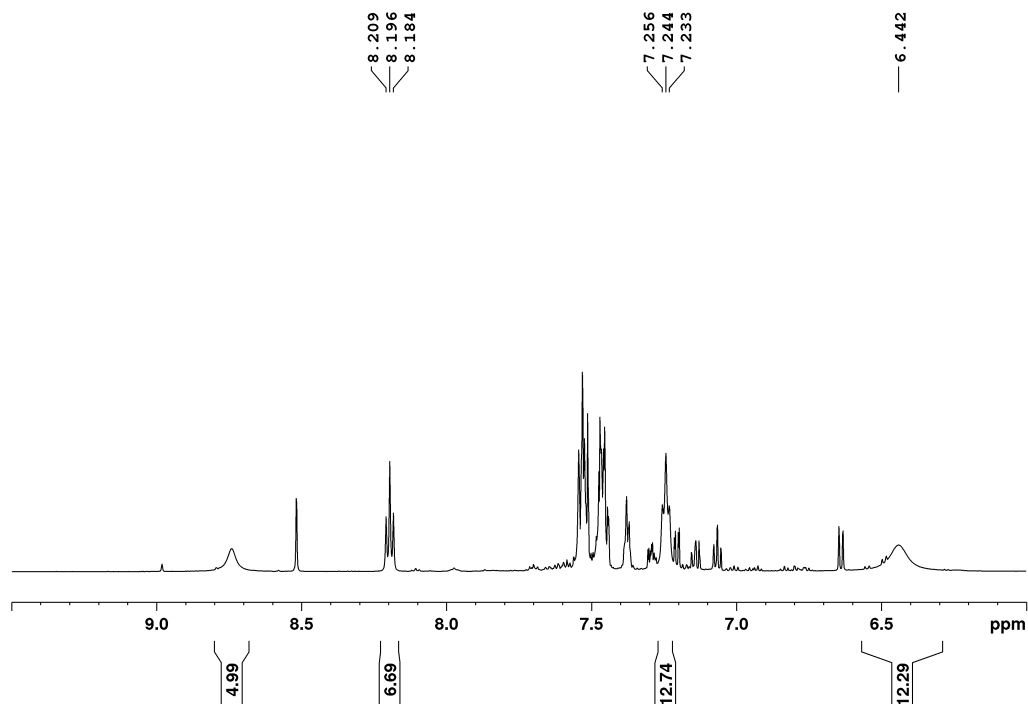
Figure B.6. Narrow view of ^{1}H NMR of **12** *trans*-[Re(PPh$_3$)$_2$(sal$_2$en)][PF$_6$] in CD$_3$CN (600 MHz, calibrated to residual CHD$_2$CN at 1.94 ppm).

^{1}H NMR [600 MHz, CD$_3$CN, r.t., δ (ppm)]: 59.37 (s, 2H, **-H**C=N-); 26.54 (d, *J* = 7.8 Hz, 2H, Ar**H**); 15.75 (t, *J* = 7.5 Hz, 2H, Ar**H**); 8.20 (t, *J* = 7.6 Hz, 6H, **PPh** meta); 7.24 (t, *J* = 7.1 12H, **PPh** meta); 6.44 (br s, 12H, **PPh** ortho); -9.30 (t, *J* = 8.1 Hz, 2H, Ar**H**); -19.51 (s, 4H, -NC**H$_2$**C**H$_2$**N-); -20.94 (d, *J* = 7.5 Hz, 2H, Ar**H**).
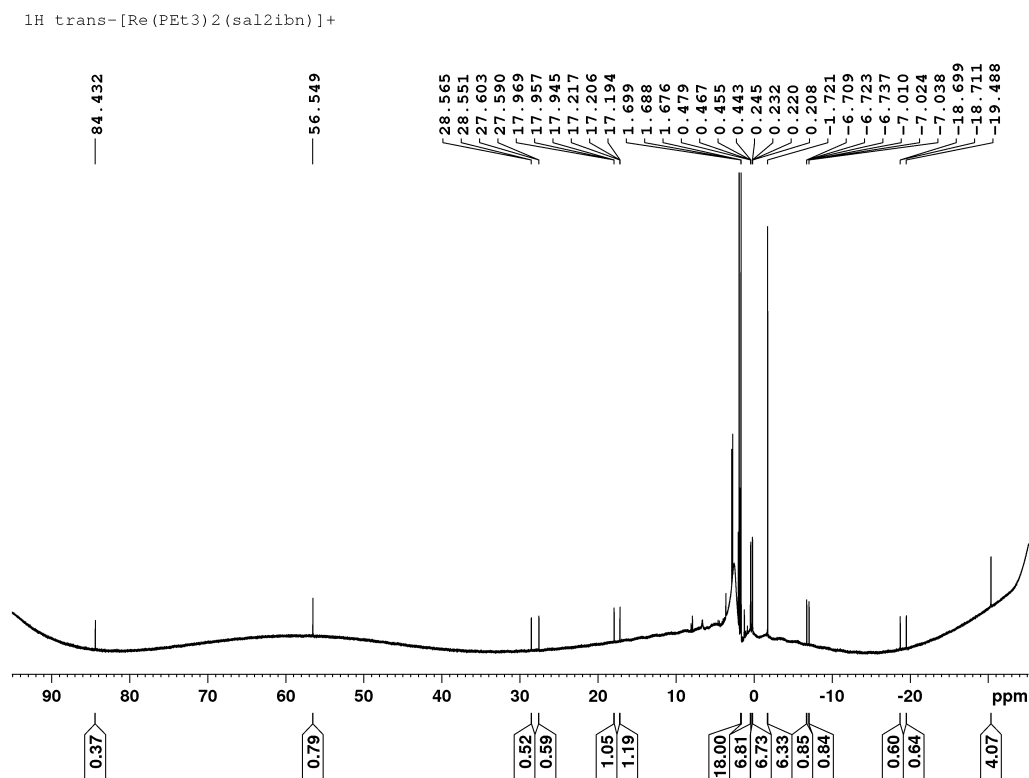
Figure B.7. Full view of ^{1}H NMR of **13** *trans*-[Re(PEt$_3$)$_2$(sal$_2$ibn)][PF$_6$] in CD$_3$CN (600 MHz, calibrated to residual CHD$_2$CN at 1.94 ppm).
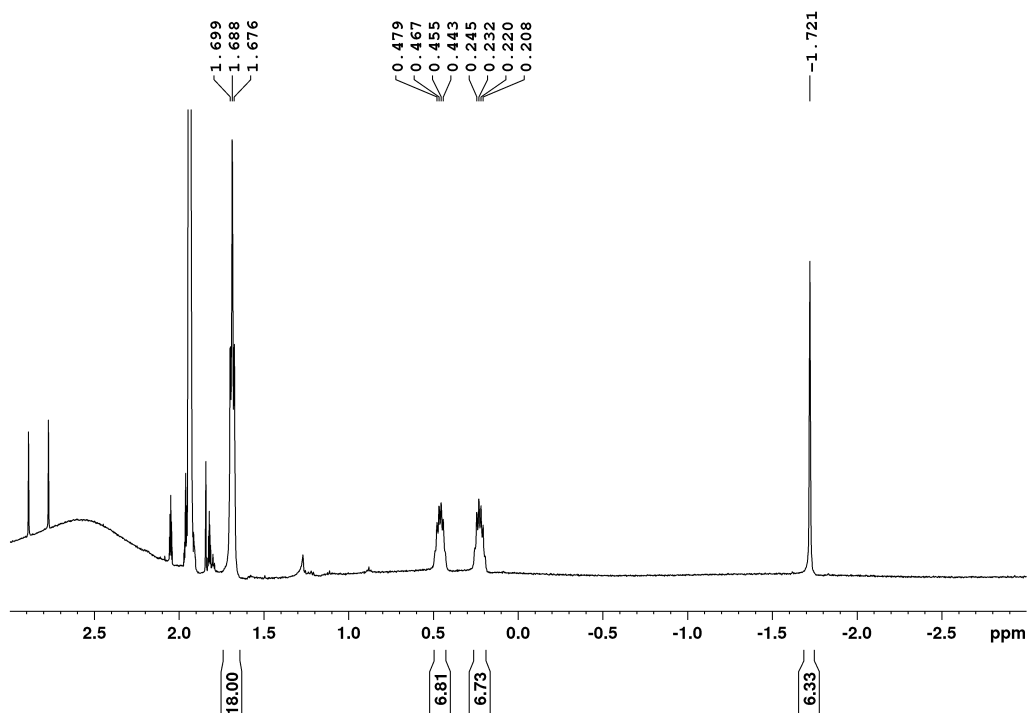
Figure B.8. Narrow view of ^{1}H NMR of **13** *trans*-[Re(PEt₃)₂(sal₂ibn)][PF₆] in CD₃CN (600 MHz, calibrated to residual CHD₂CN at 1.94 ppm).

^{1}H NMR [600 MHz, CD₃CN, r.t., δ (ppm)]: 84.49 (s, 1H, -**H**C=N-); 56.59 (s, 1H, -**H**C=N-); 28.75 (d, *J* = 8.2 Hz, 1H, Ar**H**); 27.75 (d, *J* = 8.3 Hz, 1H, Ar**H**); 18.03 (t, *J* = 7.1 Hz, 1H, Ar**H**); 17.25 (t, *J* = 7.0 Hz, 1H, Ar**H**); 1.65 (s, 18H, P(CH₂C**H₃**)₃); 0.64-0.54 (br m, 6H, P(C**H₂**CH₃)₃); 0.34-0.25 (br m, 6H, P(C**H₂**CH₃)₃); -1.65 (s, 6H, -C(C**H₃**)₂CH₂-); -6.66 (t, *J* = 8.3 Hz, 1H, Ar**H**); -6.95 (t, *J* = 8.3 Hz, 1H, Ar**H**); -18.96 (d, *J* = 7.1 Hz, 1H, Ar**H**); -19.75 (d, *J* = 7.1 Hz, 1H, Ar**H**); -31.06 (s, 2H, -C(CH₃)₂C**H₂**-).
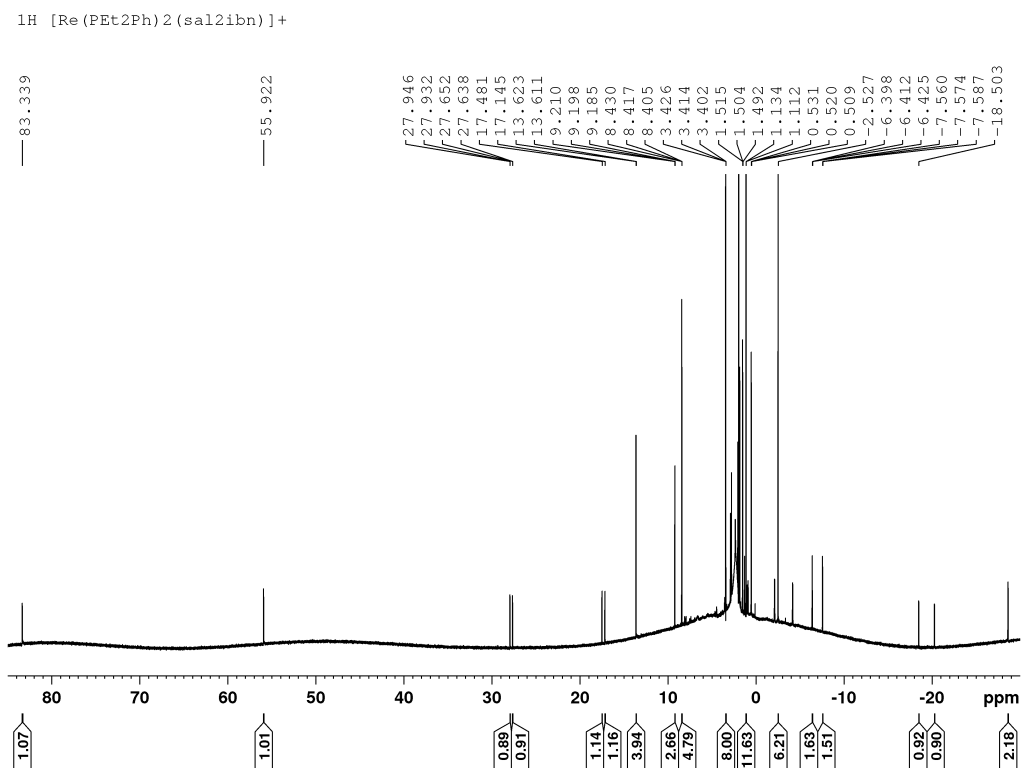
Figure B.9. Full view of ^{1}H NMR of **14** *trans*-[Re(PEt$_2$Ph)$_2$(sal$_2$ibn)][PF$_6$] in CD$_3$CN (600 MHz, calibrated to residual CHD$_2$CN at 1.94 ppm).
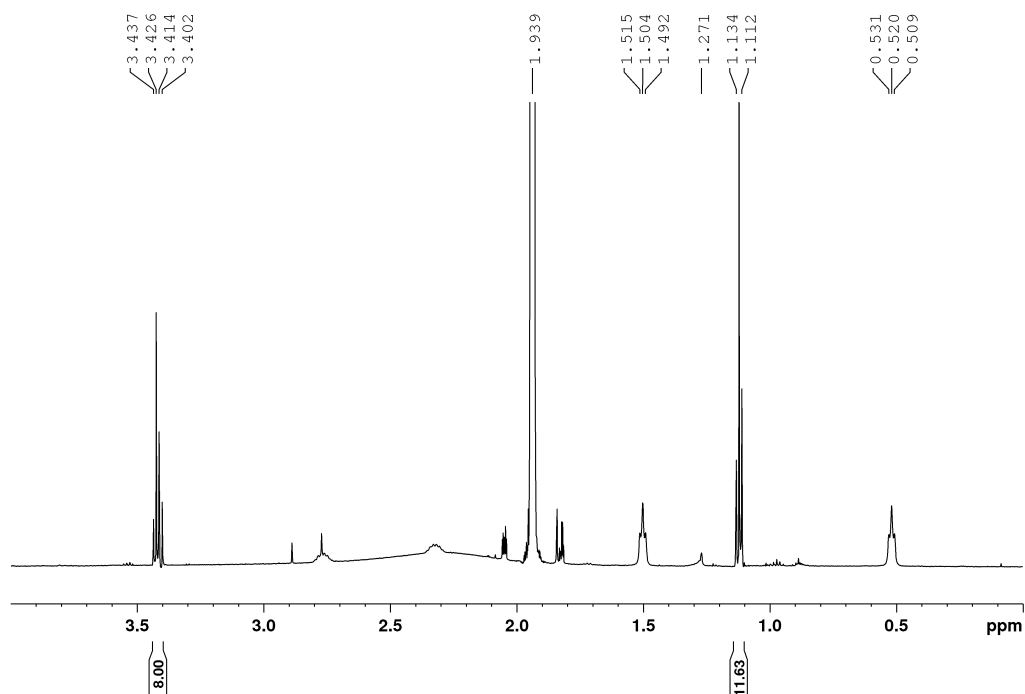
Figure B.10. Narrow view of ^{1}H NMR of **14** *trans*-[Re(PEt$_2$Ph)$_2$(sal$_2$ibn)][PF$_6$] in CD$_3$CN (600 MHz, calibrated to residual CHD$_2$CN at 1.94 ppm).

^{1}H NMR [600 MHz, CD$_3$CN, r.t., δ (ppm)]: 83.34 (s, 1H, -**CH**=N-); 55.92 (s, 1H, -**CH**=N-); 27.94 (d, *J* = 8.2 Hz, 1H, Ar**H**); 27.64 (d, *J* = 8.5 Hz, 1H, Ar**H**); 17.48 (t, *J* = 6.6 Hz, 1H, Ar**H**); 17.15 (t, *J* = 7.5 Hz, 1H, Ar**H**); 13.62 (d, *J* = 7.5 Hz, 4H, P**Ph** *ortho*); 9.20 (t, *J* = 7.4 Hz, 2H, P**Ph** *para*); 8.42 (t, *J* = 7.6 Hz, 4H, P**Ph** *meta*); 3.41 (q, *J* = 6.7 Hz, 8H, PC**H$_2$**CH$_3$); 1.12 (t, *J* = 6.6 Hz, 12H, PCH$_2$C**H$_3$**); -2.53 (s, 6H, -C(C**H$_3$**)$_2$CH$_2$-); -6.41 (t, *J* = 8.2 Hz, 1H, Ar**H**); -7.57 (t, *J* = 8.2 Hz, 1H, Ar**H**); -18.51 (d, *J* = 7.2 Hz, 1H, Ar**H**); -20.29 (d, *J* = 7.1 Hz, 1H, Ar**H**); -28.65 (s, 2H, -C(CH$_3$)$_2$C**H$_2$**-).
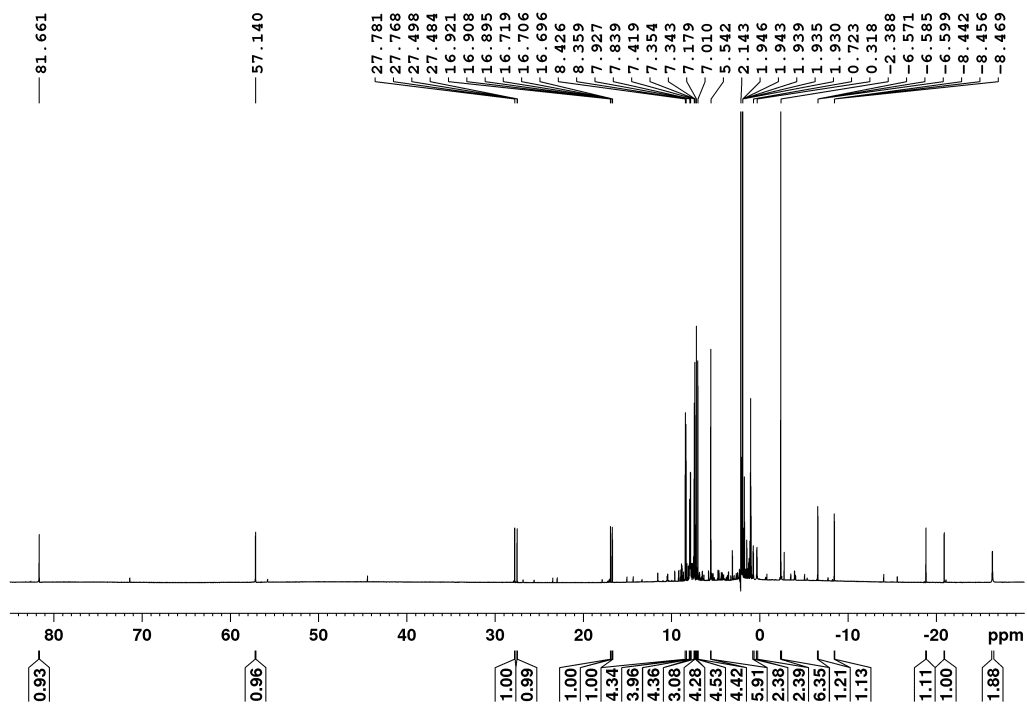
Figure B.11. Full view of ^{1}H NMR of **15** *trans*-[Re(PEtPh$_2$)$_2$(sal$_2$ibn)][PF$_6$] in CD$_3$CN

(600 MHz, calibrated to residual CHD$_2$CN at 1.94 ppm).

Figure B.12. Narrow view of ^{1}H NMR of **15** *trans*-[Re(PEtPh$_2$)$_2$(sal$_2$ibn)][PF$_6$] in CD$_3$CN (600 MHz, calibrated to residual CHD$_2$CN at 1.94 ppm).

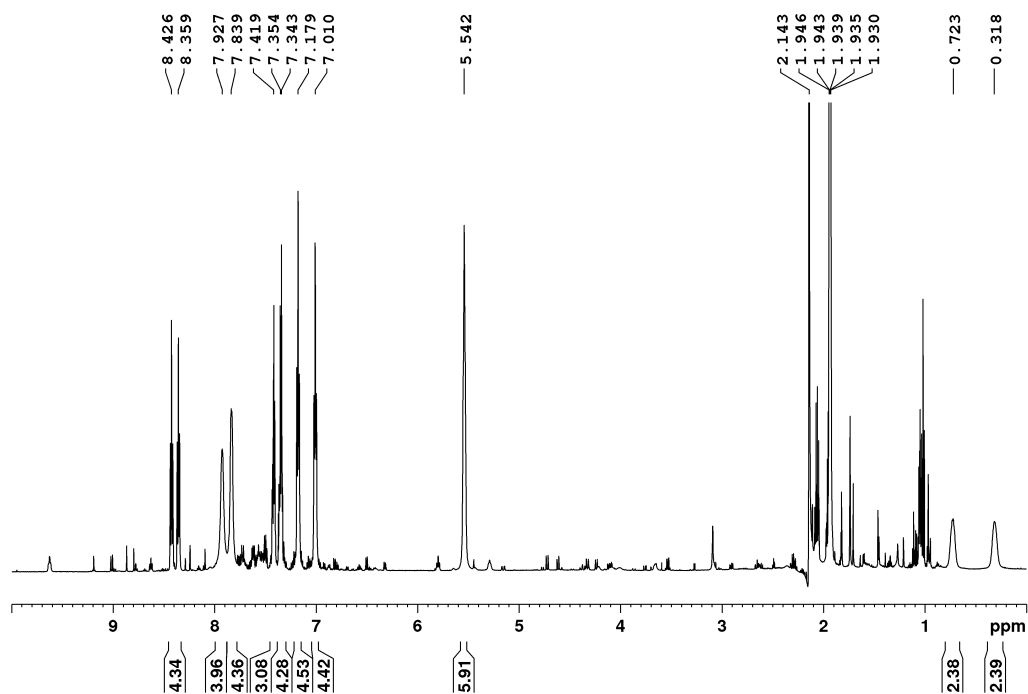^{1}H NMR [600 MHz, CD$_3$CN, r.t., δ (ppm)]: 81.68 (s, 1H, -C**H**=N-); 57.17 (s, 1H, -C**H**=N-); 27.78 (d, J = 8.2 Hz, 1H, Ar**H**); 27.50 (d, J = 8.2 Hz, 1H, Ar**H**); 16.91 (t, J = 7.6 Hz, 1H, Ar**H**); 16.71 (t, J = 7.4 Hz, 1H, Ar**H**); 8.43 (t, J = 7.6 Hz, 2H, P**Ph** para); 8.36 (t, J = 7.3 Hz, 2H, P**Ph** para); 7.93 (br s, 4H, P**Ph** ortho); 7.84 (br s, 4H, P**Ph** ortho); 7.18 (t, J = 7.6 Hz, 4H, P**Ph** meta); 7.01 (t, J = 7.4 Hz, 4H, P**Ph** meta); 5.54 (m, 6H, PCH$_2$C**H$_3$**); 0.72 (br s, 2H, PC**H$_2$**CH$_3$); 0.31 (br s, 2H, PC**H$_2$**CH$_3$); -2.39 (s, 6H, -C(C**H$_3$**)$_2$CH$_2$-); -6.59 (t, J = 8.2 Hz, 1H, Ar**H**); -8.46 (t, J = 8.2 Hz, 1H, Ar**H**); -18.85 (d, J = 7.3 Hz, 1H, Ar**H**); -20.92 (d, J = 7.3 Hz, 1H, Ar**H**); -26.39 (s, 2H, -C(CH$_3$)$_2$C**H$_2$**-).
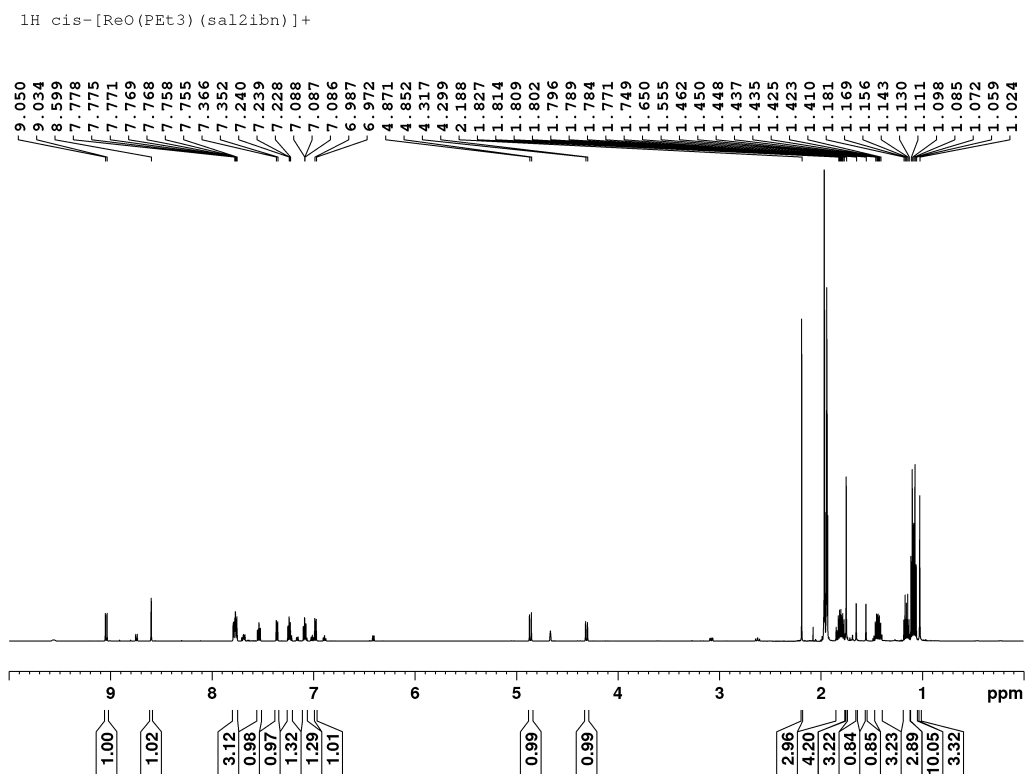
Figure B.13. ^{1}H NMR of **16** *cis*-[ReO(PEt$_3$)(sal$_2$ibn)][PF$_6$] in CD$_3$CN (500 MHz, calibrated to residual CHD$_2$CN at 1.94 ppm).

^{1}H NMR [600 MHz, CD$_3$CN, r.t., δ (ppm)]: 9.04 (d, *J* = 9.7 Hz, 1H, -**H**C=N-); 8.60 (s, 1H, -**H**C=N-); 7.75-7.79 (m, Ar**H**, 3H); 7.52-7.55 (m, Ar**H,** 1H); 7.35 (m, 1H, Ar**H**); 7.24 (m, 1H, Ar**H**); 7.09 (m, Ar**H**, 1H); 6.98 (d, *J* = 8.5 Hz, 1H, Ar**H**); 4.86 (d, *J* = 11.1 Hz, 1H, -NC**H**$_2$-C(CH$_3$)); 4.30 (d, *J* = 11.0 Hz, 1H, -NC**H**$_2$-C(CH$_3$)); 1.77-1.85 (m, 3H, PC**H**$_2$CH$_3$); 1.75 (s, 3H, -C**H$_3$**); 1.41-1.46 (m, 1H, PC**H**$_2$CH$_3$); 1.06-1.11 (m, 9H, PCH$_2$C**H$_3$**) 1.02 (s, 3H, -C**H$_3$**).
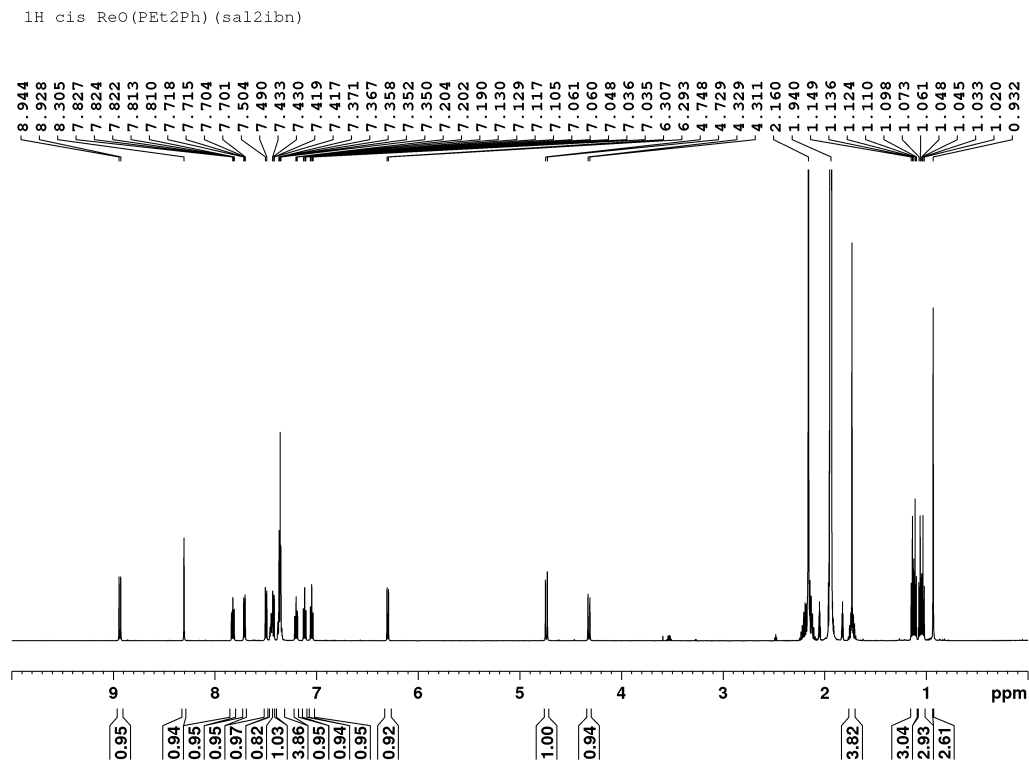
Figure B.14. ¹H NMR of **17** *cis*-[ReO(PEt₂Ph)(sal₂ibn)][PF₆] in CD₃CN (500 MHz, calibrated to residual CHD₂CN at 1.94 ppm).

¹H NMR [600 MHz, CD₃CN, r.t., δ (ppm)]: 8.94 (d, 1H, **-H**C=N-); 8.05 (s, 1H, **-H**C=N-); 7.82 (m, *J* = 1.4, 7.7 Hz, 1H, Ar**H**); 7.72, 7.70 (dd, *J* = 1.8, 7.9 Hz, 1H, Ar**H**); 7.50, 7.49 (d, *J* =8.4 Hz, 1H, Ar**H**); 7.47-7.45 (m, 1H, P**Ph** *para*); 7.37-7.35 (m, 4H, P**Ph**); 7.43, 7.42 (dd, *J* = 1.7, 8.0 Hz, 1H, Ar**H**); 7.20 (m, *J* = 1.7, 6.3 Hz, 1H, Ar**H**); 7.12 (m, *J* = 1.1, 7.5 Hz, 1H, Ar**H**); 7.05 (m, *J* = 1.0, 7.5 Hz, 1H, Ar**H**); 6.31, 6.29 (d, *J* = 8.5 Hz, 1H, Ar**H**); 4.75, 4.73 (d, *J* = 11 Hz, 1H, -NC**H₂**-C(CH₃)); 4.33, 4.31 (d, *J* = 11 Hz, 1H, -NC**H₂**-C(CH₃)-); 2.20-2.08 (m, 4H, PC**H₂**CH₃); 1.76 (s, 3H, -C**H₃**); 1.15-1.02 (d of d of t, *J* = 7.5 Hz, 6H, PCH₂C**H₃**); 1.01 (s, 3H, -C**H₃**).

1H cis-[ReO(PEtPh2)(sal2ibn)][PF6]

Figure B.15. ^{1}H NMR of **18** *cis*-[ReO(PEtPh₂)(sal₂ibn)][PF₆] in CD₃CN (500 MHz, calibrated to residual CHD₂CN at 1.94 ppm).

^{1}H NMR [500 MHz, CD₃CN, r.t., δ (ppm)]: 8.95 (d, *J* = 10 Hz, 1H, -**H**C=N-); 8.20 (s, 1H, -**H**C=N-); 7.87-6.99 (m, Ar**H,** 8H); 7.53-7.36 (m, P**Ph**, 10H); 4.69 (d, *J* = 11 Hz, 1H, -NC**H₂**-C(CH₃)); 4.33 (d, *J* = 11 Hz, 1H, -NC**H₂**-C(CH₃)); 2.68-2.58 (m, 1H, PC**H₂**CH₃); 2.25-2.15 (m, 1H, PC**H₂**CH₃); 1.73 (s, 3H, -**CH₃**); 1.15-1.02 (d of t, *J* = 7.5 Hz, 3H, PCH₂C**H₃**) 0.96 (s, 3H, -**CH₃**).
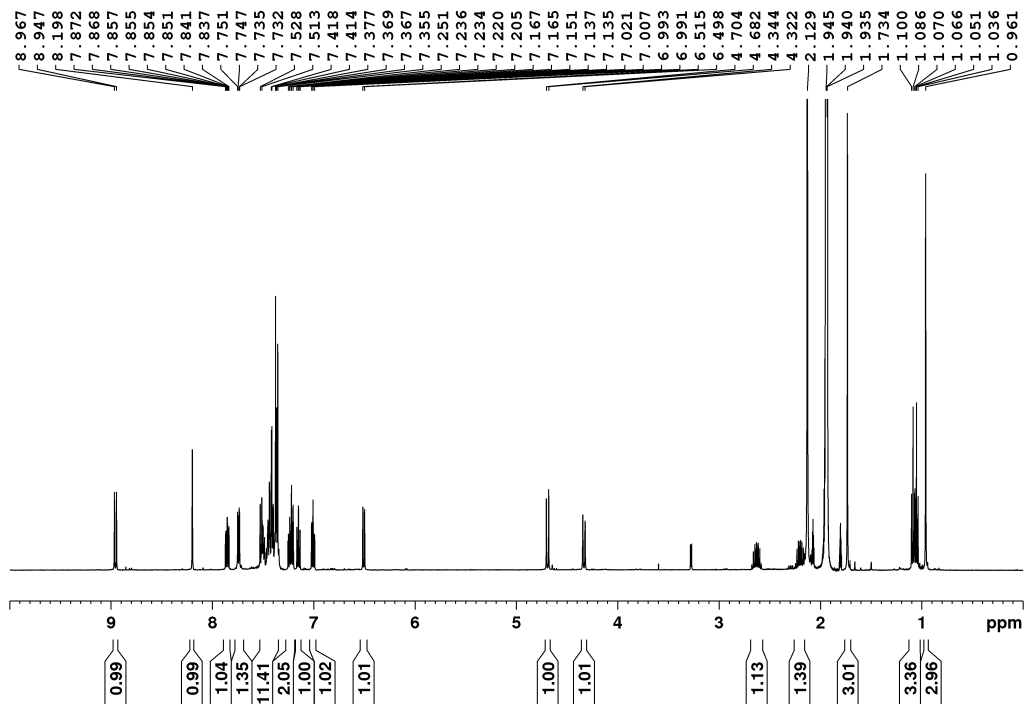
Figure B.16. ^{1}H NMR of **19** *cis*-[ReO(PPh₃)(sal₂ibn)][PF₆] in CD₃CN (600 MHz, calibrated to residual CHD₂CN at 1.94 ppm).
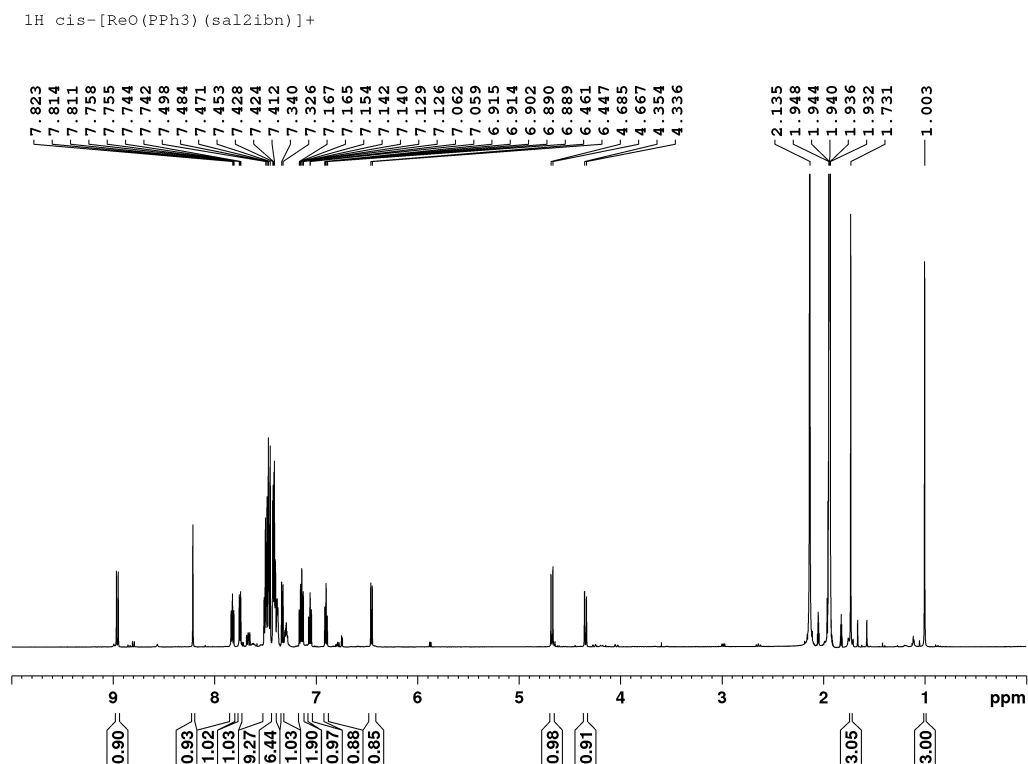
^{1}H NMR [600 MHz, CD₃CN, r.t., δ (ppm)]: 8.96 (d, *J* = 10 Hz, 1H, 8.22 (-**H**C=N-); 7.84-7.74, 7.34-6.44 (m, Ar**H**); 7.52-7.39 (m, P**Ph**, 15H); 4.67 (d, *J* = 11 Hz, 1H, -NC**H₂**-C(CH₃)); 4.34 (d, *J* = 11 Hz, 1H, -NC**H₂**-C(CH₃)); 1.73 (s, 3H, -**CH₃**); 1.00 (s, 3H, -**CH₃**).
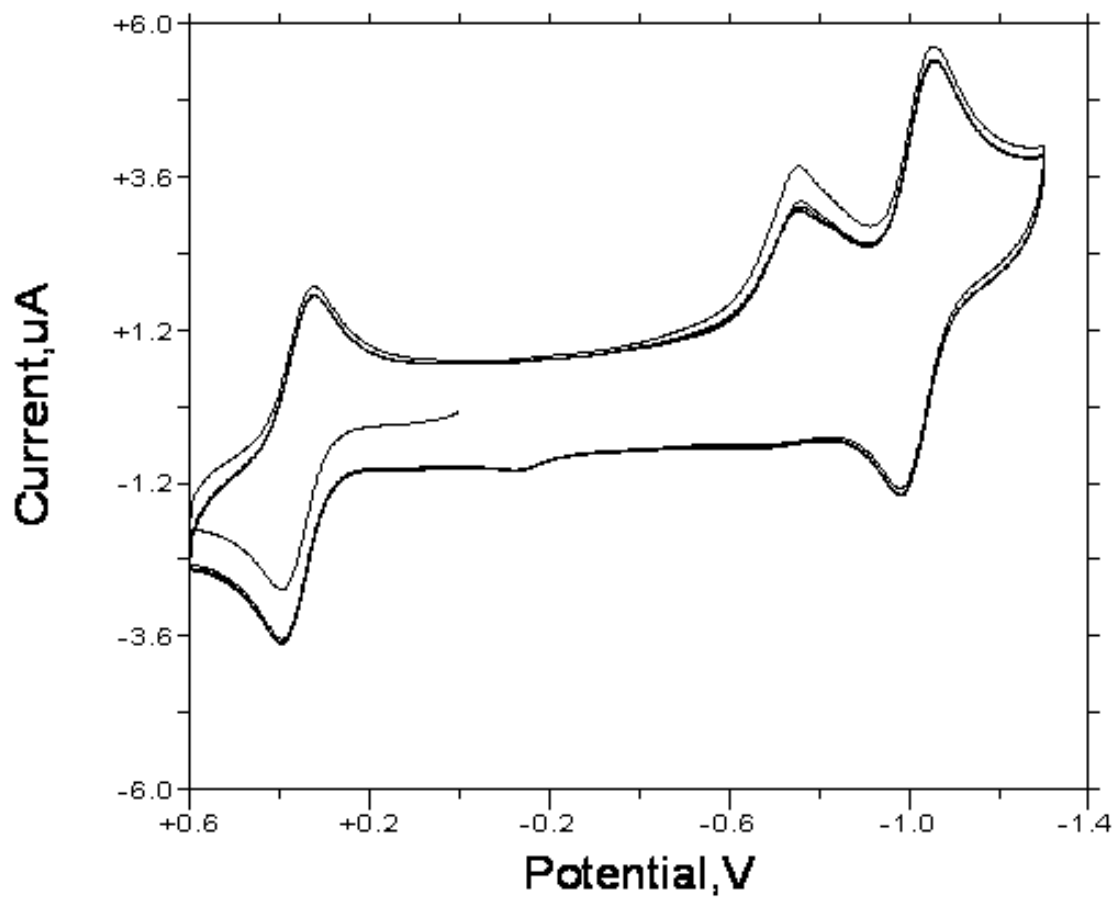
Figure B.17. Cyclic voltammogram (CV) for *trans*-[Re(PEt$_3$)$_2$(sal$_2$en)][PF$_6$] **10**
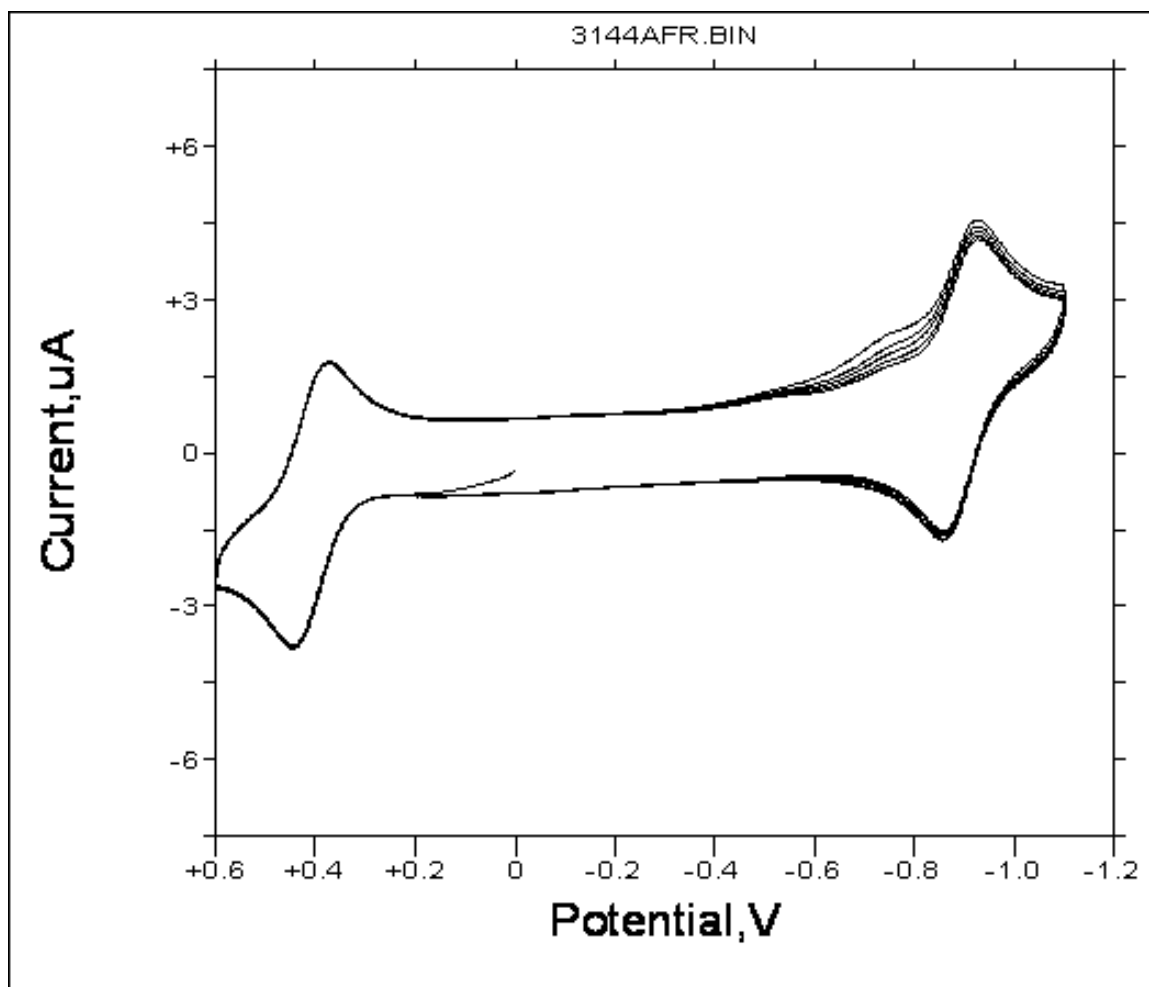
Figure B.18. Repetitive CV for *trans*-[Re(PEtPh$_2$)$_2$(sal$_2$en)][PF$_6$] **11**
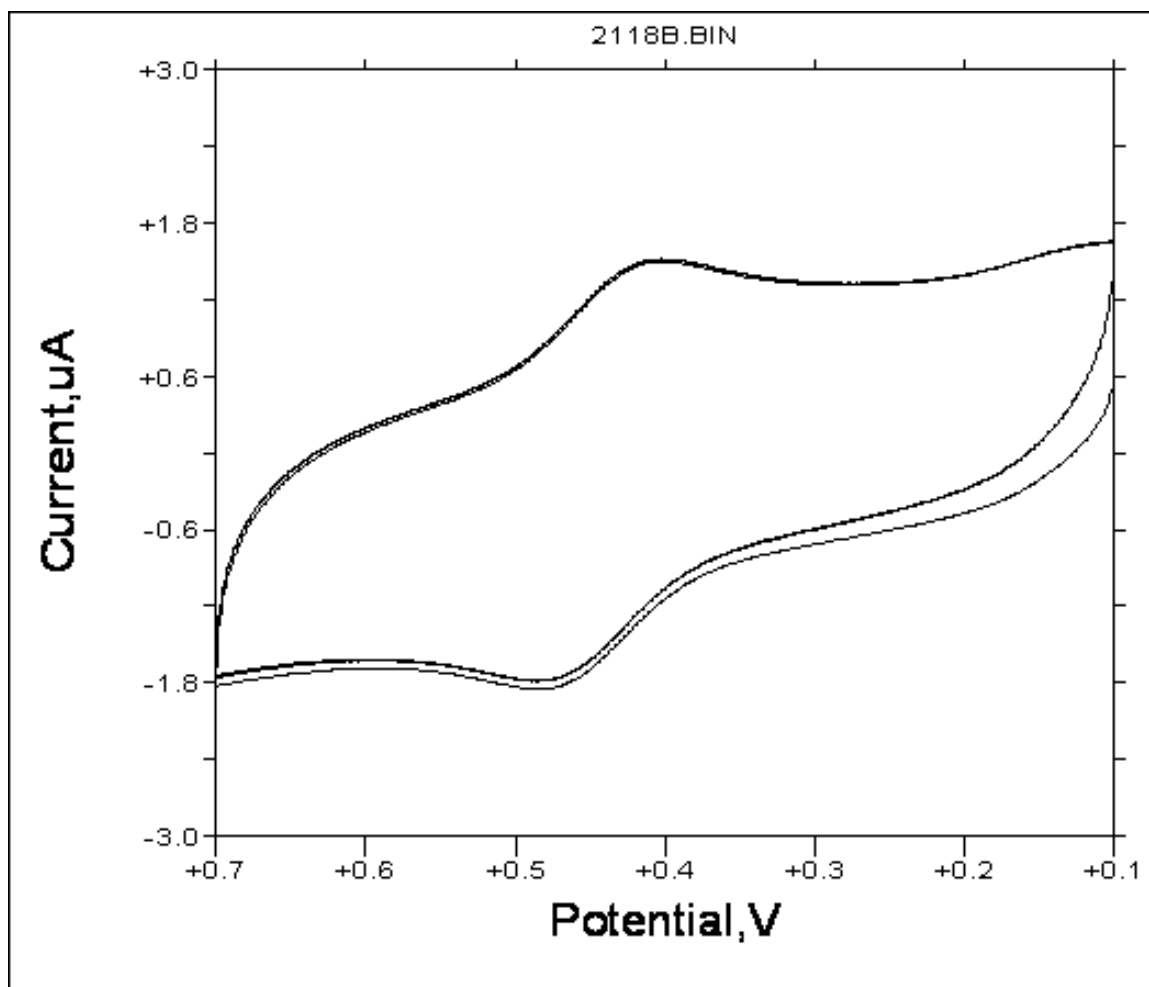
Figure B.19. Repetitive CV for *trans*-[Re(PPh$_3$)$_2$(sal$_2$en)][PF$_6$], **12**, in the region +0.1 to +0.7 V.
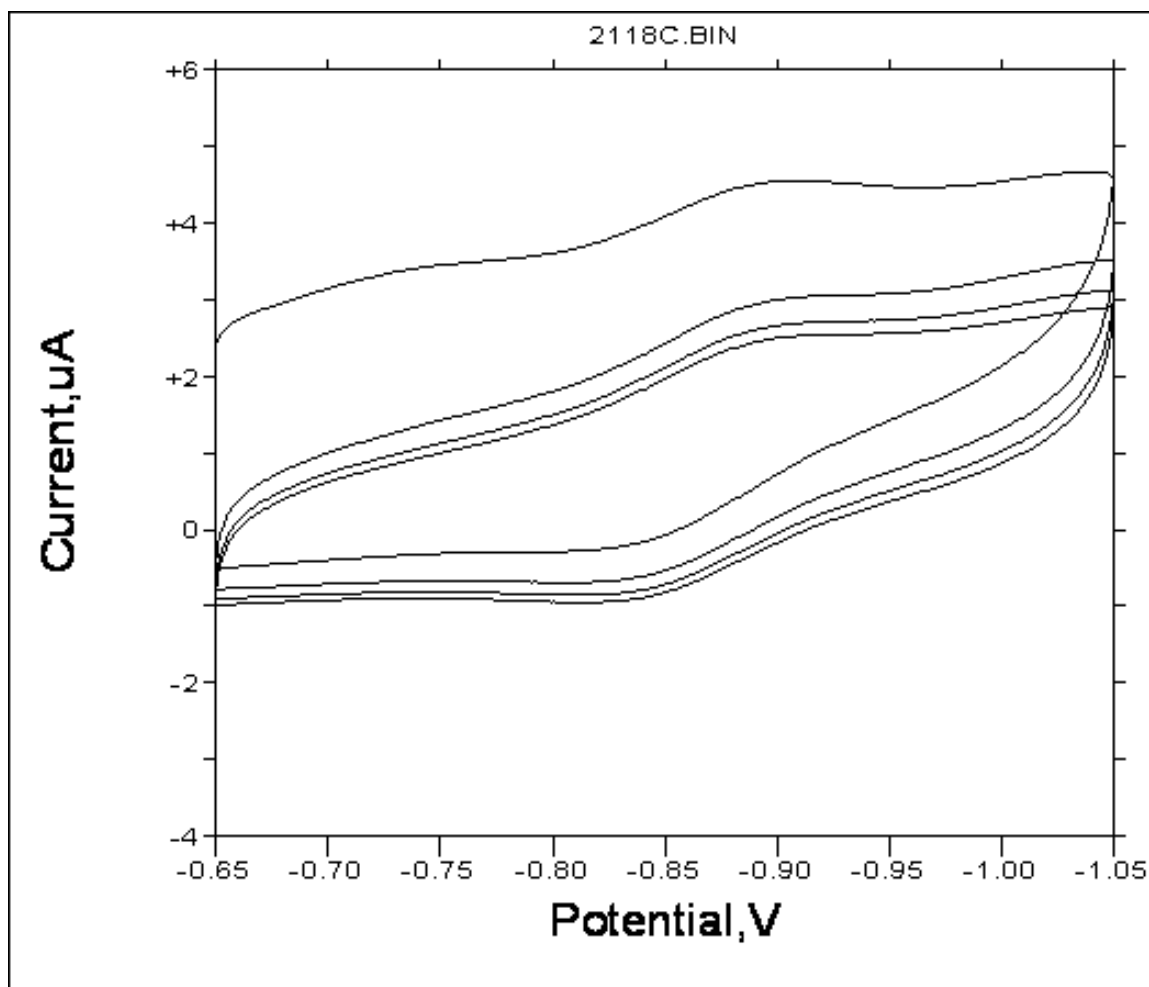
Figure B.20. Repetitive CV for *trans*-[Re(PPh$_3$)$_2$(sal$_2$en)][PF$_6$], **12**, in the region -1.05 to -0.65 V.
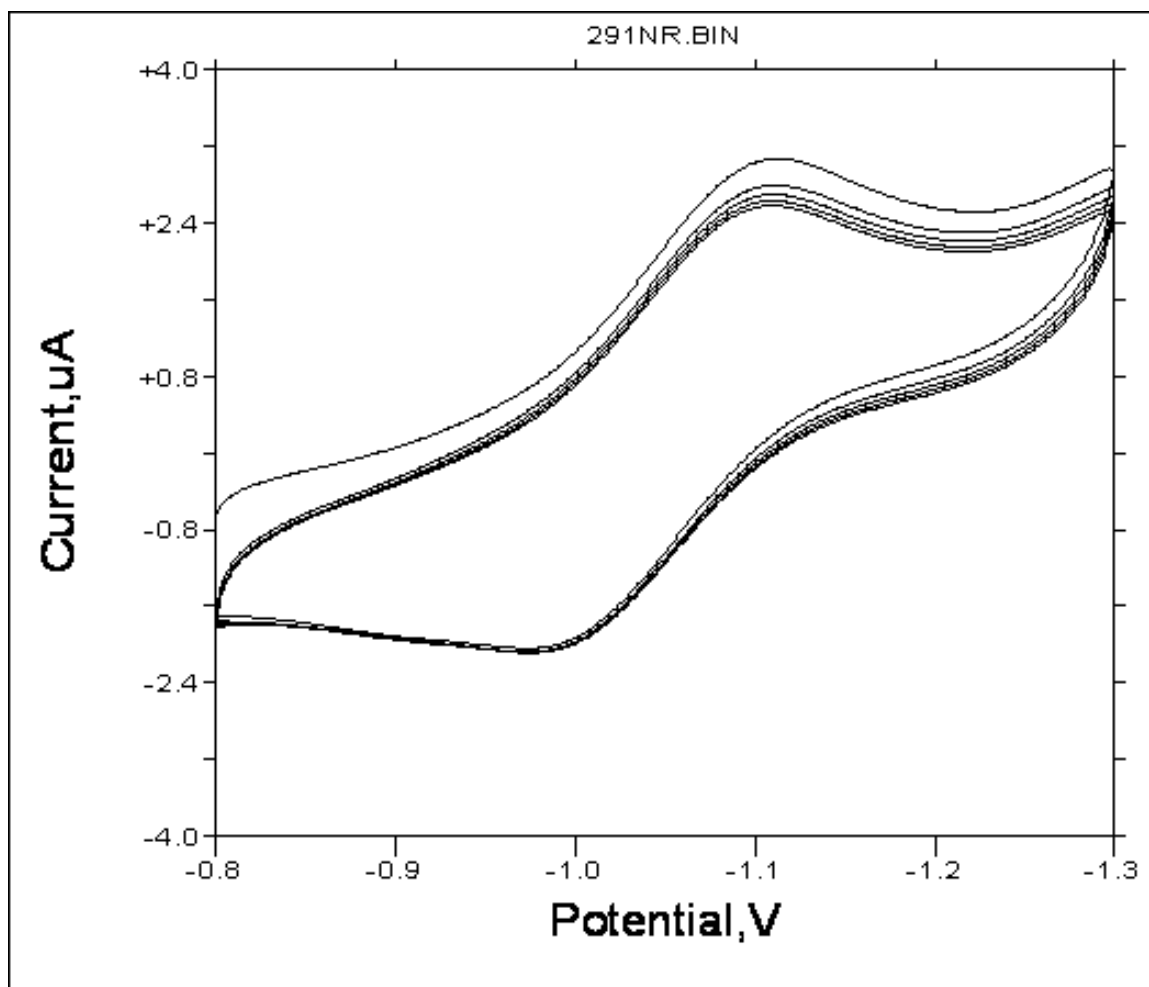
Figure B.21. Repetitive CV for *trans*-[Re(PEt$_3$)$_2$(sal$_2$ibn)][PF$_6$] **13** in the region -1.3 to -0.8 V.
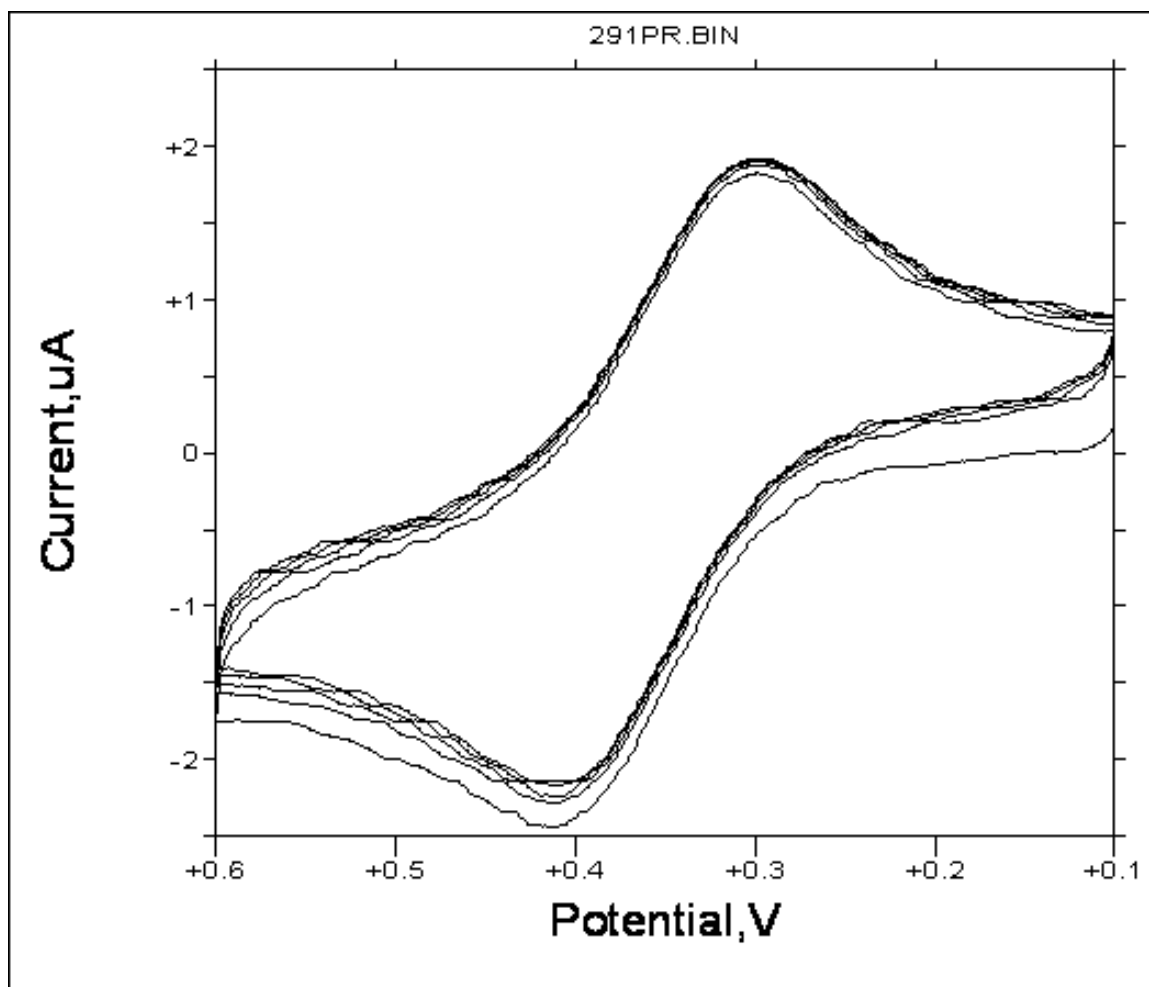
Figure B.22. Repetitive CV for *trans*-[Re(PEt$_3$)$_2$(sal$_2$ibn)][PF$_6$] **13** in the region +0.1 to +0.6 V.
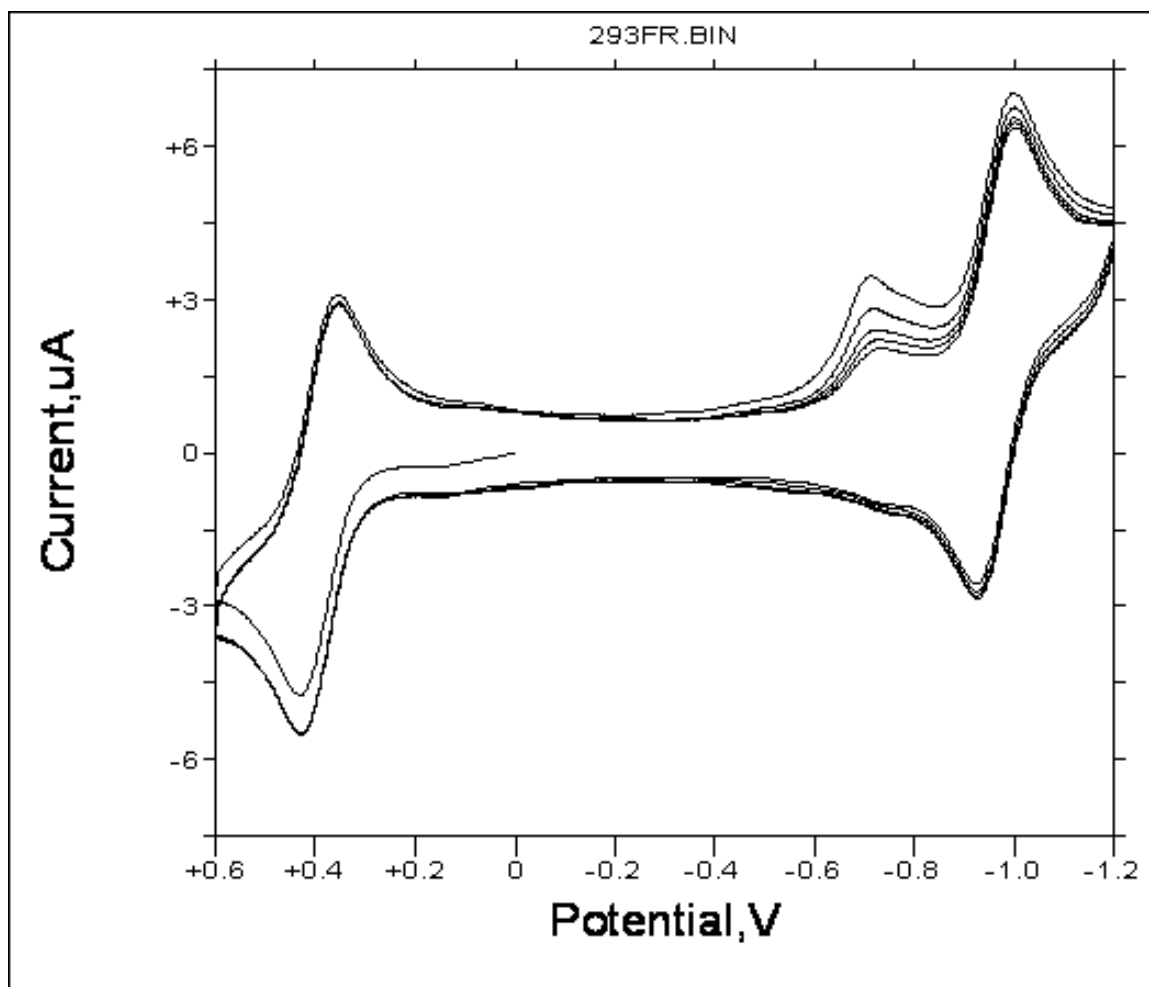
Figure B.23. Repetitive CV for *trans*-[Re(PEtPh$_2$)$_2$(sal$_2$ibn)][PF$_6$] **14**

1.   Sheldrick, G. M., *Acta Crystallogr. A* **2015,** *71*, 3-8.
2.   Sheldrick, G. M. *SHELXS, v.2013-1*, 2013.
3.   Sheldrick, G. M., *Acta Crystallogr. C* **2015,** *71*, 3-8.
4.   Thorn, A.; Dittrich, B.; Sheldrick, G. M., *Acta Crystallogr. A* **2012,** *68*, 448-451.
5.   Spek, A. L., *Acta Crystallogr. C* **2015,** *71*, 9-18.

APPENDIX C

Supporting Information for CHAPTER 4

Synthesis and Radiolabelling of Q-compounds with Backbone-functionalized N_2O_2 Schiff Base Ligands

C1. ^{1}H-NMR spectra for compounds H_2sal_2ppa, H_2sal_2bza-Bn, and **20-24**

C2. Cyclic voltammograms for compounds **20-23**
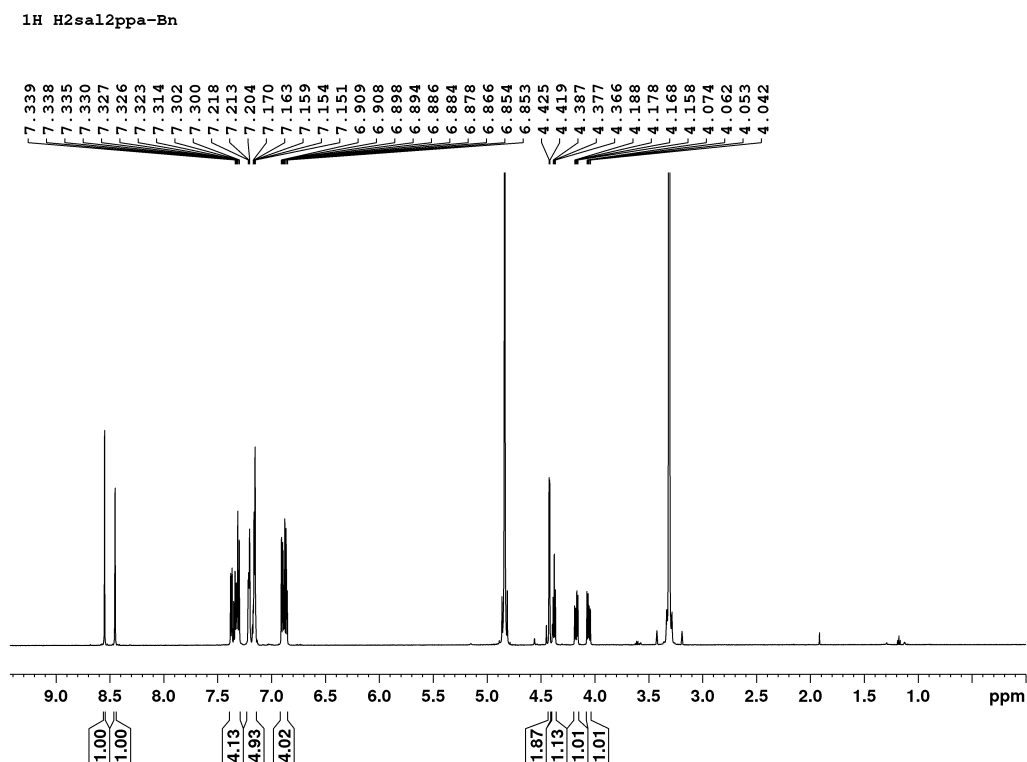
1H H2sal2ppa-Bn

Figure C.1. ¹H NMR of H₂sal₂ppa-Bn in CD₃OD (600 MHz, calibrated to residual CHD₂COD at 3.31 ppm).

¹H NMR [600 MHz, CD₃OD, r.t., δ (ppm)]: 8.55 (s, 1H, -**CH**=N-); 8.45 (s, 1H, -**CH**=N-); 7.30-7.38 (m, 4H, Ar**H**); 7.15-7.22 (m, 5H, -CH₂(C₆**H₅**)); 6.85-6.91 (m, 4H, **ArH**); 4.43 (s, 2H, -**CH₂**(C₆H₅)); 4.39 (t, 1H, **CH**), 4.05-4.20 (m, 2H, **CH₂**).
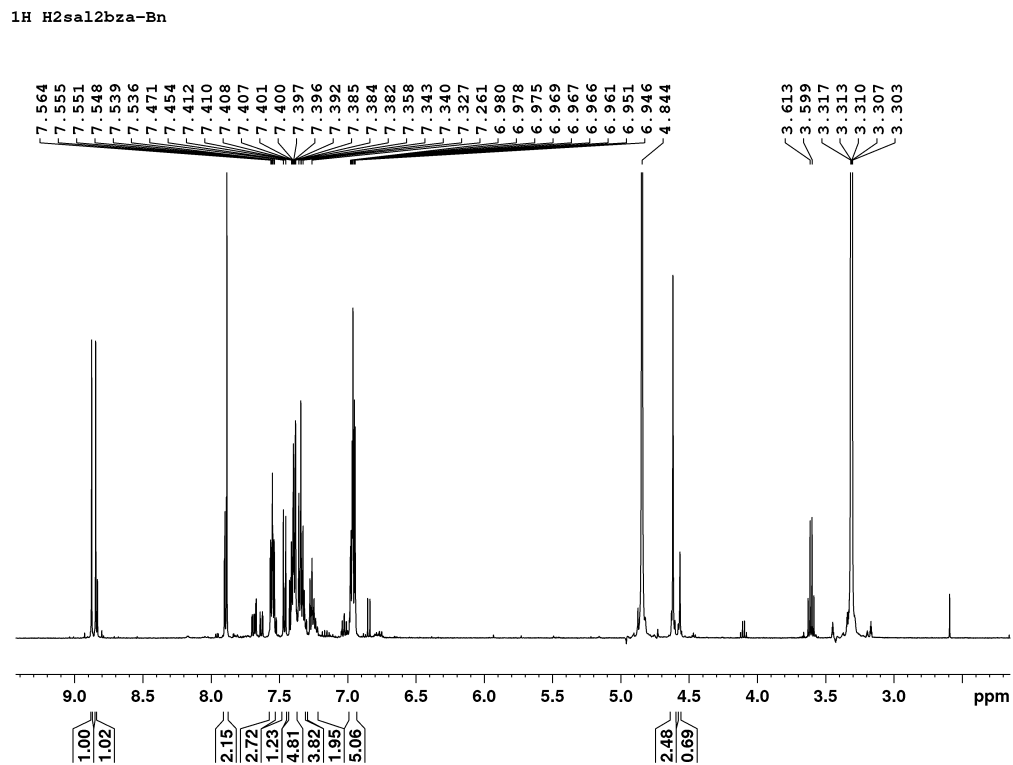
Figure C.2. ^{1}H NMR of H$_2$sal$_2$bza-Bn in CD$_3$OD (600 MHz, calibrated to residual CHD$_2$COD at 3.31 ppm).

^{1}H NMR [600 MHz, CD$_3$OD, r.t., δ (ppm)]: 8.87 (s, 1H, -**CH**=N-); 8.84 (s, 1H, -**CH**=N-); 7.90-6.95 (m, 16H, Ar**H**); 4.62 (s, 2H, -**CH$_2$**-).
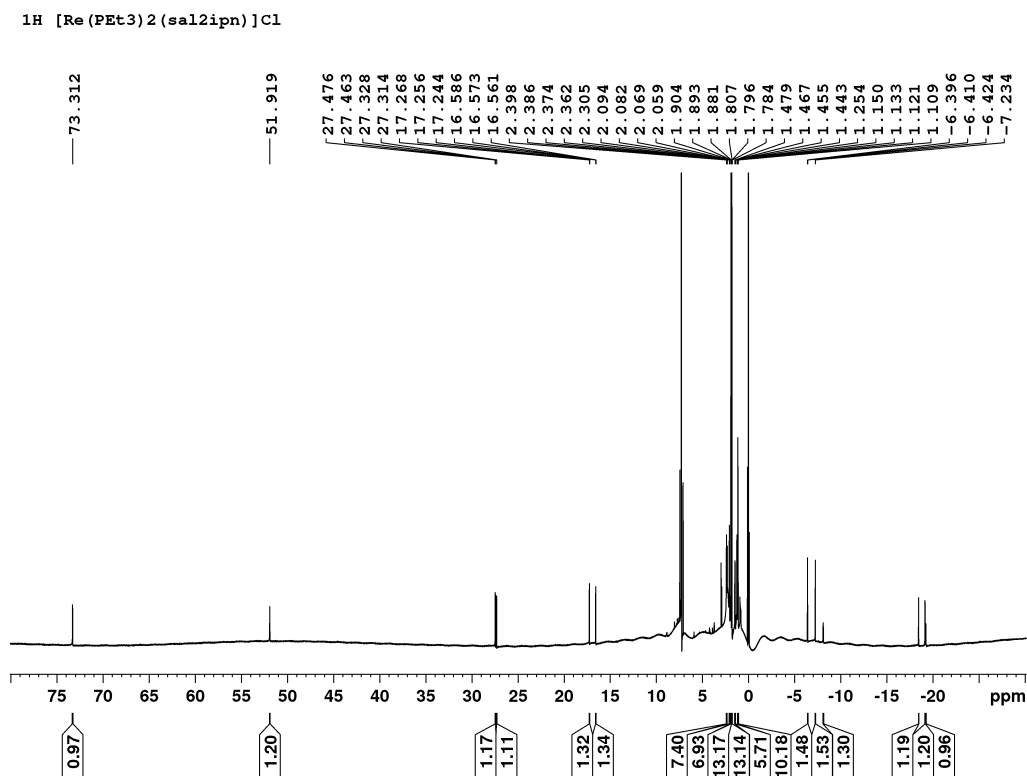
Figure C.3. Full-view ^{1}H NMR of **20** *trans*-[Re(PEt$_3$)(sal$_2$ipn)]Cl in CDCl$_3$ (600 MHz, calibrated to residual CHCl$_3$ at 7.26 ppm).

^{1}H NMR [600 MHz, CDCl$_3$, r.t., δ (ppm)]: 73.31 (s, 1H, -**CH**=N-); 51.92 (s, 1H, -**CH**=N-); 27.47 (d, *J* = 8.3 Hz, 1H, Ar**H**); 27.32 (d, *J* = 8.3 Hz, 1H, Ar**H**); 17.26 (t, *J* = 7.3 Hz, 1H, Ar**H**); 16.57 (t, *J* = 7.3 Hz, 1H, Ar**H**); 1.89 (t, 9H, PCH$_2$**CH$_3$**); 1.80 (t, 9H, PCH$_2$**CH$_3$**); 1.46 (m, 6H, P**CH$_2$**CH$_3$); 1.25 (s, 1H, -NCH$_2$**CH**(CH$_3$)N-); 1.15 (m, 3H, -NCH$_2$CH(**CH$_3$**)N-); 1.12 (m, 6H, P**CH$_2$**CH$_3$); -6.41 (t, *J* = 8.3 Hz, 1H, Ar**H**); -7.25 (t, *J* = 8.1 Hz, 1H, Ar**H**); -8.11 (s, 1H, -N**CH$_2$**CH(CH$_3$)N-); -18.45 (d, *J* = 6.8 Hz, 1H, Ar**H**); -19.15 (d, *J* = 6.0 Hz, 1H, Ar**H**); -19.23 (s, 1H, -N**CH$_2$**CH(CH$_3$)N-).

Figure C.4. Narrow-view ^{1}H NMR of **20** *trans*-[Re(PEt$_3$)(sal$_2$ipn)]Cl in CDCl$_3$ (600 MHz, calibrated to residual CHCl$_3$ at 7.26 ppm).
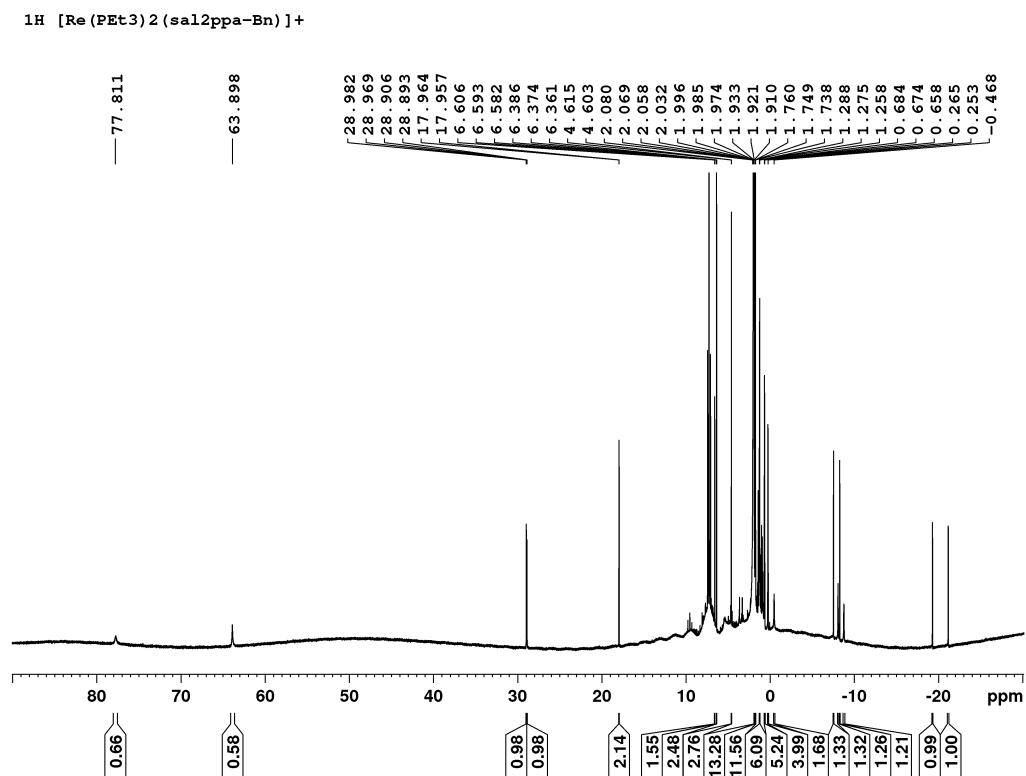
Figure C.5. Full-view ¹H NMR of **21** *trans*-[Re(PEt₃)(sal₂ppa-Bn)]Cl in CDCl₃ (600 MHz, calibrated to residual CHCl₃ at 7.26 ppm).

¹H NMR [600 MHz, CDCl₃, r.t., δ (ppm)]: 77.88 (s, 1H, -**CH**=N-); 63.90 (s, 1H, -**CH**=N-); 28.97 (d, 1H, Ar**H**); 28.90 (d, 1H, Ar**H**); 17.96 (m, 2H, Ar**H**); 6.59 (t, 1H, Bz**H** *para*); 6.37 (t, 2H, Bz**H** meta); 4.61 (d, 2H, Bz**H** ortho); 1.92, 1.75 (d of t, 18H, P(CH₂C**H₃**)₃); 1.28 (m, 5H, P(C**H₂**CH₃)₃); 0.67 (m, 4H, P(C**H₂**CH₃)₃); 0.25 (m, 3H, P(C**H₂**CH₃)₃); -0.47 (s, 1H, -NCH₂C(CH₂Bz)**H**-); -7.52 (t, 1H, Ar**H**); -8.06 (s, 1H, -NC**H₂**C(CH₂Bz)H-); -8.26 (t, 1H, Ar**H**); -8.76 (s, 1H, -NCH₂C(CH₂Bz)H-); -19.28 (d, 1H, ArH); -21.16 (d, 1H, ArH).

Figure C.6. Narrow-view ^{1}H NMR of **21** *trans*-[Re(PEt$_3$)(sal$_2$ppa-Bn)][PF$_6$] in CDCl$_3$ (600 MHz, calibrated to residual CHCl$_3$ at 7.26 ppm).
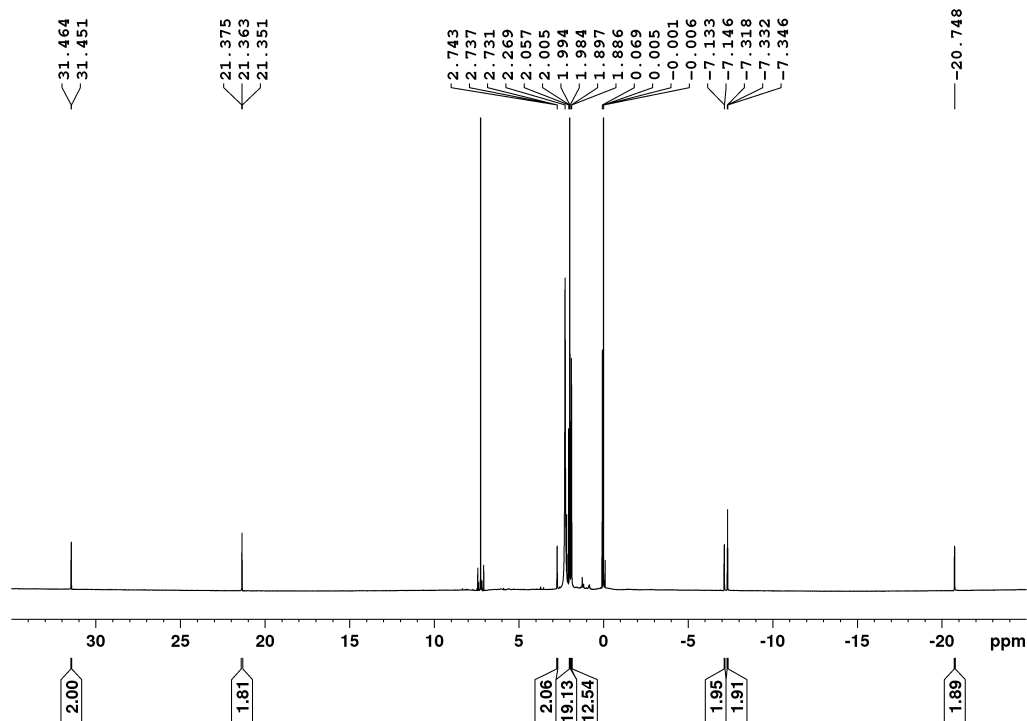
Figure C.7. Full-view ^{1}H NMR of **22** *trans*-[Re(PEt$_3$)(sal$_2$phen)][PF$_6$] in CDCl$_3$ (600 MHz, calibrated to residual CHCl$_3$ at 7.26 ppm).

^{1}H NMR [600 MHz, CDCl$_3$, r.t., δ (ppm)]: 31.45 (d, *J* = 8.0 Hz, 2H, Ar**H**); 21.36 (t, *J* = 7.2 Hz, 2H, Ar**H**); 2.74 (m, 2H, Ar**H**); 1.99 (m, 18H, PCH$_2$C**H$_3$**); 1.89 (m, 12H, PC**H$_2$**CH$_3$); -7.14 (d, *J* = 7.3 Hz, 2H, Ar**H**); -7.33 (t, *J* = 8.3 Hz, 2H, Ar**H**); -20.75 (m, 2H, Ar**H**).
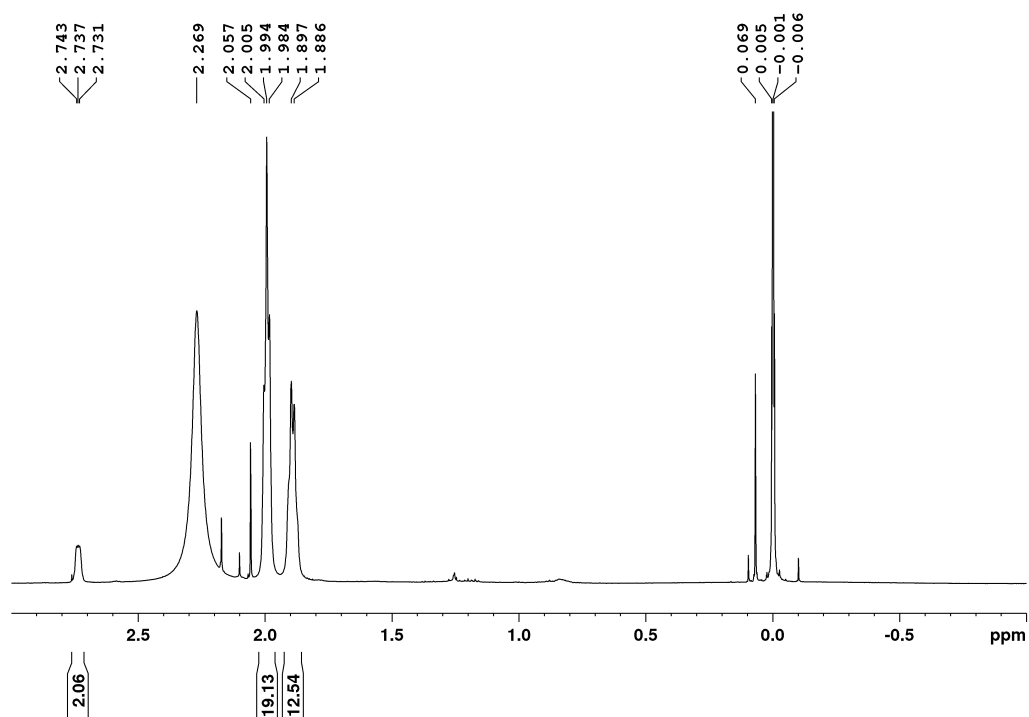
Figure C.8. Narrow-view ^{1}H NMR of **22** *trans*-[Re(PEt$_3$)(sal$_2$phen)]Cl in CDCl$_3$ (600 MHz, calibrated to residual CHCl$_3$ at 7.26 ppm).
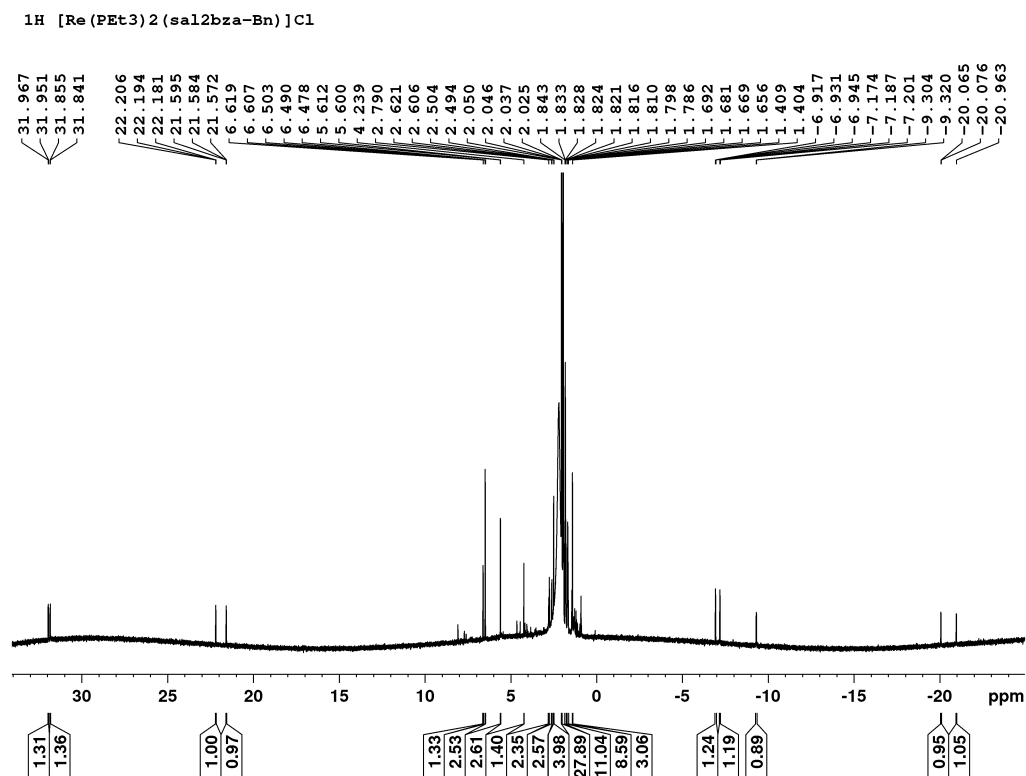
Figure C.9. Full-view ^{1}H NMR of **23** *trans*-[Re(PEt$_3$)(sal$_2$bza-Bn)]Cl in CDCl$_3$ (600 MHz, calibrated to residual CHCl$_3$ at 7.26 ppm).

^{1}H NMR [600 MHz, CD$_3$CN, r.t., δ (ppm)]: 31.96 (d, *J* = 9.1 Hz, 1H, Ar**H**); 31.85 (d, *J* = 8.2 Hz, 1H, Ar**H**); 22.19 (t, *J* = 7.0 Hz, 1H, Ar**H**); 21.58 (t, *J* = 6.8 Hz, 1H, Ar**H**); 6.61 (d, *J* = 7.4 Hz, 1H, Bn**H**); 6.49 (t, *J* = 7.5 Hz, 2H, Bn**H**); 5.61 (d, *J* = 7.3 Hz, 2H, Bn**H**); -6.94 (t, *J* = 8.5 Hz, 1H, Ar**H**); -7.19 (t, *J* = 8.4 Hz, 1H, Ar**H**); -20.07 (d, *J* = 6.6 Hz, 1H, Ar**H**); -20.96 (d, *J* = 6.5 Hz, 1H, Ar**H**).

Figure C.10. Narrow-view ^{1}H NMR of **23** *trans*-[Re(PEt$_3$)(sal$_2$bza-Bn)]Cl in CDCl$_3$ (600 MHz, calibrated to residual CHCl$_3$ at 7.26 ppm).
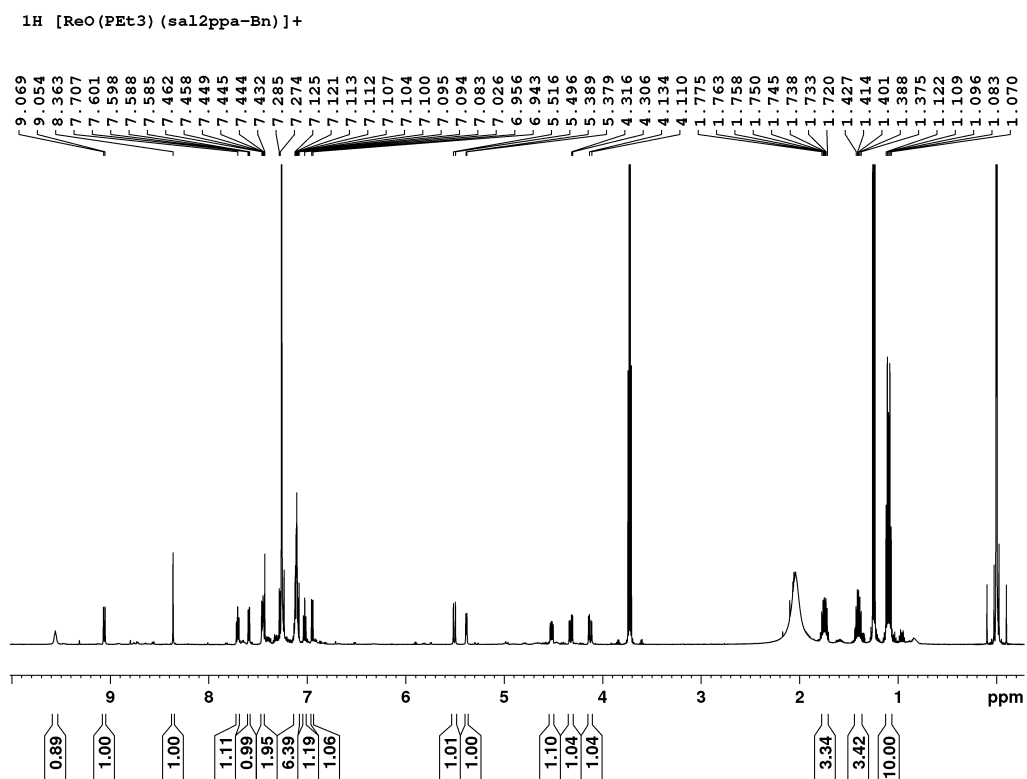
Figure C.11. ^{1}H NMR of **24** *cis*-[ReO(PEt$_3$)(sal$_2$ppa-Bn)]Cl in CDCl$_3$ (600 MHz, calibrated to residual CHCl$_3$ at 7.26 ppm).
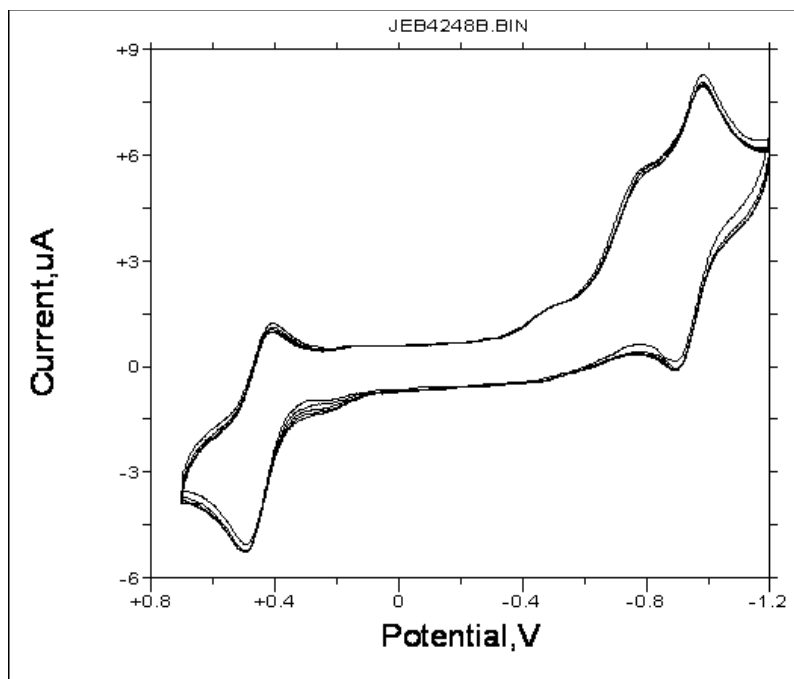
Figure C.12. Repetitive cyclic voltammogram for *trans*-[Re(PEt$_3$)$_2$(sal$_2$ipn)]$^+$, **20**
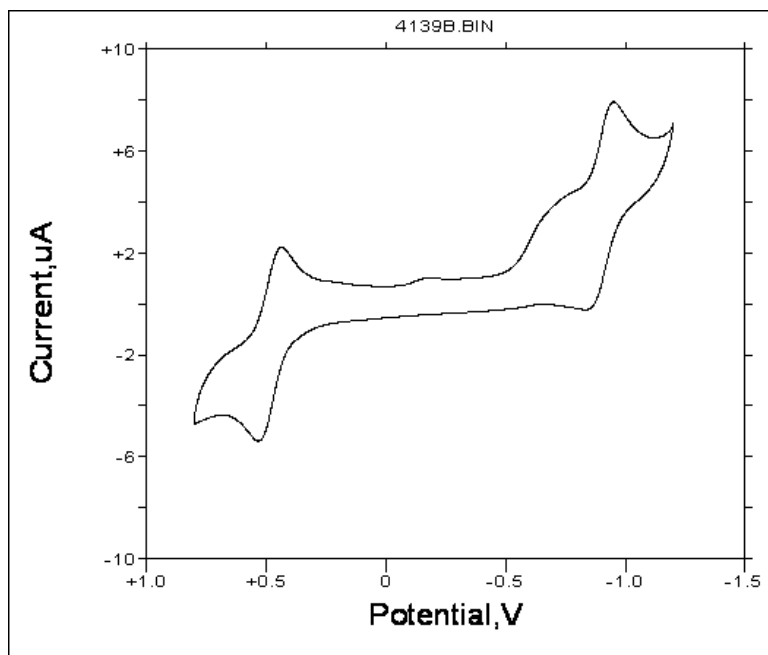
Figure C.13. Cyclic voltammogram for *trans*-[Re(PEt$_3$)$_2$(sal$_2$ppa-Bn)]$^+$, **21**
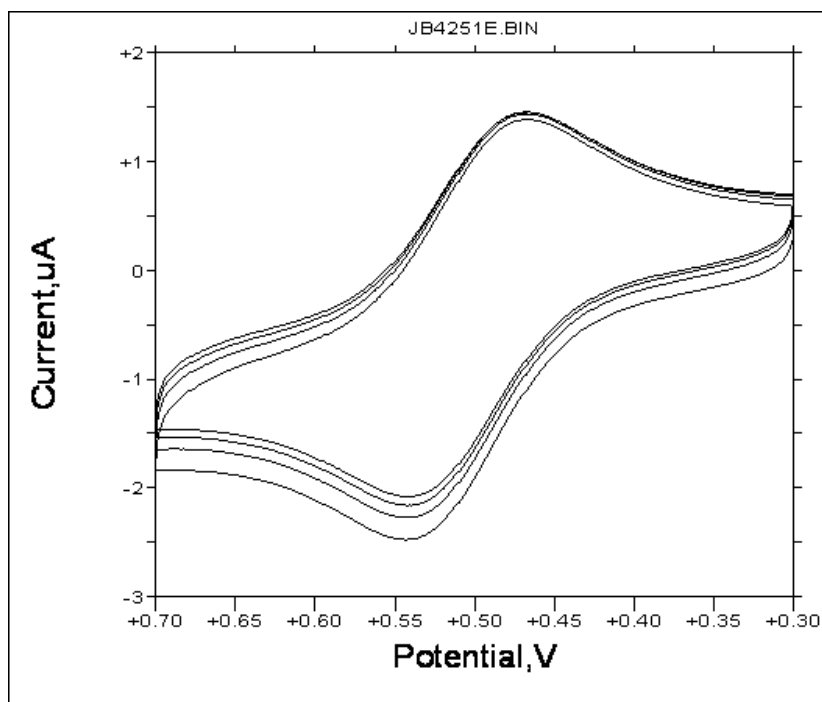
Figure C.14. Repetitive CV for *trans*-[Re(PEt₃)₂(sal₂phen)]⁺, **22**, in the region +0.3 to +0.75 V.
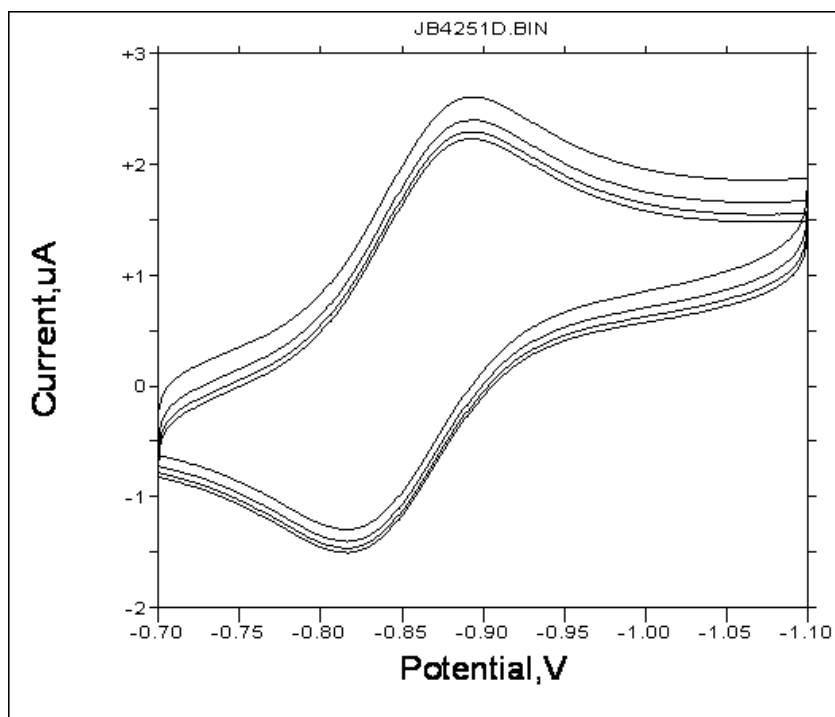
Figure C.15. Repetitive cyclic voltammogram for *trans*-[Re(PEt₃)₂(sal₂phen)]⁺, **22**, in the region -0.7 to -1.1 V.
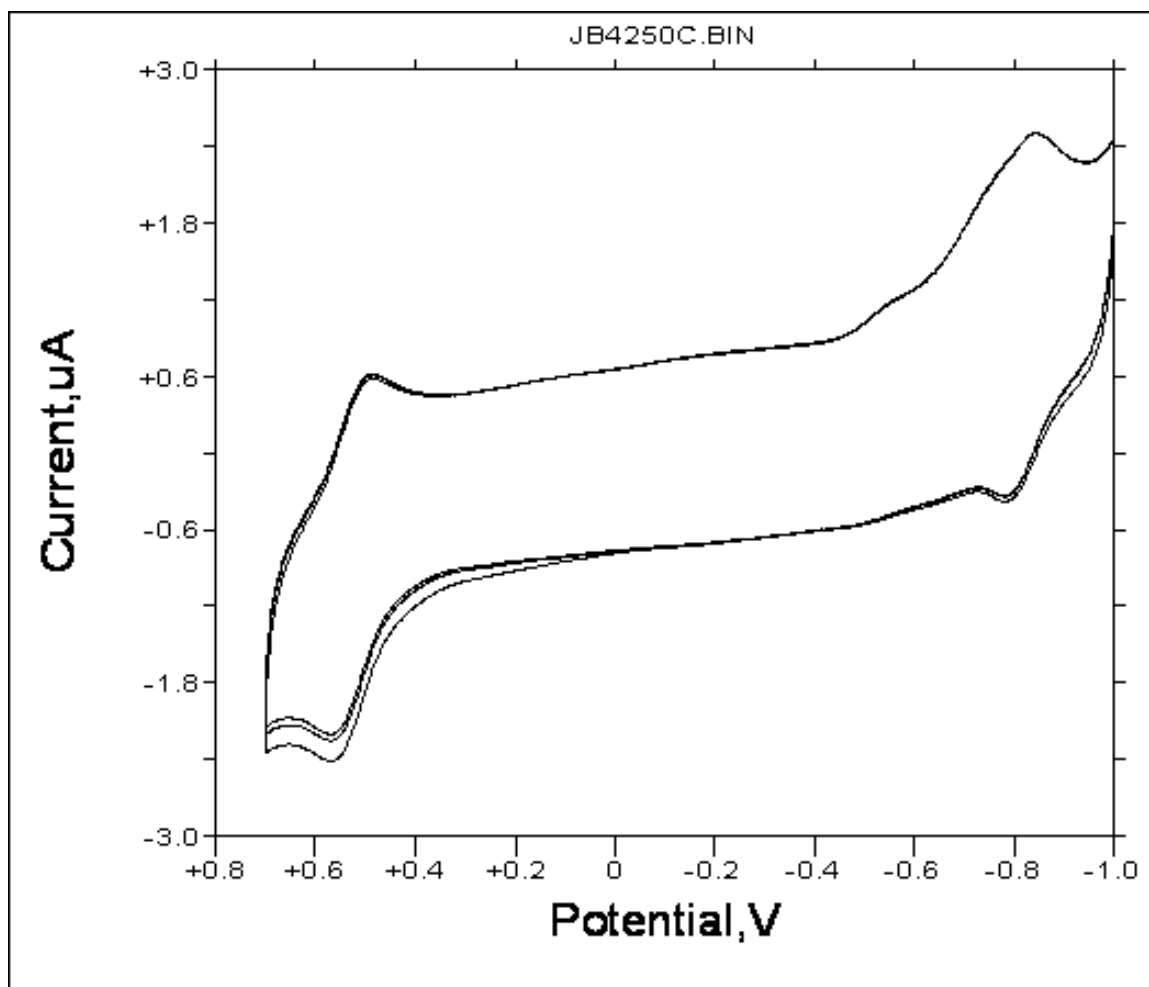
Figure C.16. Cyclic voltammogram for *trans*-[Re(PEt$_3$)$_2$(sal$_2$bza-Bn)]$^+$, **23**

REFERENCES

1.	Hevesy, G. V.; Paneth, F., *Zeitschrift für anorganische Chemie* **1913,** *82*, 323-328.

2.	Chiewitz, O.; Hevesy, G., *Nature* **1935,** *136*, 754-755.

3.	Hevesy, G., *Biochem J* **1923,** *17*, 439-445.

4.	Blumgart, H. L.; Yens, O. C., *J Clin Invest* **1927,** *4*, 1-13.

5.	Lawrence, J. H., *Radiology* **1940,** *35*, 51-60.

6.	Becker, D. V.; Sawin, C. T., *Seminars in Nuclear Medicine* **1996,** *26*, 155-164.

7.	Atkins, H. L.; Srivastava, S. C., *J. Nucl. Med. Technol.* **1998,** *26*, 80-3; quiz 85-6.

8.	Eckelman, W.; Richards, P., *J. Nucl. Med.* **1970,** *11*, 761-761.

9.	Hauser, W.; Atkins, H. L.; Nelson, K. G.; Richards, P., *Radiology* **1970,** *94*, 679-684.

10.	FDA, U. FDA approves new treatment for certain digestive tract cancers. https://www.fda.gov/news-events/press-announcements/fda-approves-new-treatment-certain-digestive-tract-cancers (August 23, 2019),

11.	Association, W. N. Radioisotopes in Medicine. https://www.world-nuclear.org/information-library/non-power-nuclear-applications/radioisotopes-research/radioisotopes-in-medicine.aspx (August 26, 2019),

12.	National Academies of Sciences, E.; Medicine, *Molybdenum-99 for Medical Imaging*. The National Academies Press: Washington, DC, 2016.

13.	Crasta, R.; Naik, H.; Suryanarayana, S. V.; Prajapati, P. M.; Jagadisan, K. C.; Thakare, S. V.; Ganesh, S.; Nimje, V. T.; Mittal, K. C.; Goswami, A., *Journal of Radioanalytical and Nuclear Chemistry* **2011,** *290*, 367.

14.	*Handbook on Photonuclear Data for Applications: Cross-sections and Spectra*. International Atomic Energy Agency: Vienna, 2000.

15.	Qaim, S. M., *Nucl. Med. Biol.* **2017,** *44*, 31-49.

16.	Minato, F.; Tsukada, K.; Sato, N.; Watanabe, S.; Saeki, H.; Kawabata, M.; Hashimoto, S.; Nagai, Y., *Journal of the Physical Society of Japan* **2017,** *86*, 114803.

17.	Wyrick, J. M.; Poenitz, W. P. *Neutron-capture-activation cross sections of 9496Zr and 98100Mo at thermal and 30 keV energy*; United States, 1982; pp 196-204.

18.   Uddin Md, S.; Afroze, N.; Hossain Syed, M.; Zakaria, A. K. M.; Islam Mohammod, A., Measurement of cross section of the 98Mo(n, γ)99Mo reaction using monochromatic thermal neutrons. In *Radiochim. Acta*, 2015; Vol. 103, p 85.

19.   Abbas, K.; Holzwarth, U.; Simonelli, F.; Kozempel, J.; Cydzik, I.; Bulgheroni, A.; Cotogno, G.; Apostolidis, C.; Bruchertseifer, F.; Morgenstern, A., *Nuclear Instruments and Methods in Physics Research Section B: Beam Interactions with Materials and Atoms* **2012,** *278*, 20-25.

20.   Duchemin, C.; Guertin, A.; Haddad, F.; Michel, N.; Métivier, V., *Physics in Medicine and Biology* **2015,** *60*, 931-946.

21.   Youker, A. J.; Chemerisov, S. D.; Tkac, P.; Kalensky, M.; Heltemes, T. A.; Rotsch, D. A.; Vandegrift, G. F.; Krebs, J. F.; Makarashvili, V.; Stepinski, D. C., *J. Nucl. Med.* **2016**.

22.   Stepinski, D. C.; Youker, A. J.; Chemerisov, S. D.; Tkac, P.; Rotsch, D. A.; Krebs, J. F.; Vandegrift, G. F., *Separation Science and Technology* **2019**, 1-13.

23.   Gagnon, K.; Bénard, F.; Kovacs, M.; Ruth, T. J.; Schaffer, P.; Wilson, J. S.; McQuarrie, S. A., *Nucl. Med. Biol.* **2011,** *38*, 907-916.

24.   Tárkányi, F.; Ditrói, F.; Hermanne, A.; Takács, S.; Ignatyuk, A. V., *Nuclear Instruments and Methods in Physics Research Section B: Beam Interactions with Materials and Atoms* **2012,** *280*, 45-73.

25.   Manenti, S.; Holzwarth, U.; Loriggiola, M.; Gini, L.; Esposito, J.; Groppi, F.; Simonelli, F., *Appl. Radiat. Isot.* **2014,** *94*, 344-348.

26.   Qaim, S. M., *Journal of Radioanalytical and Nuclear Chemistry* **2015,** *305*, 233-245.

27.   Boschi, A.; Martini, P.; Pasquali, M.; Uccelli, L., *Drug Development and Industrial Pharmacy* **2017,** *43*, 1402-1412.

28.   Papagiannopoulou, D., *J. Labelled Comp. Radiopharm.* **2017,** *60*, 502-520.

29.   Alberto, R.; Schibli, R.; Egli, A.; Schubiger, A. P.; Abram, U.; Kaden, T. A., *J. Am. Chem. Soc.* **1998,** *120*, 7987-7988.

30.   Alberto, R.; Ortner, K.; Wheatley, N.; Schibli, R.; Schubiger, A. P., *J. Am. Chem. Soc.* **2001,** *123*, 3135-3136.

31.   Okoye Nkemakonam, C.; Baumeister Jakob, E.; Najafi Khosroshahi, F.; Hennkens Heather, M.; Jurisson Silvia, S., Chelators and metal complex stability for radiopharmaceutical applications. In *Radiochim. Acta*, 2019; Vol. 0.

32.   Schiller, E.; Seifert, S.; Tisato, F.; Refosco, F.; Kraus, W.; Spies, H.; Pietzsch, H.-J., *Bioconjugate Chemistry* **2005,** *16*, 634-643.

33.   Kunstler, J.-U.; Seidel, G.; Pietzsch, H.-J., *Appl. Radiat. Isot.* **2010,** *68*, 1728-1733.

34.   Seifert, S.; Kuenstler, J. U.; Schiller, E.; Pietzsch, H. J.; Pawelke, B.; Bergmann, R.; Spies, H., *Bioconjugate Chemistry* **2004,** *15*, 856-863.

35.   Pietzsch, H. J.; Gupta, A.; Syhre, R.; Leibnitz, P.; Spies, H., *Bioconjugate Chemistry* **2001,** *12*, 538-544.

36.   Spies, H.; Glaser, M.; Pietzsch, H.-J.; Hahn, F. E.; Luegger, T., *Inorg. Chim. Acta* **1995,** *240*, 465-78.

37.   Spies, H.; Glaser, M.; Pietzsch, H.-J.; Hahn, F. E.; Kintzel, O.; Luegger, T., *Angewandte Chemie* **1994,** *106*, 1416-9.

38.   Marmion, M. E.; Woulfe, S. R.; Neumann, W. L.; Nosco, D. L.; Deutsch, E., *Nucl. Med. Biol.* **1999,** *26*, 755-70.

39.   Rossetti, C.; Vanoli, G.; Paganelli, G.; Kwiatkowski, M.; Zito, F.; Colombo, F.; Bonino, C.; Carpinelli, A.; Casati, R.; Deutsch, K.; Marmion, M.; Woulfe, S. R.; Lunghi, F.; Deutsch, E.; Fazio, F., *J. Nucl. Med.* **1994,** *35*, 1571-1580.

40.   Deutsch, E.; Vanderheyden, J.-L.; Gerundini, P.; Libson, K.; Hirth, W.; Colombo, F.; Savi, A.; Fazio, F., *J. Nucl. Med.* **1987,** *28*, 1870-1880.

41.   Jurisson, S. S.; Dancey, K.; McPartlin, M.; Tasker, P. A.; Deutsch, E., *Inorg. Chem.* **1984,** *23*, 4743-9.

42.   Peacock, R. D., *The Chemistry of Technetium and Rhenium*. Elsevier Publishing Company: Amsterdam, 1966.

43.   Johnstone, E. V.; Yates, M. A.; Poineau, F.; Sattelberger, A. P.; Czerwinski, K. R., *Journal of Chemical Education* **2017,** *94*, 320-326.

44.   Ehrhardt, G. J.; Blumer, M. E.; Su, F. M.; Vanderheyden, J. L.; Fritzberg, A. R., *Appl. Radiat. Isot.* **1996,** *48*, 1-4.

45.   Kobayashi, K.; Motoishi, S.; Terunuma, K.; Rauf, A. A.; Hashimoto, K., Production of 186Re and 188Re, and Synthesis of 188Re-DTPA. In *Proceedings of the Sixth Asian Symposium on Research reactors*, Japan Atomic Energy Research Institute: Tokai-mura, Naka-gun, Ibraki, Japan, 1999; pp 232-237.

46.   Moustapha, M. E.; Ehrhardt, G. J.; Smith, C. J.; Szajek, L. P.; Eckelman, W. C.; Jurisson, S. S., *Nucl. Med. Biol.* **2006,** *33*, 81-89.

47.   Bonardi, M. L.; Groppi, F.; Manenti, S.; Persico, E.; Gini, L., *Appl. Radiat. Isot.* **2010,** *68*, 1595-601.

48.   Fassbender, M. E.; Ballard, B.; Birnbaum, E. R.; Engle, J. W.; John, K. D.; Maassen, J. R.; Nortier, F. M.; Lenz, J. W.; Cutler, C. S.; Ketring, A. R.; Jurisson, S. S.; Wilbur, D. S., *Radiochim. Acta* **2013,** *101*, 339-346.

49.   Richards, V. N.; Rath, N.; Lapi, S. E., *Nucl. Med. Biol.* **2015,** *42*, 530-535.

50.   Groppi, F.; Manenti, S.; Gini, L.; Bonardi, M. L., *J. Radioanal. Nucl. Chem.* **2015,** *305*, 179-182.

51.   Balkin, E. R.; Gagnon, K.; Strong, K. T.; Smith, B. E.; Dorman, E. F.; Emery, R. C.; Pauzauskie, P. J.; Fassbender, M. E.; Cutler, C. S.; Ketring, A. R.; Jurisson, S. S.; Wilbur, D. S., *Appl. Radiat. Isot.* **2016,** *115*, 197-207.

52.   Gott, M. D.; Hayes, C. R.; Wycoff, D. E.; Balkin, E. R.; Smith, B. E.; Pauzauskie, P. J.; Fassbender, M. E.; Cutler, C. S.; Ketring, A. R.; Wilbur, D. S.; Jurisson, S. S., *Appl. Radiat. Isot.* **2016,** *114*, 159-166.

53.   Balkin, E. R.; Gagnon, K.; Dorman, E.; Emery, R.; Li, Y.; Wooten, A. L.; Smith, B. E.; Strong, K. T.; Pauzauskie, P. J.; Fassbender, M. E.; Cutler, C. S.; Ketring, A. R.; Jurisson, S. S.; Wilbur, D. S., *Radiochim. Acta* **2017,** *105*, 1071-1081.

54.   Mastren, T.; Radchenko, V.; Bach, H. T.; Balkin, E. R.; Birnbaum, E. R.; Brugh, M.; Engle, J. W.; Gott, M. D.; Guthrie, J.; Hennkens, H. M.; John, K. D.; Ketring, A. R.; Kuchuk, M.; Maassen, J. R.; Naranjo, C. M.; Nortier, F. M.; Phelps, T. E.; Jurisson, S. S.; Wilbur, D. S.; Fassbender, M. E., *Nucl. Med. Biol.* **2017,** *49*, 24-29.

55.   Knapp, F. F., Jr., *Cancer Biother. Radiopharm.* **1998,** *13*, 337-349.

56.   Boschi, A.; Uccelli, L.; Pasquali, M.; Duatti, A.; Taibi, A.; Pupillo, G.; Esposito, J., *Journal of Chemistry* **2014,** *2014*, 1-15.

57.   Zhao, L.; Yuan, J.; Tuo, F.; Zhang, Y.; Kong, X.; Liu, R.; Jiang, L., *Appl. Radiat. Isot.* **2008,** *66*, 1488-1491.

58.   Molla, N. I.; Qaim, S. M., *Nuclear Physics A* **1977,** *283*, 269-288.

59.   Gottesman, M. M.; Pastan, I., *Annual Review of Biochemistry* **1993,** *62*, 385-427.

60.   Mendes, F.; Paulo, A.; Santos, I., *Dalton Trans.* **2011,** *40*, 5377-5393.

61.   Ueda, K.; Cardarelli, C.; Gottesman, M. M.; Pastan, I., *Proceedings of the National Academy of Sciences* **1987,** *84*, 3004.

62.   Ballinger, J. R.; Muzzammil, T.; Moore, M. J., *J. Nucl. Med.* **1997,** *38*, 1915-1919.

63.   Piwnica-Worms, D.; Chiu, M. L.; Budding, M.; Kronauge, J. F.; Kramer, R. A.; Croop, J. M., *Cancer Research* **1993,** *53*, 977.

64.   Ballinger, J. R.; Bannerman, J.; Boxen, I.; Firby, P.; Hartman, N. G.; Moore, M. J., *J. Nucl. Med.* **1996,** *37*, 1578-1582.

65.   Rao, V. V.; Herman, L. W.; Kronauge, J. F.; Piwnica-Worms, D., *Nucl. Med. Biol.* **1998,** *25*, 225-232.

66.   Muzzammil, T.; Moore, M. J.; Ballinger, J. R., *Cancer Biother. Radiopharm.* **2000,** *15*, 339-346.

67.   Liu, Z.; Stevenson, G. D.; Barrett, H. H.; Kastis, G. A.; Bettan, M.; Furenlid, L. R.; Wilson, D. W.; Woolfenden, J. M., *Nucl. Med. Biol.* **2004,** *31*, 53-65.

68.   Aigner, R. M.; Fueger, G. F., *Eur. J. Nucl. Med.* **1997,** *24*, 1167-1170.

69.   Baumeister, J. E.; Mitchell, A. W.; Kelley, S. P.; Barnes, C. L.; Jurisson, S. S., *Dalton Trans.* **2019,** *48*, 12943-12955.

70.   Baumeister, J. E.; Reinig, K. M.; Barnes, C. L.; Kelley, S. P.; Jurisson, S. S., *Inorg. Chem.* **2018,** *57*, 12920-12933.

71.   Rotsch, D. A.; Reinig, K. M.; Weis, E. M.; Taylor, A. B.; Barnes, C. L.; Jurisson, S. S., *Dalton Trans.* **2013,** *42*, 11614-11625.

72.   Lane, S. R.; Sisay, N.; Carney, B.; Dannoon, S.; Williams, S.; Engelbrecht, H. P.; Barnes, C. L.; Jurisson, S. S., *Dalton Trans.* **2011,** *40*, 269-276.

73.   Benny, P. D.; Green, J. L.; Engelbrecht, H. P.; Barnes, C. L.; Jurisson, S. S., *Inorg. Chem.* **2005,** *44*, 2381-2390.

74.   Green, J. L.; Benny, P. D.; Engelbrecht, H. P.; Barnes, C. L.; Jurisson, S. S., *Syn. React. Inorg. Met.-Org. Nano-Met. Chem.* **2005,** *35*, 53-59.

75.   Benny, P. D.; Barnes, C. L.; Piekarski, P. M.; Lydon, J. D.; Jurisson, S. S., *Inorg. Chem.* **2003,** *42*, 6519-6527.

76.   Carroll, V.; Demoin, D. W.; Hoffman, T. J.; Jurisson, S. S., *Radiochim. Acta* **2012,** *100*, 653.

77.   Jürgens, S.; Herrmann, W. A.; Kühn, F. E., *J. Organomet. Chem.* **2014,** *751*, 83-89.

78.   Jurisson, S. S.; Lydon, J. D., *Chem. Rev.* **1999,** *99*, 2205-2218.

79.   Schwochau, K., *Angew. Chem.* **1994,** *33*, 2258-2267.

80.	Mahmood, A.; Jones, A. G., Technetium Radiopharmaceuticals. In *Handbook of Radiopharmaceuticals*, 2005.

81.	Volkert, W. A.; Hoffman, T. J., *Chem. Rev.* **1999,** *99*, 2269-2292.

82.	Heeg, M. J.; Jurisson, S. S., *Acc. Chem. Res.* **1999,** *32*, 1053-1060.

83.	Szelecsenyi, F.; Steyn, G. F.; Kovacs, Z.; Aardaneh, K.; Vermeulen, C.; Walt, T. N., *Journal of Radioanalytical and Nuclear Chemistry* **2009,** *282*, 261-263.

84.	Jurisson, S.; Lindoy, L. F.; Dancey, K. P.; McPartlin, M.; Tasker, P. A.; Uppal, D. K.; Deutsch, E., *Inorg. Chem.* **1984,** *23*, 227-31.

85.	Ichimura, A.; Heineman, W. R.; Deutsch, E., *Inorg. Chem.* **1985,** *24*, 2134-9.

86.	Luker, G. D.; Rao, V. V.; Crankshaw, C. L.; Dahlheimer, J.; Piwnica-Worms, D., *Biochemistry* **1997,** *36*, 14218-14227.

87.	Crankshaw, C. L.; Marmion, M.; Luker, G. D.; Rao, V.; Dahlheimer, J.; Burleigh, B. D.; Webb, E.; Deutsch, K. F.; Piwnica-Worms, D., *J. Nucl. Med.* **1998,** *39*, 77-86.

88.	Gerson, M. C.; Millard, R. W.; Roszell, N. J.; McGoron, A. J.; Gabel, M.; Washburn, L. C.; Biniakiewicz, D.; Blankenship, D.; Mallin, W. H.; Elder, R. C., *Circulation* **1994,** *89*, 1291-300.

89.	Schaefer, W. M.; Moka, D.; Brockmann, H. A.; Schomaecker, K.; Schicha, H., *Nucl. Med. Biol.* **2002,** *29*, 243-254.

90.	Matsunari, I.; Haas, F.; Nguyen, N. T. B.; Reidel, G.; Wolf, I.; Senekowitsch-Schmidtke, R.; Stocklin, G.; Schwaiger, M., *J. Nucl. Med.* **2001,** *42*, 818-823.

91.	Luo, H.; Liu, S.; Rettig, S. J.; Orvig, C., *Can. J. Chem.* **1995,** *73*, 2272-81.

92.	Alberto, R.; Schibli, R.; Egli, A.; Schubiger, P. A.; Herrmann, W. A.; Artus, G.; Abram, U.; Kaden, T. A., *J. Organomet. Chem.* **1995,** *493*, 119-27.

93.	Davison, A.; Trop, H. S.; Depamphilis, B. V.; Jones, A. G.; Thomas, R. W.; Jurisson, S. S., 34. Tetrabutylammonium Tetrachlorooxo-Technetate(V). In 2007; Vol. 21.

94.	*Apex3, AXScale and SAINT, version 2017.3-0.* Bruker AXS, Inc.: Madison, WI, 2017.

95.	Jurisson, S.; Schlemper, E. O.; Troutner, D. E.; Canning, L. R.; Nowotnik, D. P.; Neirinckx, R. D., *Inorg. Chem.* **1986,** *25*, 543-549.

96.	Chatt, J.; Leigh, G. J.; Mingos, D. M. P.; Randall, E. W.; Shaw, D., *Chem. Comm.* **1968**, 419-20.

97.   Randall, E. W.; Shaw, D., *J. Chem. Soc. A* **1969**, 2867-72.

98.   Pearson, C.; Beauchamp, A. L., *Inorg. Chim. Acta* **1995,** *237*, 13-18.

99.   Randall, E. W.; Shaw, D., *Mol. Phys.* **1965,** *10*, 41-8.

100.   Mitsopoulou, C. A.; Mahieu, N.; Motevalli, M.; Randall, E. W., *J. Chem. Soc., Dalton Trans.* **1996**, 4563-4566.

101.   Gunz, H. P.; Leigh, G. J., *Journal of the Chemical Society A Inorganic Physical Theoretical* **1971**, 2229-33.

102.   Shaw, D.; Randall, E. W., *Chem. Comm.* **1965**, 82-3.

103.   Bhattacharyya, S.; Banerjee, S.; Kumar Dirghangi, B.; Menon, M.; Chakravorty, A., *J. Chem. Soc., Dalton Trans.* **1999**, 155-160.

104.   Mazzi, U.; de Paoli, G.; di Bernardo, P.; Magon, L., *J. Inorg. Nucl. Chem.* **1976,** *38*, 721-5.

105.   Mazzi, U.; Bismondo, A.; Kotsev, N.; Clemente, D. A., *J. Organomet. Chem.* **1977,** *135*, 177-82.

106.   Deutsch, E.; Ketring, A. R.; Libson, K.; Vanderheyden, J. L.; Hirth, W. W., *Nucl. Med. Biol.* **1989,** *16*, 191-232.

107.   Bandoli, G.; Mazzi, U.; Wilcox, B. E.; Jurisson, S.; Deutsch, E., *Inorg. Chim. Acta* **1984,** *95*, 217-23.

108.   Bandoli, G.; Mazzi, U.; Spies, H.; Münze, R.; Ludwig, E.; Ulheman, E.; Scheller, D., *Inorg. Chim. Acta* **1987,** *132*, 177-185.

109.   Abrahams, A. R.; Cowley, A. R.; Gerber, T. I. A.; Imrie, C.; Mayer, P., *J. Coord. Chem.* **2003,** *56*, 1299-1306.

110.   Liu, J.; Su, X.; Han, M.; Wu, D.; Gray, D. L.; Shapley, J. R.; Werth, C. J.; Strathmann, T. J., *Inorg. Chem.* **2017,** *56*, 1757-1769.

111.   Duatti, A.; Marchi, A.; Luna, S. A.; Bandoli, G.; Mazzi, U.; Tisato, F., *J. Chem. Soc., Dalton Trans.* **1987**, 867-871.

112.   Mazzi, U.; Refosco, F.; Tisato, F.; Bandoli, G.; Nicolini, M., *J. Chem. Soc., Dalton Trans.* **1988**, 847-850.

113.   Zwettler, N.; Schachner, J. A.; Belaj, F.; Mösch-Zanetti, N. C., *Inorg. Chem.* **2016,** *55*, 5973-5982.

114.   Ison, E. A.; Cessarich, J. E.; Travia, N. E.; Fanwick, P. E.; Abu-Omar, M. M., *J. Am. Chem. Soc.* **2007,** *129*, 1167-1178.

115.   Du, G.; Abu-Omar, M. M., *Organomet.* **2006,** *25*, 4920-4923.

116.   Ison, E. A.; Cessarich, J. E.; Du, G.; Fanwick, P. E.; Abu-Omar, M. M., *Inorg. Chem.* **2006,** *45*, 2385-2387.

117.   Chakraborty, I.; Panda, B. K.; Gangopadhyay, J.; Chakravorty, A., *Inorg. Chem.* **2005,** *44*, 1054-1060.

118.   Lohrey, T. D.; Bergman, R. G.; Arnold, J., *Inorg. Chem.* **2016,** *55*, 11993-12000.

119.   Wang, J.; Wang, W.; Huang, L.; Yang, X.; Wei, H., *ChemPhysChem* **2015,** *16*, 1052-1060.

120.   Du, G.; Fanwick, P. E.; Abu-Omar, M. M., *Inorg. Chim. Acta* **2008,** *361*, 3184-3192.

121.   Qiu, C.-J.; Zhang, Y.-C.; Gao, Y.; Zhao, J.-Q., *J. Organomet. Chem.* **2009,** *694*, 3418-3424.

122.   Zhang, B.; Li, S.; Herdtweck, E.; Kühn, F. E., *J. Organomet. Chem.* **2013,** *739*, 63-68.

123.   Zhou, M.-D.; Yu, Y.; Capapé, A.; Jain, K. R.; Herdtweck, E.; Li, X.-R.; Li, J.; Zang, S.-L.; Kühn, F. E., *Chemistry – An Asian Journal* **2009,** *4*, 411-418.

124.   Kemp, T. J.; Thyer, A. M.; Wilson, P. D., *J. Chem. Soc., Dalton Trans.* **1993**, 2601-5.

125.   Kemp, T. J.; Thyer, A. M.; Wilson, P. D., *J. Chem. Soc., Dalton Trans.* **1993**, 2607-11.

126.   Panich, N. M.; Pirogova, G. N.; Korosteleva, R. I., *Radiochemistry (Moscow)(Transl. of Radiokhimiya)* **1997,** *39*, 223-227.

127.   Rimar, N. N.; Pirogova, G. N., *Russian Chemical Bulletin* **1998,** *47*, 398-401.

128.   Furman, D. B.; Barkova, A. P.; Kazanskii, V. B., *Kinet. Catal. (Transl. of Kinet. Katal.)* **1997,** *38*, 381-383.

129.   De Vries, N.; Jones, A. G.; Davison, A., *Inorg. Chem.* **1989,** *28*, 3728-34.

130.   Aniagyei, A.; Tia, R.; Adei, E., *Computational and Theoretical Chemistry* **2013,** *1009*, 70-80.

131.   Deutsch, E.; Vanderheyden, J. L.; Gerundini, P.; Libson, K.; Hirth, W.; Colombo, F.; Zecca, L.; Savi, A.; Fazio, F., *J. Nucl. Med.* **1987,** *28*, 1870-80.

132.   Patel, K. S.; Bailar, J. C., Jr., *J. Inorg. Nucl. Chem.* **1971,** *33*, 1399-406.

133.   Middleton, A. R.; Masters, A. F.; Wilkinson, G., *J. Chem. Soc., Dalton Trans.* **1979**, 542-546.

134.   Bottomley, L. A.; Wojciechowski, P. E.; Holder, G. N., *Inorg. Chim. Acta* **1997,** *255*, 149-155.

135.   van Bommel, K. J. C.; Verboom, W.; Kooijman, H.; Spek, A. L.; Reinhoudt, D. N., *Inorg. Chem.* **1998,** *37*, 4197-4203.

136.   Bolzati, C.; Porchia, M.; Bandoli, G.; Boschi, A.; Malago, E.; Uccelli, L., *Inorg. Chim. Acta* **2001,** *315*, 205-212.

137.   Dixon, K. R., Phosphorus-31. In *Multinuclear NMR*, Mason, J., Ed. Plenum Press: New York, 1989; pp 369-396.

138.   Rossi, R.; Duatti, A.; Magon, L.; Casellato, U.; Graziani, R.; Toniolo, L., *J. Chem. Soc., Dalton Trans.* **1982**, 1949-52.

139.   Cotton, F. A.; Luck, R. L., *Inorg. Chem.* **1989,** *28*, 2181-6.

140.   Over, D. E.; Critchlow, S. C.; Mayer, J. M., *Inorg. Chem.* **1992,** *31*, 4643-8.

141.   Tisato, F.; Refosco, F.; Bolzati, C.; Cagnolini, A.; Gatto, S.; Bandoli, G., *J. Chem. Soc., Dalton Trans.* **1997**, 1421-1427.

142.   Kirchhoff, J. R.; Heineman, W. R.; Deutsch, E., *Inorg. Chem.* **1987,** *26*, 3108-13.

143.   Takeuchi, T.; Boettcher, A.; Quezada, C. M.; Simon, M. I.; Meade, T. J.; Gray, H. B., *J. Am. Chem. Soc.* **1998,** *120*, 8555-8556.

144.   Schally, A. V.; Janaky, T.; Cai, R. Z. Preparation of somatostatin analogs. EP450480A2, 1991.

145.   Schally, A. V.; Bajuz, S.; Janaky, T. Preparation of cytotoxic LHRH analogs. EP364819A2, 1990.

146.   Bajusz, S.; Janaky, T.; Csernus, V. J.; Bokser, L.; Fekete, M.; Srkalovic, G.; Redding, T. W.; Schally, A. V., *Proc. Natl. Acad. Sci. U. S. A.* **1989,** *86*, 6313-17.

147.   Pordea, A.; Mathis, D.; Ward, T. R., *J. Organomet. Chem.* **2009,** *694*, 930-936.

148.   Oliveri, V.; Puglisi, A.; Vecchio, G., *Dalton Trans.* **2011,** *40*, 2913-2919.

149.   Moradell, S.; Lorenzo, J.; Rovira, A.; van Zutphen, S.; Aviles, F. X.; Moreno, V.; de Llorens, R.; Martinez, M. A.; Reedijk, J.; Llobet, A., *J. Inorg. Biochem.* **2004,** *98*, 1933-1946.

150.   Sheldrick, G. M., *Acta Crystallogr. A* **2015,** *71*, 3-8.

151. Sheldrick, G. M. *SHELXS, v.2013-1*, 2013.

152. Sheldrick, G. M., *Acta Crystallogr. C* **2015,** *71*, 3-8.

153. Thorn, A.; Dittrich, B.; Sheldrick, G. M., *Acta Crystallogr. A* **2012,** *68*, 448-451.

154. Spek, A. L., *Acta Crystallogr. C* **2015,** *71*, 9-18.

VITA

Jakob Edwin Baumeister was born on October 6, 1991 in Lake Jackson, Texas at Brazosport Memorial Hospital to Eldon and Mary Jo Baumeister. He spent his formative years in Lake Jackson, Texas and graduated from Brazoswood High School in 2010. He earned a Bachelors of Science in Chemistry from the University of Texas at Austin in 2014. He moved to Columbia, Missouri in 2015 to begin his doctoral studies under the supervision of Prof. Silvia Jurisson at the University of Missouri-Columbia. He received a PhD in Chemistry from the University of Missouri-Columbia in December of 2019. He accepted a postdoctoral appointment with Dr. Cathy Cutler at Brookhaven National Laboratory for the spring of 2020.

He is married to the former Haley Elizabeth Olson. The couple is expecting their first son—Ezra Barry Baumeister—in December of 2019. They hope to have many more children in the future. Soli Deo Gloria.